

# **INTERACTIONS BETWEEN AQUEOUS FLUIDS AND SILICATE MELTS**

**Equilibration, partitioning and  
complexation of trace elements**

kumulative Dissertation  
zur Erlangung des akademischen Grades  
"doctor rerum naturalium"  
(Dr. rer. nat.)

in der Wissenschaftsdisziplin "Mineralogie"

eingereicht an der  
Mathematisch-Naturwissenschaftlichen Fakultät  
der Universität Potsdam

**von**

**Dipl.-Min. Manuela Borchert**

November 2009

**Betreuer: Prof. R. Oberhänsli und Dr. Christian Schmidt**

**Projektleiter: Dr. Max Wilke**





**"But o dear, o dear, o deary,  
When the end comes sad and dreary!  
'Tis is a dreadful thing to tell  
That on Max and Moritz fell!  
All they did this book rehearses,  
Both in pictures and in verses."**

**from "Max and Moritz"  
A juvenile history in seven tricks  
by Wilhelm Busch**



---

## Acknowledgements

Many people supported me during the last three years, and this work has greatly benefited from their help. First of all, I would like to express my gratitude to Max Wilke and Christian Schmidt, who initiated and supervised this project. Without their continuous guidance, help, and encouragement, the research presented here could not have been accomplished. Their doors were always open for me to discuss various aspects of my work. Both encouraged and supported me to attend several scientific meetings, which allowed me to practice presentation of my results and to get insights into new developments and directions in my research area. All in all, I had a great time and I could not imagine a better supervisor team – thanks a lot, Max and Christian!

I would like to thank Karen Appel for her enormous support during the measurements at beamline L, and the active interest in my work, which included all the patient answers to plenty of my technical questions, the fruitful discussions, and the various comments that helped to improve the quality of the presented manuscripts.

Furthermore, I like to thank all actual and former members of the work group "Mineralogie" at the Institut für Erd- und Umweltwissenschaften (Universität Potsdam) for their support, encouragement, and the possibility to collect teaching skills. In particular, I like to mention Roland Oberhänsli, Uwe Altenberger, Romain Bousquet, Andreas Möller, Patrick O'Brien, and Beate Mocek. I also like to express my gratitude to all members of the department 3.3 at the GeoForschungsZentrum Potsdam for their support and lively discussion of my results, and the possibility to use all laboratories and analytical instruments.

I would also apply my gratitude to following people: Reiner Schulz for his technical support during the performance of the quench experiments, Antje Musiol for teaching me the usage of the ICP-OES and for her help during other laboratory work, Oona Appelt for her kind support during the EMP analyses, Andrea Gottsche, who introduced me to Ion Chromatography and her friendly support during some other laboratory work, and Jean Cauzid, Pieter Glatzel, Kristina Kvashnina, and the beamline staff at ID22 and ID26 for their technical support during the measurements at the ESRF.

Finally, many thanks to my friends (and colleges) Maik, Anke, Franzi, Gregor, Nic, Fiore, Basti, Tina, Hans-Peter, Mónica, Ati, Andre, Sylvie, Nadine, and Max for the plenty of funny "after work" activities, and for their support during the stressful last few weeks of this work.

Last but not least I am very grateful to my family for their continuous support, understanding, and encouragement during the last years. Thanks so much mum, dad, Micha, Diana, Jenny, Hanelore, Udo, grandma, grandpa, and of course, Maik and my beloved "little" son Adrian.



---

## Zusammenfassung

Die Entstehung und Entwicklung von Graniten steht seit Jahrzehnten im Fokus vieler geologischer Studien, da sich die Erdkruste zu großen Teilen aus granitoiden Gesteinen zusammensetzt. Von besonderer Bedeutung für die Bildung von granitischen Schmelzen ist neben der Temperatur, der Wassergehalt der Schmelze, da dieser Parameter die chemische Zusammensetzung der Schmelze entscheidend verändern kann. Die Entmischung wässriger Fluide aus Schmelzen führt zur Neuverteilung von Elementen zwischen diesen Phasen. Bedingt durch die geringere Dichte des wässrigen Fluids im Vergleich zur Schmelze und dem Nebengestein, beginnt dieses aus tieferen Erdschichten aufzusteigen. Damit verknüpft ist nicht nur eine räumliche Trennung von Schmelze und Fluid, sondern auch die Alterierung des Nebengestein. Dieser Prozess ist insbesondere bei der Bildung von magmatisch-hydrothermalen Lagerstätten und in späten Entwicklungsstadien magmatischer Komplexe wichtig. Für ein detailliertes Verständnis dieser Prozesse ist es notwendig, das Elementverhalten in solchen Systemen in Abhängigkeit von Parametern wie Temperatur, Druck und chemischer Zusammensetzung des Systems experimentell zu untersuchen, und Elementverteilungskoeffizienten als Funktion dieser Variablen zu bestimmen. Für die Untersuchungen sind insbesondere Spurenelemente geeignet, da diese im Gegensatz zu Hauptelementen nicht essentiell für die Stabilität weiterer auftretender Phasen sind, aber sehr sensibel auf Änderungen intensiver Variablen reagieren können. Zudem werden bei geochemischen Mineral- und Gesteinsanalysen viele Spurenelemente, Spurenelementverhältnisse, und Spurenelementisotope als petrogenetische Indikatoren verwendet, d.h. diese Daten liefern Informationen darüber, wann und in welcher Tiefe und bei welchen chemischen Bedingungen ein Gestein gebildet worden ist, und welche weiteren Prozesse es auf dem Weg zur Erdoberfläche durchlaufen hat. Allerdings sind für viele Spurenelemente die Abhängigkeiten der Verteilung zwischen Fluiden und Schmelzen von intensiven Variablen nicht, oder nur unzureichend experimentell untersucht worden. Zusätzlich dazu basiert die Mehrheit der experimentell gewonnenen Verteilungskoeffizienten und deren Interpretation, insbesondere hinsichtlich der Elementkomplexierung im Fluid, auf der Analyse von schnell abgekühlten Phasen. Bisher ist nicht geklärt, ob solche Analysen repräsentativ sind für die Zusammensetzungen der Phasen bei hohen Drücken und Temperaturen.

Das Ziel dieser Studie war die Erarbeitung eines experimentellen Datensatzes zur Spurenelementverteilung zwischen granitischen Schmelzen und wässrigen Fluiden in Abhängigkeit von der Schmelzzusammensetzung, der Salinität des Fluids, des Drucks und der Temperatur. Ein Hauptanliegen der Arbeit bestand in der Weiterentwicklung einer experimentellen Methode bei welcher der Spurenelementgehalt im Fluid in-situ, d.h. unter hohen Drücken und Temperaturen, und im Gleichgewicht mit einer silikatischen Schmelze bestimmt wird. Die so gewonnenen Daten können anschließend mit den Resultaten von Abkühlexperimenten verglichen werden, um diese und auch Literaturdaten kritisch zu bewerten. Die Daten aller untersuchten Spurenelemente dieser Arbeit (Rb, Sr, Ba, La, Y und Yb) zeigen:

1. unter den untersuchten Bedingungen eine Präferenz für die Schmelze unabhängig von der chemischen Zusammensetzung von Schmelze und Fluid, Druck oder Temperatur,
2. die Verwendung von chloridhaltigen Fluiden kann die Verteilungskoeffizienten um 1 bis 2 Größenordnungen anheben und

- 
3. für die Verteilungskoeffizienten von Sr, Ba, La, Y und Yb eine starke Abhängigkeit von der Schmelzzusammensetzung im chloridischen System.

Der Vergleich der Daten der verschiedenen Methoden zeigt, dass insbesondere für chloridfreie Fluide große Diskrepanzen zwischen den in-situ Daten und Analysen von abgeschreckten Proben bestehen. Dieses Ergebnis beweist eindeutig, dass beim Abschrecken der Proben Rückreaktionen stattfinden, und dass Daten, welche auf Analysen abgeschreckter Fluide basieren, nur eingeschränkt verwendet werden sollten. Die Variation der Verteilungskoeffizienten von Sr, Ba, La, Yb, und Y als Funktion der Schmelzzusammensetzung ist entweder auf eine Änderung der Komplexierung im Fluid und/oder einen anderen veränderten Einbau dieser Elemente in die Schmelze zurückzuführen. Daher wurde im Rahmen dieser Arbeit erstmals versucht, die Elementkomplexierung in silikatischen Fluiden direkt bei hohen Temperaturen und Drücken zu bestimmen. Die Daten für Sr zeigen, dass abhängig von der Schmelzzusammensetzung unterschiedliche Komplexe stabil sein müssen.



---

## Abstract

The origin and evolution of granites has been widely studied because granitoid rocks constitute a major portion of the Earth's crust. The formation of granitic magma is, besides temperature mainly triggered by the water content of these rocks. The presence of water in magmas plays an important role due to the ability of aqueous fluids to change the chemical composition of the magma. The exsolution of aqueous fluids from melts is closely linked to a fractionation of elements between the two phases. Then, aqueous fluids migrate to shallower parts of the Earth's crust because of its lower density compared to that of melts and adjacent rocks. This process separates fluids and melts, and furthermore, during the ascent, aqueous fluids can react with the adjacent rocks and alter their chemical signature. This is particularly important during the formation of magmatic-hydrothermal ore deposits or in the late stages of the evolution of magmatic complexes. For a deeper insight to these processes, it is essential to improve our knowledge on element behavior in such systems. In particular, trace elements are used for these studies and petrogenetic interpretations because, unlike major elements, they are not essential for the stability of the phases involved and often reflect magmatic processes with less ambiguity. However, for the majority of important trace elements, the dependence of the geochemical behavior on temperature, pressure, and in particular on the composition of the system are only incompletely or not at all experimentally studied. Former studies often focus on the determination of fluid–melt partition coefficients ( $D_X^{f/m} = c_X^{\text{fluid}}/c_X^{\text{melt}}$ ) of economically interesting elements, e.g., Mo, Sn, Cu, and there are some partitioning data available for elements that are also commonly used for petrological interpretations. At present, no systematic experimental data on trace element behavior in fluid–melt systems as function of pressure, temperature, and chemical composition are available. Additionally, almost all existing data are based on the analysis of quenched phases. This results in substantial uncertainties, particularly for the quenched aqueous fluid because trace element concentrations may change upon cooling.

The objective of this PhD thesis consisted in the study of fluid–melt partition coefficients between aqueous solutions and granitic melts for different trace elements (Rb, Sr, Ba, La, Y, and Yb) as a function of temperature, pressure, salinity of the fluid, composition of the melt, and experimental and analytical approach. The latter included the refinement of an existing method to measure trace element concentrations in fluids equilibrated with silicate melts directly at elevated pressures and temperatures using a hydrothermal diamond-anvil cell and synchrotron radiation X-ray fluorescence microanalysis. The application of this in-situ method enables to avoid the main source of error in data from quench experiments, i.e., trace element concentration in the fluid. A comparison of the in-situ results to data of conventional quench experiments allows a critical evaluation of quench data from this study and literature data.

In detail, starting materials consisted of a suite of trace element doped haplogranitic glasses with ASI varying between 0.8 and 1.4 and H<sub>2</sub>O or a chloridic solution with  $m$  NaCl/KCl=1 and different salinities (1.16 to 3.56  $m$  (NaCl+KCl)). Experiments were performed at 750 to 950°C and 0.2 or 0.5 GPa using conventional quench devices (externally and internally heated pressure vessels) with different quench rates, and at 750°C and 0.2 to 1.4 GPa with in-situ analysis of the trace element concentration in the fluids. The fluid–melt partitioning data

---

of all studied trace elements show

1. a preference for the melt ( $D^{f/m} < 1$ ) at all studied conditions,
2. one to two orders of magnitude higher  $D^{f/m}$  using chloridic solutions compared to experiments with  $H_2O$ ,
3. a clear dependence on the melt composition for fluid–melt partitioning of Sr, Ba, La, Y, and Yb in experiments using chloridic solutions,
4. quench rate–related differences of fluid–melt partition coefficients of Rb and Sr, and
5. distinctly higher fluid–melt partitioning data obtained from in-situ experiments than from comparable quench runs, particularly in the case of  $H_2O$  as starting solution.

The data point to a preference of all studied trace elements for the melt even at fairly high salinities, which contrasts with other experimental studies, but is supported by data from studies of natural co-genetically trapped fluid and melt inclusions. The in-situ measurements of trace element concentrations in the fluid verify that aqueous fluids will change their composition upon cooling, which is in particular important for Cl free systems. The distinct differences of the in-situ results to quench data of this study as well as to data from the literature signify the importance of a careful fluid sampling and analysis. Therefore, the direct measurement of trace element contents in fluids equilibrated with silicate melts at elevated PT conditions represents an important development to obtain more reliable fluid–melt partition coefficients. For further improvement, both the aqueous fluid and the silicate melt need to be analyzed in-situ because partitioning data that are based on the direct measurement of the trace element content in the fluid and analysis of a quenched melt are still not completely free of quench effects.

At present, all available data on element complexation in aqueous fluids in equilibrium with silicate melts at high PT are indirectly derived from partitioning data, which involves in these experiments assumptions on the species present in the fluid. However, the activities of chemical components in these partitioning experiments are not well constrained, which is required for the definition of exchange equilibria between melt and fluid species. For example, the melt-dependent variation of partition coefficient observed for Sr imply that this element can not only be complexed by  $Cl^-$  as suggested previously. The data indicate a more complicated complexation of Sr in the aqueous fluid. To verify this hypothesis, the in-situ setup was also used to determine strontium complexation in fluids equilibrated with silicate melts at desired PT conditions by the application of X-ray absorption near edge structure (XANES) spectroscopy. First results show a strong effect of both fluid and melt composition on the resulting XANES spectra, which indicates different complexation environments for Sr.

---

### List of abbreviations

ASI	alumina saturation index, $ASI = Al_2O_3 / (Na_2O + K_2O)$ in moles
$c_X^f$	concentration of element X in the fluid
$c_X^m$	concentration of element X in the melt
$D_X^{f/m}$	partition coefficient of element X
EHPV	externally heated pressure vessel
EMPA	electron microprobe analysis
EXAFS	extended X-ray absorption fine structure
HDAC	hydrothermal diamond-anvil cell
IC	ion chromatography
ICP-OES	Inductively-couple plasma - optical emission spectrometry
IHPV	internally heated pressure vessel
laser ablation ICP-MS	laser ablation Inductively-couple plasma - mass spectrometry
RQ	rapid quench
SR- $\mu$ XRF	Synchrotron Radiation X-ray fluorescence microanalysis
SQ	slow quench
XAFS	X-ray absorption fine structure
XANES	X-ray absorption near edge structure

# Contents

<b>1</b>	<b>Introduction</b>	<b>8</b>
<b>2</b>	<b>Partitioning and equilibration of Rb and Sr between silicate melts and aqueous fluids</b>	<b>16</b>
2.1	Introduction . . . . .	17
2.2	Experimental methods . . . . .	18
2.2.1	Starting Materials . . . . .	18
2.2.2	Hydrothermal diamond-anvil cell . . . . .	20
2.2.3	Sample preparation . . . . .	20
2.2.4	HDAC experiments . . . . .	21
2.2.5	XRF spectra acquisition and calibration . . . . .	22
2.2.6	EMP analyses . . . . .	24
2.3	Results and Discussion . . . . .	24
2.4	Conclusions . . . . .	28
<b>3</b>	<b>Rb and Sr partitioning between haplogranitic melts and aqueous solutions</b>	<b>34</b>
3.1	Introduction . . . . .	35
3.2	Experimental and analytical methods . . . . .	38
3.2.1	Starting materials and sample preparation . . . . .	38
3.2.2	Quench experiments . . . . .	39
3.2.3	In-situ experiments . . . . .	39
3.2.4	Analysis of run products . . . . .	40
3.3	Results . . . . .	41
3.4	Discussion . . . . .	44
3.4.1	Quench effects . . . . .	44
3.4.2	Fluid–melt partitioning and complexation of Rb and Sr . . . . .	46
3.4.3	Modeling of the behavior of Rb and Sr during evolution of a granitic system . . . . .	47
3.5	Conclusions . . . . .	48
<b>4</b>	<b>Partitioning of Ba, La, Yb, and Y between haplogranitic melts and aqueous solutions</b>	<b>60</b>
4.1	Introduction . . . . .	62
4.2	Experimental and analytical methods . . . . .	64
4.2.1	Starting materials and sample preparation . . . . .	64

---

4.2.2	Quench experiments . . . . .	65
4.2.3	In-situ experiments . . . . .	65
4.2.4	Analysis of run products . . . . .	67
4.3	Results . . . . .	68
4.3.1	Quench experiments . . . . .	68
4.3.2	HDAC experiments - evaluation of sensitivity . . . . .	69
4.3.3	HDAC experiments - partitioning data . . . . .	71
4.3.4	Comparison of quenched and HDAC runs . . . . .	75
4.4	Discussion and conclusions . . . . .	75
4.4.1	Fluid–melt partitioning . . . . .	75
4.4.2	In-situ XRF analyses using high excitation energies . . . . .	81
<b>5</b>	<b>Discussion and conclusions</b>	<b>92</b>
<b>6</b>	<b>Outlook</b>	<b>98</b>
6.1	Further improvements of the in-situ method . . . . .	98
6.2	Strontium complexation in fluids equilibrated with silicate melts at high PT conditions . . . . .	99
<b>References</b>		
<b>Appendix</b>		
<b>A</b>	<b>Additional fluid–melt partitioning data - the system albite-quartz</b>	<b>II</b>
<b>B</b>	<b>Methods for fluid analyses in quenched experiments</b>	<b>VI</b>
B.1	Inductively-coupled plasma - optical emission spectrometry . . . . .	VI
B.2	Ion Chromatography . . . . .	VIII
<b>C</b>	<b>Curriculum Vitae</b>	<b>X</b>

# List of Figures

2.1	A - Schematic diagram showing the details of the modified Bassett-type hydrothermal diamond anvil cell. B - Top view of the experimental setup at beamline L, HASYLAB (DESY, HAMBURG) (after Schmidt and Rickers (2003), modified). . . . .	19
2.2	View in the sample chamber at 750°C. The recess is free of melt and thus, the measured SR- $\mu$ XRF signal contains no contribution from the melt. . . . .	21
2.3	SR- $\mu$ XRF spectra of a sample containing 2.84 <i>m</i> (NaCl+KCl) + 0.03 <i>m</i> HCl and a standard solution. . . . .	23
2.4	Concentration of trace elements Rb and Sr in the aqueous fluid vs. elapsed time after attainment of the experimental temperature $T_{exp}$ for various fluid compositions: <b>A</b> - 3.56 <i>m</i> (NaCl+KCl) + 0.04 <i>m</i> HCl, <b>B</b> - 2.84 <i>m</i> (NaCl+KCl) + 0.03 <i>m</i> HCl and, <b>C</b> H <sub>2</sub> O. The error bars represent 2 $\sigma$ errors. . . . .	26
2.5	Rb/Sr ratio in the fluid vs. pressure. The diagram shows a constant Rb/Sr ratio at 750°C for various compositions and low pressures. For H <sub>2</sub> O–melt experiments at constant temperatures we see a strong pressure dependence of the Rb/Sr ratio in the fluid. . . . .	27
2.6	Fluid–melt partition coefficients of Rb and Sr vs. initial salt concentration of the fluid [ <i>m</i> (NaCl+KCl)] at 750°C. For similar pressures an increase of initial salt concentration corresponds to an increase of $D_{Rb}^{f/m}$ and $D_{Sr}^{f/m}$ . For H <sub>2</sub> O–melt experiments, we observed a pressure dependence of the D values particularly for Rb (light grey symbols = experiment at 700 MPa). . . . .	28
3.1	Rubidium partition coefficient obtained for chloridic and non-chloridic fluids vs. melt composition expressed as ASI. PT conditions are as indicated by symbols. Errors ( $\pm 1\sigma$ ) are smaller than symbol size. RQ - rapid quench, SQ - slow quench. . . . .	42
3.2	Strontium partition coefficient obtained for chloridic and non-chloridic fluids vs. melt composition expressed as ASI. PT conditions are as indicated by symbols. Errors ( $\pm 1\sigma$ ) are smaller than symbol size. RQ - rapid quench, SQ - slow quench. . . . .	43
3.3	Rb/Sr ratio in the fluid vs. pressure determined in-situ at 750°C for non-chloridic (Fig. 3.3.1 ) and chloridic fluids (Fig. 3.3.2). All starting glasses had the same metaluminous composition. Error bars - $\pm 1\sigma$ . . . . .	43

3.4	Partition coefficients of Rb and Sr at 750°C from HDAC experiments as function of pressure and salinity. Results for non-chloridic solutions are shown in Fig. 3.4.1 and data for chloridic fluids are presented in Fig. 3.4.2. Error bars - $\pm 1\sigma$ .	44
3.5	Comparison of fluid–melt partitioning data for Rb and Sr from quench and HDAC experiments, and for chloridic and non-chloridic solutions. All data are for a temperature of 750°C and metaluminous starting glass. Figure 3.5.1 shows the data for Rb as a function of pressure and analogous for Sr in Fig. 3.5.2. Error bars - $\pm 1\sigma$ .	45
3.6	Comparison of fluid–melt partition coefficients and Rb/Sr ratio in the fluid obtained in this study with literature data (Bai and Koster van Groos, 1999) for experiments at 750°C, 200 MPa, with metaluminous starting glasses. Figure 3.6.1 shows the Rb/Sr ratio in the fluid as function of pressure for two salinity intervals, and Figs. 3.6.2 and 3.6.3 display the partition coefficients of Rb and Sr for various salinities. Error bars - $\pm 1\sigma$ .	48
3.7	Models for the Rb and Sr contents, and Rb/Sr ratio of the residual melt during an isobaric crystallization path (200 MPa) assuming Rayleigh fractionation in Fig. 3.7.1 and equilibrium crystallization in Fig. 3.7.2 using the peraluminous starting composition ( $\text{Ab}_{38.92}\text{Or}_{23.46}\text{Qz}_{35.08}+\text{C}_{2.53}$ ) with 3 wt.% total water. Solid lines based on fluid–melt partitioning data from this study, dashed lines - $D^{f/m}$ from Bai and Koster van Groos (1999)).	49
4.1	Barium partition coefficient at 750°C and 200 MPa obtained from rapid and slow quenched experiments for chloridic and non-chloridic fluids vs. melt composition expressed as ASI. Errors ( $\pm 1\sigma$ ) are, in some cases, smaller than symbol size. RQ - rapid quench, IHPV - slow quench, (Pt) - Pt capsule, (Au) - Au capsule.	69
4.2	Partition coefficients from chloridic fluids of La, Yb and Y in the fluid vs. melt composition at 750°C and 200 MPa (Fig. 4.2.1), and La partition coefficient obtained from quenched experiments for various PT conditions (Fig. 4.2.2). Error bars - $\pm 1\sigma$ .	70
4.3	XRF spectra of a standard glasses SRM NIST612 and MPI DING ATHO-G. Both spectra were collected with counting times of 500 seconds.	71
4.4	XRF spectra of a standard solution ( <b>A</b> ) and two samples using a chloridic solution ( <b>B</b> ) or H <sub>2</sub> O ( <b>C</b> ) as starting fluid loaded in a HDAC.	71
4.5	Minimum detection limits (MDL) determined for various elements from two standard glasses (SRM NIST612 and MPI DING ATHO-G) and a standard solution in HDAC2 and HDACG. The slightly different MDL's from HDAC experiments are due to different excitation volumes (different depths of recesses).	72
4.6	Fluid–melt partition coefficient of Ba at 750°C and the indicated pressure vs. initial Cl-molality of the fluid. Data from HDAC and quenched experiments are shown for peraluminous (Fig. 4.6.1) and metaluminous melt (Fig. 4.6.2).	73
4.7	Fluid–melt partition coefficient of La at 750°C and the indicated pressure vs. initial Cl-molality of the fluid. Data from HDAC and quenched experiments are shown for peraluminous (Fig. 4.7.1) and metaluminous melt (Fig. 4.7.2).	73

---

4.8	Yttrium fluid-melt partition coefficient at 750°C and indicated pressures vs. initial Cl-molality (Fig. 4.8.1) and at 750°C and indicated fluid salinities vs. pressure (Fig. 4.8.2). Figures show data from HDAC and quenched experiments (this study). For comparison, we also show the Y partition coefficient obtained using F-rich starting material (Webster et al., 1989). . . . .	74
4.9	XRF intensity maps of fluorescence lines as indicated of sample chamber of HDAC after experiment (E) indicating the formation of REE-bearing silicates. . .	74
6.1	Strontium XANES spectra of peralkaline and peraluminous starting glasses. . . .	101
6.2	Strontium XANES spectra of peralkaline and peraluminous silicate fluids. . . .	102
A.1	Comparison of partition coefficients of Na, Rb, and Sr from slow and rapid quenched experiments (Fig. A.1.1) and dependence of $D^{f/m}$ on the initial NaCl concentration in the fluid (Fig. A.1.2). . . . .	IV
A.2	The dependence of fluid–melt partition coefficients on the $D_{Na}^{f/m}$ as a function of melt composition are shown in Fig. A.2.1 for Rb and Fig. A.2.2 for Sr. . . . .	V



# List of Tables

2.1	Summary of the experimental conditions, results of the <i>in-situ</i> SR- $\mu$ XRF analyses of the aqueous fluids, and of the EMP analyses of the glasses, and calculated partition coefficients ( $D^{\text{fluid/melt}} = c^{\text{fluid}}/c^{\text{melt}}$ ) at 750°C. . . . .	24
3.1	Composition of starting glasses from EMP analyses and normative composition based on the components albite, orthoclase, quartz, corundum and Na-metasilicate. . . . .	55
3.2	Data from experiments at 750°C and 200 MPa using <b>rapid quench autoclaves (RQ)</b> . For each run, the first line of the analyses refers to the quench glass and second line to the quenched fluid. . . . .	55
3.3	Data from experiments at 750°C and 200 MPa using <b>slow quench autoclaves (externally heated cold-sealed pressure vessels, SQ)</b> . For each run, the first line of the analyses refers to the quench glass and second line to the quenched fluid. . . . .	56
3.4	Experimental conditions, starting materials and quench pH of the fluids for selected glass and fluid compositions . . . . .	56
3.5	Data from experiments up to 950°C and 850 MPa using <b>internally heated cold-sealed pressure vessels (IHPV)</b> . For each run, the first line of the analyses refers to the quench glass and second line to the quenched fluid. . . . .	56
3.6	Experimentally determined fluid–melt partition coefficients of Na, K, Rb, Sr, Cl and $D_{\text{K}}/D_{\text{Na}}$ . . . . .	58
3.7	Experimental conditions and results of the HDAC experiments for <b>chloridic fluids</b> at 750°C. Concentrations of Rb and Sr in the fluid were analyzed in-situ using SR- $\mu$ XRF, the glasses were analyzed after quench using EMP. . . . .	59
3.8	Experimental conditions and results of the HDAC experiments for <b>non-chloridic fluids</b> at 750°C. Concentrations of Rb and Sr in the fluid were analyzed in-situ using SR- $\mu$ XRF, the glasses were analyzed after quench using EMP. . . . .	59
4.1	Composition of starting glasses from EMP analyses and normative composition based on the components albite, orthoclase, quartz, corundum and Na-metasilicate. . . . .	87

4.2	Data for <b>Barium</b> from experiments at 750°C and 200 MPa using <b>rapid quench autoclaves (RQ)</b> and <b>internally heated pressure vessel (IHPV)</b> . For each run, the first line of the analyses refers to the quench glass and second line to the quenched fluid. . . . .	87
4.3	Data for <b>Lanthanum, Yttrium and Ytterbium</b> from experiments from 750 to 950°C and 200 or 500 MPa using various quench apparatus. For each run, the first line of the analyses refers to the quench glass and second line to the quenched fluid. . . . .	88
4.4	Experimentally determined fluid–melt partition coefficients of Na, K, Ba, Cl. and $D_K/D_{Na}$ . . . . .	89
4.5	Experimentally determined fluid–melt partition coefficients of Na, K, La, Yb, Y, Cl. and $D_K/D_{Na}$ . . . . .	89
4.6	Experimental conditions and results of the HDAC experiments fat 750°C. Concentrations of Ba, La and Y in the fluid were analysed <i>in-situ</i> using SR- $\mu$ XRF, the glasses were analysed after quench using EMP. . . . .	90
A.1	Composition of AQ starting glasses from EMP analyses and normative composition based on the components albite, quartz and corundum. TE - trace element as indicated by sample name. . . . .	II
A.2	Analytical data and determined fluid–melt partition coefficients of Na, Rb, Sr, and Cl from experiments at 750°C and 200 MPa. For each run, the first line of the analyses refers to the quenched glass and second line to the quenched fluid. . . . .	III
B.1	ICP–OES instrumental conditions . . . . .	VI
B.2	Emission lines (upper line, [nm]) and detection limits (lower line, [mg/l]) for ICP analyses. . . . .	VII
B.3	Operation conditions for determination of chloride by Ion Chromatography . . . .	VIII

# Chapter 1

## Introduction

Granites cover a great majority of igneous rocks in the Earth's upper crust. Therefore, the origin and evolution of granitic rocks has been widely studied in the last decades (e.g., Tuttle and Bowen, 1958, Holland, 1972, Whitney, 1988, Atherton, 1993). The formation of granitic magmas is mainly a function of temperature and water content (Whitney, 1988). Therefore, the solubility of water in granitic melts has been widely studied (e.g., Tuttle and Bowen, 1958, Burnham and Jahns, 1962, Holtz et al., 1992, 1995, 2000, Pailat et al., 1992, Pichavant et al., 1992, Yamashita, 1999, Behrens and Jantos, 2001). Evidence from volcanic and plutonic lithologies suggests that water contents of 2 to 4 wt.% are present in most silicic magmas, and that at water contents of  $\geq 4$  wt.% the magma would become water saturated at high pressures. Exsolution of water from a fluid-saturated magma is a complex matter, but two main processes can be distinguished, (1) the saturation of initially volatile undersaturated magma by decompression, and (2) the volatile saturation of a stagnant, isobaric magma by cooling (e.g., Best, 2003, Robb, 2005, Philpotts and Ague, 2009). The first process commonly occurs in shallow crustal, volcanic environments because the magma exceeds water solubility during ascent. In the second process, the crystallization of anhydrous minerals, e.g., quartz, plagioclase, K-feldspar, result in an increased volatile content in the residual magma. When water saturation of the granitic melt exceeds, two liquid phases coexists: a silicate rich melt and an aqueous rich phase. The latter is, in this text, defined as an aqueous fluid. The exsolved aqueous phase is likely to migrate due to lower density and viscosity compared to the silicate melt and the adjacent rock. The aqueous fluid attempts to re-equilibrate with all coexisting magmas and rocks. Therefore, elements that show a preference for the aqueous fluid can be separated and transported from the magma extremely efficiently. This phenomenon is not only important for the formation of ore deposits, but also to understand how fluids affect magmatic processes, e.g., efficiency of degassing of volcanic systems (Carroll and Holloway, 1994), and how interactions between fluids and magmas may change the composition of the magma and/or crystallizing phases. Therefore, the determination of element partition coefficients between fluids and melts

$$D_X^{\text{fluid/melt}} = c_X^{\text{fluid}} / c_X^{\text{melt}},$$

and the knowledge of their relation to intensive variables such as temperature, pressure, oxygen fugacity, bulk chemistry of the system, and the presence of additional volatile components (Cl, F, S) is important to understand and model element behavior during crystallization

and fractionation of natural systems, particularly during late stages of the magmatic evolution (Burnham, 1979).

So far, magmatic processes and phase relations are still to insufficiently known to understand the major element variations in detail in suites of differentiated igneous rocks. Trace element variations are helpful to unravel the petrogenetic evolution of rocks because, unlike major elements, they are not essential for the stability of the phases involved and often reflect magmatic processes with less ambiguity because variations often are not linked to formation of specific phases (e.g., Philpotts and Ague, 2009). If two or more phases coexist (e.g., melt, mineral, liquid), a trace element under equilibrium conditions partitions itself between the phases. In the case of diluted concentrations, it can be expected that trace elements follow Henry's law ( $a_i = K_i/X_i$ , where  $a_i$  is the activity,  $X_i$  is the mole fraction, and  $K_i$  the Henry's law constant of component  $i$ ). Henry behavior of elements implies a strong simplification of modeling because the fractionation of elements between coexisting phases becomes independent of their concentration up to a certain maximum level. During magma differentiation, some trace elements, e.g., Ni, Cr, Co, Mg, and Fe, partition strongly into early crystallizing minerals which is described as compatible behavior. Incompatible trace elements are those that cannot substitute into the crystal structure of early forming minerals because of high ionic charge and/or large ionic radius. Therefore, differentiated magmas are, among others, enriched in Ba, Rb, Sr, Zr, Cs, rare earth elements (REE), Hf, Th, Pb, and U. Ratios of two strongly incompatible elements are useful to test for a cogenetic origin in suites of igneous rocks. Because they are independent of the fraction of liquid remaining and the phase properties, the ratios will only change by assimilation of country rocks or mixing with magmas that have different ratios. Some trace elements are sensitive indicators of the degree of fractionation because they preferentially partition into a specific mineral. The magnitude of the effect produced by a mineral depends on its relative abundance and on the magnitude of the  $D$  value for a particular element. For example,  $Ba^{2+}$ ,  $Sr^{2+}$ , and  $Eu^{2+}$  easily substitute for  $Ca^{2+}$  in plagioclase. Rare earth elements are extremely useful trace elements in the study of igneous petrogenesis because of their high charge, relatively large ionic radius, and their similar geochemical behavior (Hanson, 1980). Furthermore, as their atomic weight increases, the ionic radius decreases which is known as lanthanide contraction. However, in granitoid melts, rare earth elements do not incorporate in major granite-forming minerals. Instead, they strongly fractionate into accessory phases, e.g., monazite, apatite, or sphene (e.g., Bea, 1996). The abundance of the REE's in granitoid rocks is  $\leq 100$  ppm in the average upper continental crust, but increases with increasing potassium content of the melt (Winter, 2001).

During the last three decades, numerous studies were performed to determine fluid–melt partition coefficients of elements of economic or petrological interest. Most of the available data are based on experimental studies using quench apparatus, with synthetic or natural melts as starting materials, e.g., Cullers et al. (1973), Flynn and Burnham (1978), Candela and Holland (1984), Urabe (1985), London et al. (1988), Webster et al. (1989), Keppler and Wyllie (1990), Ayers and Eggler (1995), Bai and Koster van Groos (1999). Other studies analyze synthetic or natural co-genetic fluid and melt inclusions using Laser ablation–inductively coupled plasma–mass spectrometry (LA-ICP-MS) analysis (e.g., Schäfer et al., 1999, Audétat and Pettke, 2003, Zajacz et al., 2008) or X-ray fluorescence microanalysis (Rickers et al.,

2006). An unisonous finding of these studies is that in systems with aqueous fluids diluted in  $\text{Cl}^-$ , the majority of elements show a preference for the melt, i.e., fluid–melt partition coefficients are typically much smaller than one. The presence of complex–forming ligands in the fluid, in particular  $\text{Cl}^-$ , significantly enhances  $D^{f/m}$  (e.g., Keppler and Wyllie, 1991, Bai and Koster van Groos, 1999, Zajacz et al., 2008). For example, Ayers and Egger (1995) measured partition coefficients between a synthetic andesite melt and  $\text{H}_2\text{O}$ , 1.5 and 3 *m* NaCl fluids at 1.5–2.0 GPa and 1250°C. They observed an increase of the partition coefficients of alkali elements from 0 to 1.5 *m* NaCl solution, but no further increase for a 3 *m* NaCl solution. Bai and Koster van Groos (1999) determined  $D^{f/m}$  of various main and trace elements between various aqueous fluids (pure, chloridic, fluoridic, or carbonatic) and granitic melts at 750–800°C and 100–400 MPa. The results show that chloridic fluids significantly enhance the partition coefficients of Na, K, Rb, Sr, and Cu ( $D^{f/m} > 1$  at salinities  $\geq 3$  *m* (Na,K)Cl). In contrast, Al, Ge, Mo, W, La, and Ce strongly partition into the silicate melt. In the case of carbonatic fluids, only Mo and Cu partition into the fluid. The latter result confirms the data of Webster et al. (1989) who also determined significantly smaller partition coefficients for various trace elements for  $\text{H}_2\text{O} + \text{CO}_2$  fluids than for  $\text{CO}_2$ –free aqueous solutions. Fluid–melt partitioning of economically interesting trace elements, e.g., Cu, Mo, and W, between haplogranites and different Cl bearing solutions were studied by Keppler and Wyllie (1991) for  $\text{H}_2\text{O}$ -HCl solutions, and by Candela and Holland (1984) for aqueous (Na,K)Cl fluids at 750°C and up to 200 MPa. For copper, both studies found an increase in the partition coefficient with increasing Cl concentration in the fluid (max.  $D_{\text{Cu}}^{f/m} \approx 100$ ). In contrast, the observed partition coefficient of Mo was high if water was the only volatile component present, but decreased strongly with increasing Cl concentration (Keppler and Wyllie, 1991). This finding differs from the data by Candela and Holland (1984), who observed no correlation between  $D_{\text{Mo}}^{f/m}$  and Cl concentration of the fluid. A possible explanation can be the different fluid compositions, HCl and (Na,K)Cl solutions, used in the studies. Schäfer et al. (1999) determined, among others, Mo and W partition coefficients between a NaCl solution and a granitic melt at 850°C and 200 MPa. Their data show a five times higher partition coefficient for W than the data by Keppler and Wyllie (1991) and a similar behavior of Mo. Schäfer et al. (1999) assume that a reason for this different behavior may be the formation of hydroxyl complexes in the fluid that are not stable in the presence of high amounts of HCl but stabilized by the presence of NaCl.

Most of the elements show a qualitatively similar behavior if  $\text{F}^-$  is present instead of  $\text{Cl}^-$ . Keppler and Wyllie (1991) found increasing  $D_{\text{U}}^{f/m}$  with increasing  $\text{F}^-$  concentration in the fluid, but a decrease of the partition coefficient of Mo at the same conditions. However, thorium shows a clear dependence on the  $\text{F}^-$  content but a negligible correlation with the  $\text{Cl}^-$  concentration while the opposite behavior is observed for Cu (Keppler and Wyllie, 1991). For the rare earth elements, a less significant fractionation into the  $\text{F}^-$ -bearing fluids was found than for fluids with a similar  $\text{Cl}^-$  concentration (Flynn and Burnham, 1978). However, the data might not be comparable because the melt composition was severely affected by the HF solution.

In contrast to the effect of the fluid composition, the influence of melt composition on trace element partitioning is, so far not very well investigated. Webster (1992a,b) and Metrich and Rutherford (1992) found a strong dependence of the Cl solubility in silicate melts on the alkali/alumina ratio of the melt. Hence, the distribution of elements that form chloride complexes

in the fluid will among other variables depend on this ratio. Watson (1979) demonstrated the strong influence of the composition of the silicate melt on the solubility of Zr in melts. The data show that zircon saturation is attained with less than 100 ppm Zr in peraluminous melts, whereas the Zr content may reach several wt.% in peralkaline compositions. This large difference also reflected by much higher  $D_{Zr}^{f/m}$  for peraluminous melts than for peralkaline silicate liquids. Flynn and Burnham (1978) studied the partitioning behavior of Ce, Eu, Gd and Yb between an aqueous phase and water saturated silicate melts of different composition (Spruce Pine pegmatite and a jadeite-nepheline composition with 75 wt.% jadeite) at 800°C and 125 or 400 MPa. The data at constant  $Cl^-$  concentration showed higher  $D_{REE}^{f/m}$  for the Spruce Pine pegmatite melt than for the jadeite-nepheline composition. The authors suggested that the water-saturated jadeite-nepheline melt is less polymerized than the water-saturated Spruce Pine pegmatite melt. This is because the jadeite-nepheline melt has a higher water content and contains less tetrahedrally coordinated cations, e.g., silica. Therefore, the number of high-coordinated sites available for the substitution of REE is larger in the jadeite-nepheline melt compared to the Spruce Pine pegmatite melt due to the higher water content (Flynn and Burnham, 1978, Ponader and Brown, 1989).

A further method to derive fluid-melt partition coefficients besides quenched experiments using hydrothermal autoclaves, is the analysis of fluid and melt inclusions. Schäfer et al. (1999), Hanley et al. (2005), and Simon et al. (2007) investigated synthetic quartz-hosted fluid and melt inclusions that were trapped at magmatic conditions. Audétat and Pettke (2003), Rickers et al. (2006), Zajacz et al. (2008), and Audétat et al. (2008) determined partition coefficients based on analyses of natural co-existing fluid and melt inclusions. Partition coefficients determined from synthetic and natural fluid and melt inclusions are also afflicted by specific uncertainties. In the case of natural samples, one has to verify that natural fluid and melt inclusions are co-genetically trapped. Furthermore, the bulk salinity of the aqueous fluid is unknown for natural inclusions. The determination of the salinity of synthetic and natural fluid inclusions is difficult because aqueous fluids unmix to vapor and brine upon cooling. For a precise determination of the salinity before unmixing, one needs to know the actual phase proportions because the salinity is anywhere between the end points of the tie line. There might be also changes of the melt composition upon cooling (e.g., precipitation of quartz in quartz-hosted inclusions). However, the melt composition has a strong effect on fluid-melt partitioning of trace elements as described in a previous paragraph. Further on, the application of the laser ablation ICP-MS technique on the study of fluid and melt inclusions has two main sources of error, (1) mixed analyses of inclusions and tiny precipitates at the inclusion walls, and (2) the separation of the inclusion signal from that of the host mineral or matrix glass. The latter is minimized by using an internal standard that is also essential for the conversion of the determined element ratios into absolute element concentrations Audétat and Pettke (2003). Zajacz et al. (2008) present a nearly complete comparison of experimentally obtained fluid-melt partition coefficients and calculated partitioning data using analyses of natural co-genetic fluid and melt inclusions. The ranges of the partitioning data derived from experiments and natural data overlap, but partition coefficients derived from natural samples generally show less scattering. Zajacz et al. (2008) found good agreement between experimental data and analyses of fluid and melt inclusion for the elements Fe, Cu, Zn, Pb, Mo, W, Th, K and Rb. In contrast, the

results differ significantly for Li, Na, Sr, Sn, Zr, or Nb. For example, the data by Bai and Koster van Groos (1999) suggest a preference of Sr for the fluid at high salinities, but available results from natural co-genetic fluid and melt inclusions in granites show partition coefficients that are distinctly smaller than one even at high salinities (Audétat and Pettke, 2003, Rickers et al., 2006). In contrast, Zajacz et al. (2008) confirm the high  $D_{\text{Sr}}^{\text{f/m}}$  presented by Bai and Koster van Groos (1999), but also state that Sr concentration in silicate melt inclusions were always below detection limit and therefore, are associated with large errors.

At present, the literature does not provide a basis to develop an unifying picture because most of the experimental studies are not comparable to each other due to different elements of interest, variable PT conditions, and system compositions. Furthermore, the different behavior of the elements in chloridic, fluoridic or pure aqueous solutions clearly points to a strong effect of complex formation in the fluid in equilibrium with silicate melt on the element distribution.

Comparison between different dataset's are also difficult because systematic errors of the different experimental and analytical approaches are hard to quantify as no adequate reference measurements are available. In all studies presented above, the data are based on the analysis of quenched samples. Analyses of quenched phases, in particular of quenched fluids, are associated with large intrinsic uncertainties due to (1) back reactions between fluid and melt, (2) the tendency of fluids to unmix or (3) precipitate solutes during cooling (Adam et al., 1997). Hence, the most difficult part of quenched experiments is to obtain a representative sample of the fluid for analysis. Sampling of a quenched solution is complex and time consuming (e.g., Flynn and Burnham, 1978, Keppler and Wyllie, 1991). To avoid these difficulties of fluid sampling, some studies produced synthetic fluid inclusions, e.g., in quartz, at the desired PT conditions (Hanley et al., 2005, Simon et al., 2007) or reconstructed the fluid composition via mass balance with modeling of undetermined parameters, e.g.,  $\text{H}_2\text{O}$  solubility in the melt (e.g., Ayers and Egger, 1995, Webster, 1992a,b). However, analysis of fluid inclusions is associated with other uncertainties as described previously, and recalculation of the fluid composition using mass balancing neglects other phases that might form during the experiment. Mass balances makes use of literature data of, e.g., water solubility in the melt and solubility of melt components in the fluid. The dependencies of water solubility in silicate melts on intensive variables is relatively well-known (e.g., Tuttle and Bowen, 1958, Burnham and Jahns, 1962, Holtz et al., 1992, 1995, 2000, Pailat et al., 1992, Pichavant et al., 1992, Yamashita, 1999, Behrens and Jantos, 2001), but the solubility of melt components in aqueous fluids at elevated PT is almost unknown (Mysen and Armstrong, 2002). Approximations can be made using data on  $\text{SiO}_2$  or  $\text{NaAlSi}_3\text{O}_8$  solubility in water or chloridic fluids (e.g., Anderson and Burnham, 1965, Currie, 1968, Manning, 1994, Newton and Manning, 2000, Shmulovich et al., 2001).

A reliable determination of trace element concentrations in aqueous solutions can also be obtained by direct measurements in the fluid at elevated PT. These direct measurements make use of hydrothermal diamond-anvil cells (HDAC) and synchrotron radiation X-ray fluorescence microanalysis (SR- $\mu$ XRF) (e.g., Schmidt and Rickers, 2003, Sanchez-Valle et al., 2003, Schmidt et al., 2007, Manning et al., 2008). An important advantage of this method is the improved reliability of low trace element contents, e.g., in  $\text{Cl}^-$  free aqueous solutions because back reactions cannot alter the fluid composition. This is particularly important because here

the effect of back reactions on fluid–melt partition coefficients is larger compared to fluids with high chlorine contents. But, this technique is also limited because (1) elements with relatively low  $Z$  cannot be analyzed or have a high detection limit, and secondly, this method is limited by the interference of fluorescence lines of elements of interest with those from material outside the sample chamber. Elements that can be analyzed with confidence are for example Rb, Sr, Y, Zr, Nb, Mo, La using K fluorescence lines as well as U, Th (L fluorescence lines).

Furthermore, this experimental setup can also be used to obtain information on the complexation of elements in fluids at elevated temperatures and pressures using X-ray absorption fine structure (XAFS) spectroscopic methods (i.e., X-ray absorption near edge structure [XANES] or extended X-ray absorption fine structure [EXAFS]). This may be extremely useful because so far, the determination of the nature of the complexes in fluids at high PT and in equilibrium with silicate melts is still based on the correlation between partition coefficient and anion concentration in the fluid after quenching. For example, Flynn and Burnham (1978) concluded that the trivalent rare earths will form  $\text{REECl}_3$  complexes. Keppler and Wyllie (1991) found a linear increase of  $D_{\text{U}}^{\text{f/m}}$  with the square of the fluoride concentration or with the third power of  $\text{Cl}^-$  content in the fluid. Bai and Koster van Groos (1999) suggested the formation of  $\text{SrCl}_2$  complexes in the fluid due to the increase of the Sr partition coefficient with the square of the (Na,K)Cl molality of the initial solution. For Rubidium, a linear increase of  $D^{\text{f/m}}$  with  $m \text{Cl}$  of the fluid was found by Webster et al. (1989), Bai and Koster van Groos (1999). That kind of correlations require a defined exchange equilibrium reaction of the studied elements between the phases as shown by e.g., Frank et al. (2003). However, these correlations might be wrong because the concentrations are wrong.

So far, XAFS was applied to study the formation, structure, and stability of rare-earth element complexes (La, Nd, Eu, Gd, and Yb) in aqueous solutions under hydrothermal conditions (Mayanovic et al., 2007a,b, 2009a,b). One attempt has been made to gain information on the complexation of Nb in hydrous silicate melt equilibrated with  $\text{H}_2\text{O}$  or  $\text{Na}_2\text{CO}_3$  aqueous solution at elevated PT conditions (Mayanovic et al., 2007a). Up to now, no attempt has been made to study element complexation in fluids in equilibrium with silicate melt at magmatic conditions, but these data would elucidate whether information on the trace element complexation obtained from analyses of quenched fluids is plausible or not.

The major goal of this thesis is to obtain quantitative data on fluid–melt partitioning of petrological interesting elements, mainly Rb, Sr, Ba, La, Y, and Yb, and to understand how intensive variables, such as melt composition, fluid composition, pressure, and temperature affect the partition coefficients. So far, the effect of the melt composition on the fluid–melt partitioning of the elements listed above is almost unknown. Therefore, we used a suite of trace element doped haplogranitic glass compositions as starting material to cover a wide range of ASI (alumina saturation index of the melt) which can occur in natural granitoids. Here, we systematically varied the alkali to alumina ratio. Haplogranites were chosen because the phase relations in this system are very well studied (e.g., Tuttle and Bowen, 1958, Johannes and Holtz, 1996). In contrast, the effect of the fluid composition on fluid–melt partitioning of many elements is relatively well studied. Hence, we limited starting solutions to  $\text{H}_2\text{O}$  and  $\text{NaCl}+\text{KCl}\pm\text{HCl}$  aqueous solutions with a  $m \text{NaCl}/\text{KCl}$  ratio of one. In the latter, the salinity ranged from 1.16 to 3.6  $m$  (NaCl+KCl) because the solute content of magmatic aqueous fluids



is quite variable, but dominated by alkali and alkaline earth metal cations and chlorine as major anion (Roedder and Bodnar, 1997). Several experiments were performed with addition of HCl to investigate the effect of the pH on trace element partitioning.

In the following paragraph, I will give a brief overview on the manuscripts presented in the next chapters.

Of central importance within this project was the refinement of the technique to quantify trace element contents of the fluid phase directly at elevated PT-conditions for application to fluid–melt systems. To obtain this information, we used an analytical approach where fluid analysis is achieved by synchrotron radiation X-ray fluorescence using a hydrothermal diamond-anvil cell. This method is in detail described in chapter 2. The data presented here demonstrate that this experimental approach can be used to determine the trace element contents in fluids equilibrated with silicate melts at elevated temperatures and pressures. Furthermore, it is shown that this technique can be used to obtain information on the equilibration behavior of trace elements in fluids at different temperatures and pressures steps. The direct proof of back reactions of these elements between fluid and melt upon cooling cannot be ignored at least for Rb and Sr. Chapter 3 focusses on the main part of the thesis, and presents an extensive Rubidium and Strontium fluid–melt partitioning data set. Fluid–melt partitioning of Rb and Sr was studied as function of temperature, pressure, and fluid and melt composition using different experimental methods. The latter includes in-situ results and data obtained from quenched experiments, in which the trace element concentration in the fluid is measured by inductively coupled-plasma optical emission spectrometry and ion chromatography. The effect of different experimental techniques and the quench rates (slow vs. rapid) on fluid–melt partitioning of trace elements due to variable trace element contents of the fluid is discussed here, too. The partitioning behavior of Ba, La, Y, and Yb as function of melt and fluid composition, pressure and temperature is discussed in chapter 4. The presented data also consist of in-situ as well as of quench results. In the case of Ba, all quenched experiments and analyses of the quenched phases were performed by Matthias Ebert as part of his diploma thesis based on the quench method described in chapter 3. First results on the complexation of Sr in various silicate solutions at elevated pressures and temperatures obtained using XANES spectroscopy and HDAC are presented as part of the outlook (Chapter 6). The first qualitative results provide an explanation of the observed dependence of strontium fluid–melt partition coefficients on the melt composition (ASI).



## **Chapter 2**

# **Partitioning and equilibration of Rb and Sr between silicate melts and aqueous fluids**

*published in:*  
*Chemical Geology 259, 39–47 (2009)*

# Partitioning and equilibration of Rb and Sr between silicate melts and aqueous fluids

Manuela Borchert<sup>a,\*</sup>, Max Wilke<sup>b</sup>, Christian Schmidt<sup>b</sup>, Karen Rickers<sup>c</sup>

<sup>a</sup> Universität Potsdam, Karl-Liebknecht-Str.24, 14476 Potsdam-Golm, Germany

<sup>b</sup> Deutsches GeoForschungsZentrum (GFZ), Section 4.1, Telegrafenberg, 14473 Potsdam, Germany

<sup>c</sup> Hamburger Synchrotronstrahlungslabor at Deutsches Elektronensynchrotron, Notkestr. 85, 22607 Hamburg, Germany

## Abstract

Trace element concentrations in aqueous fluids in equilibrium with haplogranitic melt were determined *in-situ* at elevated P-T conditions using hydrothermal diamond-anvil cells and synchrotron-radiation XRF microanalyses. Time-resolved analyses showed that the Rb and Sr concentrations in the fluids became constant in less than 2000 seconds at all temperatures (500 to 780°C). Although fluid-melt equilibration was very rapid, the change in the concentration of both elements in the fluid with temperature was fairly small (a slight increase for Rb and a slight decrease for Sr). This permitted partitioning data for Rb and Sr between haplogranitic melt and H<sub>2</sub>O or NaCl+KCl+HCl aqueous solutions at 750°C and 200 to 700 MPa to be obtained from EMP analyses of the quenched melt and the *in-situ* SR-XRF analyses of the equilibrated fluid. The resulting  $D_{\text{Rb}}^{\text{f/m}}$  and  $D_{\text{Sr}}^{\text{f/m}}$  were  $0.01 \pm 0.002$  and  $0.006 \pm 0.001$  for water as starting fluid, and increased to  $0.47 \pm 0.08$  and  $0.23 \pm 0.03$  for 3.56 *m* (NaCl+KCl) + 0.04 *m* HCl at pressures of 224 to 360 MPa. In the experiments with H<sub>2</sub>O as starting fluid, the partition coefficients increased with pressure, i.e.  $D_{\text{Rb}}^{\text{f/m}}$  from  $0.01 \pm 0.002$  to  $0.22 \pm 0.02$  and  $D_{\text{Sr}}^{\text{f/m}}$  from  $0.006 \pm 0.001$  to  $0.02 \pm 0.005$  with a change in pressure from 360 to 700 MPa. At pressures to 360 MPa, the Rb/Sr ratio in the fluid was found to be independent of the initial salt concentration (Rb/Sr =  $1.45 \pm 0.6$ ). This ratio increased to  $7.89 \pm 1.95$  at 700 MPa in experiments with chloride free fluids, which indicates different changes in the Rb and Sr speciation with pressure.

**Keywords:** synchrotron-radiation X-ray fluorescence microanalysis, hydrothermal diamond-anvil cell, fluid-melt partition coefficients, melt-fluid equilibration

\* Corresponding author.

E-mail address: manu@geo.uni-potsdam.de (M.Borchert)

## 2.1 Introduction

Interactions between magmas and aqueous solutions play an important role in many geological processes, e.g., volcanic eruptions, the development of mid-ocean ridges, the formation of magmatic-hydrothermal ore deposits, and crustal metamorphic systems. Equilibria between two or more fluids often result in strong fractionation particularly of trace elements (e.g., Holland, 1972, Rickers et al., 2006). Furthermore, many trace elements are used as petrogenetic indicators in igneous systems (cf., Best, 2003, Winter, 2001). This has prompted several experimental studies on element partitioning at fluid immiscibility conditions over the last 20 years.

The trace element partitioning between aqueous fluids and granitic melts was investigated by Flynn and Burnham (1978), London et al. (1988), Keppler and Wyllie (1991), Ayers and Eggler (1995), Adam et al. (1997) and Bai and Koster van Groos (1999). However, systematic studies of fluid-melt partitioning are far from being complete, even for the petrogenetically important large ion lithophile (LIL) elements Rb and Sr. Furthermore, the majority of the experimentally determined partitioning data is based on analyses of quenched samples. However, intrinsic uncertainties are associated with fluid-melt partitioning data from quench techniques, which make it problematic to obtain unambiguous data, particularly for the trace element concentration in the fluid. The uncertainties are related to (i) the difficulty of isolating the fluid phase for sampling and analysis, (ii) fluid unmixing and (iii) precipitation of solids during quenching, and possible back reactions between fluid and melt during cooling (Adam et al., 1997, Holtz et al., 1995, Behrens et al., 2001).

In this study, we therefore applied a technique to determine the trace element concentration in the fluid phase directly at elevated pressures and temperatures using a modified hydrothermal diamond-anvil cell (HDAC) and synchrotron-radiation X-ray fluorescence microanalysis (SR- $\mu$ XRF). The first goal of this study is to determine the Rb and Sr concentrations in the fluid *in-situ* in equilibrium with a metaluminous melt at 750°C and 200 MPa. The melt droplets cannot be analysed *in-situ* with confidence due to coexcitation of the aqueous fluid around the droplets. Even if the incident beam is focused, a portion of these X-rays will be scattered in the diamond anvil, and a contribution from coexcited fluid to the XRF signal is therefore inevitable if the measurements are done in forward scattering geometry, (e.g., Bureau et al., 2007). Such a contribution can be minimised if a recess in the diamond anvil is used and the XRF signal is acquired at 90° to the beam (Schmidt and Rickers, 2003). However, in this experimental setup, it is unlikely that a melt globule occupies the entire effective excitation volume in the recess (cf., Fig.1 in Muñoz et al., 2005). In this study, electron microprobe (EMP) analyses were therefore performed on the quenched glass droplets after the run. The element contents of the glass and the *in-situ* data of the fluid were used to obtain partition coefficients. The second goal was to investigate the equilibration kinetics in order to estimate the effect on partition coefficients. This was done by time resolved analysis of the trace element signal in the fluid at several temperatures in stepwise heating and cooling experiments.

## 2.2 Experimental methods

### 2.2.1 Starting Materials

The starting materials for the experimental runs consisted of a synthetic haplogranitic metaluminous glass and two aqueous fluids. The composition of the glass (Ab<sub>47</sub>Or<sub>22</sub>Qz<sub>31</sub>) corresponds to the thermal minimum in the haplogranitic system at P = 500 MPa and a<sub>H<sub>2</sub>O</sub> = 1 (Johannes and Holtz, 1996). The glass was prepared in two steps. Firstly, an initial glass was produced using powders of SiO<sub>2</sub>, Al<sub>2</sub>O<sub>3</sub>, Na<sub>2</sub>CO<sub>3</sub> and K<sub>2</sub>CO<sub>3</sub>. The powders were mixed and stepwise heated to 1550°C for decarbonisation (12 h). After quenching, the glass was crushed and melted again for 48 h at 1550°C. Secondly, Rb and Sr were added as RbCl and SrCO<sub>3</sub> to the crushed initial glass. The glass was doped with relatively high concentrations of 2926±169

ppm Rb and  $3065 \pm 181$  ppm Sr (EMP analyses) to facilitate later *in-situ* SR- $\mu$ XRF analyses of the aqueous fluids. The doped glass powder was melted at  $1600^\circ\text{C}$  for 24 h, then quenched, crushed and melted again for 24 h at  $1600^\circ\text{C}$  to achieve chemical homogeneity. Before loading into the sample chamber of a cell, the glass was cut in pieces with parallel faces. These pieces were ground and polished to a thickness of  $60 \pm 20 \mu\text{m}$ .

The solutions,  $\text{H}_2\text{O}$  and  $\text{H}_2\text{O} + 0.5 \text{ m NaCl} + 0.5 \text{ m KCl} + 0.01 \text{ m HCl}$ , were produced from distilled de-ionised water, analytical grade powders of NaCl and KCl. A small amount of 30 vol.% hydrochloric acid was added.

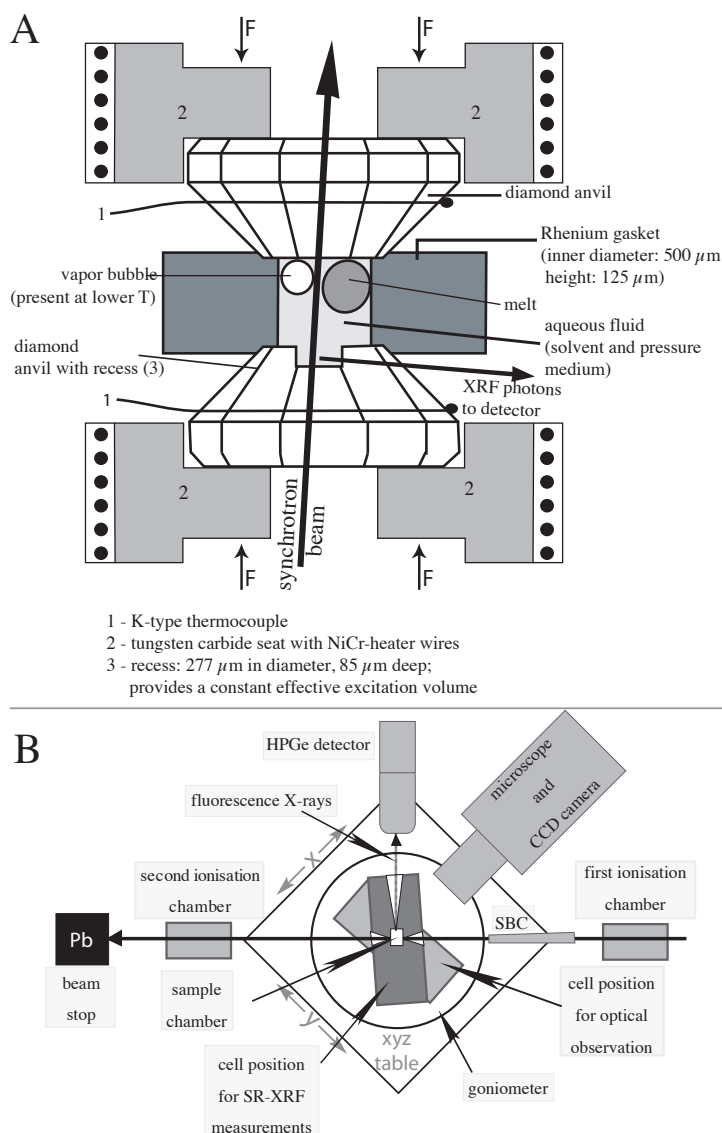


Figure 2.1: A - Schematic diagram showing the details of the modified Bassett-type hydrothermal diamond anvil cell. B - Top view of the experimental setup at beamline L, HASYLAB (DESY, HAMBURG) (after Schmidt and Rickers (2003), modified).

## 2.2.2 Hydrothermal diamond-anvil cell

We used two modified Bassett-type hydrothermal diamond-anvil cells as described by Bassett et al. (1993), Schmidt and Rickers (2003), and Schmidt et al. (2007). A schematic drawing of this cell type is shown in Fig.2.1A.

In each cell (HDAC 3 and HDAC G), the culet face of the diamond-anvil located on the side of the incident X-ray beam has a cylindrical recess of 85  $\mu\text{m}$  in depth (HDAC G) or 72  $\mu\text{m}$  in depth (HDAC 3). The recess permits collection of the fluorescence signal at 90° to the incident beam and in the polarisation plane of the beam (Bassett et al., 2000, Schmidt and Rickers, 2003). This configuration minimises the background in the spectra from elastic and Compton scattering and therefore provides an optimal signal to noise ratio. Furthermore, the recess ensures a well-defined effective excitation volume, because fluorescence X-rays generated in other parts of the sample chamber are absorbed by the gasket before reaching the detector. In both cells the path length of the fluorescence X-rays through the diamonds was  $460 \pm 50 \mu\text{m}$ . The sample volume was heated externally by NiCr coils around the tungsten carbide seats supporting the anvils. K-type thermocouples attached to the diamonds were used for temperature measurement. The power input to the two resistive heaters was controlled with Eurotherm@2408 or Eurotherm@2704 temperature controllers, which kept the temperature within  $\pm 0.5^\circ\text{C}$  of the desired value. The actual temperature in the sample chamber was calibrated using measurements of the melting point of sodium chloride ( $800.5^\circ\text{C}$ ) and of the triple point of  $\text{H}_2\text{O}$  ( $0.1^\circ\text{C}$ ) at atmospheric pressure. During heating, oxidation of the metallic parts was prevented by flushing the cell with 200 l/h  $\text{N}_2 + 1\% \text{H}_2$  gas.

## 2.2.3 Sample preparation

The sample chamber of the HDAC consists of the recess at the culet face and a cylindrical hole in the gasket separating the two anvils. Rhenium was selected as gasket material due to its relatively inert behaviour in near neutral aqueous solutions at high temperatures and its mechanical properties (Xiong and Wood, 2002). The Re gaskets had an initial thickness of 125  $\mu\text{m}$  and a hole diameter of 500  $\mu\text{m}$ . The gasket was mounted on the culet face of the lower diamond anvil and then slightly compressed between the anvils to prevent uncontrolled leakage of the fluid during loading. Then, a glass chip of known dimensions was placed in the sample chamber. The dimensions were chosen such that the glass amount was about 20 to 25 wt.% of the desired bulk composition. This liquid-glass ratio was found to be optimal, because a larger proportion of glass increased the probability that both melt and fluid were present in the recess and thus in the effective excitation volume. A smaller proportion of glass complicated later chemical analyses of the quenched melt droplets due to their small size. The mass of the glass chip was obtained using a density of  $2.4 \text{ g/cm}^3$  and the volume calculated from the measured dimensions of the glass piece because the mass of the glass chip was too small for accurate determination by weighing. The aqueous fluid was then transferred into the sample chamber. Before the sample chamber was sealed, an air bubble was allowed to grow by controlled leaking of the liquid. The actual proportion of glass was calculated from the sample chamber volume, the volume of the glass piece calculated from the known dimensions,

the glass density, the fluid density obtained from the liquid-vapour homogenisation temperature ( $T_H = T_{L+V \rightarrow L}$ ) during first heating, and the salinity. The volume ratio of the produced air bubble to the remaining liquid was chosen such that the fluid density was sufficiently low to attain a pressure between 200 and 500 MPa at 750°C. After loading, the gasket was slightly compressed further between the anvils, just enough to seal the sample chamber. This procedure minimises the reduction of the sample chamber volume due to gasket flow during first heating. For experiments with salt solutions, the actual salt concentration in the aqueous fluid after sealing was determined from the measured vapour-saturated ice liquidus temperature  $T_m = T_{(I+L+V \rightarrow L+V)}$ , the known ratio of the solutes, and literature data for the vapour-saturated ice liquidus in the system  $H_2O+NaCl+KCl$  (Hall et al., 1988).

### 2.2.4 HDAC experiments

The loaded cell was fixed on a goniometer on the top of the xyz table at the beamline (Fig.2.1B) in the position for optical observation. The cell was heated to measure the  $T_H$  of the aqueous fluid, and then to the first experimental temperature. If the excitation volume was free of melt (cf., Fig. 2.2), the cell was rotated around the vertical axis into the position for XRF spectrum acquisition. The sample chamber was aligned to the beam and the fluorescence detector. The Rb  $K\alpha$  signal was scanned across the recess to verify that the measurement position was correct and that no melt droplet had moved into the recess. Subsequently, XRF spectra of the fluid were acquired as a function of time and with time steps of 500 or 1000 seconds. After spectrum acquisition, the cell was rotated back to the microscope position, and a new temperature was set. If no melt had entered the recess, the cell was moved back to the XRF position and aligned again. This process took about 5 minutes. At each P-T condition, consecutive XRF spectra of the fluid were recorded until the XRF signal indicated that equilibrium was attained or that melt had moved into the effective excitation volume. At the end of a stepwise cooling sequence, the cell was heated again to 750°C and then quenched after attainment of equilibrium with a rate of 200°C per minute. This was done to obtain  $D^{f/m}$  values from subsequent EMP analyses of the quenched melt. During first heating, gasket creep causes a permanent sample volume change (Schmidt and Rickers, 2003). However, the sample volume is nearly constant upon cooling. The actual density of the fluid was therefore determined from measurements of the liquid-vapour homogenisation temperature after each temperature step during stepwise heating. In the case of stepwise cooling, it was measured only after the last temperature step.

For the calculation of density and pressure in experiments with salt solutions, the composition was

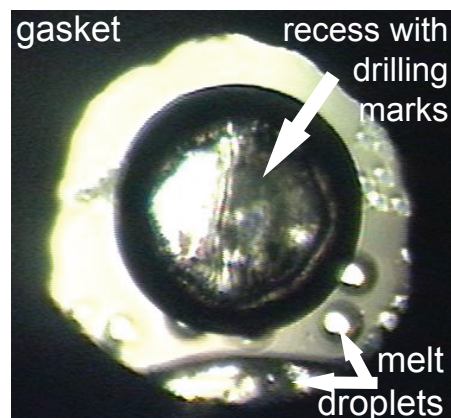


Figure 2.2: View in the sample chamber at 750°C. The recess is free of melt and thus, the measured SR- $\mu$ XRF signal contains no contribution from the melt.



first simplified by setting wt.% NaCl + wt.% KCl = wt.% (NaCl+KCl). Similar approximations of complex compositions are often used in studies of natural fluid inclusions to model isochores based on the system H<sub>2</sub>O+NaCl (Roedder, 1984, Bodnar, 2003). The density was calculated using correlations for the molar volume given by Driesner (2007) for NaCl+H<sub>2</sub>O solutions and the equation of state (EOS) by Haar et al. (1984) for pure H<sub>2</sub>O based on the determined T<sub>H</sub> and wt.% (NaCl+KCl). We used the EOS by Haar et al. (1984) because it is the reference equation of state used by Driesner (2007) for the pure water system. The pressure at the experimental temperature was calculated from the salinity expressed as wt.% (NaCl+KCl) and the homogenisation temperature measured after the experiment. The calculations were based on the slopes of the lines of constant T<sub>H</sub> given by Bodnar and Vityk (1994) for salt bearing compositions, and the EOS by Haar et al. (1984) for experiments with H<sub>2</sub>O as initial fluid composition. At the conditions of our study, the effect of dissolved silica on pressures based on isochores calculated from T<sub>H</sub> is insignificant (Shen et al., 1993). Furthermore, the solubility of melts with high aluminum content in water is low (Mysen and Acton, 1999). Moreover, the iso-T<sub>H</sub> line slopes for H<sub>2</sub>O+NaCl (Bodnar and Vityk, 1994) are from experiments at SiO<sub>2</sub> saturation. Additionally, the effect of an error in the density on the calculated pressure is much smaller at low densities (such as those in this study) than at high densities. For all these reasons, the pressures calculated here should be sufficiently accurate.

### 2.2.5 XRF spectra acquisition and calibration

The experiments were performed at beamline L (HASYLAB) of DORIS III, a second-generation synchrotron light source at DESY, Hamburg, Germany. A single-bounce capillary (SBC) was used to focus the synchrotron beam. The capillary was developed and manufactured at Cornell University for the source characteristics of beamline L (Huang and Bilderback, 2006). The SBC has a focal distance of 5 cm and focuses hard X-rays up to 40 keV into a spot of 11±1 μm. A micro-beamstop was aligned at the beam entrance into the SBC to absorb the portion of beam that would pass the capillary without focusing. Utilisation of the SBC increases the flux density by a factor of 300, and therefore decreases the lower limit of detection for elements with fluorescence energies between 12 and 20 keV to 1 to 5 ppm in HDAC experiments (Schmidt et al., 2007). In this study, the lower limit of detection of Rb was 1 to 2 ppm, as determined from SR-μXRF spectra of standard solutions loaded into HDAC 3 and HDAC G. The lower limit of detection (mdl) was calculated from  $mdl=3c\sqrt{B}/I$ , where *c* is the concentration, *B* the background intensity and *I* the peak intensity (e.g., Haller and Knöchel, 1996).

A synchrotron beam with a photon energy of 20.3±0.1 keV provided by a multilayer wide bandpass monochromator was used for excitation. All XRF spectra were recorded using a high purity Ge solid-state detector aligned in the polarisation plane of the incoming X-rays at 90° to the synchrotron beam. The spectra were collected with live counting times of 500 or 1000 seconds.

Figure 2.3 shows two examples of obtained XRF spectra, one of a standard solution and the other one of an aqueous fluid in equilibrium with melt at 750°C. The integrated intensities of the fluorescence lines were obtained from fits of the spectra using PyMca, a graphical interface for multi-channel analyser spectra visualisation and analysis developed at the ESRF

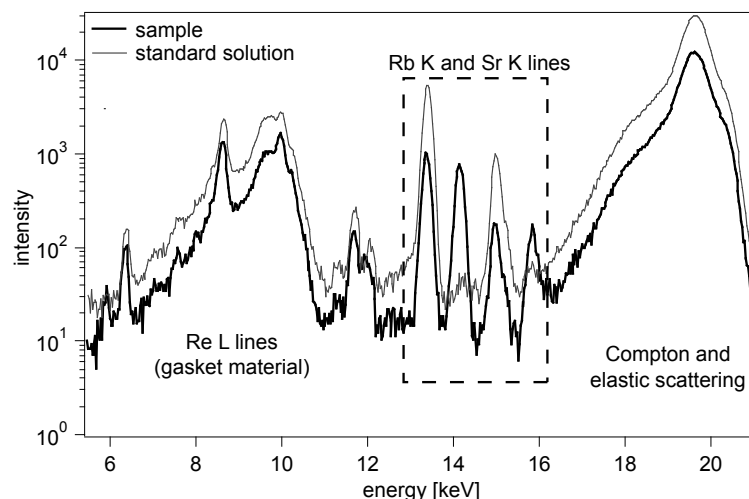


Figure 2.3: SR- $\mu$ XRF spectra of a sample containing 2.84 m (NaCl+KCl) + 0.03 m HCl and a standard solution.

(Solé et al., 2007). The integrated intensities were normalised to the intensity of the incident beam and then divided by the density of the fluid. The normalised integrated intensities were calibrated using XRF spectra of standard solutions. The standard solutions had initial concentrations of 250 and 995 ppm Rb (matrix 10 wt.% NaCl). Before the sample chamber is sealed, a small portion of the H<sub>2</sub>O of the solution evaporates, which increases the NaCl and Rb concentration. Therefore, the actual concentration of Rb in the standard solution after loading into the sample chamber was determined from the actual NaCl concentration calculated from the measured vapour-saturated ice melting temperature, and the known NaCl/RbCl ratio ( $c_{\text{actual}}^{\text{Rb}} = c_{\text{initial}}^{\text{Rb}} \cdot c_{\text{actual}}^{\text{NaCl}} / c_{\text{initial}}^{\text{NaCl}}$ ). For each cell, two XRF spectra were collected at temperatures slightly above  $T_{\text{H}}$ . The obtained integrated intensities of the Rb K fluorescence lines of the standard solutions were normalised to the intensity of the incident beam and divided by the fluid density. The Sr concentration in the fluid was determined based on normalisation of the integrated intensities of the Sr K fluorescence lines to the density of the fluid and the intensity of the incoming beam, the calibration for Rb from the standard solutions, and multiplication with a Rb/Sr correction factor. This factor corrects for different fluorescence cross-sections of Rb and Sr K fluorescence, and fluorescence transmission through the diamond. A Rb/Sr correction factor of  $0.844 \pm 0.006$  was obtained for HDAC 3 from XRF spectra of a standard solution with equal concentrations of Rb and Sr (500 ppm each) loaded into the sample chamber. These spectra were collected using the same procedure as described above. The empirical Rb/Sr factor differs only by 2 % from the theoretical value calculated by multiplying the ratio of the fluorescence-cross sections (e.g., XRAYLIB, Brunetti et al., 2004) with the ratio of the transmission of the K line fluorescence X-rays through 0.5 mm diamond. This small difference is within the uncertainties of the databases (e.g., Brunetti et al., 2004). We also applied the empirical Rb/Sr correction factor to the spectra from experiments using HDAC G, because the design of both cells and the X-ray path length were very similar.

## 2.2.6 EMP analyses

After quenching, the glass droplets in the gasket were embedded in epoxy resin, ground and polished. The EMP measurements were carried out at the GFZ Potsdam using a CAMECA SX-100. The analysed elements were Na, K, Al, Si, Rb and Sr. The measurement conditions were a beam current of 10 nA, an electron beam energy of 15 keV, and counting times of 10 seconds for Na and K, 20 seconds for Al and Si, and 30 seconds for Rb and Sr.

Table 2.1: Summary of the experimental conditions, results of the *in-situ* SR- $\mu$ XRF analyses of the aqueous fluids, and of the EMP analyses of the glasses, and calculated partition coefficients ( $D^{\text{fluid/melt}} = c^{\text{fluid}}/c^{\text{melt}}$ ) at 750°C.

sample	1	2	3	4	5
cell	HDAC 3	HDAC 3	HDAC G	HDAC G	HDAC G
$P_{\text{exp}}$ at $T_{\text{exp}}=750^\circ\text{C}$ [MPa]	224	262	360	540	700
$m$ (NaCl+KCl)	3.56	2.84	0	0	0
$m$ HCl	0.04	0.03	0	0	0
NaCl + KCl [wt.%]	16.8	14.3	0	0	0
% glass [wt.%]	24	17	24	23	35
$\rho^{\text{fluid}}$	0.6855	0.6940	0.6336	0.7494	0.8022
$T_{\text{m}}$ [ $^\circ\text{C}$ ]	-10.6	-8.6	n.d.	n.d.	n.d.
$T_{\text{H}}$ [ $^\circ\text{C}$ ] <sup>‡</sup>	439	409	333	281	248
$c_{\text{Rb}}^{\text{f}}$ [ppm]	712±6	308±4	31±5	77±6	546±42
$c_{\text{Rb}}^{\text{m}}$ [ppm]	1510±247	1028±224	3007±275	n.d.*	2487±172
$c_{\text{Sr}}^{\text{f}}$ [ppm]	495±6	205±3	22±3	19±3	69±16
$c_{\text{Sr}}^{\text{m}}$ [ppm]	2085±299	1663±333	3532±555	n.d.*	3270±142
$\text{Rb/Sr} = \frac{c_{\text{Rb}}^{\text{f}}}{c_{\text{Sr}}^{\text{f}}}$	1.44±0.02	1.51±0.03	1.39±0.15	4.16±0.42	7.89±1.59
$D_{\text{Rb}}^{\text{f/m}}$	0.47±0.08	0.30±0.07	0.01±0.002	n.d.*	0.22±0.02
$D_{\text{Sr}}^{\text{f/m}}$	0.24±0.03	0.12±0.02	0.006±0.001	n.d.*	0.02±0.005
SiO <sub>2</sub> [wt.%]	73.37	71.51	73.89	n.d.*	68.74
Al <sub>2</sub> O <sub>3</sub> [wt.%]	12.77	12.37	12.81	n.d.*	13.64
Na <sub>2</sub> O [wt.%]	3.49	2.82	4.25	n.d.*	2.58
K <sub>2</sub> O [wt.%]	5.72	6.14	3.39	n.d.*	3.93
ASI	1.07	1.10	1.20	n.d.*	1.33

The listed element concentrations in the fluid and melt represent average values.

<sup>f</sup> – fluid; <sup>m</sup> – melt;  $m$  – molality; n.d. – not determined; % glass – proportion of glass; <sup>‡</sup> – measured after collection of XRF spectra at  $T_{\text{exp}}=750^\circ\text{C}$ ; ASI =  $\text{Al}_2\text{O}_3/(\text{Na}_2\text{O} + \text{K}_2\text{O})$  in moles; n.d.\* – not determined because sample was lost during preparation for EMP analysis.

## 2.3 Results and Discussion

The experimental conditions, the Rb and Sr concentrations in the fluids coexisting with melt obtained from *in-situ* SR- $\mu$ XRF analyses, the results of the EMP analyses of the glasses after the quench, and the calculated  $D$  values are listed in Table 2.1. Figure 2.4 shows the Rb and Sr concentrations in the aqueous fluid coexisting with melt at different temperatures for 3 different initial fluid compositions as a function of the time elapsed after the run temperature was reached. The results of both the stepwise heating and cooling runs indicate rapid equilibration of Rb and Sr between fluid and melt in all experiments. For chloridic fluids (Figs. 2.4A and 2.4B), equilibrium was attained in less than 2000 seconds. If the random error in the concentrations is taken into account, it is very likely that equilibration was faster than the minimum time

required to complete acquisition of the first XRF spectrum (about 500 seconds). For chloride-free fluids (Fig. 2.4C), the time required to reach equilibrium at 750°C was probably below 3000 seconds, but this is difficult to constrain from the data due to the relatively large error in the concentrations. We believe that the trace element concentrations in the fluids obtained in this study represent equilibrium values. Our data show stable Rb and Sr concentrations over a relatively long time at  $T_{\text{exp}}$ , e.g., over 9000 seconds in the experiment with H<sub>2</sub>O as starting fluid shown in Fig. 2.4C. Furthermore, the existence of a significant concentration gradient in the aqueous phase in the recess at high temperatures is very unlikely because convection in the sample chamber is substantial and diffusion is rapid. This is supported by a study on rutile dissolution in aqueous fluids using a HDAC (Audétat and Keppler, 2005), in which a diffusion coefficient of  $8.0 \cdot 10^{-7} \text{ m}^2 \text{ s}^{-1}$  at 800°C and 2 GPa was calculated assuming a hydrated complex of Ti<sup>4+</sup>. This diffusion coefficient translated into a travel time of the complex of about 0.16 seconds across the entire sample chamber of 500 μm in diameter. In analogy to silicate melts (Koepke and Behrens, 2001), Rb and Sr diffusion in aqueous fluids can be expected to be even faster than the diffusion of this high-field strength element.

The Rb and Sr concentrations in the fluid can be directly compared for experiments with similar glass/fluid ratios and pressures (Tab. 2.1). The concentrations of both elements increased by an order of magnitude with addition of chloride to the starting fluid (from 0 to 3.56 m (NaCl+KCl) + 0.04 m HCl) due to their affinity to form Cl complexes in aqueous solutions.

The temperature dependence of the Rb and Sr concentrations in chloridic fluids shows opposite trends along an isochore, i.e., slightly decreasing Rb contents and slightly increasing Sr concentrations upon cooling. This is more pronounced for the experiment containing 3.56 m (NaCl+KCl) + 0.04 m HCl in the starting fluid (Fig. 2.4A). The Rb concentration in the fluid decreased by 17 % from 737±12 to 611±1 ppm upon cooling from 780 to 600°C, whereas the Sr content increased by 12 % from 473±8 to 531±10 ppm. The same trends were also recognisable, but less distinct, in the experiment with an initial salinity of 2.84 m (NaCl+KCl) + 0.03 m HCl (Fig. 2.4B). In this experiment, there may also have been a small pressure effect on the Sr content in the fluid at 680°C (232±8 ppm at 160 MPa and 212±8 ppm at 212 MPa), while the Rb concentration remained constant at 305±8 ppm.

In the experiment at 360 MPa with H<sub>2</sub>O as initial fluid (Fig 2.4C), XRF spectra were collected only at 750°C. The average concentrations were 31±5 ppm Rb and 22±3 ppm Sr. Due to the low concentrations, the error was too large to obtain concentration changes along an isochore with confidence. At 750°C, the Rb concentration in the fluid increased with pressure by a factor of about 2.5 from 31±5 ppm at 360 MPa to 77±6 ppm at 540 MPa for similar glass/fluid ratios. In contrast, the Sr concentration remained nearly constant (22±3 ppm at 360 MPa and 19±3 ppm at 540 MPa). The increase in the Rb concentration may indicate that the pH of the aqueous fluid becomes more basic, which would suggest that Rb complexes predominantly with OH in the absence of ligands such as Cl. Such a change in pH could be related to the enhanced water dissociation (Bandura and Lvov, 2006) and an enhanced water-melt reaction with pressure (e.g., Stalder et al., 2000). The latter may involve formation of aluminosilicate complexes in the fluid, as suggested by e.g., Manning (2004) and Manning (2007) for high pressures. In contrast, the nearly constant Sr concentrations suggests a significant difference in the complexation of Sr compared to that of Rb.

The difference in the pressure dependence of Rb and Sr becomes even more obvious

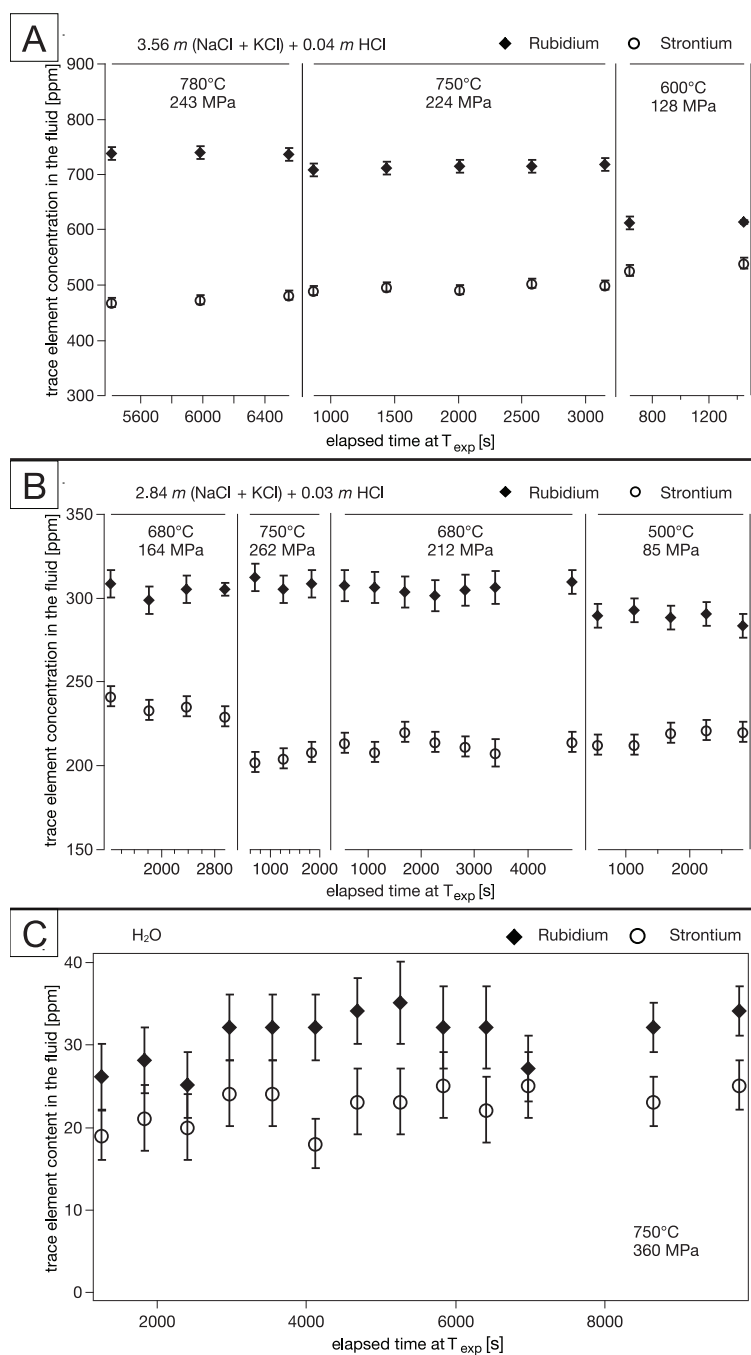


Figure 2.4: Concentration of trace elements Rb and Sr in the aqueous fluid vs. elapsed time after attainment of the experimental temperature  $T_{exp}$  for various fluid compositions: **A** - 3.56 m (NaCl+KCl) + 0.04 m HCl, **B** - 2.84 m (NaCl+KCl) + 0.03 m HCl and, **C** H<sub>2</sub>O. The error bars represent  $2\sigma$  errors.

if the Rb/Sr ratio in the fluid is considered. Figure 2.5 shows the Rb/Sr ratio in the fluid as a function of pressure and initial fluid salinity. At pressures between 224 and 360 MPa, the

Rb/Sr ratio was independent of the initial salt concentration, with a Rb/Sr value of  $1.45 \pm 0.06$ . In contrast, an increase of the Rb/Sr ratio with pressure was observed in the case of the experiments with  $\text{H}_2\text{O}$ , up to a ratio of  $7.89 \pm 1.95$  at 700 MPa. This strong change of the Rb/Sr ratio with pressure points to different trends of the speciation of the two elements in Cl-free aqueous fluids.

The relationship between the calculated fluid-melt partition coefficients  $D^{f/m}$  ( $D^{f/m} = c^f/c^m$ ,

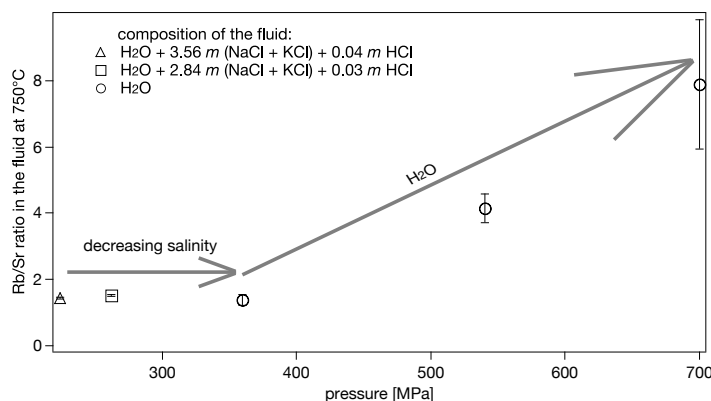


Figure 2.5: Rb/Sr ratio in the fluid vs. pressure. The diagram shows a constant Rb/Sr ratio at 750°C for various compositions and low pressures. For  $\text{H}_2\text{O}$ –melt experiments at constant temperatures we see a strong pressure dependence of the Rb/Sr ratio in the fluid.

where  $c^f$  is the concentration in the fluid and  $c^m$  is the concentration in the melt) and the initial salt concentration of the fluid is illustrated in Fig. 2.6. The fluid-melt partition coefficients of Rb and Sr were determined for different salinities at 750°C and 220 to 700 MPa. We observed a positive correlation of the  $D^{f/m}$  values with initial chlorinity of the fluid. The  $D_{\text{Rb}}^{f/m}$  increased from 0.01 for  $\text{H}_2\text{O}$  as initial fluid to 0.47 for a 3.56 m (NaCl+KCl) + 0.04 m HCl. The  $D_{\text{Sr}}^{f/m}$  were slightly smaller and changed from 0.006 to 0.24. The effect of pressure on the partition coefficients appears to be smaller compared to that of the salinity. For  $\text{H}_2\text{O}$  experiments, the  $D^{f/m}$  increased from 0.01 to 0.22 (Rb) and 0.006 to 0.02 (Sr) for a pressure increase from 360 to 700 MPa.

Fluid/melt partitioning of Rb and Sr was previously studied by Bai and Koster van Groos (1999) and Webster et al. (1989) using conventional quench experiments. The  $D^{f/m}$  obtained by Bai and Koster van Groos (1999) are much higher in the case of chloride-bearing systems. For similar P–T conditions, they reported a  $D_{\text{Rb}}^{f/m}$  of 1.56 and a  $D_{\text{Sr}}^{f/m}$  of 0.94 at 750°C and 200 MPa. This differs from our results by a factor of 3.3 for Rb and 4 for Sr. However, Bai and Koster van Groos (1999) used a different initial fluid composition (1.3 m NaCl + 2.9 m KCl), which also resulted in other melt compositions due to the exchange of sodium and potassium between melt and fluid. Webster et al. (1989) provided data at about 770°C and 200 MPa for  $\text{H}_2\text{O} + \text{HCl}$ –melt systems. For two experiments differing only in the run duration, they reported quite different  $D_{\text{Rb}}^{f/m}$  of 0.3 and 1.4. The lower value is similar to those obtained in this study at much higher Cl concentrations. This suggests that addition of HCl (and thus lowering the pH)

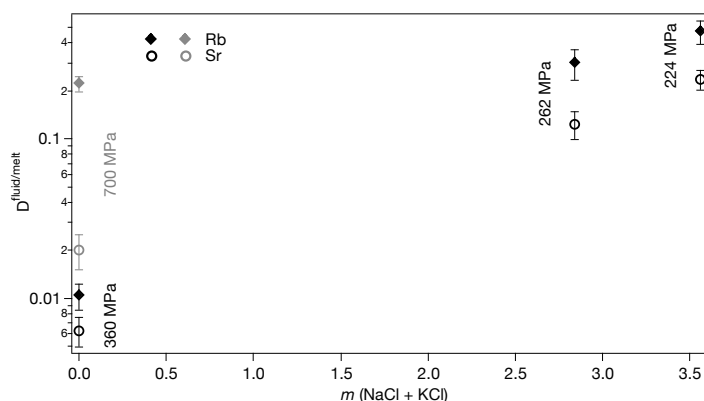


Figure 2.6: Fluid–melt partition coefficients of Rb and Sr vs. initial salt concentration of the fluid [ $m$  (NaCl+KCl)] at 750°C. For similar pressures an increase of initial salt concentration corresponds to an increase of  $D_{\text{Rb}}^{\text{f/m}}$  and  $D_{\text{Sr}}^{\text{f/m}}$ . For H<sub>2</sub>O–melt experiments, we observed a pressure dependence of the  $D$  values particularly for Rb (light grey symbols = experiment at 700 MPa).

causes a higher partitioning of Rb into the fluid than addition of NaCl+KCl. However, the large variation in the results for the 2 runs reported by Webster et al. (1989) could also be related to experimental difficulties in quench experiments (see introduction). For Sr, only one value was obtained ( $D_{\text{Sr}}^{\text{f/m}} = 0.1$ ), which differs similarly from our results as those for Rb.

Bai and Koster van Groos (1999) provided data from melt+H<sub>2</sub>O experiments at 750°C and 200 MPa. The reported partition coefficients of Rb (0.006) and Sr (0.002) are much lower than those at 360 MPa obtained in this study ( $D_{\text{Rb}}^{\text{f/m}} = 0.01$  and  $D_{\text{Sr}}^{\text{f/m}} = 0.006$  at 750°C). The experiments from both studies were at similar compositions but differed in pressure by 160 MPa, which can only in part explain the discrepancies in the  $D^{\text{f/m}}$ .

## 2.4 Conclusions

The technique successfully applied in this study has two important advantages. The trace element concentration in the fluid can be determined without the ambiguities associated with data from quench techniques. Additionally, kinetic information can be obtained.

The drawbacks are, however, limited availability of beam time and a more difficult control of the bulk composition and pressure, which complicates systematic studies.

The technique can be improved further by the following. (i) The experimental setup can be modified for permanent optical observation of the sample chamber, which would allow to study the equilibration process at shorter timescales. This is because no time is lost to rotate and align the cell before acquisition of XRF spectra. Another advantage is permanent visual monitoring of the effective excitation volume, e.g., for immediate recognition of the unwanted case that melt droplets migrate into this volume. (ii) Use of a synchrotron radiation source with higher intensity such as an undulator insertion device will improve the sensitivity and thus the data at low concentrations. In addition, spectrum acquisition times can be reduced, which

results in a better temporal resolution in kinetic studies. (iii) The trace element concentration in the glasses can be obtained more accurately using techniques with a higher sensitivity, e.g., using laser-ablation inductively-coupled plasma mass spectrometry, especially if an appropriate element is used as an internal standard, such as Si known from the EMP analyses. (iv) It may be possible to modify the geometry of the anvils and the gasket in such a way that both aqueous fluid and melt can be unambiguously analysed *in situ* in the same experiment at high PT.

The results of this study show, firstly, an increase of the concentrations of Rb and Sr in the fluid by an order of magnitude with addition of chloride to the starting fluid (from 0 to 3.56 *m* (NaCl+KCl) + 0.04 *m* HCl). Secondly, opposite trends were observed for the temperature dependence of Rb and Sr in the fluid along an isochore. The Rb content in the fluid increased but the Sr concentration decreased with temperature. Thirdly, the Sr concentration in the fluid displayed a slightly negative correlation with pressure at constant temperature, while the Rb content did not change (see Fig. 2.4B). Furthermore, we observed differences in the pressure dependence of the Rb and Sr concentrations in the fluid in H<sub>2</sub>O + melt experiments. The Rb/Sr ratio in the fluid increased from  $1.45 \pm 0.06$  to  $7.89 \pm 1.95$  with an increase in pressure from 360 to 700 MPa. The obtained partition coefficients of both elements are positively correlated with the initial Cl concentration of the fluid. In the H<sub>2</sub>O+melt experiments, we found an increase of the D values with pressure, which was more pronounced for Rb.

The results of this study demonstrate that the equilibration between aqueous fluid and melt is rapid and can therefore affect partition coefficients obtained in quench experiments. However, the observed concentration changes upon isochoric cooling were relatively small. Therefore, these changes can only account for a small portion of the differences between the fluid-melt partitioning data from quench techniques and those obtained in this study. Consequently, uncertainties in the fluid-melt partitioning data from quench techniques can mainly be attributed to the difficulty of obtaining a representative sample of the fluid. Usually, the fluid composition has to be reconstructed from the quenched products (fluid and quench precipitates). As already pointed out by Webster et al. (1989), this may be a major contribution to the error in these experiments and thus explain the often wide spread in the results of runs at similar conditions. This becomes particularly obvious if data from different studies are compared. For example,  $D^{f/m}$  reported by Bai and Koster van Groos (1999) at low HCl concentrations are significantly lower (up to a factor of 7.5 for Rb) than those obtained by Webster et al. (1989) at similar conditions. Part of this discrepancy can probably be attributed to the different experimental procedures used to obtain the partition coefficients, and the related systematic error. Therefore, the *in-situ* technique applied here can be helpful to obtain more reliable and consistent data on the trace element distribution between aqueous fluid and granitoid melts.

#### *Acknowledgements*

We thank HASYLAB at the Deutsches Elektronen-Synchrotron (DESY) for granting beamtime and O. Appelt for the benefit with EMP measurements at GFZ Potsdam. This study was supported by the German Science Foundation (DFG, Wi 2000/3-1).



- Adam, J., Green, T. H., Sie, S. H., and Ryan, C. G. (1997). Trace element partitioning between aqueous fluids, silicate melts and minerals. *Eur. J. Mineral.*, 9:569–584.
- Audétat, A. and Keppler, H. (2005). Solubility of rutile in subduction zone fluids, as determined by experiments in the hydrothermal diamond anvil cell. *Earth and Planetary Science Letters*, 232:393–402.
- Ayers, J. C. and Eggler, D. H. (1995). Partitioning of elements between silicate melt and H<sub>2</sub>O-NaCl fluids at 1.5 and 2.0 GPa pressure: Implications for mantle metasomatism. *Geochimica et Cosmochimica Acta*, 59(20):4237–4246.
- Bai, T. B. and Koster van Groos, A. F. (1999). The distribution of Na, K, Rb, Sr, Al, Ge, Cu, W, Mo, La, and Ce between granitic melts and coexisting aqueous fluids. *Geochimica et Cosmochimica Acta*, 63(7/8):1117–1131.
- Bandura, A. and Lvov, S. (2006). The ionization constant of water over a wide range of temperatures and densities. *Journal of Physical and Chemical Reference Data*, 35:15–30.
- Bassett, W. A., Anderson, A. J., Mayanovic, R. A., and Chou, I.-M. (2000). Modified hydrothermal diamond anvil cells for XAFS analyses of elements with low energy absorption edges in aqueous solutions at sub- and supercritical conditions. *Zeitschrift für Kristallographie*, 215:711–717.
- Bassett, W. A., Shen, A. H., Bucknum, M., and Chou, I.-M. (1993). A new diamond anvil cell for hydrothermal studies to 2.5 GPa and from 190 to 1200°C. *Review of scientific instruments*, 64:2340–2345.
- Behrens, H., Meyer, M., Holtz, F., Benne, D., and Nowak, M. (2001). The effect of alkali ionic radius, temperature, and pressure on the solubility of water in MAISi<sub>3</sub>O<sub>8</sub> melts (M = Li, Na, K, Rb). *Chemical Geology*, 174:275–289.
- Best, M. G. (2003). *Igneous and Metamorphic Petrology*. Blackwell.
- Bodnar, R. J. (2003). *Fluid Inclusions: Analysis and Interpretation*, volume 32, chapter Introduction to aqueous fluid systems., pages 81–99. Mineralogical Association of Canada.
- Bodnar, R. J. and Vityk, M. O. (1994). *Interpretation of microthermometric data for H<sub>2</sub>O-NaCl fluid inclusions. Fluid Inclusions in Minerals: Methods and Applications*, pages 117–130. Virginia Tech.

- 
- Brunetti, A., del Rio, M. S., Golosio, B., Simionovici, A., and Somogyi, A. (2004). A library for X-ray-matter interaction cross sections for X-ray fluorescence applications. *Spectrochimica Acta*, 59:1725–1731.
- Bureau, H., Ménez, B., Malavergne, V., Somogyi, A., Simionovici, A., Massare, D., Khodja, H., Daudin, L., Gallien, J.-P., Shaw, C., and Bonnin-Mosbah, M. (2007). In situ mapping of high-pressure fluids using hydrothermal diamond anvil cells. *High Pressure Research*, 27(2):235–247.
- Driesner, T. (2007). The system H<sub>2</sub>O-NaCl. Part II: Correlations for molar volume, enthalpy, and isobaric heat capacity from 0 to 1000°C, 1 to 5000 bar, and 0 to 1 X<sub>NaCl</sub>. *Geochimica et Cosmochimica Acta*, 71:4902–4919.
- Flynn, R. T. and Burnham, C. W. (1978). An experimental determination of rare earth partition coefficients between a chloride containing vapor phase and silicate melts. *Geochimica et Cosmochimica Acta*, 42:685–701.
- Haar, L., Gallagher, J., and Kell, G. (1984). *Steam tables*; chapter Thermodynamic and transport properties and computer programs for vapor and liquid states of water in SI units, page 320. Hemisphere Pub. Corp., Washington, D.C.
- Hall, D. L., Sterner, S. M., and Bodnar, R. J. (1988). Freezing Point depression of NaCl-KCl-H<sub>2</sub>O Solutions. *Economic Geology*, 83:197–202.
- Haller, M. and Knöchel, A. (1996). X-ray fluorescence analysis using synchrotron radiation-(SRXRF). *Journal of Trace Microprobe Technics*, 14:461–488.
- Holland, H. D. (1972). Granites, Solutions, and Base Metal Deposits. *Economic Geology*, 67(3):281–301.
- Holtz, F., Behrens, H., Dingwell, D. B., and Johannes, W. (1995). H<sub>2</sub>O solubility in haplogranitic melts: Compositional, pressure, and temperature dependence. *American Mineralogist*, 80:94–108.
- Huang, R. and Bilderback, D. H. (2006). Single-bounce monochromators for focusing synchrotron radiation: modeling, measurements and theoretical limits. *Journal of Synchrotron Radiation*, 13:74–84.
- Johannes, W. and Holtz, F. (1996). *Petrogenesis an Experimental Petrology of Granitic Rocks*. Springer, Berlin.
- Keppler, H. and Wyllie, P. J. (1991). Partitioning of Cu, Sn, Mo, W, U, and Th between melt and aqueous fluid in the systems haplogranite-H<sub>2</sub>O-HCl and haplogranite-H<sub>2</sub>O-HF. *Contributions to Mineralogy and Petrology*, 109:139–150.
- Koepke, J. and Behrens, H. (2001). Trace element diffusion in andesitic melts: an application of synchrotron X-ray fluorescence analysis. *Geochimica et Cosmochimica Acta*, 65:1481–1489.

- London, D., Hervig, R. L., and Morgan, G. B. (1988). Melt-vapor solubilities and elemental partitioning in peraluminous granite-pegmatite systems: experimental results with Macusani glass at MPa. *Contributions to Mineralogy and Petrology*, 99:360–373.
- Manning, C. E. (2004). The chemistry of subduction-zone fluids. *Earth and Planetary Science Letters*, 223:1–16.
- Manning, C. E. (2007). Solubility of corundum + kyanite in H<sub>2</sub>O at 700°C and 10 kbar: evidence for Al-Si complexing at high pressure and temperature. *Geofluids*, 7:258–269.
- Muñoz, M., Bureau, H., Malavergne, V., Ménez, B., Wilke, M., Schmidt, C., Simionovici, A., Somogyi, A., and Farges, F. (2005). In situ speciation of nickel in hydrous melts exposed to extreme conditions. *Physica Scripta*, 115:921–922.
- Mysen, B. O. and Acton, M. (1999). Water in H<sub>2</sub>O-saturated magma-fluid systems: Solubility behavior in K<sub>2</sub>O-Al<sub>2</sub>O<sub>3</sub>-SiO<sub>2</sub>-H<sub>2</sub>O to 2.0 GPa and 1300°C. *Geochimica et Cosmochimica Acta*, 63:3799–3815.
- Rickers, K., Thomas, R., and Heinrich, W. (2006). The behavior of trace elements during the chemical evolution of the H<sub>2</sub>O-, B-, and F-rich granite-pegmatite-hydrothermal system at Ehrenfriedersdorf, Germany: a SXRF study of melt and fluid inclusions. *Mineralium Deposita*, 41:229–245.
- Roedder, E. (1984). *Reviews in Mineralogy 12: Fluid Inclusions*. Mineralogical Society of America.
- Schmidt, C. and Rickers, K. (2003). In-situ determination of mineral solubilities in fluids using a hydrothermal diamond-anvil cell and SR-XRF: Solubility of AgCl in water. *American Mineralogist*, 88:288–292.
- Schmidt, C., Rickers, K., Bilderback, D. H., and Huang, R. (2007). In situ synchrotron-radiation XRF study of REE phosphate dissolution in aqueous fluids to 800°C. *Lithos*, 95:87–102.
- Shen, A. H., Bassett, W. A., and Chou, I.-M. (1993). The alpha-beta quartz transition at high temperatures and pressures in a diamond-anvil cell by laser interferometry. *American Mineralogist*, 78:694–698.
- Solé, V. A., Papillon, E., Cotte, M., Walter, P., and Susini, J. (2007). A multiplatform code for the analysis of energy-dispersive X-Ray fluorescence spectra. *Spectrochimica Acta*, B 62:63–68.
- Stalder, R., Ulmer, P., Thompson, A. B., and Günther, D. (2000). Experimental approach to constrain second critical end points in fluid/silicate systems: Near-solidus fluids and melts in the system albite-H<sub>2</sub>O. *American Mineralogist*, 85:68–77.
- Webster, J. D., Holloway, J. R., and Hervig, R. L. (1989). Partitioning of Lithophile trace elements between H<sub>2</sub>O and H<sub>2</sub>O+CO<sub>2</sub> fluids and topaz rhyolite melt. *Economic Geology*, 84:116–134.

---

Winter, J. D. (2001). *An Introduction to Igneous and Metamorphic Petrology*. Prentice Hall, New Jersey.

Xiong, Y. and Wood, S. (2002). Experimental determination of the hydrothermal solubility of  $\text{ReS}_2$  and the  $\text{Re-ReO}_2$  buffer assemblage and transport of rhenium under supercritical conditions. *Geochemical Transactions*, 3:1–10.

## Chapter 3

# **Rb and Sr partitioning between haplogranitic melts and aqueous solutions**

*accepted manuscript (Oct. 2009)*

*DOI: 10.1016/j.gca.2009.10.033*

*in press*

*Geochimica et Cosmochimica Acta*

## Partitioning and equilibration of Rb and Sr between silicate melts and aqueous fluids

Manuela Borchert<sup>a,\*</sup>, Max Wilke<sup>b</sup>, Christian Schmidt<sup>b</sup>, Karen Rickers<sup>c</sup>

<sup>a</sup> Universität Potsdam, Karl-Liebknecht-Str.24, 14476 Potsdam-Golm, Germany

<sup>b</sup> Deutsches GeoForschungsZentrum (GFZ), Section 4.1, Telegrafenberg, 14473 Potsdam, Germany

<sup>c</sup> Hamburger Synchrotronstrahlungslabor at Deutsches Elektronensynchrotron, Notkestr. 85, 22607 Hamburg, Germany

### Abstract

Rubidium and strontium partitioning experiments between haplogranitic melts and aqueous fluids (starting compositions water or 1.16 to 3.56 *m* (NaCl+KCl)±HCl) were conducted at 750 to 950°C and 0.2 to 1.4 GPa to investigate the effects of melt and fluid composition, pressure and temperature. In addition, we studied if the applied technique (rapid and slow quench, and in-situ determination of trace element concentration in the fluid) has a bearing on the obtained data. There is good agreement of the data from different techniques for chloridic solutions, whereas back reactions between fluid and melt upon cooling have a significant effect on results from the experiments with water.

The Rb fluid–melt partition coefficient shows no recognizable dependence on melt composition and temperature. For chloridic solutions, it is ~ 0.4, independent of pressure. In experiments with water, it is one to two orders of magnitude lower and increases with pressure. The strontium fluid–melt partition coefficient does not depend on temperature. It increases slightly with pressure in Cl free experiments. In chloridic fluids, there is a sharp increase in the Sr partition coefficient with the alumina saturation index (ASI) from 0.003 at an ASI of 0.8 to a maximum of 0.3 at an ASI of 1.05. At higher ASI, it decreases slightly to 0.2 at an ASI of 1.6. It is one to two orders of magnitude higher in chloridic fluids compared to those found in H<sub>2</sub>O experiments. The Rb/Sr ratio in non-chloridic solutions in equilibrium with metaluminous melts increases with pressure, whereas the Rb/Sr ratio in chloridic fluids is independent of pressure and decreases with fluid salinity.

The obtained fluid–melt partition coefficients are in good agreement with data from natural co-genetic fluid and melt inclusions. Numerical modeling shows that although the Rb/Sr ratio in the residual melt is particularly sensitive to the degree of fractional crystallization, exsolution of a fluid phase and associated fluid–melt partitioning is not a significant factor controlling Rb and Sr concentrations in the residual melt during crystallization of most granitoids.

*Keywords:* fluid–melt partition coefficients, Rubidium, Strontium, Rb/Sr ratio, quench experiments, HDAC, SR- $\mu$ XRF

\* Corresponding author.

*E-mail address:* manu@geo.uni-potsdam.de (M.Borchert)

### 3.1 Introduction

Fluid–melt interaction is common in igneous processes because ascent of magma to shallower levels of the lithosphere will usually result in saturation with respect to water and other volatiles (Robb, 2005). Elements must then partition between the silicate melt, the crystallizing minerals and the exsolved magmatic volatiles. The equilibrium distribution of trace elements

is described by partition coefficients ( $D_X^{f/m} = c_X^{\text{fluid}}/c_X^{\text{melt}}$ ). Suitable trace elements are used for petrogenetic interpretations because, unlike major elements, they are not essential for the stability of the phases involved and often reflect magmatic processes with less ambiguity (e.g., Philpotts, 1990). The large ion lithophile (LIL) elements Rb and Sr are common trace elements in granites (e.g. Johannes and Holtz, 1996). Their concentrations are highly variable and the Rb/Sr ratio can be used to distinguish between different granite types (e.g., S-type and I-type, Chappell and White (1974)). Due to differences in charge and ionic radius (Rb<sup>+</sup> 166 pm, Sr<sup>2+</sup> 132 pm), they substitute differently for main elements in typical granite-forming minerals. Strontium substitutes readily for Ca in plagioclase and into the alkali site of potassium feldspar but not in micas. Rubidium is incorporated for potassium in K-feldspar or mica (Green, 1980). Hence, the Rb/Sr ratio of granitoids depends on the initial concentrations and on the stage of evolution.

The partitioning of Rb and Sr between the typical granite-forming minerals plagioclase, feldspar, biotite, and muscovite and granitoid melts has been the subject of many studies (e.g., Murray and Rogers, 1973, Icenhower and London, 1995, 1996, Ren et al., 2003, White et al., 2003, White, 2003, Bédard, 2006). Crystal-granitic melt partition coefficients of Sr range between 2 to 23 for K-feldspar, 4 to 13 for plagioclase, and 0.01 to 0.5 for biotite, and those of Rb are 0.01 to 0.7 for K-feldspar, 2.5 to 9 for biotite, and about 2 for muscovite. The partitioning of these elements between aqueous fluid and melt has been studied less extensively. Fluid-melt partitioning data have been either determined by experimental studies (e.g., Carron and Lagache, 1980, London et al., 1988, Webster et al., 1989, Ayers and Eggler, 1995, Bai and Koster van Groos, 1999) or from natural co-genetic fluid and melt inclusions (Audétat and Pettke, 2003, Rickers et al., 2006, Audétat et al., 2008, Zajacz et al., 2008). London et al. (1988) used Macusani glass and water in their experiments and determined a  $D_{\text{Rb}}^{f/m}$  of 0.2 and a  $D_{\text{Sr}}^{f/m}$  of 0.4 at 775°C and 200 MPa. Webster et al. (1989) studied partitioning of trace elements between topaz-rhyolite melts and H<sub>2</sub>O ± CO<sub>2</sub> as a function of Cl concentration at 200 MPa and 769 to 950°C. They found a transition from melt-compatible to fluid-compatible behavior with increasing chlorinity for many trace elements including Rb and Sr. Ayers and Eggler (1995) studied element partitioning between a synthetic andesitic melt and 1.5 or 3.0 *m* NaCl-H<sub>2</sub>O fluids at 1250°C and 1.5 or 2 GPa. Their data show no effect of pressure on the  $D_{\text{Rb}_2\text{O}}^{f/m}$  and a slight increase from 0.87 to 1.01 with salinity. Partition coefficients of SrO were constant at ~0.5, independent of pressure and salinity. Bai and Koster van Groos (1999) determined fluid-melt partitioning data between granitic melts and various aqueous fluids at 750–800°C and 100–400 MPa. The reported partition coefficient of Rb was 0.006 at 750°C and 200 MPa for H<sub>2</sub>O and increased with addition of NaCl and KCl to a maximum value of 1.63 for a 1.3 *m* NaCl + 2.6 *m* KCl solution. A similar behavior was found for Sr, where the  $D^{f/m}$  at 750°C and 200 MPa increased with salinity from 0.002 (H<sub>2</sub>O) to 1.93 for a 1.3 *m* NaCl + 2.6 *m* KCl solution. There are also a few data on fluid-melt partitioning data of Rb and Sr in the system Quartz-Albite-Orthoclase-H<sub>2</sub>O + 2 M (Na,K)Cl at 200 MPa and 700 and 800°C from an earlier study by Carron and Lagache (1980). In that study, partition coefficients of Rb and Sr are nearly independent of composition and are close to one, but not directly comparable because they are normalized to the (Na+K) contents of fluid and melt.

Audétat and Pettke (2003) studied the magmatic-hydrothermal evolution of two barren granites using coeval fluid and melt inclusions trapped at 700–720°C and 110–120 MPa. The obtained fluid–melt partition coefficient of Rb was  $0.2 \pm 0.1$  at a fluid salinity of 4.9 wt.% NaCl<sub>equiv</sub>. Rickers et al. (2006) investigated the behavior of trace elements during the chemical evolution of the H<sub>2</sub>O–, B–, and F–rich granite-pegmatite-hydrothermal system at the Ehrenfriedersdorf tin deposit, Germany. They observed very high Rb values (5000 to 5400 ppm) in melt inclusions trapped at ~700°C and ~100 MPa, and Sr concentrations  $\leq 17$  ppm. co-genetic fluid inclusions with a salinity of 52 wt.% NaCl<sub>equiv</sub> showed a Rb concentration of ~1000 ppm, with no detectable Sr. Their data yield a  $D_{Rb}^{f/m} \leq 0.2$  at 700°C. The usual interpretation of very high Rb values as reported by Rickers et al. (2006) is extreme fractionation, but the very high concentrations of fluxing components (F, B) should also contribute because they modify complexation in fluid and melt. Zajacz et al. (2008) analyzed co-existing silicate melt and fluid inclusions entrapped in quartz crystals in volatile–saturated granitic systems. The reported  $D_{Rb}^{f/m}$  scatter between 0.3 and 0.9 for low salinity fluids (up to 3 m Cl) and increases up to 3 for brines with 7 to 10.5 m Cl. It should be pointed out that these salinities refer to the unmixed aqueous fluid and not to the bulk salinity of the system. The  $D_{Sr}^{f/m}$  given by Zajacz et al. (2008) have large errors, because the Sr concentrations were generally below the limit of detection in silicate melt inclusions. In summary, it is not clear if reported Rb and Sr fluid–melt partition coefficients greater than one at high salinities are real or related to experimental artifacts or to the inherent difficulties to derive partition coefficients from natural inclusion assemblages. This points to the need for a systematic investigation of the Rb and Sr partitioning between fluid and melt.

In this experimental study, we determined partition coefficients of Rb and Sr between aqueous fluids and haplogranitic melts as a function of the following parameters:

1. *Pressure and temperature.* Temperature was varied between 750 and 950°C and pressure mostly between 200 and 500 MPa, with some experiments up to 1 GPa. This was done to simulate the PT conditions of the continental crust, in which volatile-saturated granitic magmas commonly occur.
2. *Composition of the aqueous fluid.* We used H<sub>2</sub>O±(NaCl+KCl±HCl) as starting fluids. The salinity ranged from 0 to 3.6 m (NaCl+KCl) because the solute content of magmatic aqueous fluids is quite variable, but dominated by alkali and alkaline earth metal cations and chlorine as major anion (Roedder and Bodnar, 1997). A number of experiments was performed with addition of HCl (0.01 to 0.04 m HCl) to investigate if a large difference in the pH of the initial fluid and if a relatively small amount of excess Cl<sup>–</sup> have a significant effect on Rb and Sr partitioning. Chlorine partitions strongly into the fluid phase (Webster, 1997a,b) and is a highly effective complexing agent for many metals (e.g., Helgeson, 1964, Burnham, 1967, Candela and Piccoli, 1995). Furthermore, some run series were conducted with pure water as initial fluid. This was done to compare the partitioning behavior in Cl–free systems and to better single out the potential effect of Rb and Sr complexation with silicate melt components in the fluid, which may become significant due to their substantial solubility at the PT conditions of the study (e.g., Anderson and Burnham, 1965, Manning, 2007).



3. *Silicate melt composition.* The alumina saturation index (ASI,  $\text{Al}_2\text{O}_3/(\text{Na}_2\text{O}+\text{K}_2\text{O})$  in moles) of the starting glass melt varied between 0.78 and 1.38 because the partitioning behavior of a given element is not only related to its speciation in the aqueous fluid but also to its incorporation in the melt. The latter may change due to ASI-dependent differences in the melt structure.

An additional important goal was to study to what extent obtained partition coefficients are affected by the selected experimental technique. Quench experiments are associated with large intrinsic uncertainties due to the tendency of fluids to unmix or precipitate solutes during cooling (Adam et al., 1997). Hence, the most difficult part of quench experiments is to obtain a representative sample of the fluid for analysis. Sampling of a quenched solution is complex and time consuming (e.g., Flynn and Burnham, 1978, Keppler and Wyllie, 1991). Thus, the fluid composition is reconstructed in some studies via mass balance with modeling of undetermined parameters (e.g., Ayers and Egger, 1995, Webster, 1992a,b). Another technique is entrapment of coexisting melts and fluids in synthetic inclusions, and the subsequent analysis of their compositions after quenching using laser ablation ICP-MS (e.g., Hanley et al., 2005, Simon et al., 2007). Trace element concentrations in the fluid can be obtained directly at elevated PT conditions using a hydrothermal diamond-anvil cell (HDAC) and synchrotron radiation X-ray fluorescence microanalysis (SR- $\mu$ XRF) (e.g., Schmidt and Rickers, 2003, Sanchez-Valle et al., 2003, Schmidt et al., 2007, Manning et al., 2008, Borchert et al., 2009). Here, we compare results from three experimental approaches, quench experiments with slow and rapid cooling, and analysis of the fluid in-situ and the melt after quench (HDAC).

Finally, we will show the implication of the presented data for studies of natural systems. The changes in the Rb and Sr concentrations in the melt during the crystallization and fluid exsolution of a haplogranite are modeled using crystal–melt and fluid–melt partitioning data from the literature and this study.

## 3.2 Experimental and analytical methods

### 3.2.1 Starting materials and sample preparation

The starting materials for the experimental runs consisted of a suite of synthetic haplogranitic glasses with varying ASI from 0.8 to 1.4 (Tab. 3.1) and different aqueous fluids. Each glass composition was prepared in two steps. Firstly, an initial glass was produced using powders of  $\text{SiO}_2$ ,  $\text{Al}_2\text{O}_3$ ,  $\text{Na}_2\text{CO}_3$  and  $\text{K}_2\text{CO}_3$ . The powders were mixed and stepwise heated to 1600°C for decarbonatization (12 h). After quenching, the glass was crushed and melted again for 48 h at 1600°C. Secondly, Rb and Sr were added as RbCl and  $\text{SrCO}_3$  to the crushed initial glass. The glass was doped with relatively high concentrations ( $\sim 2500$  to  $\sim 3900$  ppm Rb and  $\sim 2300$  to  $\sim 2900$  ppm Sr). The doped glass powder was melted at 1600°C for 24 h, then quenched, crushed and melted again for 24 h at 1600°C to achieve chemical homogeneity. The solutions,  $\text{H}_2\text{O}$ ,  $\text{H}_2\text{O} + 1 \text{ m NaCl} + 1 \text{ m KCl}$  and  $\text{H}_2\text{O} + 1 \text{ m NaCl} + 1 \text{ m KCl} + 0.02 \text{ m HCl}$ , were produced from distilled de-ionized water and analytical grade powders of NaCl and KCl. In the HCl-bearing solution, the pH was adjusted to one whereas the other electrolyte solution had a pH of five.

Gold capsules (3.0 mm OD, 2.6 mm ID, 20 mm length) were loaded with approximately equal weight amounts of glass and fluid. The minimum weight of the fluid was 12 mg because smaller amounts complicated fluid sampling and analysis after the experiment. In most experiments, the weights of fluid and glass were 20 to 25 mg each. After loading, the capsules were crimped, welded shut under an electric arc while partly immersed in a bath of ice water to avoid fluid loss, and weighed again. To check for leakage, the capsules were stored in a furnace at 120°C for at least 30 minutes. Absence of leaks was assumed if the weight loss was less than 1 mg.

### **3.2.2 Quench experiments**

Experiments at 750°C and 200 MPa were conducted in externally heated cold-seal pressure vessels using H<sub>2</sub>O as pressure medium and for durations ranging from 120 to 288 hours. Two different setups were used. Slow quench experiments were done in horizontal autoclaves. These runs were cooled isobarically with quench rates of ~200°C/min using a compressed air jet. Rapid quench experiments were performed in vertical autoclaves and were cooled from 750°C within a few seconds. Temperature was measured with external K-type thermocouples and is considered to be accurate to ±2°C. Thermal gradients along the capsules were less than 1°C for horizontal autoclaves and 5°C in experiments using the vertical setup. Pressure was measured with strain gauges calibrated with a deadweight pressure gauge and was accurate to ±5 MPa.

Experiments at higher PT conditions, up to 950°C and 500 MPa, were conducted using an internally heated pressure vessel with argon pressure medium with durations from 24 to 144 hours. The temperature was measured with S-type thermocouples and calibrated based on measurements of the melting points of NaCl at 843°C/200 MPa and 904°C/500 MPa (Akella et al., 1969). The accuracy is about ±5°C at 200 MPa and ±20°C at 500 MPa. Thermal gradients along the capsules were ±10°C. Pressure measurement was done with a strain gauge and was accurate to ±7 MPa for experiments up to 500 MPa and to ±20 MPa at higher pressures. During the experiment, pressure was controlled automatically within ±5 MPa using the hydraulic system of the intensifier and a programmable control unit. The samples were quenched isobarically with quench rates of 150–200°C/min.

### **3.2.3 In-situ experiments**

In-situ experiments were done using modified Bassett-type hydrothermal diamond-anvil cells as described by Bassett et al. (1993), Schmidt et al. (2007) and Borchert et al. (2009). A metaluminous glass composition (MetAlu<sup>†</sup>, Tab. 3.1) and H<sub>2</sub>O or 0.5 *m* NaCl + 0.5 *m* KCl + 0.01 *m* HCl aqueous solution were used as starting materials. A detailed description of the hydrothermal diamond-anvil cells and the in-situ method is given by Borchert et al. (2009).

### 3.2.4 Analysis of run products

#### Quench experiments

After the experiments, the capsules were weighed to check for fluid loss during the run. Then, the capsules were placed in glass containers filled with 5 ml distilled de-ionized water and heated to  $\sim 80^{\circ}\text{C}$  using a heating plate to dissolve water-soluble quench solids without affecting the glass composition. Subsequently, the capsule was opened under water to release the  $\text{H}_2\text{O}$  soluble capsule content. Then, the diluted fluid was collected using a pipette and filtered to remove very small glass pieces. Distilled de-ionized water was added to the fluid until a volume of 25 ml was attained. Capsule material, glass pieces and filters were stored in a furnace at  $120^{\circ}\text{C}$  for at least one hour. Then, capsule material and glass were weighed to determine the actual fluid weight after quench by subtraction. No quench precipitates were found in the filtered material, which contained only small quenched glass globules.

The glass pieces were embedded in epoxy resin, ground and polished. The electron microprobe (EMP) measurements on the glasses were carried out using a CAMECA SX-100 and a two-condition analysis as suggested by Morgan VI and London (1996, 2005). The silicate glasses were analyzed with an electron beam energy of 15 keV, a beam current of 10 nA, and counting times of 10 s (Na, K), 20 s (Si, Al), and 30 s (Cl). Subsequently, Rb and Sr were measured with an electron beam energy of 15 keV, a beam current of 20 nA, and 30 s counting time. The beam was defocused to a diameter of  $\sim 10 \mu\text{m}$  to achieve insignificant migration of Na and K during analysis as verified by test analyses. Replicate analyses were carried out on the same sample (10 to 15 points per sample) to check for compositional homogeneity. During each microprobe session, standards for each element were analyzed to determine accuracy and precision. Precision ranges from 0.5 to 2.5 % for Si, Al, K, Na, Rb and Sr and was up to 10 % for Cl ( $1\sigma$  confidence level). Totals of the glass analyses ranged between 94 to 96 % indicating that Na-migration was small or insignificant because the difference to 100 % can be accounted for by dissolved  $\text{H}_2\text{O}$ .

The fluids were analyzed by inductively coupled plasma-atomic emission spectrometry (ICP-AES, Varian Vista MPX) for Na, K, Si, Al, Rb, and Sr. The Cl content in fluids from experiments with salt solutions was determined by ion-chromatography (IC, Dionex 100 or 120).

In a few additional runs, the quench pH of the fluid was obtained using various litmus papers (pH-Fix Macherey-Nagel) on the escaping fluid after the capsule was pierced. In these cases, no analyses of fluid and glass compositions were performed.

#### In-situ experiments

After quenching, the glass droplets were embedded together with the rhenium gasket in epoxy resin, ground and polished. The glass droplets were analyzed using EMP as described for the quench experiments except that beam current was 10 nA for all elements and the electron beam was defocused to a diameter of 5 to  $10 \mu\text{m}$  depending on glass droplet size. For most samples, replicate analyses (3 to 10 points per sample) were possible. For two runs (samples 5 and 7), the uncertainty of the analyses is higher because only one point per sample was obtained. In addition, the measured Na and K concentrations for these samples are probably

too low. Precision ranges from 0.5 to 2.5 % for Si, Al, Rb and Sr, up to 5 % for Na and K, and up to 20 % for Cl ( $1\sigma$  confidence level).

The fluids were analyzed in-situ at 750°C and various pressures using SR –  $\mu$ XRF. The integrated intensities of Rb and Sr  $K(\alpha + \beta)$  fluorescence lines were obtained from fits of the spectra using PyMCA (Solé et al., 2007). These intensities were normalized to incident beam intensity, detector live time, and fluid density. Finally, SR- $\mu$ XRF spectra of standard solutions in the sample chamber of the HDAC were used for calibration. The method is described in detail by Borchert et al. (2009).

### 3.3 Results

The experimental conditions, the composition of glasses and fluids after quenching, and the quench pH for experiments at 750°C/200 MPa are listed in Tables 3.2, 3.3, and 3.4. Conditions and results for experiments at higher PT (to 950°C and 500 MPa) are given in Table 3.5. In all experiments, differences in the run duration had no effect on the data independent of the technique. Table 3.6 shows fluid–melt partition coefficients for Na, K, Rb, Sr and Cl obtained from quench experiments. For the in-situ experiments, conditions, results of fluid and melt analyses, and calculated fluid–melt partition coefficients of Rb and Sr are listed in Tab. 3.7 for chloridic and Tab. 3.8 for non-chloridic fluids.

The fluid–melt partition coefficients of Rb and Sr from quench experiments are shown in Figs. 3.1 and 3.2 as a function of the ASI after the run, for pressures of 200 and 500 MPa, and temperatures of 750, 850 and 950°C. The ASI of the resulting glasses is generally shifted to higher values compared to those of the starting glasses. This shift is more pronounced at 500 MPa than at 200 MPa (Tabs. 3.2, 3.3, and 3.5). Rubidium partition coefficients (Fig. 3.1) show no recognizable dependence on melt composition, pressure and temperature. For chloridic solutions,  $D_{\text{Rb}}^{\text{f/m}}$  scatters around 0.4. In the case of non-chloridic fluids, Rb partition coefficients are one to two orders of magnitude lower ( $D_{\text{Rb}}^{\text{f/m}} = 0.002$  to 0.09) and show a much larger scatter in the data. Strontium fluid–melt partition coefficients do, likewise, not depend on pressure and temperature in the investigated PT-range (Fig. 3.2). However,  $D_{\text{Sr}}^{\text{f/m}}$  displays a sharp increase with ASI from 0.003 at an ASI of 0.8 to a maximum of 0.3 at an ASI of 1.05. At higher ASI,  $D_{\text{Sr}}^{\text{f/m}}$  decreases slightly to 0.2 at an ASI of 1.6. As for Rb, the  $D_{\text{Sr}}^{\text{f/m}}$  for chloridic fluids is one to two orders of magnitude higher compared to those using H<sub>2</sub>O as starting fluid. Only a few Sr partitioning data are available for non-chloridic fluids, because the Sr content in the fluid was below detection limit in almost all experiments, except in a few slow quench experiments at 750°C and 200 MPa.

The quench pH of the fluid shows large differences depending on initial glass and fluid composition (Tab. 3.4). For experiments with peralkaline starting glass, a basic quench pH was found for all runs. The pH value varies from 8 in experiments with H<sub>2</sub>O to 9.5 in those with chloridic solutions. Runs with per- and metaluminous glass compositions resulted in near neutral pH if water was used as starting fluid, but acidic pH in the quenched fluids if chloridic solutions were used. Addition of HCl to the starting (NaCl+KCl) fluid does not have an effect on the quench pH although the difference in the pH of the starting fluid is large (pH 1 vs.

pH 5). Figures 3.1 and 3.2 also contain information on the effect of the quench rate on the  $D^{f/m}$  from experiments at 200 MPa and 750°C. For chloridic solutions, there is no discernible relationship between quench rate and Rb and Sr partitioning data if the concentrations in the fluid were relatively high ( $D^{f/m} > 0.1$ ). In the case of Sr, partition coefficients from experiments with slow quench rates were higher than those from rapid quench at  $ASI < 1.05$ , i.e., at low Sr concentrations in the fluid (Tabs. 3.2 and 3.3). If  $H_2O$  was used as starting solution, there are discernible differences in the  $D^{f/m}$  related to quench rate. The Rb contents of fluids and  $D_{Rb}^{f/m}$  in rapid quench experiments are generally higher than those from comparable slow quench runs. In contrast, the Sr concentrations in fluids from rapid quench experiments were always below the detection limit, but small Sr contents were often found in fluids from slowly quenched samples (Tabs. 3.2 and 3.3).

Figures 3.3 and 3.4 present the data of HDAC experiments, in which the Rb and

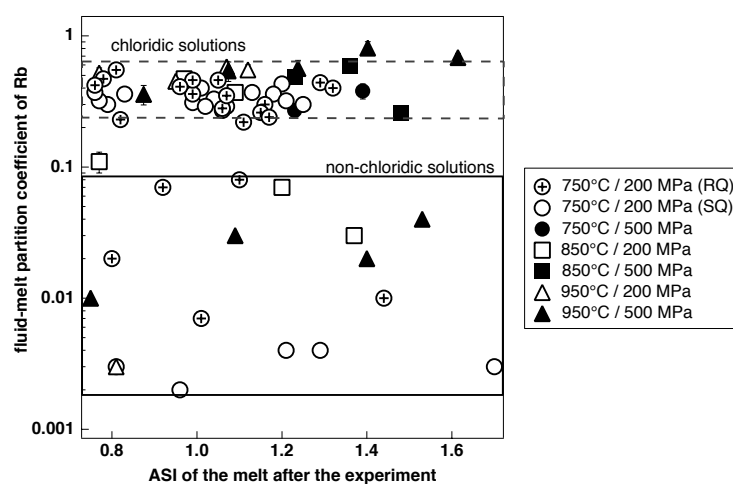


Figure 3.1: Rubidium partition coefficient obtained for chloridic and non-chloridic fluids vs. melt composition expressed as ASI. PT conditions are as indicated by symbols. Errors ( $\pm 1\sigma$ ) are smaller than symbol size. RQ - rapid quench, SQ - slow quench.

Sr concentrations in the fluid were determined in-situ at high PT. The same metaluminous starting glass was used in these runs. The Rb/Sr ratio in the fluids at 750°C and various pressures are shown in Fig. 3.3.1 for non-chloridic and in Fig. 3.3.2 for chloridic solutions. The Rb/Sr ratio in non-chloridic solutions increases with pressure. Although the uncertainty in the measurements is small, the data do not form a single trend. The trend with the steeper slope shows a correlation with ASI of the melt after the run, which increases with the Rb/Sr ratio in the fluid. The value at  $\sim 900$  MPa differs from the other data because the melt was nearly completely dissolved in the fluid at the run PT. The Rb/Sr ratio in the chloridic fluids is shown in Fig. 3.3.2 as a function of pressure for two different salinity intervals. The Rb/Sr ratio in these fluids is mainly controlled by the salinity and increases by a factor of  $\sim 2$  with a decrease in the salt concentration from 3 to 1.5  $m$  (NaCl+KCl). In contrast to non-chloridic solutions (Fig. 3.3.1), the Rb/Sr ratio in chloridic fluids is approximately constant or decreases slightly with pressure (Fig. 3.3.2).

Fluid–melt partition coefficients of Rb and Sr obtained from HDAC experiments are

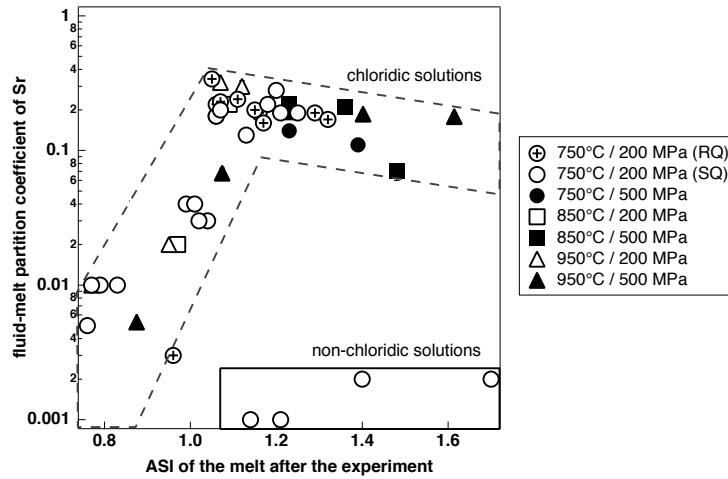


Figure 3.2: Strontium partition coefficient obtained for chloridic and non-chloridic fluids vs. melt composition expressed as ASI. PT conditions are as indicated by symbols. Errors ( $\pm 1\sigma$ ) are smaller than symbol size. RQ - rapid quench, SQ - slow quench.

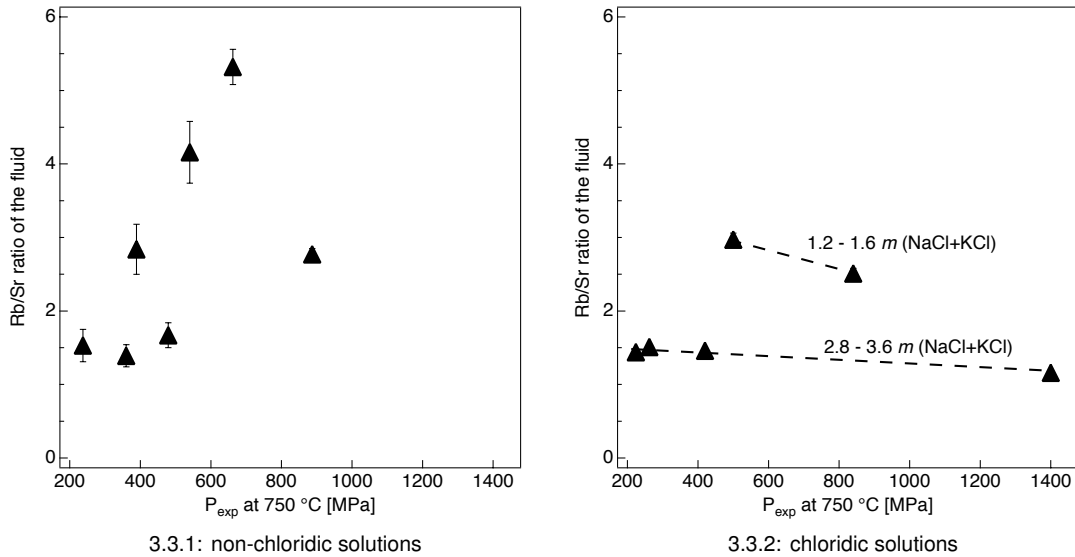


Figure 3.3: Rb/Sr ratio in the fluid vs. pressure determined in-situ at 750°C for non-chloridic (Fig. 3.3.1) and chloridic fluids (Fig. 3.3.2). All starting glasses had the same metaluminous composition. Error bars -  $\pm 1\sigma$ .

presented as a function of pressure in Fig. 3.4.1 for non-chloridic solutions and in Fig. 3.4.2 for chloridic fluids as function of salt concentration. The partition coefficients from experiments with non-chloridic solutions increase with pressure,  $D_{Rb}^{f/m}$  from  $\sim 0.006$  at  $\sim 250$  MPa to  $> 0.03$  at  $P > 900$  MPa, but the Sr partition coefficient only from  $\sim 0.004$  at  $\sim 250$  MPa to  $\sim 0.009$  at  $\sim 900$  MPa. For chloridic solutions, the fluid–melt partition coefficients of both elements depend on the salinity of the fluid (Fig. 3.4.2, Tabs. 3.7 and 3.8). Rubidium partition coefficients increase slightly and approximately linearly with salinity from  $\sim 0.3$  at  $\sim 1.2$  m (NaCl+KCl) to  $\sim 0.5$  at  $\sim 3.5$  m (NaCl+KCl). An effect of pressure is not discernible for Rb but likely present

for Sr. At a fluid salinity of  $\sim 3.5$   $m$  (NaCl+KCl),  $D_{\text{Sr}}^{\text{f/m}}$  increases from 0.14 at 420 MPa to 0.57 at 1400 MPa. Still, Sr fluid–melt partitioning is mainly controlled by the salinity. The  $D_{\text{Sr}}^{\text{f/m}}$  values increase from 0.06 at 1.16  $m$  (NaCl+KCl) to 0.24 at 3.56  $m$  (NaCl+KCl) while pressure decreases from 500 to 220 MPa.

Figure 3.5 shows a comparison of fluid–melt partition coefficients from quench and

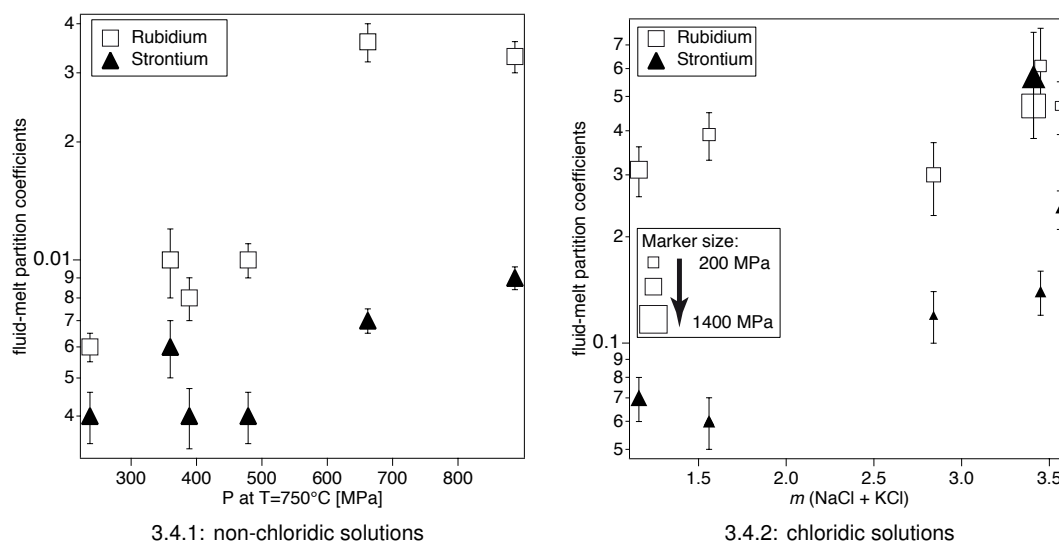


Figure 3.4: Partition coefficients of Rb and Sr at 750°C from HDAC experiments as function of pressure and salinity. Results for non-chloridic solutions are shown in Fig. 3.4.1 and data for chloridic fluids are presented in Fig. 3.4.2. Error bars -  $\pm 1\sigma$ .

from HDAC experiments with metaluminous starting glass and various fluid compositions at 750°C as a function of pressure. In quench experiments, the Rb and Sr concentrations in the fluid were determined after the run, but in HDAC experiments in-situ directly at the run PT. Partition coefficients of Rb (Fig. 3.5.1) and Sr (Fig. 3.5.2), and the Rb/Sr ratio in the fluid (Fig. 3.6.1) obtained from experiments using chloridic solutions show good agreement between the data from both techniques over the studied salinity range. However, there are obvious differences in the data for non-chloridic solutions. At similar conditions (750°C/500 MPa), partitioning data from HDAC experiments are about three times higher than those from quench runs for both elements (Rb 0.01 vs. 0.003 and Sr 0.004 vs. 0.0015). Furthermore, the HDAC data show increasing  $D^{\text{f/m}}$  with pressure, whereas no effect of pressure is recognizable in the quench data. The possible cause of these differences is discussed below.

## 3.4 Discussion

### 3.4.1 Quench effects

In this study, we investigated to what extent obtained fluid–melt partition coefficients for Rb and Sr are affected by the applied experimental technique. The comparison between rapidly and slowly quenched experiments shows clear differences for experiments with H<sub>2</sub>O as starting fluid. For comparable runs, rapidly quenched fluids contain up to 20 times more Rb and have

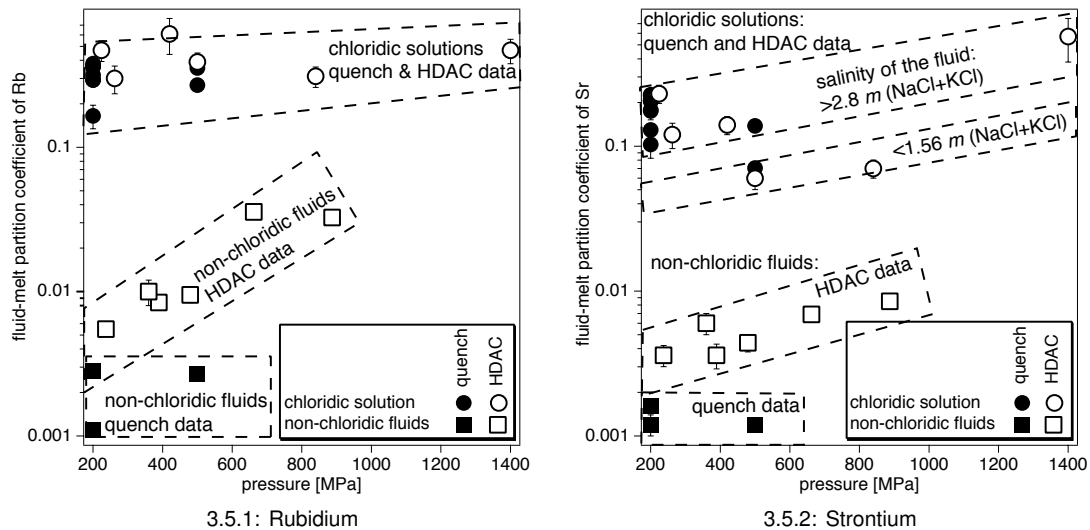


Figure 3.5: Comparison of fluid–melt partitioning data for Rb and Sr from quench and HDAC experiments, and for chloridic and non-chloridic solutions. All data are for a temperature of 750°C and metaluminous starting glass. Figure 3.5.1 shows the data for Rb as a function of pressure and analogous for Sr in Fig. 3.5.2. Error bars -  $\pm 1\sigma$ .

lower Sr concentrations, which are below the limit of detection. For chloridic solutions and peralkaline melts, rapid–quench experiments yield, likewise, much lower Sr concentrations in the fluid. This indicates a fast re-equilibration between melt and fluid during cooling. The effect of the back-reaction is more obvious at low concentrations in the fluid, whereas concentration shifts due to re-equilibration remain within error at high trace element concentrations in the fluid. This confirms the results of the study by Borchert et al. (2009). Their in-situ data for fluids coexisting with haplogranitic melts show a decreasing Rb content but a slightly increasing Sr concentration with decreasing temperature along an isochore. The data of our study clearly demonstrate that, at similar PTx conditions, partition coefficients obtained with H<sub>2</sub>O as starting fluid are higher if the fluid was analyzed in-situ, compared to that from analyses after quench. This difference is very likely mainly caused by back reactions and not by water–insoluble Rb and Sr–bearing quench phases. Such precipitates were not observed in the filtered material or optically in the HDAC experiments. Furthermore, the fact that the Rb and Sr concentrations in the quenched glasses showed no significant differences from the initial concentrations of the glasses before the run, if Rb and Sr contents in the aqueous fluids were small, is another argument against such quench phases (cp. Tabs. 3.1 and 3.2). In other words, Rb and Sr contents in aqueous solutions in equilibrium with haplogranitic melt are not quenchable, but data from experiments with chloridic solution are less affected. Consequently, fluid–melt partitioning data from quench experiments have to be used with caution particularly at low trace element contents in fluids.



### 3.4.2 Fluid–melt partitioning and complexation of Rb and Sr

This study is the first systematic investigation of Rb and Sr partitioning between aqueous fluid and haplogranitic melt as function of pressure, temperature, and fluid and melt composition. Between 750 and 950°C and between 200 to 500 MPa, pressure and temperature effects on  $D_{\text{Rb,Sr}}^{\text{f/m}}$  are small or indiscernible. This can be related to the fact that these PT conditions are well below that of the critical curve for haplogranite–water (Bureau and Keppler, 1999). That is, they are located at the steep portions of the solvi, where compositions of the coexisting phases change little with P and T. The few experiments above 500 MPa show that the partition coefficients of Rb and Sr increase with pressure. This correlates with the increased solubility of melt in the aqueous fluid, which results in a smaller chemical contrast between the phases, and indicates formation of significant amounts of complexes of Rb and Sr with melt components in the aqueous phase.

However, the effect of melt composition on the partition coefficients is very different for Rb and Sr, which suggests that these element complex in a different manner with melt components. Fluid–melt partitioning of Rb was found to be independent of the ASI of the melt, whereas  $D_{\text{Sr}}^{\text{f/m}}$  is strongly controlled by this parameter. Increasing alkalinity of the melt results in a sharp decrease of  $D_{\text{Sr}}^{\text{f/m}}$ . This partitioning behavior of Sr is related to changes in the speciation in the aqueous fluid or changes in the incorporation of Sr in the melt, or both. Dissolution of peralkaline melt will release  $\text{Na}^+$  and  $\text{K}^+$  into the aqueous fluid, which will decrease the activity of  $\text{Cl}^-$  and  $\text{OH}^-$  and thus the concentration of Sr-Cl and Sr-OH complexes in the fluid. This is supported by the basic quench pH of the runs with peralkaline melt (Tab. 3.4). Because of increasing ion association with temperature, this points to the presence of significant quantities of  $\text{NaOH}^0$  and  $\text{KOH}^0$  complexes in the fluid at the run conditions. It is currently unknown to what extent the partitioning of Sr is affected by changes in the structural environment of Sr in the melt. Kohn et al. (1990) found only small changes in the first coordination shell of Sr in a suite of glasses with different degrees of polymerization, and suggested that these changes should not play a major role in Sr partitioning between crystals and melt.

The importance of the  $\text{Cl}^-$  activity for the partitioning of Rb and Sr is emphasized by the observation that the  $D_{\text{Rb,Sr}}^{\text{f/m}}$  from experiments with chloridic solutions were generally much higher than in experiments with  $\text{H}_2\text{O}$  as starting fluid. This is also indicated by the different behavior of the Rb/Sr ratio in the fluid as a function of pressure for water or chloridic solutions as starting fluids (Figs. 3.3.1 and 3.3.2). Only the HDAC results are shown in Fig. 3.3.1 because they are much more reliable than any quench data because of the back reaction upon cooling as discussed in a previous paragraph. For metaluminous starting glasses, the Rb/Sr ratio in the non-chloridic fluid clearly increases with pressure. However, this increase must cease at even higher pressures than that studied here because the Rb/Sr ratio must approach its initial value of  $\sim 1$  at the critical pressure. As  $\text{Cl}^-$  is added to the system, this behavior changes completely. The Rb/Sr ratio in chloridic fluids decreases somewhat with salinity and is, within error, independent of pressure. This implies that the partitioning of Rb and Sr at these conditions is controlled by complexation of Rb and Sr with Cl, whereas other complexes only play a subordinate role.

For all melt and fluid compositions studied here, partition coefficients of both elements

show a preference for the melt ( $D^{f/m} < 1$ ). This is distinctly different to the experimental data of Bai and Koster van Groos (1999), which show a preference of Rb and Sr for the fluid at high salt concentration. The results presented here are consistent with data from natural co-genetic fluid and melt inclusions (Audétat and Pettke, 2003, Rickers et al., 2006, most of the data reported by Zajacz et al., 2008), that also point to a preference of Rb and Sr for the melt. Bai and Koster van Groos (1999) inferred a linear relationship between  $D_{Rb}^{f/m}$  and salinity (Fig. 3.6.2) but a quadratic correlation for  $D_{Sr}^{f/m}$  (Fig. 3.6.3). The latter is not supported by our results. A further strong difference between the two studies is observed for the Rb/Sr ratio in the fluid. For a given salinity, the Rb/Sr ratio from the data by Bai and Koster van Groos (1999) is much lower compared to our data, which covers both quench and HDAC experiments. The differences between the data from both studies are probably due to artifacts from the fluid extraction procedure for analyses after quenching.

### 3.4.3 Modeling of the behavior of Rb and Sr during evolution of a granitic system

Rubidium and Strontium concentrations in granitoids are important petrogenetic indicators. In the following, we will discuss the effect of fluid exsolution on the Rb and Sr concentrations during the evolution of a granitic melt. Figure 3.7.1 and 3.7.2 show models for the Rb and Sr contents of the residual melt during an isobaric crystallization path using the peraluminous starting composition (peralu1\*) with 3 wt.% total water. Two models were applied, Rayleigh fractionation ( $C_Z^L/C_Z^0 = F^{(D_Z^{bulk}-1)}$ ) and equilibrium crystallization ( $C_Z^L/C_Z^0 = 1/[D_Z^{bulk} + F \cdot (1 - D_Z^{bulk})]$ ), where  $C_Z^0$  and  $C_Z^L$  are the initial and actual concentrations of a trace element Z in the primary magma,  $D_Z^{bulk}$  the bulk partition coefficient, and F the remaining melt fraction. The crystallization sequence and the proportions of the phases were modeled using MELTS (Ghiorso and Sack, 1995, Asimov and Ghiorso, 1998) starting from the liquidus temperature ( $\sim 885^\circ\text{C}$ ) in increments of  $1^\circ\text{C}$ . For each step of the crystallization, a bulk partition coefficient of an element Z can be defined as:

$$D_{Z,(c+f)/m}^{bulk} = W_{c_1} \cdot D_{Z,c_1/m} + W_{c_2} \cdot D_{Z,c_2/m} + W_{c_3} \cdot D_{Z,c_3/m} + \dots + W_f \cdot D_{Z,f/m}$$

where c, f, and m refer to crystal(s), fluid and melt, and  $W_i$  corresponds to the weight fraction of the phase i exsolving from the crystallizing melt. We used the appropriate feldspar–melt partition coefficients reported by White (2003) ( $D_{Rb}^{fsp/m} = 0.3$ ,  $D_{Sr}^{fsp/m} = 5$ ). For fluid–melt partitioning, we applied values for metaluminous melts, because the residual melt composition modeled by MELTS is metaluminous. We compared  $D^{f/m}$  obtained in this study and by Bai and Koster van Groos (1999) for chloridic fluids, which differ in the preference for melt and fluid. The initial trace element contents were 110 ppm Rb and 350 ppm Sr, which is representative for upper continental crust granitoids (Winter, 2001). First, feldspar crystallizes, which is followed by quartz crystallization at  $745^\circ\text{C}$  at a melt fraction of 0.68. Fluid saturation of the melt ( $\sim 6$  wt.% at  $750^\circ\text{C} / 200$  MPa, Johannes and Holtz (1996)) is attained at  $715^\circ\text{C}$  at a melt fraction of 0.56. For both Rayleigh fractionation and equilibrium crystallization, the Sr concentration decreases and Rb concentration and Rb/Sr ratio increase continuously in the residual melt. However, the increase in the Rb/Sr ratio in the residual melt is much more pronounced for Rayleigh fractionation because Sr is more efficiently removed from the melt. Fluid–melt

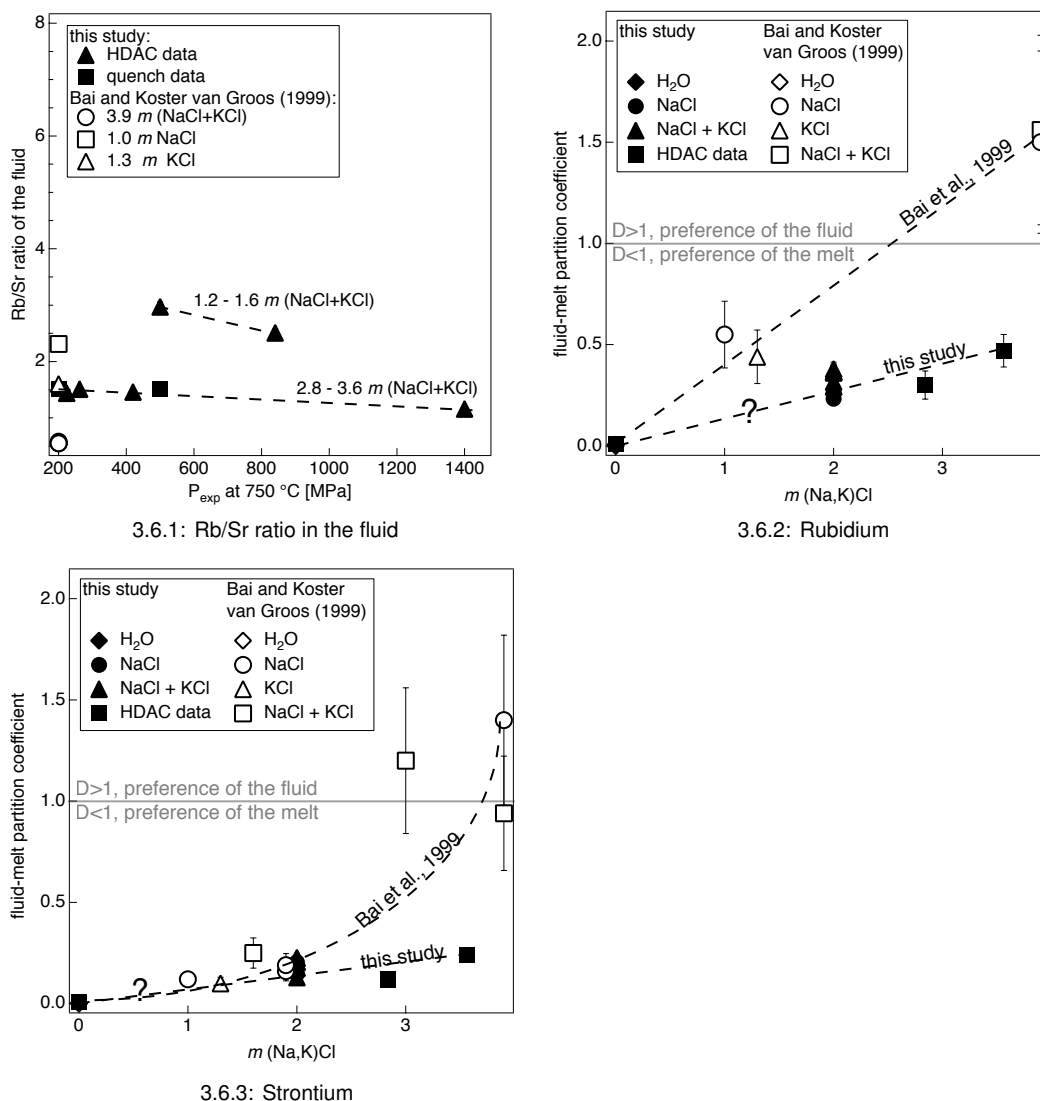


Figure 3.6: Comparison of fluid–melt partition coefficients and Rb/Sr ratio in the fluid obtained in this study with literature data (Bai and Koster van Groos, 1999) for experiments at 750°C, 200 MPa, with metaluminous starting glasses. Figure 3.6.1 shows the Rb/Sr ratio in the fluid as function of pressure for two salinity intervals, and Figs. 3.6.2 and 3.6.3 display the partition coefficients of Rb and Sr for various salinities. Error bars -  $\pm 1\sigma$ .

partitioning has no significant effect on the evolution of the trace element pattern no matter if the data from this study or from Bai and Koster van Groos (1999) are used. This is because the onset of fluid exsolution is late, the weight fraction of aqueous fluid is small, and  $D_{Rb,Sr}^{f/m}$  are low.

## 3.5 Conclusions

The comparison of fluid–melt partition coefficients obtained with quench and HDAC experiments demonstrates the advantage of the in-situ method for the determination of trace element

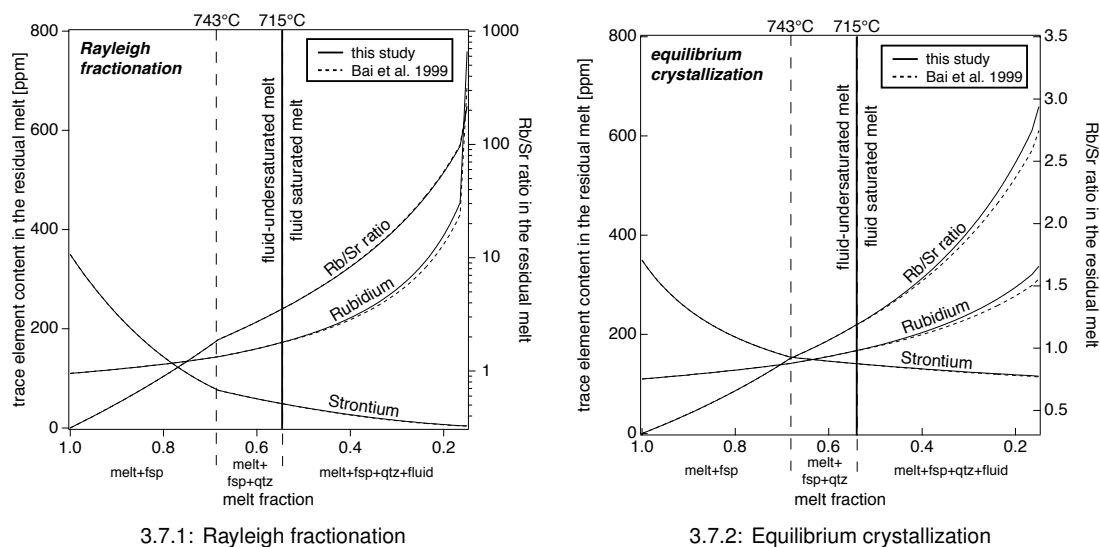


Figure 3.7: Models for the Rb and Sr contents, and Rb/Sr ratio of the residual melt during an isobaric crystallization path (200 MPa) assuming Rayleigh fractionation in Fig. 3.7.1 and equilibrium crystallization in Fig. 3.7.2 using the peraluminous starting composition ( $Ab_{38.92}Or_{23.46}Qz_{35.08}+C_{2.53}$ ) with 3 wt.% total water. Solid lines based on fluid–melt partitioning data from this study, dashed lines -  $D^{f/m}$  from Bai and Koster van Groos (1999).

concentrations in the fluid, especially in the case of non-chloridic solutions. The results of this study are clear evidence that Rb and Sr contents in such fluids are not quenchable. The good agreement between HDAC and quench data for chloridic fluids found in this study is likely due to high trace element concentrations, which make the effect of back-reaction less significant. The distinct differences to other quench data (Bai and Koster van Groos, 1999) signify the importance of a careful fluid sampling procedure. Hence, although more complex, an in-situ method is more appropriate to study fluid–melt interactions. Currently, significant progress has been made because the actual trace element concentrations in the aqueous fluid can now be determined directly high PT, but obtained fluid–melt partition coefficients are still not free of quench effects. In-situ analysis of both fluid and melt is needed particularly for water–silicate systems, and technical developments may solve this problem in the near future.

The fluid–melt partition coefficients of Rb and Sr are mainly controlled by the fluid composition. They are one to two orders of magnitude higher in chloridic fluids compared to those found in experiments with water, which clearly shows that both elements complex with chlorine as stated before, e.g., by Helgeson (1964), Burnham (1967), Candela and Piccoli (1995) and Bai and Koster van Groos (1999). In contrast to Rb, the behavior of Sr also depends on the alkalinity of the system. Our data suggest that the release of  $Na^+$  and  $K^+$  into the aqueous fluid in peralkaline systems changes the Sr speciation in the aqueous fluid. The exact nature of the Sr complexation in the fluid is not clear. Insight could be gained by spectroscopic investigations, e.g., by X-ray absorption spectroscopy.

Based on our results, the fractionation of Rb and Sr between chloridic fluids and aluminous melts is weaker than the fractionation between feldspars (or micas) and melts, and nearly independent of pressure and temperature at most conditions. Additionally, the weight

fraction of the exsolved aqueous fluid is small in natural granitoids. Therefore, the Rb/Sr ratio in granitic systems is primarily controlled by crystal–melt partitioning, and can thus be used, at least for non-alkaline granites, to gain information on its stage of evolution and particularly on the degree of fractional crystallization. Extreme Rb/Sr ratios in the melt of more than 500 and Rb concentrations of more than 5000 ppm as described by Rickers et al. (2006) are strong indication of a very high degree of fractional crystallization, perhaps coupled with re-melting of already fractionated material. The results of our study also confirm that irregular Rb and Sr patterns can not be attributed to fluid-melt partitioning (London, 2005) because their partition coefficients vary systematically with fluid and melt composition and are relatively insensitive to temperature and pressure in a wide range.

A possible application is the study of melt inclusions. Particularly melt inclusions in quartz are useful because of the abundance of this mineral in acidic igneous rocks and its resistance to weathering. In sedimentology, the Rb/Sr ratio in such inclusions can provide information on the crustal evolution of the source area. This can also be a useful tool in the search of ore deposits closely related to differentiated granites (e.g., Sn and W) in areas with no outcrops. If co-genetic fluid and melt inclusions are present, the initial salinity of the system before unmixing may be roughly estimated from Rb partitioning, which is independent of ASI. Comparison of the experimental results to natural data is limited because only very few studies report Rb and Sr concentrations in co-genetic fluid and melt inclusions. These studies (Audé-*tat* and Pettke, 2003, Rickers et al., 2006, most of the data reported by Zajacz et al., 2008) show a preference of Rb and Sr for the melt and are also in good quantitative agreement with our data.

## Acknowledgements

We thank HASYLAB at the Deutsches Elektronen-Synchrotron (DESY) for granting beamtime, R. Botcharnikov at Leibniz Universität Hannover for performing some of the quench experiments (IHPV), O. Appelt for the help with EMP measurements at Deutsches GeoForschungsZentrum GFZ, A. Musiol for the introduction to ICP-OES analysis at Universität Potsdam, and A. Gottsche and G. Schettler for the introduction to IC analysis and performance of some of the analysis at Deutsches GeoForschungsZentrum GFZ. We are grateful to Zoltan Zajacz, John C. White and David London for their constructive reviews, which helped us to improve the manuscript, and to Mike Toplis for his editorial work. This study was supported by the German Science Foundation (DFG, Wi 2000/3-1 and Wi 2000/3-2).

- Adam, J., Green, T. H., Sie, S. H., and Ryan, C. G. (1997). Trace element partitioning between aqueous fluids, silicate melts and minerals. *Eur. J. Mineral.*, 9:569–584.
- Akella, J., Vaidya, S. N., and Kennedy, G. C. (1969). Melting of Sodium Chloride at Pressures to 65 kbar. *Physical Review*, 185(3):1135–1140.
- Anderson, G. M. and Burnham, C. W. (1965). The solubility of quartz in supercritical water. *American Journal of Science*, 263:494–511.
- Asimov, P. and Ghiorso, M. (1998). Algorithmic modifications extending MELTS to calculate subsolidus phase relations. *American Mineralogist*, 83:1127–1131.
- Audétat, A. and Pettke, T. (2003). The magmatic-hydrothermal evolution of two barren granites: A melt and fluid inclusion study of the Rito del Medio and Canada Pinabete plutons in northern New Mexico (USA). *Geochimica et Cosmochimica Acta*, 67(1):97–121.
- Audétat, A., Pettke, T., Heinrich, C. A., and Bodnar, B. J. (2008). The Composition of Magmatic-Hydrothermal Fluids in Barren and Mineralized Intrusions. *Economic Geology*, 103(5):877–905.
- Ayers, J. C. and Eggler, D. H. (1995). Partitioning of elements between silicate melt and H<sub>2</sub>O-NaCl fluids at 1.5 and 2.0 GPa pressure: Implications for mantle metasomatism. *Geochimica et Cosmochimica Acta*, 59(20):4237–4246.
- Bai, T. B. and Koster van Groos, A. F. (1999). The distribution of Na, K, Rb, Sr, Al, Ge, Cu, W, Mo, La, and Ce between granitic melts and coexisting aqueous fluids. *Geochimica et Cosmochimica Acta*, 63(7/8):1117–1131.
- Bassett, W. A., Shen, A. H., Bucknum, M., and Chou, I.-M. (1993). A new diamond anvil cell for hydrothermal studies to 2.5 GPa and from 190 to 1200°C. *Review of scientific instruments*, 64:2340–2345.
- Bédard, J. H. (2006). Trace element partitioning in plagioclase feldspar. *Geochimica et Cosmochimica Acta*, 70:3717–3742.
- Borchert, M., Wilke, M., Schmidt, C., and Rickers, K. (2009). Partitioning and equilibration of Rb and Sr between silicate melts and aqueous fluids. *Chemical Geology*, 259:39–47.
- Bureau, H. and Keppler, H. (1999). Complete miscibility between silicate melts and hydrous fluids in the upper mantle: experimental evidence and geochemical implications. *Earth and Planetary Science Letters*, 165:187–196.

- Burnham, C. W. (1967). *Hydrothermal fluids at the magmatic stage*. In: *Geochemistry of Hydrothermal Ore Deposits*, pages 34–67. John Wiley, New York.
- Candela, P. A. and Piccoli, P. M. (1995). *Model ore-metal partitioning from melts into vapor and vapor/brine mixtures*. In: *Magmas, Fluids, and Ore Deposits*, volume 23, pages 101–127. Mineralogical Association of Canada Short Course.
- Carron, J.-P. and Lagache, M. (1980). Étude expérimentale du fractionnement des éléments Rb, Cs, Sr et Ba entre feldspaths alcalins, solutions hydrothermales et liquides silicatés dans le système Q.Ab.Or.H<sub>2</sub>O à 2 kbar entre 700 to 800°C. *Bull. Mineral.*, 103:571–578.
- Chappell, B. W. and White, A. J. R. (1974). Two contrasting granite types. *Pac Geol*, 8:173–174.
- Flynn, R. T. and Burnham, C. W. (1978). An experimental determination of rare earth partition coefficients between a chloride containing vapor phase and silicate melts. *Geochimica et Cosmochimica Acta*, 42:685–701.
- Ghiorso, M. and Sack, R. (1995). Chemical mass transfer in magmatic processes. IV. A revised and internally consistent thermodynamic model for the interpolation and extrapolation of liquid-solid equilibria in magmatic systems at elevated temperatures and pressures. *Contrib Mineralogy Petrology*, 119:197–212.
- Green, T. H. (1980). Island arc and continent-building magmatism - A review of petrogenic models based on experimental petrology and geochemistry. *Tectonophysics*, 63:367–385.
- Hanley, J. J., Pettke, T., Mungall, J. E., and Spooner, E. T. C. (2005). The solubility of platinum and gold in NaCl brines at 1.5 kbar, 600 to 800°C: A laser ablation ICP-MS pilot study of synthetic fluid inclusions. *Geochimica et Cosmochimica Acta*, 69(10):2593–2611.
- Helgeson, H. (1964). *Complexing and Hydrothermal Ore Deposition*. Pergamon, New York.
- Icenhower, J. and London, D. (1995). An experimental study of element partitioning among biotite, muscovite, and coexisting peraluminous silicic melt at 200 MPa (H<sub>2</sub>O). *American Mineralogist*, 80:1229–1251.
- Icenhower, J. and London, D. (1996). Experimental partitioning of Rb, Cs, Sr, and Ba between alkali feldspar and peraluminous melt. *American Mineralogist*, 81:719–734.
- Johannes, W. and Holtz, F. (1996). *Petrogenesis an Experimental Petrology of Granitic Rocks*. Springer, Berlin.
- Keppler, H. and Wyllie, P. J. (1991). Partitioning of Cu, Sn, Mo, W, U, and Th between melt and aqueous fluid in the systems haplogranite-H<sub>2</sub>O-HCl and haplogranite-H<sub>2</sub>O-HF. *Contributions to Mineralogy and Petrology*, 109:139–150.
- Kohn, S. C., Charnock, J. M., Henderson, C. M. B., and Greaves, G. N. (1990). The structural environments of trace elements in dry and hydrous silicate glasses; a manganese and strontium K-edge X-ray absorption spectroscopic study. *Contributions to Mineralogy Petrology*, 105:359–368.

- 
- London, D. (2005). *Geochemistry of alkali and alkaline earth elements in ore-forming granites, pegmatites, and rhyolites*. In: *Rare-element geochemistry of ore deposits*, volume 17, pages 17–43. Geological association of Canada Short Course Handbook.
- London, D., Hervig, R. L., and Morgan, G. B. (1988). Melt-vapor solubilities and elemental partitioning in peraluminous granite-pegmatite systems: experimental results with Macusani glass at MPa. *Contributions to Mineralogy and Petrology*, 99:360–373.
- Manning, C. E. (2007). Solubility of corundum + kyanite in H<sub>2</sub>O at 700°C and 10 kbar: evidence for Al-Si complexing at high pressure and temperature. *Geofluids*, 7:258–269.
- Manning, C. E., Wilke, M., Schmidt, C., and Cauzid, J. (2008). Rutile solubility in albite-H<sub>2</sub>O and Na<sub>2</sub>Si<sub>3</sub>O<sub>7</sub>-H<sub>2</sub>O at high temperatures and pressures by in-situ synchrotron radiation micro-XRF. *Earth and Planetary Science Letters*, 272:730–737.
- Morgan VI, G. B. and London, D. (1996). Optimizing the electron microprobe analysis of hydrous alkali aluminosilicate glasses. *American Mineralogist*, 81:1176–1185.
- Morgan VI, G. B. and London, D. (2005). Effect of current density on the electron microprobe analysis of alkali aluminosilicate glasses. *American Mineralogist*, 90:1131–1138.
- Murray, M. M. and Rogers, J. W. (1973). Distribution of rubidium and strontium in the potassium feldspar of two granite batholiths. *Geochemical Journal*, 6:117–130.
- Philpotts, A. R. (1990). *Principles of igneous and metamorphic petrology*. Prentice Hall, London.
- Ren, M., Parker, D. F., and White, J. C. (2003). Partitioning of Sr, Ba, Rb, Y, and REE between plagioclase and peraluminous silicic magma. *American Mineralogist*, 88:1091–1103.
- Rickers, K., Thomas, R., and Heinrich, W. (2006). The behavior of trace elements during the chemical evolution of the H<sub>2</sub>O-, B-, and F-rich granite-pegmatite-hydrothermal system at Ehrenfriedersdorf, Germany: a SXRF study of melt and fluid inclusions. *Mineralium Deposita*, 41:229–245.
- Robb, L. (2005). *Introduction to ore-forming processes*. Blackwell Publishing, Oxford.
- Roedder, E. and Bodnar, R. J. (1997). *Fluid inclusion studies of hydrothermal or deposits*. In: *Geochemistry of Hydrothermal Ore Deposits*. John Wiley & Sons, New York.
- Sanchez-Valle, C., Martinez, I., Daniel, I., Philippot, P., Bohic, S., and Simionovici, A. (2003). Dissolution of strontianite at high P-T conditions: An in-situ synchrotron X-ray fluorescence study. *American Mineralogist*, 88:978–985.
- Schmidt, C. and Rickers, K. (2003). In-situ determination of mineral solubilities in fluids using a hydrothermal diamond-anvil cell and SR-XRF: Solubility of AgCl in water. *American Mineralogist*, 88:288–292.
- Schmidt, C., Rickers, K., Bilderback, D. H., and Huang, R. (2007). In situ synchrotron-radiation XRF study of REE phosphate dissolution in aqueous fluids to 800°C. *Lithos*, 95:87–102.



- Simon, A. C., Frank, M. R., Pettke, T., Candela, P. A., Piccoli, P. M., Heinrich, C. A., and Glascock, M. (2007). An evaluation of synthetic fluid inclusions for the purpose of trapping equilibrated, coexisting, immiscible fluid phases at magmatic conditions. *American Mineralogist*, 92:124–138.
- Solé, V. A., Papillon, E., Cotte, M., Walter, P., and Susini, J. (2007). A multiplatform code for the analysis of energy-dispersive X-Ray fluorescence spectra. *Spectrochimica Acta, B* 62:63–68.
- Webster, J. D. (1992a). Fluid-melt interactions involving Cl-rich granites: Experimental study from 2 to 8 kbar. *Geochimica et Cosmochimica Acta*, 56:659–678.
- Webster, J. D. (1992b). Water solubility and chlorine partitioning in Cl-rich granitic systems: Effects of melt composition at 2 kbar and 800°C. *Geochimica et Cosmochimica Acta*, 56:679–687.
- Webster, J. D. (1997a). Chloride solubility in felsic melts and the role of chloride in magmatic degassing. *Journal of Petrology*, 38:1793–1807.
- Webster, J. D. (1997b). Exsolution of magmatic volatile phases from Cl-enriched mineralizing granitic magmas and implications for ore metal transport. *Geochimica et Cosmochimica Acta*, 61:1017–1029.
- Webster, J. D., Holloway, J. R., and Hervig, R. L. (1989). Partitioning of Lithophile trace elements between H<sub>2</sub>O and H<sub>2</sub>O+CO<sub>2</sub> fluids and topaz rhyolite melt. *Economic Geology*, 84:116–134.
- White, J. C. (2003). Trace-element partitioning between alkali feldspar and peralkalic quartz trachyte to rhyolite magma. Part II: Empirical equations for calculating trace-element partition coefficients of large-ion lithophile, high field-strength, and rare-earth elements. *American Mineralogist*, 88:330–337.
- White, J. C., Holt, G. S., Parker, D. F., and Ren, M. (2003). Trace-element partitioning between alkali feldspar and peralkalic quartz trachyte to rhyolite magma. Part I: Systematics of trace-element partitioning. *American Mineralogist*, 88:316–329.
- Winter, J. D. (2001). *An Introduction to Igneous and Metamorphic Petrology*. Prentice Hall, New Jersey.
- Zajacz, Z., Halter, W. E., Pettke, T., and Guillong, M. (2008). Determination of fluid/melt partition coefficients by LA-ICPMS analysis of co-existing fluid and silicate melt inclusions: Controls on element partitioning. *Geochimica et Cosmochimica Acta*, 72:2169–2197.

# Appendix

Table 3.1: Composition of starting glasses from EMP analyses and normative composition based on the components albite, orthoclase, quartz, corundum and Na-metasilicate.

	SiO <sub>2</sub> [wt.%]	Al <sub>2</sub> O <sub>3</sub> [wt.%]	Na <sub>2</sub> O [wt.%]	K <sub>2</sub> O [wt.%]	ASI	Rb [ppm]	Sr [ppm]	normative - composition
PerAlu1*	75.83	14.17	4.53	3.91	1.21	3862±455	2628±443	Ab <sub>38.92</sub> Or <sub>23.46</sub> Qz <sub>35.08</sub> +C <sub>2.53</sub>
MetAlu1*	77.71	12.31	4.46	3.95	1.06	3853±488	2763±470	Ab <sub>38.33</sub> Or <sub>23.69</sub> Qz <sub>37.25</sub> +C <sub>0.72</sub>
PerAlk2*	78.75	12.56	5.41	3.64	0.98	2587±156	2742±178	Ab <sub>44.19</sub> Or <sub>21.42</sub> Qz <sub>34.05</sub> +Ns <sub>0.33</sub>
PerAlk1*	79.18	12.37	7.45	3.38	0.78	2483±259	2675±167	Ab <sub>43.73</sub> Or <sub>19.53</sub> Qz <sub>32.57</sub> +Ns <sub>4.16</sub>
PerAlu2†	72.98	16.86	4.87	3.86	1.38	2667±226	2322±257	Ab <sub>41.80</sub> Or <sub>23.16</sub> Qz <sub>30.30</sub> +C <sub>4.73</sub>
PerAlu1†	77.26	14.50	4.30	3.94	1.28	3081±155	2514±182	Ab <sub>36.37</sub> Or <sub>23.30</sub> Qz <sub>37.16</sub> +C <sub>3.16</sub>
MetAlu1†	78.68	12.67	4.04	3.85	1.17	2690±149	2821±182	Ab <sub>34.46</sub> Or <sub>22.93</sub> Qz <sub>40.74</sub> +C <sub>1.87</sub>
PerAlk2†	79.21	12.65	5.00	3.47	1.06	2548±229	2538±252	Ab <sub>42.13</sub> Or <sub>20.44</sub> Qz <sub>36.74</sub> +C <sub>0.67</sub>
PerAlk1†	78.80	12.27	7.24	3.31	0.79	2795±150	2840±178	Ab <sub>43.96</sub> Or <sub>19.23</sub> Qz <sub>32.99</sub> +Ns <sub>3.81</sub>

\* - starting glass also doped with La and Yb

† - starting glass also doped with La and Y

Ab-albite, Or-orthoclase, Qz-quartz, C-corundum, Ns-Na<sub>2</sub>SiO<sub>3</sub>

Table 3.2: Data from experiments at 750°C and 200 MPa using rapid quench autoclaves (RQ). For each run, the first line of the analyses refers to the quench glass and second line to the quenched fluid.

run	experimental conditions			analyses of run products							
	P [MPa]	T [°C]	starting materials [melt / fluid]	Na <sub>2</sub> O [wt.%]	K <sub>2</sub> O [wt.%]	SiO <sub>2</sub> [wt.%]	Al <sub>2</sub> O <sub>3</sub> [wt.%]	ASI	Rb [ppm]	Sr [ppm]	Cl [ppm]
RQH1-1	200	750	PerAlu1*	4.20	3.67	72.23	13.14	1.21	2645±178	2368±238	bdl
			H <sub>2</sub> O	0.19	0.05	bdl	bdl		bdl	bdl	na
RQH1-4	200	750	PerAlk2*	4.80	3.33	72.44	11.65	1.01	2467±119	2423±152	bdl
			H <sub>2</sub> O	bdl	0.03	0.02	bdl		17±10	bdl	na
RQH1-3	200	750	PerAlk1*	6.45	3.09	71.28	11.10	0.80	2374±136	2454±176	bdl
			H <sub>2</sub> O	bdl	0.01	0.003	bdl		40±10	bdl	na
RQH2-0	200	750	PerAlu2†	4.13	3.64	70.58	15.46	1.44	2516±180	2315±191	bdl
			H <sub>2</sub> O	bdl	0.03	0.03	bdl		29±10	bdl	na
RQH2-2	200	750	MetAlu1†	4.02	3.73	72.47	11.66	1.10	2656±212	2697±246	bdl
			H <sub>2</sub> O	0.04	0.05	bdl	bdl		202±20	bdl	na
RQH2-4	200	750	PerAlk2†	5.27	3.45	72.56	11.42	0.92	2481±196	2895±215	bdl
			H <sub>2</sub> O	bdl	0.02	bdl	bdl		163±15	bdl	na
RQH2-3	200	750	PerAlk1†	6.77	3.60	68.21	14.13	0.94	3801±159	2864±232	bdl
			H <sub>2</sub> O	bdl	0.02	bdl	bdl		bdl	bdl	na
ROA1	200	750	PerAlu1*	3.59	5.02	72.43	13.12	1.16	1444±191	1506±172	1210±102
			1H + 1S (pH 1)	1.98	1.87	0.01	0.002		432±43	291±29	40667±4070
ROA2	200	750	MetAlu1*	3.24	4.95	73.73	11.37	1.06	1498±157	1649±220	704±83
			1H + 1S (pH 1)	2.16	1.79	bdl	bdl		402±40	297±30	41532±4150
ROA3	200	750	PerAlk1*	5.60	4.57	69.78	11.07	0.78	1337±130	2370±175	2140±321
			1H + 1S (pH 1)	3.12	2.31	0.03	0.003		628±21	bdl	65364±6536
RQB0	200	750	PerAlu2†	3.97	5.00	68.81	15.42	1.29	1556±133	1813±197	1896±211
			1H + 1S (pH 1)	2.71	2.51	0.001	bdl		684±8	352±4	54870±5487
RQB1	200	750	PerAlu1†	3.62	5.09	73.04	13.22	1.15	1657±180	1372±203	1128±114
			1H + 1S (pH 1)	1.81	1.69	0.06	0.002		435±44	279±28	38189±3820
RQB2	200	750	MetAlu1†	3.50	5.00	75.00	11.84	1.06	1516±174	1730±189	871±91
			1H + 1S (pH 1)	1.88	1.72	bdl	bdl		417±42	388±39	37413±3741
RQB4	200	750	PerAlk2†	4.07	4.52	72.79	11.48	0.99	1607±107	2577±210	1434±199
			1H + 1S (pH 1)	2.55	1.98	bdl	bdl		576±9	bdl	48295±4830
RQB3	200	750	PerAlk1†	5.36	4.82	70.67	11.00	0.82	1747±146	2662±157	1697±248
			1H + 1S (pH 1)	2.16	1.41	0.02	bdl		410±9	bdl	36123±3612
RQC1	200	750	PerAlu1*	3.65	5.10	67.67	12.80	1.11	1711±299	13.16±278	986±201
			1H + 1S	1.50	1.51	0.04	0.001		384±38	315±31	33070±3307
RQC2	200	750	MetAlu1*	3.41	5.09	74.18	11.70	1.05	1565±167	1550±241	976±94
			1H + 1S	3.72	2.70	0.03	0.002		727±73	523±52	63235±6324
RQC4	200	750	PerAlk2*	3.94	4.71	73.95	11.44	0.99	1624±119	2363±163	1242±208
			1H + 1S	3.20	2.42	0.06	0.02		740±150	bdl	64190±6419
RQC3	200	750	PerAlk1*	5.85	4.45	70.32	10.93	0.76	1472±105	2521±157	2009±271
			1H + 1S	3.09	2.14	0.04	bdl		616±19	bdl	57054±5705
RQD0	200	750	PerAlu2†	3.77	4.74	68.44	15.01	1.32	1676±118	1490±153	1454±175
			1H + 1S	2.63	2.29	0.007	bdl		668±21	257±3	56660±5670
RQD1	200	750	PerAlu1†	3.51	5.00	72.59	13.09	1.17	1655±194	1459±221	986±133
			1H + 1S	1.64	1.48	0.02	bdl		397±40	236±24	33500±3350
RQD2	200	750	MetAlu1†	3.34	4.91	74.37	11.59	1.07	1522±203	1602±158	693±91
			1H + 1S	2.21	2.00	0.1	0.001		527±53	375±38	42808±4281
RQD4	200	750	PerAlk2†	4.22	4.62	73.83	11.52	0.96	1738±163	2607±397	1196±360
			1H + 1S	3.36	2.57	0.001	0.004		718±37	8±1	49205±4921
RQD3	200	750	PerAlk1†	5.27	4.69	70.99	11.09	0.81	1528±139	2640±180	1462±199
			1H + 1S	4.44	3.26	0.04	bdl		844±22	bdl	79318±7932

na - not analyzed

bdl - below detection limit

1H - 1m NaCl, 1S - 1m KCl

\* - starting glass also doped with La and Yb

† - starting glass also doped with La and Y

ASI - Al<sub>2</sub>O<sub>3</sub>/(Na<sub>2</sub>O+K<sub>2</sub>O) in moles

Table 3.3: Data from experiments at 750 °C and 200 MPa using **slow quench autoclaves (externally heated cold-sealed pressure vessels, SQ)**. For each run, the first line of the analyses refers to the quench glass and second line to the quenched fluid.

run	experimental conditions			analyses of run products							
	P [MPa]	T [°C]	starting materials [melt / fluid]	Na <sub>2</sub> O [wt.%]	K <sub>2</sub> O [wt.%]	SiO <sub>2</sub> [wt.%]	Al <sub>2</sub> O <sub>3</sub> [wt.%]	ASI	Rb [ppm]	Sr [ppm]	Cl [ppm]
EHPVH1-1	200	750	PerAlu1*	2.43	3.60	74.09	13.45	1.70	2626±260	2234±220	na
			H <sub>2</sub> O	0.21	0.07	bdl	bdl		4±0.5	na	
EHPVH1-2	200	750	MetAlu1*	2.70	3.64	75.27	11.77	1.40	2444±240	2490±250	na
			H <sub>2</sub> O	0.11	0.06	bdl	bdl		4±1	na	
EHPVH1-4	200	750	PerAlk2*	3.63	3.35	75.90	11.66	1.21	2374±240	2306±230	na
			H <sub>2</sub> O	0.14	0.04	bdl	bdl		10±1	2±0.5	na
EHPVH1-3	200	750	PerAlu1*	6.49	3.19	74.25	11.24	0.80	2717±391	2729±402	na
			H <sub>2</sub> O	0.18	0.06	bdl	bdl		bdl	bdl	na
EHPVH2-1	200	750	PerAlu1†	3.88	3.68	73.57	13.36	1.29	3094±341	2602±335	na
			H <sub>2</sub> O	0.05	0.04	bdl	bdl		4±1	bdl	na
EHPVH2-2	200	750	MetAlu1†	3.85	3.70	75.49	11.76	1.14	2858±335	2621±407	na
			H <sub>2</sub> O	0.08	0.06	bdl	bdl		bdl	3±0.5	na
EHPVH2-4	200	750	PerAlk2†	4.99	3.49	75.22	11.50	0.96	2623±339	3019±417	na
			H <sub>2</sub> O	0.13	0.05	bdl	bdl		6±1	bdl	na
EHPVH2-3	200	750	PerAlu1†	6.33	3.14	73.67	11.20	0.81	2961±383	2839±377	na
			H <sub>2</sub> O	0.19	0.04	bdl	bdl		10±1	bdl	na
EHPVA1	200	750	PerAlu1*	3.55	4.80	71.38	13.26	1.20	1807±181	1872±294	na
			1H + 1S (pH 1)	3.03	2.48	bdl	bdl		779±3	524±9	na
EHPVA2	200	750	MetAlu1*	3.42	4.91	73.43	11.63	1.06	1675±170	1825±266	na
			1H + 1S (pH 1)	2.13	1.82	bdl	bdl		490±3	325±2	na
EHPVA4	200	750	PerAlk2*	3.58	4.79	73.10	11.56	1.04	1566±151	2476±208	na
			1H + 1S (pH 1)	2.69	2.08	bdl	bdl		519±6	80±1	na
EHPVA3	200	750	PerAlk1*	5.48	4.61	70.89	11.03	0.79	1387±182	2454±220	na
			1H + 1S (pH 1)	2.57	1.66	bdl	bdl		418±5	28±1	na
EHPVB1	200	750	PerAlu1†	3.37	5.06	71.42	13.02	1.18	1884±137	1706±203	na
			1H + 1S (pH 1)	2.65	2.37	bdl	bdl		678±6	377±9	na
EHPVB2	200	750	MetAlu1†	3.34	5.03	73.83	11.73	1.07	1683±152	2002±163	na
			1H + 1S (pH 1)	2.12	1.75	bdl	bdl		493±8	409±5	na
EHPVB4	200	750	PerAlk2†	3.97	4.77	73.44	11.63	0.99	1654±154	2686±150	na
			1H + 1S (pH 1)	2.62	2.01	bdl	bdl		511±12	105±1	na
EHPVB3	200	750	PerAlk1†	5.50	4.76	71.85	10.94	0.77	1653±141	2587±180	na
			1H + 1S (pH 1)	2.98	2.02	bdl	bdl		530±16	15±1	na
EHPVC1	200	750	PerAlu*	3.27	4.88	72.83	13.31	1.25	1706±140	1724±293	na
			1H + 1S	2.32	1.92	bdl	bdl		518±11	319±4	na
EHPVC2	200	750	MetAlu1*	3.15	4.82	74.16	11.73	1.13	1670±173	2165±226	na
			1H + 1S	2.52	2.30	bdl	bdl		611±11	280±2	na
EHPVC4	200	750	PerAlk2*	3.78	4.74	73.79	11.60	1.02	1529±210	2518±189	na
			1H + 1S	2.32	1.69	bdl	bdl		436±14	66±1	na
EHPVC3	200	750	PerAlk1*	5.96	4.72	72.79	11.27	0.76	1622±302	2626±376	na
			1H + 1S	3.24	2.18	bdl	bdl		597±11	12±1	na
EHPVD1	200	750	PerAlu1†	3.36	4.99	72.48	13.21	1.21	1886±227	1672±173	na
			1H + 1S	2.20	1.95	bdl	bdl		598±10	314±5	na
EHPVD4	200	750	PerAlk2†	3.69	4.80	73.60	11.44	1.01	1537±190	2819±195	na
			1H + 1S	3.22	2.63	bdl	bdl		608±8	126±1	na
EHPVD3	200	750	PerAlk1†	4.96	4.67	71.75	10.91	0.83	1635±169	2605±225	na
			1H + 1S	3.06	2.17	bdl	bdl		585±3	21±1	na

na — not analyzed

bdl — below detection limit

1H — 1m NaCl, 1S — 1m KCl

\* — starting glass also doped with La and Yb

† — starting glass also doped with La and Y

ASI — Al<sub>2</sub>O<sub>3</sub>/(Na<sub>2</sub>O+K<sub>2</sub>O) in moles

Table 3.4: Experimental conditions, starting materials and quench pH of the fluids for selected glass and fluid compositions

run	experimental conditions			quench pH
	P [MPa]	T [°C]	starting materials [glass / fluid]	
200	750	PerAlu2†	1H + 1S (pH 1)	1.7
200	750	MetAlu1†	1H + 1S (pH 1)	3–4
200	750	PerAlk1†	1H + 1S (pH 1)	9.5
200	750	MetAlu1†	1H + 1S (pH 5)	2
200	750	PerAlk1†	1H + 1S (pH 5)	9.5
200	750	PerAlu2†	H <sub>2</sub> O	7
200	750	MetAlu1†	H <sub>2</sub> O	6
200	750	PerAlk1†	H <sub>2</sub> O	7.5–7.9

† — starting glass also doped with La and Y

1H - 1m NaCl, 1S - 1m KCl

pH-Fix 0-14 - reading accuracy ±0.5 pH, steps of 1 pH

pH-Fix 1.7-3.8; pH-Fix 3.6-6.1; pH-Fix 7.5-9.5 - reading accuracy ±0.1 pH, steps of 0.3 pH

Table 3.5: Data from experiments up to 950 °C and 850 MPa using **internally heated cold-sealed pressure vessels (IHPV)**. For each run, the first line of the analyses refers to the quench glass and second line to the quenched fluid.

run	experimental conditions			analyses of run products							
	P [MPa]	T [°C]	starting materials [melt / fluid]	Na <sub>2</sub> O [wt.%]	K <sub>2</sub> O [wt.%]	SiO <sub>2</sub> [wt.%]	Al <sub>2</sub> O <sub>3</sub> [wt.%]	ASI	Rb [ppm]	Sr [ppm]	Cl [ppm]
IHPV-G1†	500	750	PerAlu1*	3.23	3.24	71.03	14.36	1.63	2599±260	2471±240	bdl
			H <sub>2</sub> O	0.26	0.19	na	na		18±3	3±1	na
IHPV-G2†	500	750	MetAlu1*	3.51	3.26	73.67	12.52	1.35	2707±270	2764±277	bdl
			H <sub>2</sub> O	0.15	0.07	na	na		7±1	bdl	na
IHPV-E1†	500	750	PerAlu1*	3.39	4.52	69.90	14.52	1.39	1767±214	2401±238	bdl
			1H + 1S (pH 1)	2.79	2.19	na	na		677±11	255±3	na
IHPV-E2†	500	750	MetAlu1*	3.24	4.29	71.79	12.32	1.23	1868±174	2415±179	bdl
			1H + 1S (pH 1)	2.25	1.58	na	na		503±5	333±2	na
IHPV-F1†	500	750	PerAlu1*	3.23	4.36	69.28	14.27	1.42	1820±181	2426±172	bdl
			1H + 1S	1.75	1.37	na	na		441±3	157±2	na

Table 3.5 - continued from previous page

run	experimental conditions			analyses of run products							
	P [MPa]	T [°C]	starting materials [melt / fluid]	Na <sub>2</sub> O [wt. %]	K <sub>2</sub> O [wt. %]	SiO <sub>2</sub> [wt. %]	Al <sub>2</sub> O <sub>3</sub> [wt. %]	ASI	Rb [ppm]	Sr [ppm]	Cl [ppm]
IHPV-F2 <sup>‡</sup>	500	750	MetAlu1* 1H + 1S	2.82 2.57	4.59 1.95	73.57 na	12.17 na	1.27	1499±150 531±10	2414±241 170±2	bdl na
IHPV-H1	200	850	PerAlu1* H <sub>2</sub> O	3.59 0.17	3.70 0.11	72.56 0.04	13.56 0.02	1.37	2603±123 66±45	2551±104 bdl	bdl na
IHPV-H1	200	850	PerAlu1* H <sub>2</sub> O	3.59 0.17	3.70 0.11	72.56 0.04	13.56 0.02	1.37	2603±123 66±45	2551±104 bdl	bdl na
IHPV-H2	200	850	MetAlu1* H <sub>2</sub> O	3.57 0.12	3.66 0.08	74.68 0.05	11.83 0.02	1.20	2661±118 180±56	2625±166 bdl	bdl na
IHPV-H4	200	850	PerAlk2* H <sub>2</sub> O	4.51 0.44	3.41 0.15	74.21 0.13	11.58 0.02	1.04	2451±157 bdl	2452±111 bdl	bdl na
IHPV-H3	200	850	PerAlk1* H <sub>2</sub> O	6.37 0.18	3.15 0.07	73.05 0.21	11.28 0.02	0.81	2309±106 bdl	2440±151 bdl	bdl na
IHPV-A1	200	850	PerAlu1* 1H + 1S (pH 1)	3.70 2.79	4.86 2.45	72.05 0.06	13.34 0.02	1.18	1782±120 829±50	1784±136 770±10	1961±191 54088±5409
IHPV-A2	200	850	MetAlu1* 1H + 1S (pH 1)	3.53 2.31	4.81 2.23	72.46 0.01	11.98 bdl	1.09	1689±112 626±16	1917±129 424±7	1407±225 48667±4867
IHPV-A4	200	850	PerAlk2* 1H + 1S (pH 1)	4.22 2.94	4.66 2.48	71.79 bdl	11.61 bdl	0.97	1449±141 687±26	2358±198 40±1	1655±251 56387±5639
IHPV-A3	200	850	PerAlk1* 1H + 1S (pH 1)	5.79 0.97	4.49 0.74	70.67 0.01	11.07 bdl	0.77	1481±174 170±27	2493±159 bdl	2814±402 59564±5956
IHPV5	200	950	PerAlu1 <sup>†</sup> H <sub>2</sub> O	3.83 bdl	3.58 bdl	72.89 bdl	13.66 bdl	1.34	3040±174 bdl	2455±155 bdl	bdl na
IHPV6	200	950	MetAlu1 <sup>†</sup> H <sub>2</sub> O	3.77 bdl	3.64 bdl	74.49 bdl	11.98 bdl	1.18	2712±112 bdl	2729±150 bdl	bdl na
IHPV8	200	950	PerAlk2 <sup>†</sup> H <sub>2</sub> O	5.81 bdl	3.56 bdl	76.37 bdl	12.31 bdl	0.92	2668±192 bdl	2971±228 bdl	bdl na
IHPV7	200	950	PerAlk1 <sup>†</sup> H <sub>2</sub> O	6.35 0.04	3.00 0.02	72.08 0.02	11.10 bdl	0.81	2698±139 7±1	2614±130 bdl	bdl na
IHPV9	200	950	PerAlu1 <sup>†</sup> 1H + 1S (pH 1)	4.02 3.00	5.01 2.89	71.92 bdl	13.50 bdl	1.12	1835±155 1003±12	1908±171 571±4	2492±333 59609±5961
IHPV10	200	950	MetAlu1 <sup>†</sup> 1H + 1S (pH 1)	3.68 3.2	4.58 73.16	72.33 bdl	11.81 bdl	1.07	1653±150 965±26	2015±139 640±5	2238±546 60299±6030
IHPV12	200	950	PerAlk2 <sup>†</sup> 1H + 1S (pH 1)	4.43 3.19	4.58 2.63	70.66 bdl	11.66 bdl	0.95	1570±113 706±12	2577±209 40±1	2235±349 48958±4896
IHPV11	200	950	PerAlk1 <sup>†</sup> 1H + 1S (pH 1)	5.72 3.55	4.72 2.71	71.47 0.03	11.17 bdl	0.77	1433±125 739±12	2657±124 15±1	3862±233 46774±4677
IHPV13	500	850	PerAlu2 <sup>†</sup> H <sub>2</sub> O	3.46 bdl	3.37 bdl	67.69 0.01	14.61 bdl	1.56	2460±110 bdl	2310±175 bdl	bdl na
IHPV14	500	850	PerAlu1 <sup>†</sup> H <sub>2</sub> O	3.27 bdl	3.44 bdl	70.26 bdl	13.28 bdl	1.46	2868±133 bdl	2395±156 bdl	bdl na
IHPV15	500	850	MetAlu1 <sup>†</sup> H <sub>2</sub> O	3.65 bdl	3.61 bdl	72.15 0.03	12.01 bdl	1.21	2649±112 bdl	2806±162 bdl	bdl na
IHPV17	500	850	PerAlk2 <sup>†</sup> H <sub>2</sub> O	4.84 0.06	3.22 0.01	70.33 0.04	11.81 bdl	1.03	2405±152 bdl	2816±168 bdl	bdl na
IHPV18	500	850	PerAlu2 <sup>†</sup> 1H + 1S (pH 1)	3.28 1.64	4.43 1.48	68.56 0.004	15.05 0.003	1.48	1544±105 395±12	1961±184 128±1	1204±527 32704±3270
IHPV19	500	850	PerAlu1 <sup>†</sup> 1H + 1S (pH 1)	3.12 3.45	4.37 3.22	69.70 0.003	13.42 0.004	1.36	1798±157 1059±6	2013±128 415±5	710±248 53393±5339
IHPV20	500	850	MetAlu1 <sup>†</sup> 1H + 1S (pH 1)	3.12 3.06	4.33 2.82	72.78 0.002	12.08 0.004	1.23	1369±103 670±10	1567±193 352±2	610±337 48129±4813
IHPV23	500	950	PerAlu2 <sup>†</sup> H <sub>2</sub> O	3.68 0.10	3.44 0.07	68.93 0.03	14.99 0.02	1.53	2395±145 88±25	2181±138 bdl	bdl na
IHPV24	500	950	PerAlu1 <sup>†</sup> H <sub>2</sub> O	3.42 0.16	3.53 0.09	69.62 0.30	13.23 0.02	1.40	2784±155 52±18	2485±159 bdl	bdl na
IHPV25	500	950	MetAlu1 <sup>†</sup> H <sub>2</sub> O	3.72 0.18	3.62 0.07	70.91 0.06	11.84 0.02	1.18	2594±152 bdl	2794±187 bdl	bdl na
IHPV27	500	950	PerAlk2 <sup>†</sup> H <sub>2</sub> O	4.33 0.32	3.30 0.07	71.22 0.55	11.62 0.02	1.09	2352±105 62±38	2878±145 bdl	bdl na
IHPV26	500	950	PerAlk1* H <sub>2</sub> O	6.97 0.58	3.09 0.14	70.34 1.94	11.16 0.02	0.75	2187±167 79±23	2629±152 bdl	bdl na
IHPV28	500	950	PerAlu2 <sup>†</sup> 1H + 1S (pH 1)	2.92 3.57	4.46 3.49	68.40 0.05	15.56 0.02	1.61	1498±114 1023±4	1879±135 335±1	1057±399 57172±5717
IHPV29	500	950	PerAlu1 <sup>†</sup> 1H + 1S (pH 1)	2.89 3.95	4.43 4.08	70.94 0.04	13.40 0.02	1.40	1848±163 1492±121	2203±135 410±8	931±262 62716±6272
IHPV30	500	950	MetAlu1 <sup>†</sup> 1H + 1S (pH 1)	2.89 2.50	4.62 2.75	72.67 0.02	12.09 0.02	1.24	1495±134 842±104	2312±183 449±15	699±251 66494±6649
IHPV32	500	950	PerAlk2 <sup>†</sup> 1H + 1S (pH 1)	3.57 3.12	4.58 2.71	71.68 0.68	11.64 0.02	1.07	1422±159 770±99	2778±200 189±11	498±139 68731±6873
IHPV31	500	950	PerAlk1 <sup>†</sup> 1H + 1S (pH 1)	4.90 2.98	4.66 2.12	71.17 1.64	11.46 0.02	0.87	1608±159 576±79	2626±125 14±1	563±259 67177±6718

<sup>‡</sup> – experiments done at Institut für Mineralogie, Leibniz Universität Hannover

nd – not analyzed

bdl – below detection limit

1H – 1m NaCl, 1S – 1m KCl

\* – starting glass also doped with La and Yb

† – starting glass also doped with La and Y

ASI – Al<sub>2</sub>O<sub>3</sub>/(Na<sub>2</sub>O+K<sub>2</sub>O) in moles

Table 3.6: Experimentally determined fluid–melt partition coefficients of Na, K, Rb, Sr, Cl, and  $D_{K/D_{Na}}$ .

run	experimental conditions			Fluid–melt partition coefficients					
	P [MPa]	T [°C]	ASI	$D_{Na}$	$D_K$	$D_{K/D_{Na}}$	$D_{Rb}$	$D_{Sr}$	$D_{Cl}$
RQH1-1*	200	750	1.21	0.05	0.01	0.02±0.002	nc	nc	nc
RQH1-4*	200	750	1.01	nc	0.009	nc	0.007±0.004	nc	nc
RQH1-3*	200	750	0.80	nc	0.003	nc	0.02±0.004	nc	nc
RQH2-0*	200	750	1.44	nc	0.008	nc	0.01±0.004	nc	nc
RQH2-2*	200	750	1.10	0.01	0.01	1.34±0.3	0.08±0.01	nc	nc
RQH2-4*	200	750	0.92	nc	0.006	nc	0.07±0.008	nc	nc
RQH2-3*	200	750	0.94	nc	0.006	nc	nc	nc	nc
RQA1	200	750	1.16	0.55	0.37	0.67±0.10	0.30±0.05	0.19±0.03	33.62±4.40
RQA2	200	750	1.06	0.67	0.36	0.54±0.08	0.27±0.04	0.18±0.03	59.00±9.11
RQA3	200	750	0.78	0.56	0.51	0.91±0.10	0.47±0.05	nc	30.55±5.51
RQB0	200	750	1.29	0.68	0.50	0.73±0.15	0.44±0.04	0.19±0.02	28.94±4.32
RQB1	200	750	1.15	0.50	0.33	0.67±0.11	0.26±0.04	0.20±0.04	33.86±4.82
RQB2	200	750	1.06	0.54	0.34	0.64±0.09	0.28±0.04	0.22±0.03	42.97±6.22
RQB4	200	750	0.99	0.63	0.44	0.70±0.15	0.36±0.02	nc	33.68±5.76
RQB3	200	750	0.82	0.40	0.33	0.81±0.16	0.23±0.02	nc	21.28±3.77
RQC1	200	750	1.11	0.41	0.30	0.71±0.11	0.22±0.05	0.24±0.06	33.55±7.61
RQC2	200	750	1.05	1.09	0.53	0.49±0.07	0.46±0.07	0.34±0.06	64.79±9.02
RQC4	200	750	0.99	0.81	0.51	0.63±0.03	0.46	nc	2.01
RQC3	200	750	0.76	0.53	0.48	0.91±0.15	0.42±0.03	nc	28.39±4.76
RQD0	200	750	1.32	0.70	0.48	0.69±0.05	0.40±0.03	0.17±0.02	38.96±6.10
RQD1	200	750	1.17	0.47	0.30	0.63±0.09	0.24±0.04	0.16±0.03	33.99±5.71
RQD2	200	750	1.07	0.66	0.41	0.62±0.09	0.35±0.06	0.23±0.03	61.81±10.24
RQD4	200	750	0.96	0.79	0.56	0.70±0.11	0.41±0.04	0.003±0.0005	41.14±13.04
RQD3	200	750	0.81	0.84	0.70	0.82±0.13	0.55±0.05	nc	54.24±9.15
EHPVH1-1*	200	750	1.70	0.09	0.02	0.23±0.003	0.003±0.0005	0.002±0.0003	nc
EHPVH1-2*	200	750	1.40	0.04	0.02	0.39±0.01	nc	0.002±0.0004	nc
EHPVH1-4*	200	750	1.21	0.04	0.01	0.30±0.01	0.004±0.0006	0.001±0.0002	nc
EHPVH1-3*	200	750	0.80	0.03	0.02	0.67±0.07	nc	nc	nc
EHPVH2-1*	200	750	1.29	0.01	0.01	0.86±0.09	0.004±0.0004	nc	nc
EHPVH2-2*	200	750	1.14	0.02	0.02	0.80±0.13	nc	0.001±0.0003	nc
EHPVH2-4*	200	750	0.96	0.03	0.01	0.56±0.06	0.002±0.0005	nc	nc
EHPVH2-3*	200	750	0.81	0.03	0.01	0.41±0.06	0.003±0.0006	nc	nc
EHPVA1	200	750	1.20	0.85	0.52	0.60±0.03	0.43±0.04	0.28±0.04	nc
EHPVA2	200	750	1.06	0.62	0.37	0.60±0.03	0.29±0.03	0.18±0.03	nc
EHPVA4	200	750	1.04	0.75	0.43	0.58±0.03	0.33±0.03	0.03±0.003	nc
EHPVA3	200	750	0.79	0.47	0.36	0.77±0.04	0.30±0.04	0.01±0.001	nc
EHPVB1	200	750	1.18	0.79	0.47	0.60±0.06	0.36±0.03	0.22±0.03	nc
EHPVB2	200	750	1.07	0.63	0.35	0.55±0.05	0.29±0.03	0.20±0.02	nc
EHPVB4	200	750	0.99	0.66	0.42	0.64±0.04	0.31±0.03	0.04±0.002	nc
EHPVB3	200	750	0.77	0.54	0.42	0.78±0.06	0.32±0.03	0.01±0.0004	nc
EHPVC1	200	750	1.25	0.71	0.39	0.55±0.03	0.30±0.03	0.19±0.03	nc
EHPVC2	200	750	1.13	0.80	0.48	0.60±0.04	0.37±0.04	0.13±0.01	nc
EHPVC4	200	750	1.02	0.61	0.36	0.58±0.03	0.29±0.04	0.03±0.002	nc
EHPVC3	200	750	0.76	0.54	0.46	0.85±0.03	0.37±0.07	0.005±0.0007	nc
EHPVD1	200	750	1.21	0.66	0.39	0.60±0.03	0.32±0.04	0.19±0.02	nc
EHPVD4	200	750	1.01	0.87	0.55	0.63±0.03	0.40±0.05	0.04±0.003	nc
EHPVD3	200	750	0.83	0.62	0.46	0.75±0.04	0.36±0.04	0.01±0.0007	nc
IHPV-G1 <sup>‡</sup> *	500	750	1.63	0.08	0.06	0.71±0.01	0.01±0.001	0.001±0.0001	nc
IHPV-G2 <sup>‡</sup> *	500	750	1.35	0.04	0.02	0.51±0.01	0.003±0.0001	nc	nc
IHPV-E1 <sup>‡</sup>	500	750	1.39	0.82	0.48	0.59±0.05	0.38±0.05	0.11±0.01	nc
IHPV-E2 <sup>‡</sup>	500	750	1.23	0.69	0.37	0.53±0.04	0.27±0.03	0.14±0.01	nc
IHPV-F1 <sup>‡</sup>	500	750	1.42	0.54	0.31	0.58±0.04	0.24±0.02	0.06±0.005	nc
IHPV-F2 <sup>‡</sup>	500	750	1.27	0.91	0.43	0.47±0.01	0.35±0.01	0.07±0.0008	nc
IHPV-H1*	200	850	1.37	0.05	0.03	0.60±0.08	0.03±0.02	nc	nc
IHPV-H2*	200	850	1.20	0.03	0.02	0.65±0.07	0.07±0.02	nc	nc
IHPV-H4*	200	850	1.04	0.10	0.04	0.45±0.02	nc	nc	nc
IHPV-H3*	200	850	0.81	0.03	0.02	0.79±0.04	nc	nc	nc
IHPV-A1	200	850	1.18	0.76	0.50	0.67±0.03	0.47±0.04	0.43±0.03	27.58±2.76
IHPV-A2	200	850	1.09	0.66	0.46	0.71±0.04	0.37±0.03	0.22±0.02	34.59±5.52
IHPV-A4	200	850	0.97	0.70	0.53	0.76±0.03	0.47±0.05	0.02±0.001	34.06±5.17
IHPV-A3	200	850	0.77	0.17	0.16	0.98±0.04	0.11±0.02	nc	21.17±3.03
IHPV5*	200	950	1.34	nc	nc	nc	nc	nc	nc
IHPV6*	200	950	1.18	nc	nc	nc	nc	nc	nc
IHPV8*	200	950	0.92	nc	nc	nc	nc	nc	nc
IHPV7*	200	950	0.81	0.01	0.01	0.92±0.06	0.003±0.0002	nc	nc
IHPV9	200	950	1.12	0.75	0.58	0.77±0.03	0.55±0.05	0.30±0.03	23.92±3.19
IHPV10	200	950	1.07	0.89	0.69	0.78±0.04	0.58±0.06	0.32±0.02	26.94±6.57
IHPV12	200	950	0.95	0.72	0.57	0.80±0.04	0.45±0.03	0.02±0.001	21.01±3.28
IHPV11	200	950	0.77	0.62	0.57	0.93±0.06	0.52±0.05	0.01±0.0003	12.11±6.06
IHPV13*	500	850	1.56	nc	nc	nc	nc	nc	nc
IHPV14*	500	850	1.46	nc	nc	nc	nc	nc	nc
IHPV15*	500	850	1.21	nc	nc	nc	nc	nc	nc
IHPV17*	500	850	1.03	0.01	0.002	0.15±0.03	nc	nc	nc
IHPV18	500	850	1.48	0.50	0.33	0.67±0.05	0.26±0.02	0.07±0.01	27.17±11.90
IHPV19	500	850	1.36	1.10	0.74	0.67±0.04	0.59±0.05	0.21±0.01	75.24±26.34
IHPV20	500	850	1.23	0.98	0.65	0.66±0.04	0.49±0.04	0.22±0.03	78.95±43.58
IHPV23*	500	950	1.53	0.03	0.02	0.72±0.08	0.04±0.01	nc	nc
IHPV24*	500	950	1.40	0.05	0.03	0.57±0.05	0.02±0.01	nc	nc
IHPV25*	500	950	1.18	0.05	0.02	0.43±0.02	nc	nc	nc
IHPV27*	500	950	1.09	0.07	0.02	0.30±0.04	0.03±0.02	nc	nc
IHPV26*	500	950	0.75	0.08	0.05	0.56±0.03	0.04±0.01	nc	nc
IHPV28	500	950	1.61	1.22	0.78	0.64±0.05	0.68±0.05	0.18±0.01	54.10±20.43
IHPV29	500	950	1.40	1.36	0.92	0.67±0.06	0.81±0.10	0.19±0.01	67.40±18.96
IHPV30	500	950	1.24	0.86	0.59	0.69±0.05	0.56±0.09	0.19±0.02	95.13±77.42
IHPV32	500	950	1.07	0.87	0.59	0.68±0.10	0.54±0.09	0.07±0.01	138.08±38.59
IHPV31	500	950	0.87	0.61	0.45	0.75±0.03	0.36±0.06	0.01±0.0003	119.28±54.96
IHPVT1	850	750	1.09	2.30	1.54	0.67±0.09	1.04±0.19	0.62±0.11	

nc — not calculated because element concentration in the fluid was below detection limit or was not analyzed

ASI =  $Al_2O_3/(Na_2O+K_2O)$  in moles\* - experiments using  $H_2O$  as starting fluid

‡ - experiments done at Institut für Mineralogie, Leibniz Universität Hannover

Table 3.7: Experimental conditions and results of the HDAC experiments for **chloridic fluids** at 750°C. Concentrations of Rb and Sr in the fluid were analyzed in-situ using SR- $\mu$ XRF, the glasses were analyzed after quench using EMP.

sample	1	2	3	4	5	6
Cell	HDAC3	HDAC3	HDAC3	HDAC3	HDAC3	HDAC3
$P_{exp}$ at $T_{exp}=750^\circ\text{C}$ [MPa]	224	262	500	840	420	1400
$m$ (NaCl+KCl), NaCl/KCl=1	3.56	2.84	1.56	1.16	3.45	3.41
$m$ HCl	0.04	0.03	0.02	0.01	0.04	0.04
wt.% (NaCl+KCl)	16.8	14.3	8.4	6.5	16.8	16.6
wt.% glass (initial)	24	27	22	16	12	17
$\rho_{fluid}$ [ $\text{g}/\text{cm}^3$ ]	0.6885	0.6940	0.7843	0.9073	0.8085	1.086
$T_m$ [ $^\circ\text{C}$ ]	-10.6	-8.6	-5.4	-4.0	-12.9	-12.7
$T_H$ [ $^\circ\text{C}$ ]	439	409	315	208	357	86
$C_{Rb}^f$ [ppm]	712 $\pm$ 6	308 $\pm$ 4	482 $\pm$ 6	334 $\pm$ 5	383 $\pm$ 3	586 $\pm$ 4
$C_{Rb}^{Rb}$ [ppm]	1510 $\pm$ 247	1028 $\pm$ 224	1223 $\pm$ 199	1078 $\pm$ 191	629 $\pm$ 176	1251 $\pm$ 233
$C_{Sr}^f$ [ppm]	495 $\pm$ 6	205 $\pm$ 3	162 $\pm$ 4	133 $\pm$ 3	262 $\pm$ 3	505 $\pm$ 4
$C_{Sr}^{Sr}$ [ppm]	2085 $\pm$ 299	1663 $\pm$ 333	2562 $\pm$ 230	2019 $\pm$ 385	1875 $\pm$ 222	883 $\pm$ 294
$C_{Rb}^f/C_{Sr}^f$	1.44 $\pm$ 0.02	1.51 $\pm$ 0.03	2.97 $\pm$ 0.09	2.51 $\pm$ 0.07	1.46 $\pm$ 0.02	1.16 $\pm$ 0.02
$D_{Rb}^f/m$	0.47 $\pm$ 0.08	0.30 $\pm$ 0.07	0.39 $\pm$ 0.06	0.31 $\pm$ 0.05	0.61 $\pm$ 0.17	0.47 $\pm$ 0.09
$D_{Sr}^f/m$	0.24 $\pm$ 0.03	0.12 $\pm$ 0.02	0.06 $\pm$ 0.01	0.07 $\pm$ 0.01	0.14 $\pm$ 0.02	0.57 $\pm$ 0.19
wt.% SiO <sub>2</sub>	73.37	71.51	69.27	68.25	67.96	70.96
wt.% Al <sub>2</sub> O <sub>3</sub>	12.77	12.37	14.31	14.49	14.24	13.64
wt.% Na <sub>2</sub> O	3.49	2.82	2.52	2.22	3.31	2.47
wt.% K <sub>2</sub> O	5.72	6.14	6.67	8.20	7.17	7.26
ASI	1.07	1.10	1.26	1.16	1.08	1.14

$m$  – molality  
 $T_m$  – freezing point depression determined by cryometry  
 $T_H$  – Homogenization temperature measured after collection of XRF spectra at  $T_{exp}=750^\circ\text{C}$   
 $f$  – fluid,  $m$  – melt  
 ASI – Al<sub>2</sub>O<sub>3</sub>/(Na<sub>2</sub>O+K<sub>2</sub>O) in moles

Table 3.8: Experimental conditions and results of the HDAC experiments for **non-chloridic fluids** at 750°C. Concentrations of Rb and Sr in the fluid were analyzed in-situ using SR- $\mu$ XRF, the glasses were analyzed after quench using EMP.

sample	1	2	3	4	5*	6	7*
Cell	HDACG	HDACG	HDACG	HDAC3	HDACG	HDAC3	HDACG
$P_{exp}$ at $T_{exp}=750^\circ\text{C}$ [MPa]	360	540	662	237	479	389	887
wt.% glass (initial)	24	23	31	18	21	21	16
$\rho_{fluid}$ [ $\text{g}/\text{cm}^3$ ]	0.6336	0.7494	0.7989	0.53	0.7121	0.65	0.87
$T_H$ [ $^\circ\text{C}$ ]	333	281	252	363	301	325	194
$C_{Rb}^f$ [ppm]	31 $\pm$ 5	77 $\pm$ 6	101 $\pm$ 1	15 $\pm$ 1	14 $\pm$ 1	23 $\pm$ 1	68 $\pm$ 1
$C_{Rb}^{Rb}$ [ppm]	3007 $\pm$ 275	na	2818 $\pm$ 285	2816 $\pm$ 223	1479 $\pm$ 154	2786 $\pm$ 336	2092 $\pm$ 164
$C_{Sr}^f$ [ppm]	22 $\pm$ 3	19 $\pm$ 3	19 $\pm$ 1	10 $\pm$ 1	8 $\pm$ 1	8 $\pm$ 1	25 $\pm$ 1
$C_{Sr}^{Sr}$ [ppm]	3532 $\pm$ 555	na	2750 $\pm$ 213	2797 $\pm$ 182	1897 $\pm$ 179	2302 $\pm$ 362	2906 $\pm$ 189
$C_{Rb}^f/C_{Sr}^f$	1.39 $\pm$ 0.15	4.16 $\pm$ 0.42	5.32 $\pm$ 0.24	1.53 $\pm$ 0.22	1.67 $\pm$ 0.17	2.84 $\pm$ 0.34	2.77 $\pm$ 0.08
$D_{Rb}^f/m$	0.01 $\pm$ 0.002	nc	0.036 $\pm$ 0.004	0.006 $\pm$ 0.0005	0.01 $\pm$ 0.001	0.008 $\pm$ 0.001	0.033 $\pm$ 0.003
$D_{Sr}^f/m$	0.006 $\pm$ 0.001	nc	0.007 $\pm$ 0.0005	0.004 $\pm$ 0.0006	0.004 $\pm$ 0.0006	0.004 $\pm$ 0.0007	0.009 $\pm$ 0.0006
wt.% SiO <sub>2</sub>	73.89	na	70.76	72.60	79.32	71.17	72.41
wt.% Al <sub>2</sub> O <sub>3</sub>	12.81	na	12.31	12.49	9.67	12.45	13.22
wt.% Na <sub>2</sub> O	4.25	na	2.38	3.73	0.69	3.12	1.81
wt.% K <sub>2</sub> O	3.39	na	3.62	3.42	1.97	3.67	3.62
ASI	1.20	na	1.57	1.27	2.96	1.37	1.92

\* – only one glass analysis  
 nd – not determined because sample was lost during preparation for EMP analysis  
 nc – not calculated  
 $T_H$  – Homogenization temperature measured after collection of XRF spectra at  $T_{exp}=750^\circ\text{C}$   
 $f$  – fluid,  $m$  – melt  
 ASI – Al<sub>2</sub>O<sub>3</sub>/(Na<sub>2</sub>O+K<sub>2</sub>O) in moles

## **Chapter 4**

# **Partitioning of Ba, La, Yb and Y between haplogranitic melts and aqueous solutions: an experimental study**

*revised manuscript*

## **Partitioning of Ba, La, Yb and Y between haplogranitic melts and aqueous solutions: an experimental study**

Manuela Borchert<sup>a,\*</sup>, Max Wilke<sup>b</sup>, Christian Schmidt<sup>b</sup>, Jean Cauzid<sup>c</sup>, Rémi Tucoulou<sup>d</sup>

<sup>a</sup> Universität Potsdam, Karl-Liebknecht-Str.24, 14476 Potsdam-Golm, Germany

<sup>b</sup> Deutsches GeoForschungsZentrum (GFZ), Section 4.1, Telegrafenberg, 14473 Potsdam, Germany

<sup>c</sup> Département Sciences de la Terre, et de l'Univers, G2R, Université Henri Poincaré, 54506 Vandœuvre-lès-Nancy, France

<sup>d</sup> European Synchrotron Radiation Facility, Grenoble, France

### **Abstract**

Barium, lanthanum, ytterbium, and yttrium partitioning experiments between fluid-saturated haplogranitic melts and aqueous solutions were conducted at 750 to 950°C and 0.2 to 1 GPa to investigate the effects of melt and fluid composition, pressure, and temperature. Partition coefficients were determined using different experimental methods. On one hand quenched experiments were performed, and on the other hand, trace element contents in the aqueous fluid were determined directly using a hydrothermal diamond-anvil cell and synchrotron radiation X-ray fluorescence microanalysis of K-lines. The latter required a high excitation energy of 50 keV due to the high energies necessary to excite the K-lines of the studied elements. The data from these two techniques showed good agreement for chloridic solutions, whereas quenching had a significant effect on results of the experiments with only water in the case of Ba. In Cl-free experiments, lanthanum and yttrium, trace element contents were even below detection limit in the quenched fluids, whereas small concentrations were detected in comparable in-situ experiments. This distinct difference is likely due to back reactions between fluid and melt upon cooling.

The partitioning data of all elements show no dependence on the temperature and only small dependence on pressure. In contrast, the partitioning are strongly influenced by the composition of the starting fluid and melt. For chloridic fluids, there was a sharp increase in the Ba, La, Y and Yb partition coefficients with the alumina saturation index (ASI). The Ba partition coefficient increased from 0.002 at an ASI of 0.8 to 0.55 at an ASI of 1.07. At higher ASI, it decreased slightly to 0.2 at an ASI of ~1.3. Likewise, it was one to two orders of magnitude higher in chloridic fluids compared to those found in H<sub>2</sub>O experiments. Fluid-melt partition coefficients of La and Y increased from 0.002 at an ASI of ~0.8 to ~0.1 at an ASI of 1.2. In the same ASI range, the Yb partition coefficient increased to a maximum value of 0.02. Even at high salinities all elements fractionate into the melt. The compositional dependence of the partitioning data imply that both melt composition and fluid composition have a strong influence on trace element behavior and that complexation of Ba, REE and Y in the fluid is not only controlled by the presence of Cl<sup>-</sup> in the fluid. Instead, interaction of these elements with major melt components dissolved in the fluid is very likely.

*Keywords:* fluid–melt partition coefficients, Barium, REE, quenched experiments, HDAC, SR- $\mu$ XRF

\* Corresponding author. *E-mail address:* manu.Borchert@gmx.net (M.Borchert), *present address:* Hamburger Synchrotronstrahlungslabor at Deutsches Elektronensynchrotron, Notkestr. 85, 20607 Hamburg, Germany



## 4.1 Introduction

Granitoid magmas contain substantial amounts of dissolved H<sub>2</sub>O. The solubility of water in granitoid melts strongly decreases with decreasing pressure (Burnham and Jahns, 1962, Tuttle and Bowen, 1958) and is dependent on melt composition (Behrens and Jantos, 2001). At constant pressure, water solubility increases with decreasing temperature (Yamashita, 1999). Influences of melt composition and temperature on water solubility in silicate melts are usually less pronounced than the effect of pressure. Thus, as granitoid melt rise to shallower depth and/or crystallize, they will become saturated in water, and consequently exsolution of aqueous fluids will take place. The aqueous fluid is likely to migrate due to low density and viscosity, and will interact with melt, crystals, and subsequently also with the host rock. During these processes, elements partition between melt, volatile fluids, and crystals, which, for equilibrium and trace elements, is described by partition coefficients (e.g.,  $D_X^{f/m} = c_X^{\text{fluid}} / c_X^{\text{melt}}$ ). Trace elements of geochemically different behavior are often used as petrogenetic indicators to study these processes (e.g., Philpotts, 1990). Interpretation of trace element patterns, however, requires knowledge of all relevant partition coefficients between melts, crystals, and aqueous fluids. Here, we studied trace elements that are important for petrogenetic investigations of granitoid rocks. Barium was chosen as a representative for the large ion lithophile elements (LILE), lanthanum and ytterbium to represent light and heavy rare earth elements (LREE, HREE), and yttrium as analogue for middle to heavy rare earth elements. Granitoid rocks contain up to 500 ppm Ba (Johannes and Holtz, 1996). Barium substitutes for K in micas and potassium feldspar, and Ca in plagioclase. Its behavior is geochemically similar to that of Sr, but Sr does not partition into micas. The Ba/Sr ratio is larger in upper crust granitoids than in lower crust granitoids, and the Ba/Sr ratio in different types of granites decreases with decreasing K<sub>2</sub>O and increasing CaO content (Ba/Sr ratio: A-type>S-type>I-type>M-type>plagiogranite, Chappell and White (1974) and Winter (2001)).

The partitioning of Ba between the typical granite-forming minerals plagioclase, feldspar, and biotite and granitoid melts has been the subject of many studies. Crystal-granitic melt partition coefficients of Ba from natural samples range between 1 to 44 for K-feldspar (e.g., Mahood and Hildreth, 1983, Stix and Gorton, 1990, Bea et al., 1994), 1 to 20 for plagioclase (e.g., Ewart and Griffin, 1994, Bea et al., 1994, Streck and Grunder, 1997), and 0.6 to 7 for biotite (e.g., Mahood and Hildreth, 1983, Bea et al., 1994). Other particularly useful trace elements in the study of igneous petrogenesis are the rare earth elements (REE) because of their similar geochemical behavior. The combination of high charge and relatively large ionic radius makes the REE highly incompatible in the most early crystallizing minerals (e.g., Best, 2003, Philpotts and Ague, 2009). With increasing atomic weight, the REE show a decrease of the ionic radius, which is known as the 'lanthanide contraction'. Their partition coefficients vary slightly, and the degree of incompatibility increases with ionic radius. In granites, the rare earth elements are not incorporated in typical rock forming minerals. Instead, they are incorporated in accessory minerals such as allanite, xenotime, monazite, and titanite (Bea, 1996). The concentrations of REE in different types of granites are low, generally less than 100 ppm, and decrease slightly with decreasing K<sub>2</sub>O content (Winter, 2001). Partition coefficients of lanthanum, ytterbium, and yttrium between granitoid melts and the typical granite-forming minerals plagioclase, feldspar,

and biotite have been determined from phenocryst - whole rock data (e.g., Nash and Crecraft, 1985, Stix and Gorton, 1990, Streck and Grunder, 1997, Ren et al., 2003, Bédard, 2006), from high-silica rhyolitic glass-feldspar phenocryst pairs (Leeman and Phelps, 1981, Mahood and Hildreth, 1983, Bea et al., 1994, Ewart and Griffin, 1994), or from experiments (Blundy et al., 1998, Bédard, 2006). For lanthanum, determined crystal-melt partition coefficients range between 0.76 and 3.55 for biotite, 0.026 and 0.15 for K-feldspar, and are 0.07 to 0.17 in the case of plagioclase. For yttrium, reported crystal-melt partition coefficients vary from 0.1 to 2.4 for biotite, 0.015 to 0.5 for potassium feldspar, and 0.005 to 0.78 for plagioclase. The available crystal-melt partitioning data for ytterbium are 0.12 to 3 for biotite, 0.002 to 0.64 for potassium feldspar, and 0.012 to 0.82 for plagioclase. The large variability in these mineral-melt partition coefficients is thought to reflect differences in melt and crystal compositions as well as in temperature and pressure (e.g., Albarede, 1975, Green and Pearson, 1983, Blundy and Wood, 1991, Ren et al., 2003).

Much less is known on fluid-melt partitioning of Ba, La, Yb, and Y. There are sporadic experimental fluid-melt partitioning data for Ba, La, Y, and Yb (e.g., Webster et al., 1989, Bai and Koster van Groos, 1999, Reed et al., 2000, Bureau et al., 2003). In addition, two studies present data based on analyses of natural co-genetic fluid and melt inclusions (Audétat and Pettke, 2003, Zajacz et al., 2008). Webster et al. (1989) studied partitioning of trace elements between topaz-rhyolite melts and  $H_2O \pm CO_2$  fluids as a function of Cl concentration at 200 MPa and 769 to 950°C. They found a transition from melt-compatible to fluid-compatible behavior with increasing chlorinity from 0.16 to 6.13 *m* Cl for many trace elements including Ba and Y. Bai and Koster van Groos (1999) determined fluid-melt partitioning of trace elements between metaluminous melts and various aqueous fluids at 750–800°C and 100–400 MPa. For  $H_2O$ , the reported partition coefficient of La was 0.02 at 750°C and 200 MPa. The La partition coefficient did not change significantly with addition of NaCl and KCl to the fluid, but increased strongly with addition of HCl. Reed et al. (2000) studied partitioning of the rare earth elements between a peraluminous monzogranitic melt and a chloride-bearing aqueous phase as a function of chloride and major element concentrations at 800°C and 200 MPa. Their results show linearly increasing partition coefficients of the REE with Cl concentration in the fluid. Bureau et al. (2003) attempted to determine partition coefficients of barium and lead between silicate melts and aqueous fluids at high pressures and temperatures using hydrothermal diamond-anvil cells and  $\mu$ PIXE (proton induced X-ray emission) mapping on the quenched glass globules. Although partition coefficients could not be obtained, the Ba content of the melts was close to the initial content of the starting glass, which suggests a preference for the melt at high PT conditions.

Audétat and Pettke (2003) used an example from the field and studied the magmatic-hydrothermal evolution of two barren granites. Based on analyses of coeval fluid and melt inclusions trapped at 700–720°C and 110–120 MPa, the fluid-melt partition coefficient of Y was  $\leq 0.006$  at a fluid salinity of 4.9 wt.% NaCl<sub>equiv.</sub>. Zajacz et al. (2008) likewise analyzed naturally occurring co-existing silicate melt and fluid inclusions trapped in quartz crystals at 650 to 700°C and 80 to 170 MPa. The uncertainty in the determined fluid-melt partition coefficient for Ba was large, because the concentration was very close to the limit of detection in both melt and fluid inclusions. The reported fluid-melt partition coefficient of Ba was 0.49 at

a fluid salinity of 6.5 wt.%, and increased to 19 at a salinity of ~34 wt.%. For lanthanum, the partition coefficient decreased slightly from 0.31 to 0.1 with increasing fluid salinity from 6.5 to ~34 wt.%.

In summary, the present knowledge on fluid–melt partitioning of these elements is only fragmentary, and the data are inconsistent. For example, experimental studies suggest a preference of the REE and particular yttrium for the fluid at high salinities, but available results from natural cogenetic fluid and melt inclusions in granites show  $D^{f/m}$  distinctly smaller than one. Therefore, the question is still unanswered if exsolution of an aqueous fluid from a granitoid melt can significantly change the Ba, La, Yb, and Yb signature of the residual melt.

Here, we experimentally investigated fluid–melt partition coefficients of Ba, La, Yb, and Y as a function of silicate melt composition, salinity of the aqueous fluid, pressure and temperature. We used a suite of haplogranitic glasses with varying alumina saturation index (ASI,  $\text{Al}_2\text{O}_3/(\text{Na}_2\text{O}+\text{K}_2\text{O})$  in moles) from peralkaline to peraluminous, and  $\text{H}_2\text{O}\pm(\text{NaCl}+\text{KCl}\pm\text{HCl})$  fluids as starting materials. The experiments were performed at temperatures between 750 and 950°C and pressures mostly between 200 and 500 MPa, with some experiments up to 900 MPa.

The majority of the presented data is based on the analysis of quenched phases from experiments in high-pressure apparatuses. For Ba, La, and Y, the concentrations in the aqueous fluid were also determined directly at elevated PT conditions using a hydrothermal diamond-anvil cell (HDAC) and synchrotron radiation X-ray fluorescence microanalysis (SR- $\mu$ XRF). This experimental approach was described in detail by Borchert et al. (2009). In contrast to Rb and Sr (Borchert et al., 2009, 2010), the analysis of K-lines of the elements studied here requires a much higher excitation energy. In addition, a small spot size is of advantage to avoid mixed analyses of fluid and melt. Both, a high excitation energy and a small beam size, were achieved in this study for the first time via application of a new Kirkpatrick-Baez mirror designed for energies up to 65 keV. Therefore, the in-situ analyses of Ba, La, and Y in the aqueous fluids were also used to evaluate the sensitivity of this setup for the analyzed elements, and to obtain information on the potential and further improvements of this experimental approach.

## 4.2 Experimental and analytical methods

### 4.2.1 Starting materials and sample preparation

The starting materials were suites of synthetic haplogranitic glasses with varying ASI from 0.8 to 1.5 and  $\text{H}_2\text{O}\pm(\text{NaCl}+\text{KCl}\pm\text{HCl})$  fluids. For quenched experiments, three different glass series were produced. The glasses were doped with the following trace elements: (I) Ba, (II) La and Y, and (III) La and Yb. For experiments using the HDAC, metaluminous and peraluminous glasses doped with Ba, La, Y, Sm, and Y were synthesized. Each glass composition was prepared in two steps. Firstly, an initial glass was produced using powders of  $\text{SiO}_2$ ,  $\text{Al}_2\text{O}_3$ ,  $\text{Na}_2\text{CO}_3$  and  $\text{K}_2\text{CO}_3$ . The powders were mixed and stepwise heated to 1600°C for decarbonatization (12 h). After quenching, the glass was crushed and melted again for 48 h at 1600°C. Secondly, trace elements were added to the crushed initial glass. The doped glass powder was melted at 1600°C for 24 h, then quenched, crushed and melted again for 24 h at 1600°C

to achieve chemical homogeneity. The compositions of the starting glasses are listed in Tab. 4.1. The  $\text{H}_2\text{O} \pm (\text{NaCl} + \text{KCl} \pm \text{HCl})$  fluids were produced from distilled de-ionized water, analytical grade powders of NaCl and KCl, and 30 vol.% hydrochloric acid. Their compositions were  $\text{H}_2\text{O}$ ,  $\text{H}_2\text{O} + 1 \text{ m NaCl} + 1 \text{ m KCl}$ , and  $\text{H}_2\text{O} + 1 \text{ m NaCl} + 1 \text{ m KCl} + 0.02 \text{ m HCl}$  (pH 1). The starting fluid compositions of the individual experiments are given in Tabs. 4.2, 4.3, and 4.6.

#### **4.2.2 Quench experiments**

Quench experiments were prepared and performed as described previously by Borchert et al. (2010). Gold capsules (3.0 mm OD, 2.6 mm ID, 20 mm length) and in some cases platinum capsules (3.5 mm OD, 3.1 mm ID, 20 mm length) were loaded with approximately equal weight amounts of glass and fluid. The minimum weight of the fluid was 12 mg because smaller amounts complicated fluid sampling and analysis after the experiment. After loading, the capsules were crimped, welded shut under an electric arc while partly immersed in a bath of ice water to avoid fluid loss, and weighed again. To check for leakage, the capsules were stored in a furnace at 120°C for at least 30 minutes. Absence of leaks was assumed if the weight loss was less than 1 mg. Experiments at 750°C and 200 MPa were conducted in externally heated cold-seal pressure vessels using  $\text{H}_2\text{O}$  as pressure medium and for durations ranging from 120 to 288 hours. Two different setups were used. Slow quenched experiments were done in horizontal autoclaves. These runs were cooled isobarically with quench rates of  $\sim 200^\circ\text{C}/\text{min}$  using a compressed air jet. Rapid quenched experiments were performed in vertical autoclaves and were cooled from 750°C within a few seconds. Temperature was measured with external K-type thermocouples and is considered to be accurate to  $\pm 2^\circ\text{C}$ . Thermal gradients along the capsules were less than  $1^\circ\text{C}$  for horizontal autoclaves and  $5^\circ\text{C}$  in experiments using the vertical setup. Pressure was measured with strain gauges calibrated with a deadweight pressure gauge and was accurate to  $\pm 5 \text{ MPa}$ .

Experiments at higher PT conditions, up to 950°C and 500 MPa, were conducted using an internally heated argon pressure vessel with durations from 24 to 144 hours. The temperature was measured with S-type thermocouples and calibrated based on measurements of the melting points of NaCl at 843°C/200 MPa and 904°C/500 MPa (Akella et al., 1969). The accuracy is about  $\pm 5^\circ\text{C}$  at 200 MPa and  $\pm 20^\circ\text{C}$  at 500 MPa. Thermal gradients along the capsules were  $\pm 10^\circ\text{C}$ . Pressure measurement was done with a strain gauge and was accurate to  $\pm 7 \text{ MPa}$  for experiments up to 500 MPa and to  $\pm 20 \text{ MPa}$  at higher pressures. During the experiment, pressure was controlled automatically within  $\pm 5 \text{ MPa}$ . The samples were quenched isobarically with quench rates of 150–200°C/min.

#### **4.2.3 In-situ experiments**

The in-situ experiments were done at ID22, ESRF, Grenoble, France. In these experiments, the concentrations of Ba, La, and Y in the aqueous fluid in equilibrium with melt were determined in situ using synchrotron radiation XRF microanalysis and modified Bassett-type HDACs (Bassett et al., 1993). In these cells, the culet face of the diamond anvil located on the side of the incident X-ray beam has a cylindrical recess of  $\sim 80 \mu\text{m}$  in depth. The recess permits

collection of the fluorescence signal at  $90^\circ$  to the incident beam and in the polarization plane of the beam (Bassett et al., 2000, Schmidt and Rickers, 2003). This configuration minimizes the background in the spectra from elastic and Compton scattering and therefore, provides an optimal signal to noise ratio. Furthermore, the recess ensures a well-defined effective excitation volume, because fluorescence X-rays generated in other portions of the sample chamber are mostly absorbed by the gasket before reaching the detector. Detailed descriptions of the cells and the in-situ method are given by Schmidt and Rickers (2003), Schmidt et al. (2007) and Borchert et al. (2009). Here, starting materials consisted of a peraluminous or metaluminous glass chip of known dimensions and  $\text{H}_2\text{O}$  or a  $0.5\text{ m NaCl} + 0.5\text{ m KCl} + 0.01\text{ m HCl}$  aqueous solution. The compositions of the starting glasses are listed in Tab. 4.1.

A glass chip of known dimensions and an aqueous solution in excess were loaded in the sample chamber. Before the sample chamber was sealed, a vapor bubble was allowed to grow by controlled leaking of the liquid. For experiments with salt solutions, the actual salt concentration in the fluid after sealing was determined from measurements of the vapor-saturated ice liquidus temperature, the known ratio of the solutes, and literature data for the vapor-saturated ice liquidus in the system  $\text{H}_2\text{O}+\text{NaCl}+\text{KCl}$  (Hall et al., 1988). Then, the cell was fixed on a goniometer on the top of the xyz table at the beamline. The cell was heated to measure the homogenization temperature ( $T_{\text{H}}=T_{\text{L}+\text{V}\rightarrow\text{L}}$ ) of the aqueous fluid, and then to the experimental temperature of  $\sim 750^\circ\text{C}$ . During heating, the glass completely melted and equilibrated with the aqueous fluid. If the excitation volume was free of melt, the cell was set to the position for XRF spectrum acquisition. After alignment of the sample chamber to the beam and the fluorescence detector, the Ba  $K\alpha$  signal was scanned across the recess to verify the measurement position. Finally, after acquisition of XRF spectra of the fluid, the cell was cooled down using cooling rates of  $100^\circ\text{C}/\text{min}$ . The glass transition occurs at  $\sim 360^\circ\text{C}$  (calculated after Hui et al. (2009)). Therefore, we approximately needed 4 minutes to pass through glass transition. During cooling, the homogenization temperature was measured again. We used this homogenization temperature and the salinity to approximate the pressure at experimental temperature. These calculations were based on the slopes of the lines of constant  $T_{\text{H}}$  given by Bodnar and Vityk (1994) for salt salt-bearing compositions, and the EOS by Haar et al. (1984).

In this study, we attempted to analyze Ba, La, Sm and Eu via  $K\alpha$  emission. This required an excitation energy of at least 50 keV due to the high electron binding energies (K 1s), e.g., 46.834 keV for Sm and 48.519 keV for Eu. In our experiments, the excitation energy was set to 50 keV (the maximum energy presently commissioned for general users) using a Si(311) double-crystal fixed-exit monochromator. The synchrotron beam was focused with a new Kirkpatrick-Baez (KB) mirror developed at the ESRF. This new X-ray optical device is based on a multilayer structure and focuses hard X-rays up to 65 keV into a spot of a few  $\mu\text{m}$ . We achieved a spot size of  $5\times 2\ \mu\text{m}$  at 50 keV. The fluorescence spectra were acquired using a Ge-detector. The advantage of this experimental setup is that K lines can be analyzed, for which there are less line overlaps in the XRF spectra, particularly in those from samples in a HDAC, and less absorption of the fluorescence photons along the path towards the detector in comparison to L lines.

## **4.2.4 Analysis of run products**

### **Quench experiments**

Capsule opening, separation of the quenched phases, and preparation of quenched fluids and glasses for analysis was performed in the same way as described by Borchert et al. (2010).

After the experiments, the capsules were weighed to check for fluid loss during the run. Then, the capsules were placed in glass containers filled with 5 ml distilled de-ionized water and heated to  $\sim 80^{\circ}\text{C}$  using a heating plate to dissolve water-soluble quench solids without affecting the glass composition. Subsequently, the capsule was opened under water to release the  $\text{H}_2\text{O}$  soluble capsule content. Then, the diluted fluid was collected using a pipette and filtered to remove very small glass pieces. Distilled de-ionized water was added to the fluid until a volume of 25 ml was attained. Capsule material, glass pieces and filters were stored in a furnace at  $120^{\circ}\text{C}$  for at least one hour. Then, capsule material and glass were weighed to determine the actual fluid weight after quench by subtraction. No quench precipitates were found in the filtered material, which contained only small quenched glass globules.

The electron microprobe (EMP) measurements on the polished glasses were carried out using a CAMECA SX-100. The silicate glasses were analyzed with an electron beam energy of 15 kV, a beam current of 10 nA, and counting times of 10 s (Na, K), 20 s (Si, Al), and 30 s (Cl). Then, barium was measured with an electron beam of 15 kV, a beam current of 20 nA, and 30 s counting time. Subsequently, lanthanum, yttrium and ytterbium were analyzed using an electron beam energy of 15 kV, a beam current of 100 nA, and 30 s counting time. The beam was defocused to a diameter of 10  $\mu\text{m}$  to achieve insignificant migration of Na and K during analysis as verified by test analyses. Replicate analyses were carried out on the same sample (10 to 15 points per sample) to check for compositional homogeneity. During each microprobe session, standards for each element were analyzed to determine accuracy and precision. Precision ranged from 0.5 to 2.5 % for Si, Al, K, Na, Ba, La, Y and Yb and was up to 10 % for Cl ( $1\sigma$  confidence level).

The fluids were analyzed by inductively coupled plasma-atomic emission spectrometry (ICP-AES, Varian Vista MPX) for Na, K, Si, Al, Ba, La, Y, and Y. The Cl content in fluids from experiments with salt solutions was determined by ion chromatography (IC, Dionex 100 or 120).

### **In-situ experiments**

After quenching, the glass droplets were embedded together with the gasket in epoxy resin, ground and polished. The glass droplets were analyzed using EMP as described for the quenched experiments but using a one step analysis. The beam current was 10 nA for all elements and the electron beam was defocused to a diameter of 5 to 10  $\mu\text{m}$  depending on glass droplet size to avoid migration of Na and K during analysis. For most samples, replicate analyses (3 to 10 points per sample) were possible. Precision ranged from 0.5 to 2.5 % for Si, Al, Na, K, Ba, La, Y, Sm and Eu, and up to 11 % for Cl ( $1\sigma$  confidence level).

The fluids were analyzed in-situ at  $750^{\circ}\text{C}$  and various pressures using SR- $\mu\text{XRF}$ . The integrated intensities were obtained for the K fluorescence lines of Ba, La and Y from fits of

the spectra using PyMCA, a graphical interface for multi-channel analyzer spectra visualization and analysis developed at the ESRF (Solé et al., 2007). No reliable quantification of Eu and Sm was possible because the K-lines of these elements were strongly affected by the superimposed inelastic scattering signal. The integrated intensities were normalized to the intensity of the incident beam and then divided by the density of the fluid. The normalized integrated intensities were calibrated using SR- $\mu$ XRF spectra measured on standard solutions in the sample chamber of the HDAC. The standard solutions had initial concentrations of 250 ppm Ba and 100 ppm each of La, Y, Eu, and Sm or 500 ppm Ba and 250 ppm each of La, Y, Eu, and Sm, both in a matrix of  $\sim 6.7$  wt.%  $\text{HNO}_3$ . Before the sample chamber is sealed, a small portion of the  $\text{H}_2\text{O}$  of the solution evaporates, which increases the  $\text{HNO}_3$  and trace element concentrations. Therefore, the actual concentrations of Ba, La, and Y in the standard solution after loading into the sample chamber were calculated from the actual  $\text{HNO}_3$  concentration, which was determined from measurement of the vapor-saturated ice melting temperature (Wolf et al., 1981). Then, SR- $\mu$ XRF spectra of the standard solutions were collected on the single-phase fluid. The obtained integrated intensities of the K fluorescence lines of Ba, La, and Y of the standard solutions were likewise normalized to the intensity of the incident beam and divided by the fluid density.

## 4.3 Results

### 4.3.1 Quench experiments

For barium, Tab. 4.2 lists the experimental conditions and the compositions of glasses and fluids after quenching for experiments at  $750^\circ\text{C}$  and 200 MPa. For lanthanum, yttrium and ytterbium, Tab. 4.3 summarizes the experimental conditions and results for experiments at  $750$ – $950^\circ\text{C}$  and 200 or 500 MPa. Tables 4.4 and 4.5 show fluid–melt partition coefficients for Na, K, Ba, La, Y, Yb and Cl obtained from quenched experiments. Differences in the run duration had no effect on the partitioning data.

The fluid–melt partition coefficient of Ba from quenched experiments at  $750^\circ\text{C}$  and 200 MPa is shown in Fig. 4.1 as a function of the ASI after the run, taking into account high-pressure device, quench method, used capsule material, and use of chloridic or non-chloridic solutions. In experiments with chloridic solutions, the  $D_{\text{Ba}}^{f/m}$  shows a sharp increase with ASI from 0.002 at an ASI of 0.8 to 0.55 at an ASI of 1.07. At higher ASI, the Ba partition coefficient decreases slightly to 0.2 at an ASI of  $\sim 1.3$ . In the case of non-chloridic fluids, the  $D_{\text{Ba}}^{f/m}$  is one to two orders of magnitude lower for  $\text{ASI} \geq 1$ . For lower ASI values, partitioning data obtained with chloridic and non-chloridic solutions are similarly low. For non-chloridic solutions, an apparent dependence on the capsule material is observed in experiments using rapid quench autoclaves (Fig. 4.1), with a difference in the Ba partition coefficient of one order of magnitude. The reason for this difference remains unclear as we did not find any correlation with other parameters.

For La, Y, and Yb, fluid–melt partition coefficients from quenched experiments at  $750^\circ\text{C}$  and 200 MPa using chloridic fluids are shown in Fig. 4.2.1 as function of the ASI of the melt after the run and for slow and rapid quench rates. The data show a sharp increase of partition

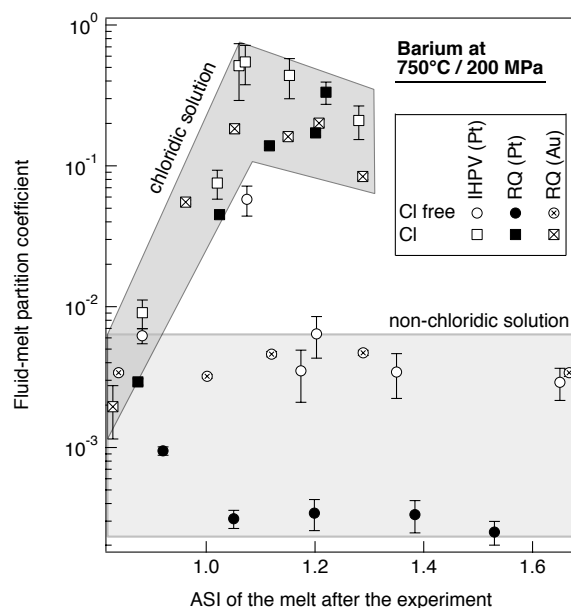


Figure 4.1: Barium partition coefficient at 750°C and 200 MPa obtained from rapid and slow quenched experiments for chloridic and non-chloridic fluids vs. melt composition expressed as ASI. Errors ( $\pm 1\sigma$ ) are, in some cases, smaller than symbol size. RQ - rapid quench, IHPV - slow quench, (Pt) - Pt capsule, (Au) - Au capsule.

coefficients with melt composition by more than one order of magnitude at an ASI of  $\sim 1.1$  to  $\sim 1.2$ . The onset of that increase appears to depend on the quench rate. For slow quenched experiments,  $D_{La,Y}^{f/m}$  increase from 0.002 at an ASI of  $\sim 0.8$  to  $\sim 0.1$  at an ASI of 1.2. In the same ASI range, the Yb partition coefficient increase to maximum values of 0.02. In the case of rapid quenching, all fluid analyses of samples using peralkaline starting glasses show trace element contents below detection limit, and therefore, no partition coefficients could be calculated. For rapid quenched experiments using metaluminous or peraluminous starting glasses, the strong increase in the partition coefficients is shifted to higher ASI of  $\sim 1.3$ , but with similar  $D_{La,Y,Yb}^{f/m}$  (Tab. 4.5). For experiments using H<sub>2</sub>O as starting fluid, concentrations of La, Y, and Yb were always below detection limit. In Fig. 4.2.2, the fluid–melt partition coefficient of La is shown as function of the ASI of the melt after the experiment for various pressure and temperature conditions (200 and 500 MPa, 750, 850, and 950°C). The data indicate no effect of temperature, but a drop of  $D_{La}^{f/m}$  with increasing pressure by one order of magnitude.

### 4.3.2 HDAC experiments - evaluation of sensitivity

Figure 4.3 shows XRF-spectra collected on glass standards SRM NIST 612 (Pearce et al., 1997) and MPI-DING ATHO-G (Jochum et al., 2000, 2006). With the excitation conditions of this study, fluorescence lines of elements with atomic numbers from 20 to 63 were detectable. Concentrations of trace elements in SRM NIST612 vary between 5 to 120 ppm (Pearce et al., 1997). Only calcium, the element with the highest intensity in the spectra, has a concentration of 12 wt.% in the standard glass. Element concentrations in MPI DING ATHO-G are much



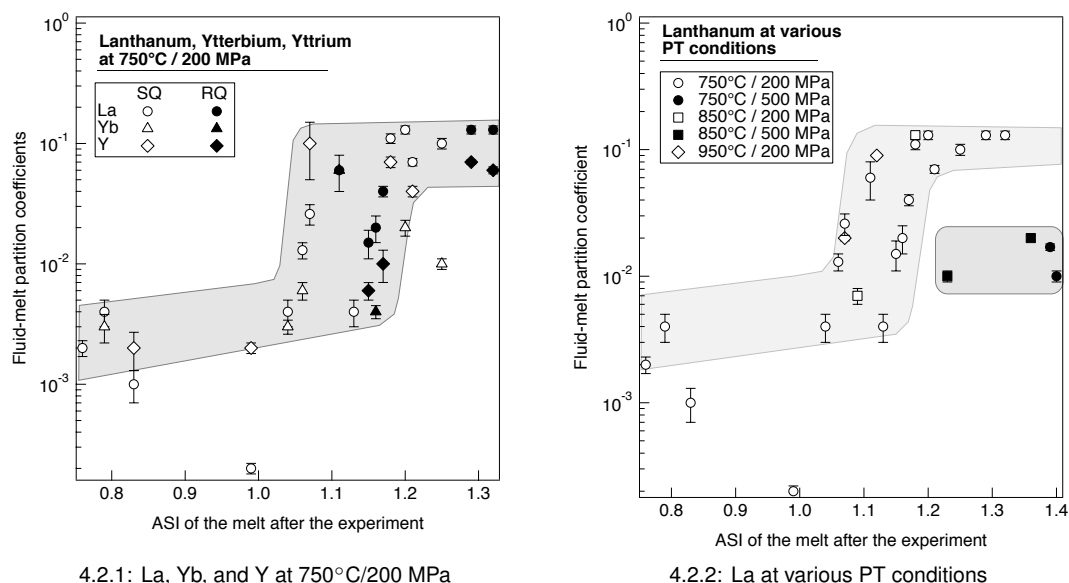


Figure 4.2: Partition coefficients from chloridic fluids of La, Yb and Y in the fluid vs. melt composition at 750°C and 200 MPa (Fig. 4.2.1), and La partition coefficient obtained from quenched experiments for various PT conditions (Fig. 4.2.2). Error bars -  $\pm 1\sigma$ .

more variable (Jochum et al., 2000, 2006). The highest concentrations are those of Fe (3.27 wt.% FeO), Zr (512 ppm), and Ba (547 ppm). The concentrations in the standard glass SRM NIST612 are 38 ppm Ba, 34 ppm La, 39 ppm Y, 36 ppm Sm, and 33 ppm Eu (Pearce et al., 1997). The MPI-DING ATHO-G standard glass contains 547 ppm Ba, 55.6 ppm La, 94.5 ppm Y, 14.2 ppm Sm, and 2.76 ppm Eu (Jochum et al., 2006).

Figure 4.4 shows XRF spectra of HDAC experiments at high PT, and a spectrum of a standard solution loaded in a HDAC containing 630 ppm Ba and 315 ppm La, Eu, Sm and Y each. These spectra show a very broad inelastic scattering peak between 35 and 50 keV. This signal mostly stems from Compton scattering of the incoming beam on the path through the diamond anvil. In the spectra of the standard solution and the experiment with chloridic fluid, the fluorescence lines of Ba, La and Y are clearly distinguishable from the background. However, Sm (at ~40 keV) and Eu (at ~41 keV) peaks are hardly visible due to the very strong contribution by the inelastic scatter signal to the background in this energy region. In the case of H<sub>2</sub>O as initial fluid, there is only a very small signal from Y, and the signals from Sm and Eu are superimposed by the high background from inelastically scattered radiation. Due to these constraints on the sensitivity and further reasons as explained below, the fluids of the in-situ HDAC experiments were only analyzed for Ba, La and Y.

In order to estimate the sensitivity of the experimental setup, a minimum detection limit MDL was calculated using the equation

$$\text{MDL}(x) = c_x \cdot 3 \cdot \frac{\sqrt{B_x}}{I_x},$$

where B is the background signal, I the intensity of the signal from element x, and c is the concentration of x. The MDL were calculated for the two standard glasses (SRM NIST612

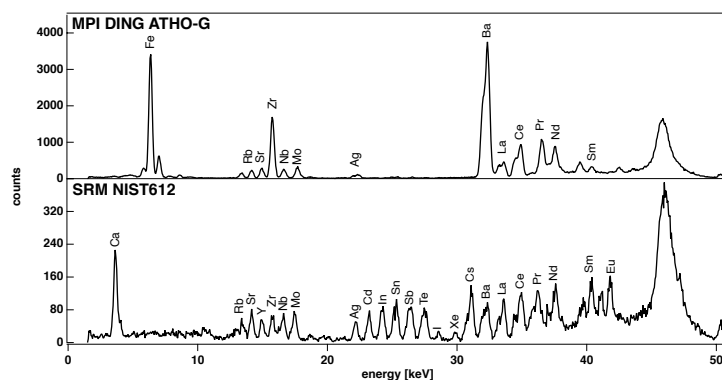


Figure 4.3: XRF spectra of a standard glasses SRM NIST612 and MPI DING ATHO-G. Both spectra were collected with counting times of 500 seconds.

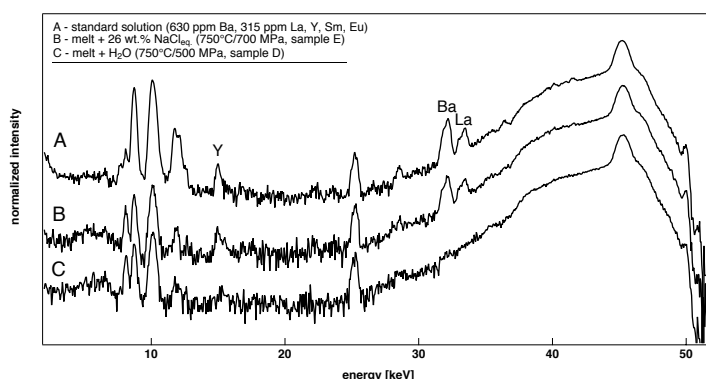


Figure 4.4: XRF spectra of a standard solution (A) and two samples using a chloridic solution (B) or H<sub>2</sub>O (C) as starting fluid loaded in a HDAC.

and MPI DING ATHO-G) and a standard solution measured in two hydrothermal diamond-anvil cells (Fig. 4.5). For the standard glasses, the minimum detection limits were  $\leq 20$  ppm for elements with atomic numbers ( $Z$ ) between 25 and 47, and  $\sim 1$  ppm for elements with  $48 < Z < 60$ . The minimum detection limits of the standard solution measured in the HDAC were generally higher, with values of  $\sim 30$  ppm for Y,  $\sim 15$  ppm for Ba and La.

### 4.3.3 HDAC experiments - partitioning data

For the in-situ experiments, Tab. 4.6 lists the experimental conditions, results of fluid and melt analyses, and calculated fluid-melt partition coefficients of Ba, La and Y. Figures 4.6 and 4.7 present the partition coefficients from HDAC experiments, in which the trace element concentrations in the fluid were determined in-situ at high PT. For these experiments, we used peraluminous and metaluminous starting glasses doped with Ba, La, Y, Sm and Eu (Tab. 4.1). As described in the previous paragraph, the SR- $\mu$ XRF analyses were limited to elements with photon energies  $\leq 35$  keV due to the high background from the inelastic scattering peak. Barium partitioning data at 750°C and various pressures are shown in Fig. 4.6.1 for experiments using peraluminous starting glass, and in Fig. 4.6.2 for metaluminous compositions, in both

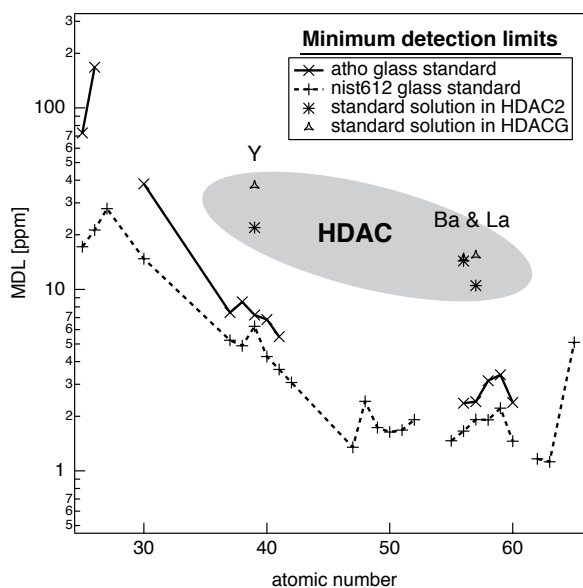


Figure 4.5: Minimum detection limits (MDL) determined for various elements from two standard glasses (SRM NIST612 and MPI DING ATHO-G) and a standard solution in HDAC2 and HDACG. The slightly different MDL's from HDAC experiments are due to different excitation volumes (different depths of recesses).

figures as a function of the initial salinity of the fluid.

Considering only data from HDAC experiments, the  $D_{Ba}^{f/m}$  increases slightly from 0.03 for  $H_2O$  to 0.3 at a Cl molality of the fluid of 6 for peraluminous melts. The few data suggest that pressure does not have a large effect. For metaluminous compositions, the Ba partition coefficient also increases with salinity of the fluid from 0.06 at 1.7  $m$  (Na,K)Cl to 0.79 at 6  $m$  (Na,K)Cl. In this case, there may be a small effect of pressure. At a salinity of 6  $m$  (Na,K)Cl, the partition coefficient of Ba increases from 0.33 at 300 MPa to 0.79 at 700 MPa. The same is observed at a salinity of  $\sim 1.6 m$  (Na,K)Cl, at which the Ba partition coefficient increases from 0.03 at 250 MPa to 0.06 at 750 MPa. The  $D_{Ba}^{f/m}$  from experiments using peraluminous and metaluminous melt compositions show no significant differences in their dependence on salinity.

For lanthanum, a similar behavior is observed. The partition coefficient from experiments using peraluminous melt compositions increases from 0.03 for water to 0.13 at  $m$  (Na,K)Cl of 6 (Fig. 4.7.1). No effect of pressure is discernible. For metaluminous melts, the  $D_{La}^{f/m}$  is similar and may depend slightly on pressure (Fig. 4.7.2). At a salinity of 6  $m$  (Na,K)Cl, the  $D_{La}^{f/m}$  increases from 0.03 at 300 MPa to 0.12 at 700 MPa.

The yttrium partition coefficient for both metaluminous and peraluminous melts is of same order of magnitude as that of La, and scatters between 0.05 and 0.43 (Fig. 4.8). The in-situ data have substantial errors (Tab. 4.6) because yttrium concentrations were close to the minimum detection limit. Therefore, these data represent maximum values, and it remains unclear if the  $D_Y^{f/m}$  depends on salinity or pressure (Fig. 4.8.1 and 4.8.2). During some of these experiments, (REE,Y)-rich crystals formed (cp. Fig. 4.9), which caused a depletion in these

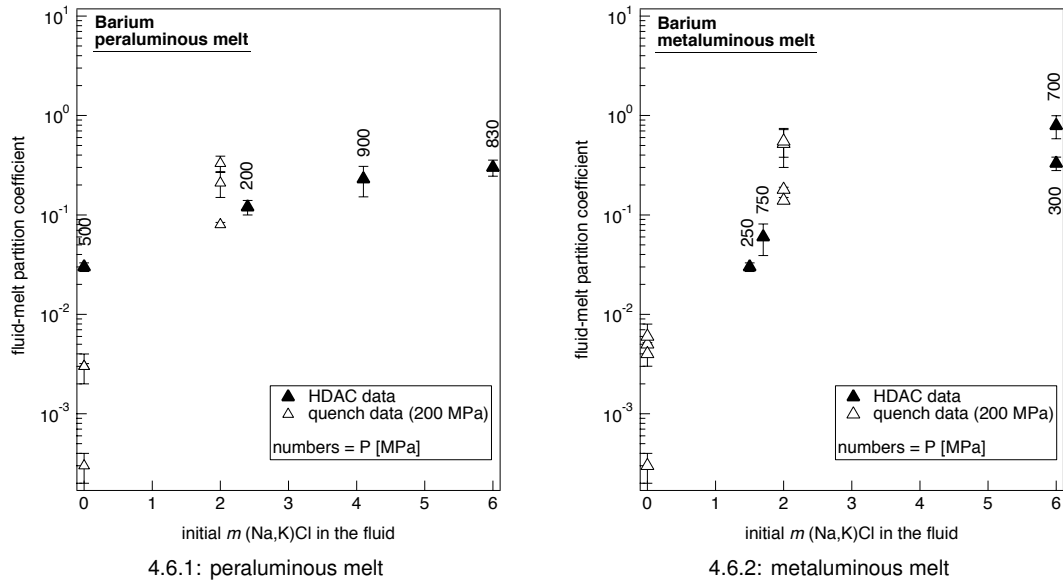


Figure 4.6: Fluid–melt partition coefficient of Ba at 750°C and the indicated pressure vs. initial Cl-molality of the fluid. Data from HDAC and quenched experiments are shown for peraluminous (Fig. 4.6.1) and metaluminous melt (Fig. 4.6.2).

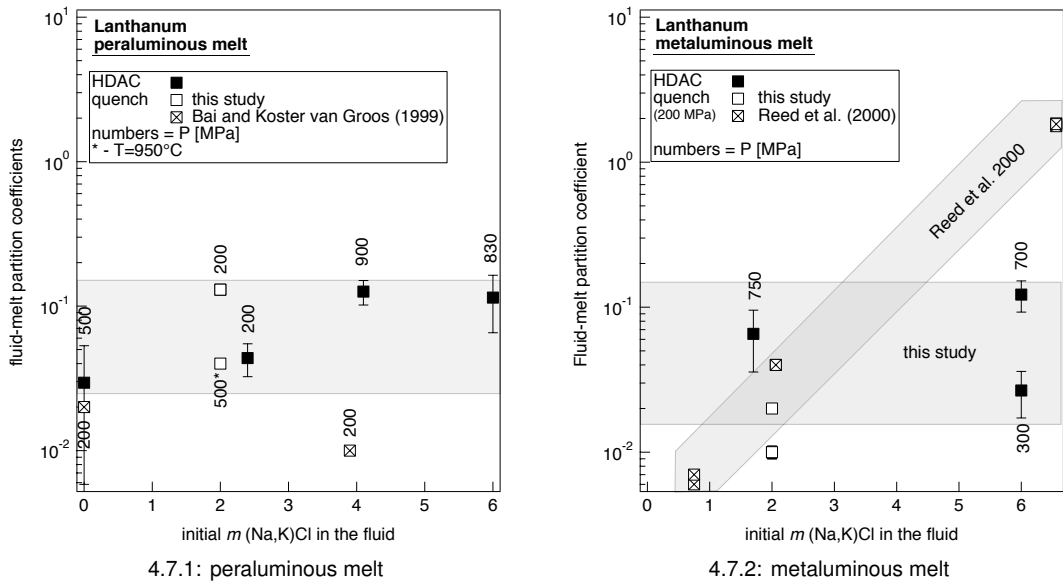
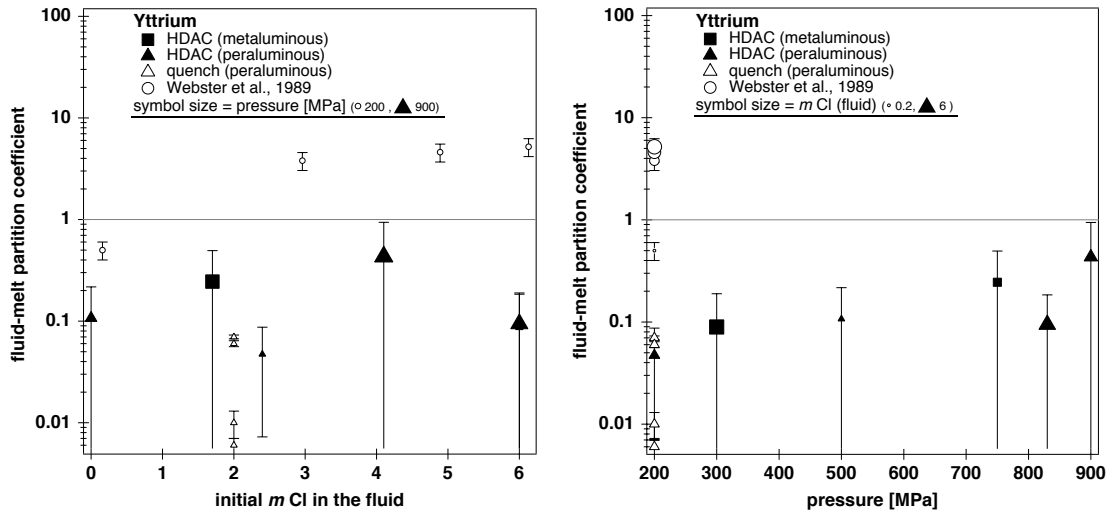


Figure 4.7: Fluid–melt partition coefficient of La at 750°C and the indicated pressure vs. initial Cl-molality of the fluid. Data from HDAC and quenched experiments are shown for peraluminous (Fig. 4.7.1) and metaluminous melt (Fig. 4.7.2).

elements in the melt and the fluid. The formation of the (REE,Y)-rich crystals was observed in experiments A and E, which were characterized by a high fluid salinity of 6 m (Na,K)Cl and high pressures of 830 and 750 MPa (Fig. 4.9). In these cases, repeated measurements showed that the Y concentration in the fluid first increased to a maximum of 114 ppm and subsequently decreased to ~30 ppm, which is close to detection limit. A similar behavior was

found for lanthanum. The La concentration increased during the experiment to a maximum of 230 ppm, and then decreased to  $\sim 30$  ppm. The minimum detection limit of La is  $\sim 15$  ppm, and therefore obtained La contents in the fluids are somewhat more reliable than those for yttrium. Samarium and europium were not analyzed for the reason given in section 4.3.2.



4.8.1: Y at 750°C and various pressures vs. fluid salinity

4.8.2: Y at 750°C and various fluid salinities vs. pressure

Figure 4.8: Yttrium fluid-melt partition coefficient at 750°C and indicated pressures vs. initial Cl-molality (Fig. 4.8.1) and at 750°C and indicated fluid salinities vs. pressure (Fig. 4.8.2). Figures show data from HDAC and quenched experiments (this study). For comparison, we also show the Y partition coefficient obtained using F-rich starting material (Webster et al., 1989).

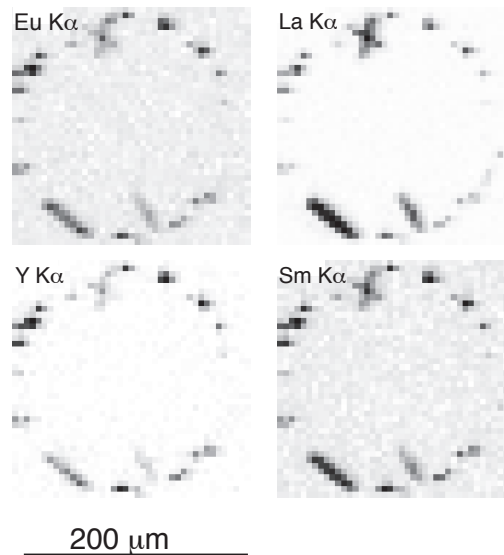


Figure 4.9: XRF intensity maps of fluorescence lines as indicated of sample chamber of HDAC after experiment (E) indicating the formation of REE-bearing silicates.

### **4.3.4 Comparison of quenched and HDAC runs**

For barium, fluid–melt partition coefficients from quench and HDAC experiments are in good agreement for experiments with peraluminous melts and chloridic solutions (cp. Fig. 4.6.1). If water was used as starting fluid, partitioning data from quenched experiments are one to two orders of magnitude lower than comparable HDAC results. For metaluminous compositions, quenched experiments show up to one magnitude higher  $D_{\text{Ba}}^{f/m}$  than comparable HDAC runs with similar fluid salinities and pressures (Fig. 4.6.2). No HDAC data for Cl free fluids could be obtained for these melt compositions. Altogether, the data for Ba from both techniques show qualitative agreement, i.e., melt compatible behavior ( $D < 1$ ) for all melt and fluid compositions, even at high fluid salinities.

For lanthanum and yttrium, the concentrations in the quenched solutions after the run were below detection limit in experiments using  $\text{H}_2\text{O}$  as starting fluid. Therefore, no partition coefficients could be obtained that could be compared to HDAC data. For chloridic fluids, La partition coefficients from both techniques are in relatively good agreement and show a melt compatible behavior at all studied fluid salinities. The observed maximum fluid–melt partition coefficient of La is associated with high salinities, high pressures, or both, and scatters around 0.1. Results for metaluminous and peraluminous melts are similar for HDAC experiments, but quite different for quenched experiments. For yttrium, the HDAC data represent maximum partition coefficients, and are also associated with a substantial error due to Y contents in the fluid that are close to detection limit. Therefore, it remains unclear if there is a quench effect. Nevertheless, HDAC and quenched data are roughly similar, and show always a preference for the melt.

## **4.4 Discussion and conclusions**

### **4.4.1 Fluid–melt partitioning**

This study presents the first systematic dataset for Ba, La, Yb, and Y partitioning between aqueous fluid and haplogranitic melt as function of temperature, pressure, fluid and melt composition. Furthermore, we also present the first data for Ba, La, and Y that are based on the direct determination of trace element contents in the fluid at elevated PT conditions.

In the following, we will compare the results of this study to literature and discuss possible effects of composition and quenching on trace element partition coefficients. Then, we present some ideas about trace element complexation in chloridic and non-chloridic aqueous fluids. Finally, we will draw some possible conclusions for natural systems.

#### **Comparison to other experimental data**

Only a few experimental data are available on fluid–melt partitioning of Ba, La, and Y. Most of these studies report data from quenched experiments using hydrothermal autoclaves (Webster et al., 1989, Bai and Koster van Groos, 1999, Reed et al., 2000) except Bureau et al. (2003), who applied hydrothermal diamond-anvil cells and  $\mu\text{PIXE}$  mapping to determine fluid–melt partition coefficients. All these studies also use different analytical techniques (plasma

emission spectrometry,  $\mu$ PIXE, or instrumental neutron activation analysis) or apply mass balance to recalculate the trace element contents in the fluid (Webster et al., 1989). Thus, a comparison of data is further complicated by the potentially different systematic errors of the experimental and analytical procedures applied. Furthermore, all these studies use different starting material and slightly differing PT conditions, which also complicates comparison of data and their discussion.

Bureau et al. (2003) studied Ba partitioning between silicate melts and water or saline fluids. Their data suggests a preference of Ba for the silicate melt. An effect of fluid salinity was not detected. This is in contrast to Webster et al. (1989) who studied partitioning of trace elements between fluorine-rich topaz–rhyolite melts and  $\text{H}_2\text{O}\pm\text{CO}_2$  as a function of Cl concentration. They found a transition from melt-compatible to fluid-compatible behavior with increasing chlorinity for Ba and also for Y. Bai and Koster van Groos (1999) studied element partitioning between metaluminous melts and various aqueous fluids and reported partition coefficient of La of 0.02 for  $\text{H}_2\text{O}$ . The  $D_{\text{La}}^{\text{f/m}}$  did not increase by addition of NaCl and KCl to the fluid, but addition of HCl lead to a significant rise of La partition coefficient. Reed et al. (2000) used peraluminous monzogranitic melt and a chloride-bearing aqueous volatile phase as starting materials. Their REE partitioning data linearly increase with  $\text{Cl}^-$  concentration in the fluid and showed a preference for the aqueous fluid at high salinities.

The Ba partitioning data of this study show a preference for the silicate melt at all studied fluid salinities and therefore, confirms the suggestions of Bureau et al. (2003). However, the  $D_{\text{Ba}}^{\text{f/m}}$  slightly increases with salinity of the fluid. In contrast to Webster et al. (1989), we do not observe a change to fluid-compatible behavior. The lanthanum data of this study are partly different to results by Reed et al. (2000), who found a preference of La and other rare earth elements for the fluid at high salinities (Fig. 4.7.2). At lower fluid salinities, the La partition coefficients from this study and from Reed et al. (2000) are in relatively good agreement. The La data from Bai and Koster van Groos (1999) show no difference between  $\text{H}_2\text{O}$  and (Na,K)Cl fluids. This is in contrast to the data of Reed et al. (2000) and also to the results of this study, which show increasing values with increasing salinity. Nevertheless, their  $D_{\text{La}}^{\text{f/m}}$  of 0.02 for  $\text{H}_2\text{O}$  as starting fluid is in very good agreement with in-situ data of this study. The Yttrium partition coefficient determined by Webster et al. (1989) shows a preference for the fluid at most fluid salinities studied and found a strong dependence on fluid salinity. This is a distinct difference to the results of this study (Fig. 4.8) because the  $D_{\text{Y}}^{\text{f/m}}$  is always smaller than one even at high fluid salinities. The most probable explanation for distinctions of Y and also Ba partition coefficients is the presence of up to 1.25 wt.% F in the starting material of Webster et al. (1989), whereas our experiments were performed in a F-free system. Fluor is known to be fluid-compatible and is a suitable complexing agent for many trace elements in hydrothermal solutions (e.g., Christiansen et al., 1984, Keppler and Wyllie, 1991, Bau and Dulski, 1995, Williams-Jones et al., 2000). Moreover, Christiansen et al. (1984) suggest that the trace element evolution of rhyolitic magmas is sensitive to F/Cl in the melt. That is, with differentiation, F-dominated systems display increases in Al, Na, Rb, Li, Cs, Be, Ta, and Th, while Cl-dominated systems are usually peralkaline and are associated with enrichments of e.g., LREE, Fe, Ti, Zn, Nb, and Zr. Although magmas with variable proportions of  $\text{H}_2\text{O}$ , F, Cl and  $\text{CO}_2$  exist, topaz rhyolites as the one Webster et al. (1989) used for their experiments, rep-

resent a fluorine-dominated end member (Christiansen et al., 1984). The differences between the results of this study and the data by Bai and Koster van Groos (1999), Reed et al. (2000) and Bureau et al. (2003) are most probably related to slightly different system composition and may also be caused by the usage of different experimental and analytical techniques as described earlier in this paragraph.

### **Comparison to data of natural cogenetic fluid and melt inclusions**

A comparison of the experimental results to natural data is very limited because only two studies report Ba, La, and Y concentrations in cogenetic fluid and melt inclusions (Audétat and Pettke, 2003, Zajacz et al., 2008). Zajacz et al. (2008) analyzed co-existing silicate melt and fluid inclusions, entrapped in quartz crystals for a series of elements including Ba and La. The fluid–melt partition coefficient of Ba is 0.49 at a fluid salinity of 6.5 wt.%, and increases to 19 at a salinity of ~34 wt.%. For Lanthanum, the partition coefficient slightly decreases from 0.31 to 0.1 with increasing fluid salinity from 6.5 to ~34 wt.%. Audétat and Pettke (2003) studied the magmatic-hydrothermal evolution of two barren granites using analyses of coeval fluid and melt inclusions trapped at 700–720°C and 110–120 MPa. Here, the fluid–melt partition coefficient of Y is max. ~0.006 at a fluid salinity of 4.9 wt.% NaCl<sub>equiv.</sub>. All in all, these data show a distinct preference of Ba, La, and Y for the melt at salinities of at least up to 6.5 wt.%, which is in good quantitative agreement with the data of this study.

### **Effects of chemical composition**

Any effect of the melt composition on the partitioning can be explained by i) changes in the incorporation of the trace element in the melt or ii) changes in the complexation of trace element in the fluid.

#### **i) Silicate melt.**

Flynn and Burnham (1978) and Ponader and Brown (1989) figured out that the incorporation of rare earth elements in silicate melts strongly depends on the availability of highly-coordinated sites, which increase as a function of the melt depolymerization. This hypothesis is in agreement with our data that show significantly higher fluid–melt partition coefficients of La, Yb, and also Y for experiments using peraluminous melts ( $ASI \geq 1$ ) than for those with peralkaline melts. The reason for that is the lower degree of polymerization of peralkaline melts compared to peraluminous melts. That is, these melts offer a higher quantity of sites coordinated by non-bridging oxygen (NBO). Therefore, peralkaline melts can incorporate higher REE contents than peraluminous melts. For barium, such studies are still missing. However, one can speculate that the barium incorporation in silicate melts will also depend on the degree of polymerization. The reasons are the divalent character of Ba and its large ion radius of 149 pm that is similar to that of K<sup>+</sup> (152 pm). This means, barium likely prefers also NBO to be incorporated in silicate melts, and therefore, Ba should preferentially be incorporated in peralkaline melts due the higher quantity of NBO sites compared to peraluminous melts. This surmise is supported by the Ba fluid–melt partition coefficient of this study that increases with ASI and thus increasing polymerization of the melt. However, the strong correlation between partition coefficients of Ba, La, Yb, and Y and ASI of the melt was only found in the case of chloridic fluids. Therefore, one



has also to discuss the structural role of  $\text{Cl}^-$  in different silicate melts. Stebbins and Du (2002) studied chloride ion sites in silicate and aluminosilicate glasses by  $^{35}\text{Cl}$  solid-state NMR. They found similar  $^{35}\text{Cl}$  peak positions in Al-free and Al-containing alkali glasses and suggested that even in the latter, most of the  $\text{Cl}^-$  ions are coordinated only by the alkali cations. Webster and De Vivo (2002) found a strong influence of doubly charged alkaline-earth metals on Cl solubility in the melt. They suggested that Cl interacts with and removes these divalent ions, previously associated with network-forming Al, to form alkaline earth metal-chloride species in the melt. One can speculate that this reaction might be stronger in the case of peralkaline melts due to the higher degree of depolymerization.

#### ii) Aqueous fluid.

Tracking down the effect of fluid composition is more complex, because apart from trace elements also major components are exchanged between the silicate melt and the aqueous fluid. Alkali ions will fractionate stronger into the fluid than Al and Si. The degree of this exchange varies with pressure on one hand side as the mutual solubility of melt and fluid increases. On the other hand, the effect of this exchange on the fluid composition will certainly vary with the ASI of the starting melt. Consequently, the ASI of the resulting melts will shift. In the case of  $\text{H}_2\text{O}$  as starting solution, small amounts of sodium partition into the aqueous fluid and thus, the ASI of the melt is shifted to higher values. Part of the alkalis might be exchanged with protons from the fluid leading to a change of the pH of the solution. For runs with  $\text{H}_2\text{O}$  only, this exchange is relatively small as can be deduced from data of Borchert et al. (2010) who report quench pH of 6 to 7.9 for experiments with  $\text{H}_2\text{O}$  independent of the ASI. It should be kept in mind, that at high PT conditions,  $\text{H}_2\text{O}$  is nearly completely associated (Tagirov et al., 1997), so that the measured pH does not equal the one at PT. Still, as shown below, the quench pH shows some systematic variation offering insight to the exchange equilibria between melt and fluid.

For chloridic fluids we observed a much more complicated behavior of the major compounds that can be directly related to the composition of the melt. Here, the ASI is shifted to higher values in the case of peralkaline starting glasses, but decreases in the case of peraluminous starting material (cp. Tab. 4.2 and 4.4). In experiments using initially peralkaline compositions, on one side alkalis will strongly partition into the aqueous fluid, and on the other side some of the Cl will be incorporated in the silicate melt. The incorporation of Cl in the melt is favored by the presence of divalent cations (Webster and De Vivo, 2002). For these fluids, the pH will increase because on the one hand alkalis strongly partition into the aqueous fluid which leads to a decrease of the activity of  $\text{Cl}^-$  and on the other hand protons are incorporated in the melt producing  $\text{OH}^-$  in the fluid. The latter is consistent with a basic quench pH of 9.5 in the case of peralkaline melts (Borchert et al., 2010). In the case of peraluminous melts, the ASI is shifted to lower values. Here, alkalis partition from the aqueous fluid into the silicate melt, which is correlated with a release of protons and highly charged trace elements from the melt into the aqueous fluid. The release of protons can be deduced from the acidic quench pH of 2 for fluids equilibrated with peraluminous melts (Borchert et al., 2010). The highly charged elements are only weakly bonded in peraluminous melts due to the lower amount of NBO coordinated sites compared to peralkaline melts. The solubility of Cl in peraluminous melts is somewhat lower than in the case of peralkaline melts. In addition, fractionation of alkalis

from the fluid into the melt increases the activity of  $\text{Cl}^-$  in the fluid. Thus, highly charged trace elements can be complexed more efficiently by Cl in the aqueous fluid.

### **Quench effect**

The comparison of partitioning data determined with in-situ analysis of trace element contents in fluids at elevated PT conditions to those from quenched experiments proves that the experimental fluids change their trace element signature upon cooling ('quench effect'). This is particularly important if  $D^{f/m}$  values are very different from one. This is highlighted by the fact, that the concentration of rare earth elements was always below detection limit in analyses of quenched fluids, whereas small REE contents were determined using the in-situ method although the minimum detection limit for the latter method was higher. Thus, if analyses of aqueous fluids are required for a certain experimental procedure, they should be performed in-situ. An alternative method is recalculation of the trace element contents in the aqueous fluid via mass balance (e.g., Ayers and Eggler, 1995, Webster et al., 1989, Webster, 1992a,b). The main advantage of in-situ analyses over mass balancing is the reliable determination of trace element contents of the aqueous fluid also in the case of formation of trace element-bearing crystals during the run.

There are two different mechanisms that can account for a quench effect, precipitation of phases during the quench and at room temperature and back reactions between aqueous fluid and silicate melt. The precipitation of new compounds from the aqueous fluid during cooling was not observed in our in-situ experiments by microscopic observation. We also did not find precipitated material in run products of conventionally quenched experiments. Surely, these negative results do not prove the complete absence of precipitation but reduce their probability. The data by Borchert et al. (2009) show a rapid equilibration of trace element contents between aqueous fluid and silicate melt, and thus, prove that back reactions between aqueous fluid and silicate melt are feasible. The comparison of slowly and rapidly quenched data (conventionally quenched experiments) show a strong effect of quenching on sodium and potassium in the resulting melt. Consequently, the ASI of rapidly quenched melts is slightly higher than that of slowly cooled melts. This caused a shift in the onset of the increase of fluid-melt partition data of La, Yb, and Y (see Fig. 4.2.1 and 4.2.2, Tab. 4.3 and 4.5). Based on these observations, we suggest that the observed quench effect is most likely due to back reactions between fluid and melt during cooling although it could not be proven by spatially resolved analyses on the quenched melts, most likely because any gradient potentially present is too small to be analyzed with techniques used here.

It should be noted, fluid–melt partition coefficients from HDAC experiments are still based in part on analyses of quenched samples, and thus are not free of quench effects. Further improvements should be aimed at the in-situ determination of trace element contents in both the fluid and the melt.

### **Complexation of trace elements in the fluid**

Interestingly, the in-situ analyses show roughly the same La and Y concentrations in chloride-free and chloridic solutions (cp. Tab. 4.6). In contrast, in conventionally quenched experiments

trace element contents of these elements in Cl-free fluids were always below the detection limit whereas this was not the case for chloridic solutions. This points to a strong effect of  $\text{Cl}^-$  on the quench process and suggests a stabilization of REE complexes in the fluid upon cooling in the presence of chlorine. Moreover, the very similar in-situ fluid–melt partition coefficients of La and Y for Cl-free and Cl-bearing fluids point to a complexation of these elements with dissolved silicate melt components. In detail, these complexes may be somewhat different for fluids with or without chlorine. For barium, the in-situ partition coefficient increases with salinity of the fluid, and  $D_{\text{Ba}}^{\text{f/m}}$  of chloridic fluids are 4 to 10 times higher than those the Cl-free fluid in the case of peraluminous melts. That is, Ba likely complexes with both,  $\text{Cl}^-$  and with dissolved melt components in fluids equilibrated with melts with an ASI  $\geq 1$ . For peralkaline melt compositions, we suggest a primal complexation with dissolved melt components because of the strong decrease of the Ba partition coefficient with decreasing ASI of the melt at constant fluid salinity.

### Further implications

Comparison of the data of this study and recent results (Borchert et al., 2010) show a similar dependence of Sr, Ba, La, Yb, and Y partitioning between aqueous fluids and haplogranitic melts on fluid salinity and on the melt composition. Therefore, we infer that fluid–melt partitioning of other divalent large ion lithophile elements (e.g., Pb) as well as of other lanthanides will show a similar dependence on the melt composition. The data show that  $\text{H}_2\text{O} \pm (\text{Na,K})\text{Cl}$  fluids exsolving from peralkaline silicate melts do not have the ability to significantly change the concentrations of Ba, La, Yb, and Y in the melt, even if the salinity of the fluid is high. The observed stronger enrichment of rare earth elements in peralkaline melts during exsolution of an aqueous fluid is also found in nature (e.g., Hedenquist and Lowenstern, 1994, Kovalenko et al., 1995, Williams-Jones et al., 2000, Tassinari et al., 2001). However, because the weight fraction of the exsolved aqueous fluids is small, this cannot be the main parameter controlling the final trace element content of granitic rocks. Here, fractionation of trace elements into crystalline phases will have a much larger effect. An enrichment of these elements in residual granitic melts is mainly controlled by the fractionation of these elements into crystallizing phases and the abundance of these crystals. For example, Ba will fractionate into feldspar and mica during crystallization of granites (e.g., Winter, 2001) and therefore, will be depleted in the residual melt. In contrast to large ion lithophile elements, the REE do not fractionate into granite forming minerals (except  $\text{Eu}^{2+}$ ). Thus, the exsolution of an aqueous fluid together with fractional crystallization of feldspars, quartz, and mica will result in an enrichment of the REE in the residual melt. Due to lower fluid–melt partition coefficients in peralkaline systems, it is suggested that this effect will be slightly stronger for melts with an ASI  $< 1$ . Our experiments also show that, for hydrothermal REE mineralizations derived from alkali granites, complexing of the REE must take place with other ligands than  $\text{Cl}^-$  to explain the enrichment in the fluid phase. Such anions are probably  $\text{F}^-$  and  $\text{CO}_3^{2-}$  (Ponader and Brown, 1989, Gieré, 1996, Williams-Jones et al., 2000).

#### **4.4.2 In-situ XRF analyses using high excitation energies**

Borchert et al. (2009, 2010) demonstrated that Rb and Sr concentrations in aqueous fluids equilibrated with silicate melts at elevated temperatures and pressures can be determined with a very good reliability using a HDAC and SR-XRF microanalysis, particularly for Cl<sup>-</sup> free systems. The experimental setup used in this study was similar to that used by Borchert et al. (2009, 2010), but with application of a much higher excitation energy (50 keV instead of 20 keV) to evaluate if analysis of XRF K line of elements with  $Z > 40$  is promising for diamond confined samples. The utilization of a new Kirkpatrick-Baez (KB) mirror based on a multilayer structure allowed measurements with spot sizes in the  $\mu\text{m}$  range and high excitation energies. At an excitation energy of 50 keV, the spectra showed a very broad background increase, which was related to Compton scattering from the incoming beam in the diamond anvil, which precluded analysis of small concentrations of elements with  $Z > 60$ . For the analysis of these elements, the following two improvements are suggested:

- A shift to a higher excitation energy ( $\sim 65$  keV). This should provide a better background in the energy range of interest because the inelastic scatter peak will also shift to higher energies. However, a shift to higher excitation energy will result in less flux and in lower fluorescence cross sections for low  $Z$  elements (like Y), and thus, will decrease the sensitivity for these elements. The use of a pink beam may compensate these trade-offs because application of the full bandwidth of the undulator harmonics would increase the flux by a factor of  $\sim 100$ .
- Realization of these experiments using a wavelength-dispersive spectrometer. Wavelength-dispersive analysis facilitates use of REE L lines because of the much better energy resolution compared to energy dispersive solid state detectors. For HDAC experiments, REE L lines can be better separated from each other and from K lines of the 3d-transition metals (e.g., excitation from gasket or thermocouple). That is, lower excitation energies can be applied. Another advantage of utilization of a wavelength-dispersive spectrometer is the lower background. However, the disadvantages are lower fluorescence yields and a much stronger absorption of lower energy fluorescence lines along the path towards the detection.

## **Acknowledgements**

We thank the European Synchrotron Radiation Facility (ESRF) for granting beamtime, M. Ebert for performing the Barium quenched experiments and data evaluation of these experimental runs, O. Appelt for the help with EMP measurements at Deutsches GeoForschungsZentrum, A. Musiol for the introduction to ICP-OES analysis at Universität Potsdam, and A. Gottsche for the introduction to IC analysis and performance of some of the analysis at Deutsches GeoForschungsZentrum GFZ. The great help and support of K. Appel, L. Vincze, and S. Labouré are highly appreciated. We thank D. Dingwell for editorial handling, A. C. Simon for the constructive review, and J. D. Webster for useful comments on this manuscript. This study was supported by the German Science Foundation (DFG, Wi 2000/3-1 and Wi 2000/3-2).

- Akella, J., Vaidya, S. N., and Kennedy, G. C. (1969). Melting of Sodium Chloride at Pressures to 65 kbar. *Physical Review*, 185(3):1135–1140.
- Albarede, F. (1975). Some trace element relationships among liquid and solid phases in the course of the fractional crystallization of magmas. *Geochimica et Cosmochimica Acta*, 40:667–673.
- Audétat, A. and Pettke, T. (2003). The magmatic-hydrothermal evolution of two barren granites: A melt and fluid inclusion study of the Rito del Medio and Canada Pinabete plutons in northern New Mexico (USA). *Geochimica et Cosmochimica Acta*, 67(1):97–121.
- Ayers, J. C. and Eggler, D. H. (1995). Partitioning of elements between silicate melt and H<sub>2</sub>O-NaCl fluids at 1.5 and 2.0 GPa pressure: Implications for mantle metasomatism. *Geochimica et Cosmochimica Acta*, 59(20):4237–4246.
- Bai, T. B. and Koster van Groos, A. F. (1999). The distribution of Na, K, Rb, Sr, Al, Ge, Cu, W, Mo, La, and Ce between granitic melts and coexisting aqueous fluids. *Geochimica et Cosmochimica Acta*, 63(7/8):1117–1131.
- Bassett, W. A., Anderson, A. J., Mayanovic, R. A., and Chou, I.-M. (2000). Modified hydrothermal diamond anvil cells for XAFS analyses of elements with low energy absorption edges in aqueous solutions at sub- and supercritical conditions. *Zeitschrift für Kristallographie*, 215:711–717.
- Bassett, W. A., Shen, A. H., Bucknum, M., and Chou, I.-M. (1993). A new diamond anvil cell for hydrothermal studies to 2.5 GPa and from 190 to 1200°C. *Review of scientific instruments*, 64:2340–2345.
- Bau, M. and Dulski, P. (1995). Comparative study of yttrium and rare-earth element behaviours in fluorine-rich hydrothermal fluids. *Contributions to Mineralogy and Petrology*, 119:213–223.
- Bea, F. (1996). Residence of REE, Y, Th and U in Granites and Grustal Protoliths; Implications for the Chemistry of Crustal Melts. *Journal of Petrology*, 37(3):521–552.
- Bea, F., Pereira, M. D., and Stroh, A. (1994). Mineral/leucosome trace-element partitioning in a peraluminous migmatite (a laser ablation-ICP-MS study). *Chemical Geology*, 117:291–312.
- Bédard, J. H. (2006). Trace element partitioning in plagioclase feldspar. *Geochimica et Cosmochimica Acta*, 70:3717–3742.

- 
- Behrens, H. and Jantos, N. (2001). The effect of anhydrous composition on water solubility in granitic melts. *American Mineralogist*, 86:14–20.
- Best, M. G. (2003). *Igneous and Metamorphic Petrology*. Blackwell.
- Blundy, J., Robinson, J., and Wood, B. (1998). Heavy REE are compatible in clinopyroxene on the spinel lherzolite solidus. *Earth and Planetary Science Letters*, 160:493–504.
- Blundy, J. D. and Wood, B. J. (1991). Crystal-chemical controls on the partitioning of Sr and Ba between plagioclase feldspar, silicate melts, and hydrothermal solutions. *Geochimica et Cosmochimica Acta*, 55:193–209.
- Bodnar, R. J. and Vityk, M. O. (1994). *Interpretation of microthermometric data for H<sub>2</sub>O-NaCl fluid inclusions. Fluid Inclusions in Minerals: Methods and Applications*, pages 117–130. Virginia Tech.
- Borchert, M., Wilke, M., Schmidt, C., and Rickers, K. (2009). Partitioning and equilibration of Rb and Sr between silicate melts and aqueous fluids. *Chemical Geology*, 259:39–47.
- Borchert, M., Wilke, M., Schmidt, C., and Rickers, K. (2010). Rb and Sr partitioning between haplogranitic melts and aqueous solutions. *Geochimica et Cosmochimica Acta*, 74:1057–1076.
- Bureau, H., Ménez, B., Khodja, H., Daudin, L., Gallien, J.-P., Massare, D., Shaw, C., and Métrich, N. (2003). The partitioning of barium and lead between silicate melts and aqueous fluids at high pressures and temperatures. *Nuclear Instruments and Methods in Physics Research*, 210:434–440.
- Burnham, C. W. and Jahns, R. H. (1962). A method for determining the solubility of water in silicate melts. *American Journal of Science*, 260:721–745.
- Chappell, B. W. and White, A. J. R. (1974). Two contrasting granite types. *Pac Geol*, 8:173–174.
- Christiansen, E. H., Bikun, J. V., Sheridan, M. F., and Burt, D. M. (1984). Geochemical evolution of topaz rhyolites from the Thomas Range and Spor Mountain, Utah. *American Mineralogist*, 69:223–236.
- Ewart, A. and Griffin, W. L. (1994). Application of Proton-Microprobe Data to Trace-Element Partitioning in Volcanic-Rocks. *Chemical Geology*, 117:251–284.
- Flynn, R. T. and Burnham, C. W. (1978). An experimental determination of rare earth partition coefficients between a chloride containing vapor phase and silicate melts. *Geochimica et Cosmochimica Acta*, 42:685–701.
- Gieré, R. (1996). *Formation of rare earth minerals in hydrothermal systems. In: Rare earth minerals: Chemistry, origin and ore deposits*, chapter 5, pages 105–150. Chapman & Hall.
- Green, T. H. and Pearson, N. J. (1983). Effect of pressure on rare earth element partition coefficients in common magmas. *Nature*, 305:414–416.

- Haar, L., Gallagher, J., and Kell, G. (1984). *Steam tables*; chapter Thermodynamic and transport properties and computer programs for vapor and liquid states of water in SI units, page 320. Hemisphere Pub. Corp., Washington, D.C.
- Hall, D. L., Sterner, S. M., and Bodnar, R. J. (1988). Freezing Point depression of NaCl-KCl-H<sub>2</sub>O Solutions. *Economic Geology*, 83:197–202.
- Hedenquist, J. W. and Lowenstern, J. B. (1994). The role of magmas in the formation of hydrothermal ore deposits. *Nature*, 370:519–527.
- Hui, H., Zhang, Y., Xu, Z., Del Gaudio, P., and Behrens, H. (2009). Pressure dependence of viscosity of rhyolitic melts. *Geochimica et Cosmochimica Acta*, 73:3680–3693.
- Jochum, K. P., Dingwell, D. B., Rocholl, A., Stoll, B., Hofmann, A. W., and many others (2000). The preparation and preliminary characterisation of eight geological MPI-DING reference glasses for in-situ microanalysis. *Geostandards Newsletter*, 24(1):87–133.
- Jochum, K. P., Stoll, B., Herwig, K., Willbold, M., Hofmann, A. W., and many others (2006). MPI-DING reference glasses for in situ microanalysis: New reference values for element concentrations and isotope ratios. *Geochemistry, Geophysics, Geosystems*, 7(2):1–44.
- Johannes, W. and Holtz, F. (1996). *Petrogenesis an Experimental Petrology of Granitic Rocks*. Springer, Berlin.
- Keppler, H. and Wyllie, P. J. (1991). Partitioning of Cu, Sn, Mo, W, U, and Th between melt and aqueous fluid in the systems haplogranite-H<sub>2</sub>O-HCl and haplogranite-H<sub>2</sub>O-HF. *Contributions to Mineralogy and Petrology*, 109:139–150.
- Kovalenko, V. I., Tsaryeva, G. M., Goreglyad, A. V., Yarmolyuk, V. V., Troitsky, V. A., Hervig, R. L., and Farmer, G. L. (1995). The peralkaline granite-related Khaldzan-Buregtey rare metal (Zr, Nb, REE) deposit, western Mongolia. *Economic Geology*, 90:530–547.
- Leeman, W. and Phelps, D. (1981). Partitioning of rare earths and other trace elements between sanidine and coexisting volcanic glass. *Journal of Geophysical Research*, 86:10193–10199.
- Mahood, G. A. and Hildreth, E. W. (1983). Large partition coefficients for trace elements in high-silica rhyolites. *Geochimica et Cosmochimica Acta*, 47:11–30.
- Nash, W. P. and Crecraft, H. R. (1985). Partition coefficients for trace elements in silicic magmas. *Geochimica et Cosmochimica Acta*, 49:2309–2322.
- Pearce, J. G., Perkins, W. T., Westgate, J. A., Gorton, M. P., Jackson, S. E., Neal, C. R., and Chenery, S. P. (1997). A compilation of new and published major and trace element data for NIST SRM 610 and NIST SRM 612 glass reference materials. *Geostandards Newsletter*, 21(1):115–144.
- Philpotts, A. R. (1990). *Principles of igneous and metamorphic petrology*. Prentice Hall, London.

- 
- Philpotts, A. R. and Ague, J. J. (2009). *Principles of igneous and metamorphic petrology*. Cambridge University Press, 2nd edition.
- Ponader, C. W. and Brown, C. E. (1989). Rare earth elements in silicate glass/melt systems: II. Interactions of La, Gd, and Yb with halogens. *Geochimica et Cosmochimica Acta*, 53:2905–2914.
- Reed, M. J., Candela, P. A., and Piccoli, P. M. (2000). The distribution of rare earth elements between monzogranitic melt and the aqueous volatile phase in experimental investigations at 800°C and 200 MPa. *Contributions to Mineralogy and Petrology*, 140:251–262.
- Ren, M., Parker, D. F., and White, J. C. (2003). Partitioning of Sr, Ba, Rb, Y, and REE between plagioclase and peraluminous silicic magma. *American Mineralogist*, 88:1091–1103.
- Schmidt, C. and Rickers, K. (2003). In-situ determination of mineral solubilities in fluids using a hydrothermal diamond-anvil cell and SR-XRF: Solubility of AgCl in water. *American Mineralogist*, 88:288–292.
- Schmidt, C., Rickers, K., Bilderback, D. H., and Huang, R. (2007). In situ synchrotron-radiation XRF study of REE phosphate dissolution in aqueous fluids to 800°C. *Lithos*, 95:87–102.
- Solé, V. A., Papillon, E., Cotte, M., Walter, P., and Susini, J. (2007). A multiplatform code for the analysis of energy-dispersive X-Ray fluorescence spectra. *Spectrochimica Acta, B* 62:63–68.
- Stebbins, J. F. and Du, L.-S. (2002). Chloride ion sites in silicate and aluminosilicate glasses: A preliminary study by <sup>35</sup>Cl solid-state NMR. *American Mineralogist*, 87:359–363.
- Stix, J. and Gorton, M. P. (1990). Variations in trace element partition coefficients in sanidine in the Cerro Toledo Rhyolite, Jemez Mountains, New Mexico - Effects of composition, temperature, and volatiles. *Geochimica et Cosmochimica Acta*, 54:2697–2708.
- Streck, M. J. and Grunder, A. L. (1997). Compositional gradients and gaps in high-silica rhyolites of the Rattlesnake Tuff, Oregon. *Journal of Petrology*, 38(1):133–163.
- Tagirov, B. R., Zotov, A. V., and Akinfiev, N. N. (1997). Experimental study of dissociation of HCl from 350 to 500°C and from 500 to 2500 bars: Thermodynamic properties of HCl<sub>(aq)</sub><sup>o</sup>. *Geochimica et Cosmochimica Acta*, 61(20):4267–4280.
- Tassinari, M. M. L., Kahn, H., and Ratti, G. (2001). Process mineralogy studies of Corrego Do Garimpo REE ore, Catalao-I alkaline complex, Goias, Brasil. *Minerals Engineering*, 14(12):1609–1617.
- Tuttle, O. F. and Bowen, N. L. (1958). *Origin of granite in the light of experimental studies in the system NaAlSi<sub>3</sub>O<sub>8</sub>–KAlSi<sub>3</sub>O<sub>8</sub>–SiO<sub>2</sub>–H<sub>2</sub>O*. The Geological Society of America.
- Webster, J. D. (1992a). Fluid-melt interactions involving Cl-rich granites: Experimental study from 2 to 8 kbar. *Geochimica et Cosmochimica Acta*, 56:659–678.



- Webster, J. D. (1992b). Water solubility and chlorine partitioning in Cl-rich granitic systems: Effects of melt composition at 2 kbar and 800°C. *Geochimica et Cosmochimica Acta*, 56:679–687.
- Webster, J. D. and De Vivo, B. (2002). Experimental and modeled solubilities of chlorine in aluminosilicate melts, consequences of magma evolution, and implications for exsolution of hydrous chloride melt at Mt. Somma-Vesuvius. *American Mineralogist*, 87:1046–1061.
- Webster, J. D., Holloway, J. R., and Hervig, R. L. (1989). Partitioning of Lithophile trace elements between H<sub>2</sub>O and H<sub>2</sub>O+CO<sub>2</sub> fluids and topaz rhyolite melt. *Economic Geology*, 84:116–134.
- Williams-Jones, A. E., Sampson, I. M., and Olivo, G. R. (2000). The genesis of hydrothermal fluorite-REE deposits in the Gallinas mountains, New Mexico. *Economic Geology*, 95:327–342.
- Winter, J. D. (2001). *An Introduction to Igneous and Metamorphic Petrology*. Prentice Hall, New Jersey.
- Wolf, A. V., Brown, M. G., and Prentiss, P. G. (1981). *Concentrative properties of aqueous solutions: conversion tables*. In: Weast, R.C. (Ed.), *CRC Handbook of Chemistry and Physics*, pages D198–D247. CRC Press.
- Yamashita, S. (1999). Experimental study of the effect of temperature on water solubility in natural rhyolite melt to 100 MPa. *Journal of Petrology*, 40(10).
- Zajacz, Z., Halter, W. E., Pettke, T., and Guillong, M. (2008). Determination of fluid/melt partition coefficients by LA-ICPMS analysis of co-existing fluid and silicate melt inclusions: Controls on element partitioning. *Geochimica et Cosmochimica Acta*, 72:2169–2197.

# Appendix

Table 4.1: Composition of starting glasses from EMP analyses and normative composition based on the components albite, orthoclase, quartz, corundum and Na-metasilicate.

	SiO <sub>2</sub> [wt.%]	Al <sub>2</sub> O <sub>3</sub> [wt.%]	Na <sub>2</sub> O [wt.%]	K <sub>2</sub> O [wt.%]	ASI	Ba [ppm]	La [ppm]	Y [ppm]	Yb [ppm]	normative - composition	
<b>quenched experiments - glasses doped with Ba</b>											
PerAlu2*	75.04	16.82	4.72	3.89	1.40	1739±74				Ab <sub>39.93</sub> Or <sub>22.98</sub> Qz <sub>32.70</sub> + C <sub>4.85</sub>	
PerAlu1*	76.15	14.36	4.42	3.80	1.26	1995±121				Ab <sub>37.40</sub> Or <sub>22.45</sub> Qz <sub>35.89</sub> + C <sub>2.98</sub>	
MetAlu1*	77.53	12.56	4.34	3.85	1.11	1957±90				Ab <sub>36.72</sub> Or <sub>22.75</sub> Qz <sub>37.55</sub> + C <sub>1.25</sub>	
PerAlk2*	77.34	12.48	5.53	3.54	0.97	2138±84				Ab <sub>44.48</sub> Or <sub>20.92</sub> Qz <sub>32.95</sub> + N <sub>80.54</sub>	
PerAlk1*	77.62	12.24	7.03	3.14	0.82	2067±84				Ab <sub>45.47</sub> Or <sub>18.55</sub> Qz <sub>32.73</sub> + N <sub>83.26</sub>	
<b>quenched experiments - glasses doped with La and Y</b>											
PerAlu2†	72.98	16.86	4.87	3.86	1.38	420±75	610±44			Ab <sub>41.80</sub> Or <sub>23.16</sub> Qz <sub>30.30</sub> + C <sub>4.73</sub>	
PerAlu1†	77.26	14.50	4.30	3.94	1.28	1385±81	442±58			Ab <sub>36.37</sub> Or <sub>23.30</sub> Qz <sub>37.16</sub> + C <sub>3.16</sub>	
MetAlu1†	78.68	12.67	4.04	3.85	1.17	1833±389	513±80			Ab <sub>34.46</sub> Or <sub>22.93</sub> Qz <sub>40.74</sub> + C <sub>1.87</sub>	
PerAlk2†	79.21	12.65	5.00	3.47	1.06	993±81	413±63			Ab <sub>42.13</sub> Or <sub>20.44</sub> Qz <sub>36.74</sub> + C <sub>0.67</sub>	
PerAlk1†	78.80	12.27	7.24	3.31	0.79	1182±85	907±98			Ab <sub>43.96</sub> Or <sub>19.23</sub> Qz <sub>32.99</sub> + N <sub>83.81</sub>	
<b>quenched experiments - glasses doped with La and Yb</b>											
PerAlu2*	75.83	14.17	4.53	3.91	1.21	1091±267		2050±276		Ab <sub>38.92</sub> Or <sub>23.46</sub> Qz <sub>35.08</sub> + C <sub>2.53</sub>	
MetAlu1*	77.71	12.31	4.46	3.95	1.06	930±241		2002±253		Ab <sub>38.33</sub> Or <sub>23.69</sub> Qz <sub>37.25</sub> + C <sub>0.72</sub>	
PerAlk2*	78.75	12.56	5.41	3.64	0.98	993±175		934±61		Ab <sub>44.19</sub> Or <sub>21.42</sub> Qz <sub>34.05</sub> + N <sub>80.33</sub>	
PerAlk1*	79.18	12.37	7.45	3.38	0.78	1019±67		984±69		Ab <sub>43.73</sub> Or <sub>19.53</sub> Qz <sub>32.57</sub> + N <sub>84.16</sub>	
	SiO <sub>2</sub> [wt.%]	Al <sub>2</sub> O <sub>3</sub> [wt.%]	Na <sub>2</sub> O [wt.%]	K <sub>2</sub> O [wt.%]	ASI	Ba [ppm]	La [ppm]	Y [ppm]	Sm [ppm]	Eu [ppm]	normative - composition
<b>HDAC experiments - glasses doped with Ba, La, Y, Sm, and Eu</b>											
PerAlu2	72.89	18.44	5.17	3.5	1.50	1609±175	1681±136	1644±127	1526±196	1216±144	Ab <sub>43.74</sub> Or <sub>20.68</sub> Qz <sub>29.42</sub> + C <sub>6.15</sub>
MetAlu1	77.07	13.78	5.54	3.61	1.06	2247±215	792±130	1604±97	1636±150	1394±110	Ab <sub>46.87</sub> Or <sub>21.33</sub> Qz <sub>31.03</sub> + C <sub>0.76</sub>

Ab - albite, Or - orthoclase, Qz - quartz, C - corundum, Ns - Na<sub>2</sub>SiO<sub>3</sub>

Table 4.2: Data for Barium from experiments at 750°C and 200 MPa using rapid quench autoclaves (RQ) and internally heated pressure vessel (IHPV). For each run, the first line of the analyses refers to the quench glass and second line to the quenched fluid.

run	experimental conditions			starting materials [melt / fluid]	analyses of run products						
	technique	P [MPa]	T [°C]		Na <sub>2</sub> O [wt.%]	K <sub>2</sub> O [wt.%]	SiO <sub>2</sub> [wt.%]	Al <sub>2</sub> O <sub>3</sub> [wt.%]	ASI	Ba [ppm]	Cl [ppm]
PerAlu2HB	RQ	200	750	PerAlu2*	3.21	3.63	71.22	15.36	1.67	1960±99	bdl
				H <sub>2</sub> O	0.01	0.03	0.44	bdl		7±1	na
PerAlu1HB	RQ	200	750	PerAlu1*	3.81	3.70	72.76	13.22	1.29	1891±102	bdl
				H <sub>2</sub> O	0.03	0.05	0.58	bdl		9±1	na
MetAlu1HB	RQ	200	750	MetAlu1*	3.87	3.74	74.65	11.67	1.12	1792±71	bdl
				H <sub>2</sub> O	0.04	0.05	0.58	bdl		8±1	na
PerAlk2HB	RQ	200	750	PerAlk2*	4.78	3.45	74.46	11.63	1.00	2008±37	bdl
				H <sub>2</sub> O	0.06	0.04	0.48	bdl		6±1	na
PerAlk1HB	RQ	200	750	PerAlk1*	6.21	3.04	74.60	11.34	0.84	1954±80	bdl
				H <sub>2</sub> O	0.07	0.05	0.54	bdl		7±1	na
PerAlu2LB	RQ	200	750	PerAlu2*	3.79	4.95	70.18	14.93	1.29	1642±81	1347±158
				1H + 1S	1.41	1.39	0.02	bdl		138±1	25667±2567
PerAlu1LB	RQ	200	750	PerAlu1*	3.66	4.90	71.95	13.03	1.15	1376±70	1013±196
				1H + 1S	2.28	2.07	0.17	bdl		222±1	55236±5524
PerAluL3	EHPV	200	750	PerAlu1*	3.56	4.75	71.54	13.28	1.21	1457±86	1510±187
				1H + 1S	2.78	2.61	bdl	bdl		293±2	42908±4291
MetAlu1LB	RQ	200	750	MetAlu1*	3.44	4.89	73.26	11.51	1.05	1383±105	825±106
				1H + 1S	2.56	2.40	0.16	bdl		254±1	47663±4766
PerAlk2LB	RQ	200	750	PerAlk2*	4.16	4.67	73.61	11.45	0.96	1885±61	1154±155
				1H + 1S	2.95	2.52	0.02	bdl		104±1	51214±5121
PerAlk1LB	RQ	200	750	PerAlk1*	5.15	4.43	73.58	10.99	0.83	1919±77	1324±140
				1H + 1S	3.00	2.24	0.37	bdl		37±1	47587±4759
PerAlu2HP	RQ	200	750	PerAlu2*	4.08	3.72	69.94	16.42	1.53	2055±128	bdl
				H <sub>2</sub> O	0.04	0.02	0.32	bdl		1±0.1	na
PerAlu1HP	RQ	200	750	PerAlu1*	3.70	3.73	72.53	14.01	1.38	1929±96	bdl
				H <sub>2</sub> O	0.02	0.01	0.04	bdl		1±0.2	na
MetAlu1HP	RQ	200	750	MetAlu1*	3.77	3.76	74.48	12.32	1.20	1765±112	bdl
				H <sub>2</sub> O	0.04	0.01	0.03	bdl		1±0.1	na
PerAlk2HP	RQ	200	750	PerAlk2*	4.84	3.60	73.72	12.46	1.05	2108±162	bdl
				H <sub>2</sub> O	0.04	0.02	0.01	bdl		1±0.1	na
PerAlk1HP	RQ	200	750	PerAlk1*	5.71	3.06	73.65	11.69	0.92	2045±104	bdl
				H <sub>2</sub> O	0.19	0.12	0.21	bdl		2±0.1	na
PerAlu2LPx	RQ	200	750	PerAlu1*	3.99	5.18	70.27	14.84	1.22	568±102	1352±183
				1H + 1S	2.18	2.01	0.04	bdl		189±1	42653±4265
PerAlu1LP	RQ	200	750	PerAlu1*	3.75	4.97	71.75	13.87	1.20	1570±119	695±190
				1H + 1S	2.64	2.55	0.06	bdl		269±2	49472±4947
MetAlu1LP	RQ	200	750	MetAlu1*	3.49	4.83	73.10	12.25	1.12	1356±136	1921±234
				1H + 1S	2.07	1.94	0.37	bdl		188±2	35687±3569
PerAlk2LP	RQ	200	750	PerAlk2*	4.18	4.71	72.91	12.26	1.02	1868±180	1224±150
				1H + 1S	2.73	2.26	0.02	bdl		84±3	45388±4539
PerAlk1LP	RQ	200	750	PerAlk1*	5.14	4.53	72.39	11.68	0.87	1905±212	2044±196
				1H + 1S	2.39	1.78	0.06	bdl		6±0.1	37389±3739
PerAlu2HPi	IHPV	200	750	PerAlu2*	3.38	3.69	70.36	15.78	1.65	586±141	bdl
				H <sub>2</sub> O	0.04	0.02	0.05	bdl		2±0.1	na
PerAlu1HPi	IHPV	200	750	PerAlu1*	3.53	3.68	72.42	13.21	1.35	417±141	bdl
				H <sub>2</sub> O	0.04	0.03	0.05	bdl		1±0.1	na
MetAlu1HPi	IHPV	200	750	MetAlu1*	3.45	3.73	73.99	11.67	1.20	463±151	bdl
				H <sub>2</sub> O	0.04	0.01	0.07	bdl		3±0.1	na
PerAlk2HPi	IHPV	200	750	PerAlk2*	4.26	3.45	73.28	11.55	1.07	720±171	bdl
				H <sub>2</sub> O	0.93	0.53	0.51	bdl		42±2	na
PerAlk1HPi	IHPV	200	750	PerAlk1*	5.64	3.10	73.37	11.14	0.88	703±83	bdl
				H <sub>2</sub> O	0.14	0.04	0.15	bdl		4±0.1	na
PerAlu2LPi	IHPV	200	750	PerAlu2*	4.00	4.98	70.18	15.33	1.28	601±161	1165±141
				1H + 1S	1.67	1.47	0.02	bdl		126±1	27761±2776
PerAlu1LPi	IHPV	200	750	PerAlu1*	3.73	4.89	72.51	13.18	1.15	400±127	995±130
				1H + 1S	2.37	2.28	0.04	bdl		176±1	44386±4439
MetAlu1LPi	IHPV	200	750	MetAlu1*	3.49	4.86	74.39	11.67	1.06	336±146	796±125
				1H + 1S	2.38	2.12	0.02	bdl		173±1	40393±4039

Table 4.2 – continued from previous page

run	experimental conditions			starting materials [melt / fluid]	analyses of run products						
	tech.	P [MPa]	T [°C]		Na <sub>2</sub> O [wt.%]	K <sub>2</sub> O [wt.%]	SiO <sub>2</sub> [wt.%]	Al <sub>2</sub> O <sub>3</sub> [wt.%]	ASI	Ba [ppm]	Cl [ppm]
PerAlk2LPi	IHPV	200	750	PerAlk2* 1H + 1S	3.79 1.97	4.63 1.60	73.58 0.02	11.48 bdl	1.02	667±148 50±4	962±121 28225±2823
PerAlk1LPi	IHPV	200	750	PerAlk1* 1H + 1S	4.76 1.98	4.31 1.29	72.58 0.03	11.03 bdl	0.88	677±138 6±1	1314±128 23892±2389
MetAlu1HPi2	IHPV	200	750	MetAlu1* H <sub>2</sub> O	3.44 0.08	4.00 0.04	74.73 0.02	11.73 bdl	1.17	412±162 1±0.1	bdl na
MetAlu1LPi2	IHPV	200	750	MetAlu1* 1H + 1S	3.47 2.85	4.86 2.68	73.93 0.02	11.75 bdl	1.07	367±114 200±2	753±6 51572±5157

\* – initial glass composition as described in Tab.4.1

na – not analysed

bdl – below detection limit

1H – 1m NaCl, 1S – 1m KCl

ASI – Al<sub>2</sub>O<sub>3</sub>/(Na<sub>2</sub>O+K<sub>2</sub>O) in moles

Table 4.3: Data for Lanthanum, Yttrium and Ytterbium from experiments from 750 to 950°C and 200 or 500 MPa using various quench apparatus. For each run, the first line of the analyses refers to the quench glass and second line to the quenched fluid.

run	experimental conditions			starting materials [melt / fluid]	analyses of run products							
	tech.	P [MPa]	T [°C]		Na <sub>2</sub> O [wt.%]	K <sub>2</sub> O [wt.%]	SiO <sub>2</sub> [wt.%]	Al <sub>2</sub> O <sub>3</sub> [wt.%]	ASI	La [ppm]	Y [ppm]	Yb [ppm]
A1	EHPV	200	750	PerAlu1* 1H + 1S (pH 1)	3.55 3.03	4.80 2.48	71.38 bdl	13.26 bdl	1.20	893±79 113±1	1180±189 26±1	na na
A2	EHPV	200	750	MetAlu1* 1H + 1S (pH 1)	3.42 2.13	4.91 1.82	73.43 bdl	11.63 bdl	1.06	595±99 8±1	582±116 4±1	na na
A4	EHPV	200	750	PerAlk2* 1H + 1S (pH 1)	3.58 2.69	4.79 2.08	73.10 bdl	11.56 bdl	1.04	987±75 4±1	1080±71 3±1	na na
A3	EHPV	200	750	PerAlk1* 1H + 1S (pH 1)	5.48 2.57	4.61 1.66	70.89 bdl	11.03 bdl	0.79	973±82 4±1	964±68 3±1	na na
B1	EHPV	200	750	PerAlu1† 1H + 1S (pH 1)	3.37 2.65	5.06 2.37	71.42 bdl	13.02 bdl	1.18	997±131 106±1	406±44 28±1	na na
B2	EHPV	200	750	MetAlu1† 1H + 1S (pH 1)	3.34 2.12	5.03 1.75	73.83 bdl	11.73 bdl	1.07	354±65 9±1	27±31 3±1	na na
B4	EHPV	200	750	PerAlk2† 1H + 1S (pH 1)	3.97 2.62	4.77 2.01	73.44 bdl	11.63 bdl	0.99	1023±64 1±1	614±58 1±1	na na
C1	EHPV	200	750	PerAlu* 1H + 1S	3.27 2.32	4.88 1.92	72.83 bdl	13.31 bdl	1.25	817±105 82±1	1337±136 19±1	na na
C2	EHPV	200	750	MetAlu1* 1H + 1S	3.15 2.52	4.82 2.30	74.16 bdl	11.73 bdl	1.13	467±76 2±1	834±61 bdl	na na
C3	EHPV	200	750	PerAlk1* 1H + 1S	5.96 3.24	4.72 2.18	72.79 bdl	11.27 bdl	0.76	1000±108 2±1	953±110 bdl	na na
D1	EHPV	200	750	PerAlu1† 1H + 1S	3.36 2.20	4.99 1.95	72.48 bdl	13.21 bdl	1.21	1152±79 82±1	550±55 21±1	na na
D3	EHPV	200	750	PerAlk1† 1H + 1S	4.96 3.06	4.67 2.17	71.75 bdl	10.91 bdl	0.83	1117±65 1±1	726±75 1±1	na na
A1	RQ	200	750	PerAlu1* 1H + 1S (pH 1)	3.59 1.98	5.02 1.87	72.43 0.01	13.12 0.002	1.16	829±176 17±2	1708±131 7±1	1210±102 40667±4070
A2	RQ	200	750	MetAlu1* 1H + 1S (pH 1)	3.24 2.16	4.95 1.79	73.73 bdl	11.37 bdl	1.06	274±113 bdl	446±145 bdl	704±83 41532±4150
A3	RQ	200	750	PerAlk1* 1H + 1S (pH 1)	5.60 3.12	4.57 2.31	69.78 0.03	11.07 0.003	0.78	900±55 bdl	882±91 bdl	2140±321 65364±6536
B0	RQ	200	750	PerAlu2† 1H + 1S (pH 1)	3.97 2.71	5.00 2.51	68.81 0.001	15.42 bdl	1.29	805±62 106±1	544±18 38±1	1896±211 54870±5487
B1	RQ	200	750	PerAlu1† 1H + 1S (pH 1)	3.62 1.81	5.09 1.69	73.04 0.06	13.22 0.002	1.15	748±170 11±1	447±54 3±1	1128±114 38189±3820
B2	RQ	200	750	MetAlu1† 1H + 1S (pH 1)	3.50 1.88	5.00 1.72	75.00 bdl	11.84 bdl	1.06	279±123 bdl	bdl bdl	871±91 37413±3741
B4	RQ	200	750	PerAlk2† 1H + 1S (pH 1)	4.07 2.55	4.52 1.98	72.79 bdl	11.48 bdl	0.99	1255±120 bdl	495±101 bdl	1434±199 48295±4830
B3	RQ	200	750	PerAlk1† 1H + 1S (pH 1)	5.36 2.16	4.82 1.41	70.67 0.02	11.00 bdl	0.82	1031±70 bdl	771±49 bdl	1697±248 36123±3612
C1	RQ	200	750	PerAlu1* 1H + 1S	3.65 1.50	5.10 1.51	67.67 0.04	12.80 0.001	1.11	617±160 40±4	1530±161 9±1	986±201 33070±3307
C2	RQ	200	750	MetAlu1* 1H + 1S	3.41 3.72	5.09 2.70	74.18 0.03	11.70 0.002	1.05	507±137 bdl	1226±273 bdl	976±94 63235±6324
C4	RQ	200	750	PerAlk2* 1H + 1S	3.94 3.20	4.71 2.42	73.95 0.06	11.44 0.02	0.99	1062±39 bdl	921±97 bdl	1242±208 64190±6419
C3	RQ	200	750	PerAlk1* 1H + 1S	5.65 3.09	4.45 2.14	70.32 0.04	10.93 bdl	0.76	946±71 bdl	978±63 bdl	2009±271 57054±5705
D0	RQ	200	750	PerAlu2† 1H + 1S	3.77 2.63	4.74 2.29	68.44 0.007	15.01 bdl	1.32	695±44 88±2	582±40 33±1	1454±175 56660±5670
D1	RQ	200	750	PerAlu1† 1H + 1S	3.51 1.64	5.00 1.48	72.59 0.02	13.09 bdl	1.17	622±101 23±2	364±64 5±1	986±133 33500±3350
D2	RQ	200	750	MetAlu1† 1H + 1S	3.34 2.21	4.91 2.00	74.37 0.1	11.59 0.001	1.07	557±143 bdl	153±69 bdl	693±91 42808±4281
D4	RQ	200	750	PerAlk2† 1H + 1S	4.22 3.36	4.62 2.57	73.83 0.001	11.52 0.004	0.96	1054±79 bdl	559±99 bdl	1196±360 49205±4921
D3	RQ	200	750	PerAlk1† 1H + 1S	5.27 4.44	4.69 3.26	70.99 0.04	11.09 bdl	0.81	1077±70 bdl	730±35 bdl	1462±199 79318±7932
E1†	IHPV	500	750	PerAlu1* 1H + 1S (pH 1)	3.39 2.79	4.52 2.19	69.90 na	14.52 na	1.39	1127±70 20±1	634±74 5±1	bdl na
F1†	IHPV	500	750	PerAlu1* 1H + 1S	3.23 1.75	4.36 1.37	69.28 na	14.27 na	1.42	1086±84 10±1	688±163 3±1	bdl na
A1	IHPV	200	850	PerAlu1* 1H + 1S (pH 1)	3.70 2.79	4.86 2.45	72.05 0.06	13.34 0.02	1.18	943±24 104±2	1240±79 38±1	1961±191 54088±5409
A2	IHPV	200	850	MetAlu1* 1H + 1S (pH 1)	3.53 2.31	4.81 2.23	72.46 0.01	11.98 bdl	1.09	713±84 5±1	1168±110 bdl	1407±225 48667±4867
A4	IHPV	200	850	PerAlk2* 1H + 1S (pH 1)	4.22 2.94	4.66 2.48	71.79 bdl	11.61 bdl	0.97	895±50 bdl	937±76 bdl	1655±251 56387±5639
A3	IHPV	200	850	PerAlk1* 1H + 1S (pH 1)	5.79 0.97	4.49 0.74	70.67 0.01	11.07 bdl	0.77	951±57 bdl	963±78 bdl	2814±402 59564±5956
V9	IHPV	200	950	PerAlu1† 1H + 1S (pH 1)	4.02 3.00	5.01 2.89	71.92 bdl	13.50 bdl	1.12	1042±38 96±1	571±26 22±1	2492±333 59609±5961
V10	IHPV	200	950	MetAlu1† 1H + 1S (pH 1)	3.68 3.2	4.58 73.16	72.33 bdl	11.81 bdl	1.07	1003±36 22±1	612±58 2±1	2238±546 60299±6030

Table 4.3 - continued from previous page

experimental conditions					analyses of run products								
run	tech.	P	T	starting materials	Na <sub>2</sub> O	K <sub>2</sub> O	SiO <sub>2</sub>	Al <sub>2</sub> O <sub>3</sub>	ASI	La	Y	Yb	Cl
p0.1cm		[MPa]	[°C]	[melt / fluid]	[wt. %]	[wt. %]	[wt. %]	[wt. %]		[ppm]	[ppm]	[ppm]	[ppm]
V12	IHPV	200	950	PerAlk2 <sup>†</sup> 1H + 1S (pH 1)	4.43 3.19	4.58 2.63	70.66 bdl	11.66 bdl	0.95	1035±34 bdl	574±33 bdl		2235±349 46958±4696
V11	IHPV	200	950	PerAlk1 <sup>†</sup> 1H + 1S (pH 1)	5.72 3.55	4.72 2.71	71.47 0.03	11.17 bdl	0.77	1075±46 bdl	812±36 bdl		3862±233 46774±4677
V19	IHPV	500	850	PerAlu1 <sup>†</sup> 1H + 1S (pH 1)	3.12 3.45	4.37 3.22	69.70 0.003	13.42 0.004	1.36	1046±37 20±1	560±24 2±1		710±248 53393±5339
V20	IHPV	500	850	MetAlu1 <sup>†</sup> 1H + 1S (pH 1)	3.12 3.06	4.33 2.82	72.78 0.002	12.08 0.004	1.23	735±46 8±1	400±54 bdl		610±337 48129±4813

\* / † – initial glass composition as described in Tab.4.1

na – not analysed

bdl – below detection limit

1H – 1m NaCl, 1S – 1m KCl

† – experiments done at Institut für Mineralogie, Leibniz Universität Hannover

ASI – Al<sub>2</sub>O<sub>3</sub> / (Na<sub>2</sub>O + K<sub>2</sub>O) in molesTable 4.4: Experimentally determined fluid–melt partition coefficients of Na, K, Ba, Cl, and D<sub>K</sub>/D<sub>Na</sub>.

experimental conditions				Fluid–melt partition coefficients				
run	P	T	ASI	D <sub>Na</sub>	D <sub>K</sub>	D <sub>K</sub> /D <sub>Na</sub>	D <sub>Ba</sub>	D <sub>Cl</sub>
	[MPa]	[°C]						
PerAlu2HB*	200	750	1.67	0.004	0.009	2.27	0.003±0.0002	nc
PerAlu1HB*	200	750	1.29	0.008	0.01	1.62	0.005±0.0003	nc
MetAlu1HB*	200	750	1.12	0.01	0.01	1.37	0.005±0.0002	nc
PerAlk2HB*	200	750	1.00	0.01	0.01	0.83	0.003±0.0001	nc
PerAlk1HB*	200	750	0.84	0.01	0.02	1.45	0.003±0.0001	19±3
PerAlu2LB	200	750	1.29	0.37	0.28	0.75	0.08±0.004	
PerAlu1LB	200	750	1.15	0.76	0.53	0.70	0.16±0.008	55±12
PerAluL3	200	750	1.21	0.64	0.44	0.68	0.20±0.01	28±5
MetAlu1LB	200	750	1.05	0.75	0.49	0.66	0.18±0.01	58±9
PerAlk2LB	200	750	0.96	0.71	0.54	0.76	0.06±0.002	44±7
PerAlk1LB	200	750	0.83	0.58	0.51	0.87	0.002±0.001	36±5
PerAlu2HP*	200	750	1.53	0.01	0.004	0.39	0.0003±0.0001	nc
PerAlu1HP*	200	750	1.38	0.004	0.001	0.37	0.0003±0.0001	nc
MetAlu1HP*	200	750	1.20	0.01	0.003	0.27	0.0003±0.0001	nc
PerAlk2HP*	200	750	1.05	0.01	0.005	0.61	0.0003±0.0001	nc
PerAlk1HP*	200	750	0.92	0.03	0.04	1.14	0.001±0.0001	nc
PerAlu2LPx	200	750	1.22	0.55	0.39	0.71	0.33±0.06	32±5
PerAlu1LP	200	750	1.20	0.70	0.51	0.73	0.17±0.01	71±21
MetAlu1LP	200	750	1.12	0.59	0.40	0.68	0.14±0.01	19±3
PerAlk2LP	200	750	1.02	0.65	0.48	0.73	0.05±0.003	37±6
PerAlk1LP	200	750	0.87	0.47	0.39	0.84	0.003±0.0001	18±3
PerAlu2HPi*	200	750	1.65	0.01	0.02	0.55	0.003±0.001	nc
PerAlu1HPi*	200	750	1.35	0.01	0.03	0.59	0.003±0.001	nc
MetAlu1HPi*	200	750	1.20	0.01	0.01	0.26	0.006±0.002	nc
PerAlk2HPi*	200	750	1.07	0.22	0.53	0.69	0.06±0.01	nc
PerAlk1HPi*	200	750	0.88	0.03	0.04	0.45	0.006±0.001	nc
PerAlu2LPi	200	750	1.28	0.42	0.29	0.70	0.21±0.06	24±4
PerAlu1LPi	200	750	1.15	0.64	0.47	0.73	0.44±0.14	45±7
MetAlu1LPi	200	750	1.06	0.68	0.44	0.64	0.52±0.22	51±9
PerAlk2LPi	200	750	1.02	0.52	0.35	0.67	0.08±0.02	29±5
PerAlk1LPi	200	750	0.88	0.42	0.30	0.72	0.01±0.002	18±3
MetAlu1HPi2*	200	750	1.17	0.02	0.01	0.51	0.004±0.001	nc
MetAlu1LPi2	200	750	1.07	0.82	0.55	0.67	0.55±0.17	68±7

nc – not calculated because element concentration in the fluid was below detection limit or was not analyzed

ASI – Al<sub>2</sub>O<sub>3</sub> / (Na<sub>2</sub>O + K<sub>2</sub>O) in moles\* - experiments using H<sub>2</sub>O as starting fluidTable 4.5: Experimentally determined fluid–melt partition coefficients of Na, K, La, Y, Cl, and D<sub>K</sub>/D<sub>Na</sub>.

experimental conditions					Fluid–melt partition coefficients						
run	technique	P	T	ASI	D <sub>Na</sub>	D <sub>K</sub>	D <sub>K</sub> /D <sub>Na</sub>	D <sub>La</sub>	D <sub>Y</sub>	D <sub>Yb</sub>	D <sub>Cl</sub>
		[MPa]	[°C]								
A1	EHPV	200	750	1.20	0.85	0.52	0.60±0.03	0.13±0.01		0.02±0.003	nc
A2	EHPV	200	750	1.06	0.62	0.37	0.60±0.03	0.013±0.002		0.006±0.001	nc
A3	EHPV	200	750	1.04	0.75	0.43	0.58±0.03	0.004±0.001		0.003±0.0004	nc
A4	EHPV	200	750	0.79	0.47	0.36	0.77±0.04	0.004±0.001		0.003±0.0008	nc
B1	EHPV	200	750	1.18	0.79	0.47	0.60±0.06	0.11±0.01	0.07±0.007		nc
B2	EHPV	200	750	1.07	0.63	0.35	0.55±0.05	0.026±0.005	0.10±0.10		nc
B4	EHPV	200	750	0.99	0.66	0.42	0.64±0.04	0.0002±0.00002	0.002±0.0002		nc
C1	EHPV	200	750	1.25	0.71	0.39	0.55±0.03	0.10±0.01		0.01±0.001	nc
C2	EHPV	200	750	1.13	0.80	0.48	0.60±0.04	0.004±0.001		nc	nc
C3	EHPV	200	750	0.83	0.54	0.46	0.85±0.03	0.002±0.0003		nc	nc
D1	EHPV	200	750	1.21	0.66	0.39	0.60±0.03	0.07±0.005	0.04±0.004		nc
D3	EHPV	200	750	0.83	0.62	0.46	0.75±0.04	0.001±0.0003	0.002±0.0007		nc
A1	RQ	200	750	1.16	0.55	0.37	0.67±0.10	0.02±0.005		0.004±0.0005	34±4
B0	RQ	200	750	1.29	0.68	0.50	0.73±0.15	0.13±0.01	0.07±0.003		29±4
B1	RQ	200	750	1.15	0.50	0.33	0.67±0.11	0.015±0.004	0.006±0.001		34±5
C1	RQ	200	750	1.11	0.41	0.30	0.71±0.11	0.06±0.02		0.06±0.001	34±8
D0	RQ	200	750	1.32	0.70	0.48	0.69±0.05	0.13±0.01	0.06±0.004		39±6
D1	RQ	200	750	1.17	0.47	0.30	0.63±0.09	0.04±0.007	0.01±0.003		34±6
E1 <sup>‡</sup>	IHPV	500	750	1.39	0.82	0.48	0.59±0.05	0.017±0.001		nc	nc
F1 <sup>‡</sup>	IHPV	500	750	1.42	0.54	0.31	0.58±0.04	0.01±0.001		nc	nc
A1	IHPV	200	850	1.18	0.76	0.50	0.67±0.03	0.13±0.006		nc	28±3
A2	IHPV	200	850	1.09	0.66	0.46	0.71±0.04	0.007±0.001		nc	35±6
V9	IHPV	200	950	1.12	0.75	0.58	0.77±0.03	0.09±0.003	nc		24±3
V10	IHPV	200	950	1.07	0.89	0.69	0.78±0.04	0.02±0.001	nc		27±7
V19	IHPV	500	850	1.36	1.10	0.74	0.67±0.04	0.02±0.001	nc		75±26
V20	IHPV	500	850	1.23	0.98	0.65	0.66±0.04	0.01±0.001	nc		79±44

nc – not calculated because element concentration in the fluid was below detection limit or was not analyzed

ASI – Al<sub>2</sub>O<sub>3</sub> / (Na<sub>2</sub>O + K<sub>2</sub>O) in moles\* – experiments using H<sub>2</sub>O as starting fluid

‡ – experiments done at Institut für Mineralogie, Leibniz Universität Hannover

Table 4.6: Experimental conditions and results of the HDAC experiments at 750 °C. Concentrations of Ba, La and Y in the fluid were analysed *in-situ* using SR- $\mu$ XRF, the glasses were analysed after quench using EMP.

sample	A	B	C	D	E	F	G	H
Cell	HDACG	HDAC2	HDAC2	HDACG	HDACG	HDAC2	HDACG	HDAC2
initial glass composition <sup>†</sup>	PerAlu	PerAlu	MetAlu	PerAlu	MetAlu	MetAlu	PerAlu	MetAlu
$P_{\text{exp}}$ at $T_{\text{exp}} = 750^\circ\text{C}$ [MPa]	830	900	250	500	700	750	200	300
$m$ (NaCl + KCl)	6	4.1	1.5	0	6	1.7	2.4	6
$m$ HCl	0.06	0.04	0.01	0	0.06	0.01	0.02	0.06
wt.% (NaCl + KCl)	26	19.3	8	0	26	9	12.1	26
wt.% glass (initial)	23	25	28	29	29	35	30	33
$\rho_{\text{fluid}}$ [ $\text{g}/\text{cm}^3$ ]	1.06	0.991	0.621	0.712	0.985	0.903	0.588	0.848
$T_m$ [ $^\circ\text{C}$ ]	-0.3	-12.8	-4.4	—	-3.1*	-5.0	-7.05	13.2*
$T_H$ [ $^\circ\text{C}$ ]	216	218	391	289	288	234	443	419
$c_{\text{Ba}}^f$ [ppm]	292±42	313±4102	60±6	49±4	363±22	116±34	224±33	365±33
$c_{\text{Ba}}^m$ [ppm]	963±156	1389±161	1940±98	1813±123	459±116	1883±304	1841±134	1091±134
$c_{\text{La}}^f$ [ppm]	62±9	50±6	bdl	17±13	52±9	22±6	41±10	19±6
$c_{\text{La}}^m$ [ppm]	540±217	396±61	408±340	569±76	426±74	336±120	937±91	726±147
$c_{\text{Y}}^f$ [ppm]	30±30	25±25	22±22	20±20	39±30	25±25	33±30	22±22
$c_{\text{Y}}^m$ [ppm]	320±23	59±39	bdl	188±23	bdl	100±19	706±78	246±108
$D_{\text{Ba}}^f/m$	0.30±0.06	0.23±0.08	0.03±0.003	0.03±0.003	0.79±0.21	0.06±0.02	0.12±0.02	0.33±0.05
$D_{\text{La}}^f/m$	0.11±0.05	0.13±0.02	nc	0.03±0.02	0.12±0.03	0.07±0.03	0.04±0.01	0.03±0.01
$D_{\text{Y}}^f/m$	0.09±0.09	0.43±0.51	nc	0.11±0.11	nc	0.25±0.25	0.05±0.04	0.09±0.1
wt.% SiO <sub>2</sub>	63.58	61.99	70.60	67.16	67.58	68.88	63.44	70.06
wt.% Al <sub>2</sub> O <sub>3</sub>	17.21	16.58	13.04	16.58	13.90	13.28	15.90	12.83
wt.% Na <sub>2</sub> O	4.04	3.52	3.59	4.92	2.95	3.09	5.63	3.07
wt.% K <sub>2</sub> O	8.37	8.29	6.72	4.00	7.56	7.01	7.78	7.49
ASI	1.10	1.12	0.99	1.33	1.07	1.05	0.90	0.97

<sup>†</sup> – initial glass composition as described in Tab. 4.1

$m$  – molality

$T_m$  – freezing point depression determined by cryometry

$T_H$  – Homogenisation temperature measured after collection of XRF spectra at  $T_{\text{exp}}=750^\circ\text{C}$

$f$  – fluid,  $m$  – melt

\* – melting point of Hydrohalite

bdl – below detection limit

nc – not calculated

ASI –  $\text{Al}_2\text{O}_3/(\text{Na}_2\text{O} + \text{K}_2\text{O})$  in moles



## Chapter 5

# Discussion and conclusions

The goal of this thesis was the experimental investigation of the partitioning of petrogenetically important trace elements between aqueous fluids and silicate melts over a wide range of PTx conditions. This resulted in a comprehensive dataset of fluid–melt partition coefficients particularly for Rb, Sr, and Ba, and in addition for La, Y, and Yb. An essential part of this thesis was utilization of different experimental approaches to evaluate their applicability to fluid–melt partitioning experiments. The presented partition coefficients are always based on analyses of both, fluid and melt. In all experiments, the composition of the melt was measured after quenching using EMP analysis. In the case of quenched experiments, the fluid was analyzed after quenching using ICP-OES and IC. In the in-situ approach, the trace element content of the fluid was determined directly at elevated PT conditions using SR- $\mu$ XRF.

The results of this study on fluid–melt partitioning of Rb, Sr, Ba, La, Yb, and Y can be summarized in the following five points. (1) These trace elements show a preference for the melt ( $D^{f/m} < 1$ ) at all studied conditions. (2) The  $D^{f/m}$  of these elements are up to two orders of magnitude higher in experiments using chloridic solutions compared to experiments with H<sub>2</sub>O as starting solution. (3) For chloridic fluids, partition coefficients of Sr, Ba, La, Y, and Yb show a clear dependence on the melt composition expressed as ASI. The  $D^{f/m}$  of these elements are distinctly lower for peralkaline melt than for peraluminous melts. (4) Partition coefficients obtained from quenched experiments display quench rate–related differences. (5) For H<sub>2</sub>O as starting solution, distinctly higher fluid–melt partitioning data were obtained in the cases of in-situ experiments compared to those from comparable quench runs. In the following paragraphs, I will discuss the results of this thesis with regard to the effects of different experimental and analytical techniques, quench rates, pressure, temperature, salinity of the fluid and melt composition on fluid–melt partition coefficients. Then, I will compare the results to literature data. This includes a short discussion of the differences in the light of experimental difficulties. Furthermore, I will discuss the consequences for the trace element signature of granitic melts and exsolved magmatic fluids.

### 1. *Effect of experimental and analytical method (in-situ vs. quench):*

A major goal of this thesis consisted in the refinement an existing method to measure trace element contents in an aqueous fluid equilibrated with silicate melt directly at elevated pressures and temperatures. The presented manuscripts show that this objective

was successfully attained. An important advantage of the in-situ approach consists in the direct observation of the kinetics of trace element equilibration between aqueous fluid and coexisting silicate melt. At present, no other experimental technique can provide such data on trace element behavior in fluid–melt systems. The data presented in Chapter 2 clearly demonstrate that the equilibration between aqueous fluid and melt is rapid and can therefore affect partition coefficients obtained in quenched experiments. The comparison of partition coefficients obtained with different experimental and analytical methods shows distinctly higher  $D^{f/m}$ , particularly for non-chloridic solutions, if in-situ analysis of the aqueous fluid was used. Back reactions between fluid and melt upon cooling were identified as one cause of these differences. In the case of Cl-bearing solutions, partition coefficients from both methods are in fairly good agreement. This is likely due to the higher trace element concentrations which make the effect of back reactions less significant.

Nevertheless, the here determined "in-situ partition coefficients" are still not truly in-situ because the melt had to be analyzed after quench. The equilibration experiments presented in Chapter 2 clearly show that back reactions between aqueous fluids and silicate melts occur. Rubidium concentrations in the aqueous fluid slightly decrease with decreasing temperature and pressure, whereas Sr contents increase at the same time. Thus, obtained in-situ fluid–melt partition coefficients of Rb represent minimum values, and  $D_{Sr}^{f/m}$  are maximum values. As stated in the previous paragraph, these partition coefficients should be considerably closer to the true value and more reliable than most partition coefficients based only on analyses after quench. For chloridic fluids, one can reasonably assume that the "in-situ fluid–melt partition coefficients" are do not deviate much from the true value because the observed changes of trace element concentrations in the aqueous fluid upon cooling were relatively small.

2. *Quench rate–related differences:*

Quenched experiments were performed in hydrothermal autoclaves with rapid and slow quench rates. The results presented in Chapters 3 and 4 show that quench rates affect partition coefficients of the studied trace elements. For experiments with H<sub>2</sub>O as starting fluid, the comparison between rapidly and slowly quenched experiments reveals distinct differences. For example, rapidly quenched fluids contain up to 20 times more Rb and have Sr concentrations below the limit of detection compared to slowly quenched solutions. In the case of Cl-bearing fluids and peralkaline melts, rapid-quenched experiments yield, likewise, much lower Sr concentrations in the fluid. The effect of the back reactions is more obvious at low trace element concentrations in the fluid. For higher trace element contents in the fluid, concentration shifts due to re-equilibration remain within error. All in all, these findings can be explained with fast re-equilibration between melt and fluid upon cooling and are thus consistent with the observations made for Rb and Sr using the in-situ approach.

3. *Effects of temperature and pressure:*

Quenched experiments were performed at 750, 850, and 950°C and 200 or 500 MPa. In this PT range, obtained fluid–melt partition coefficients of all studied trace elements



show only small or indiscernible variation. Therefore, it can be concluded that temperature and pressure have no strong effect on fluid–melt partitioning of the studied trace elements. This result is likely due the fact that these PT conditions are well below that of the critical curve for haplogranite-water. That is, they are located at the steep portions of the solvus, where compositions of the coexisting phases change little with P and T. This interpretation is supported by in-situ experiments performed at 750°C and pressures up to 1 GPa. In these experiments, fluid–melt partition coefficients increase slightly with pressure, at least in the case of Rb and Sr. This behavior correlates with the increased solubility of melt in the aqueous fluid, which results in a smaller chemical contrast between the phases. This also suggests that trace elements form significant amounts of complexes with melt components in the aqueous phase at higher pressures.

4. *Effect of fluid composition:*

For all studied elements, fluid–melt partition coefficients obtained from experiments with Cl-bearing solutions are one to two orders of magnitude higher than those at comparable conditions using H<sub>2</sub>O as starting fluid. The results of the in-situ experiments also indicate that partition coefficients, at least of Rb, Sr, Ba, and La, increase slightly with the initial salinity of the aqueous fluid. This finding is confirmed by results of additionally performed experiments in the system albite-quartz (Appendix A). Here, fluid–melt partition coefficients of Rb and Sr increase slightly and linearly with initial salinity of the fluid to maximum values of 0.4 at initial NaCl concentrations in the fluid of 3 or 4 *m*. Therefore, the data presented here underscore the key role of the Cl<sup>−</sup> activity for the partitioning of most trace elements between aqueous fluids and silicate melts. For the studies trace elements, one can reasonably assume that the presence of Cl<sup>−</sup> will result in the formation of significant amounts of chlorine complexes in the fluid. At higher salinities, however, the observed changes in the partitioning coefficients with Cl<sup>−</sup> concentration are often smaller than reported in the literature, i.e., the studied trace elements still preferred the melt.

5. *Effect of melt composition:*

The results presented in Chapter 3 and 4 point to a strong effect of melt composition on fluid–melt partitioning of Sr, Ba, La, Yb, and Y. In experiments with chloridic solutions, partition coefficients of these elements show a distinct increase with the ASI of the melt. This dependence on melt composition is either related to changes in the speciation in the aqueous fluid, or to changes in the incorporation of these elements in the melt, or to both factors. Dissolution of peralkaline melt in aqueous fluids will result in an enhanced release of Na<sup>+</sup> and K<sup>+</sup> into the fluid compared to the release from peraluminous melts. Therefore, the activities of Cl<sup>−</sup> and OH<sup>−</sup> will decrease more strongly in fluids equilibrated with peralkaline melts. Thus, less Cl<sup>−</sup> and OH<sup>−</sup> is available in these fluids to form complexes with Sr, Ba, La, Yb, and Y. This explanation is supported by the basic quench pH of the fluids in experiments with peralkaline melts reported in Chapter 3. Because of the increasing ion association with temperature, the basic quench pH implies the presence of significant quantities of NaOH<sup>0</sup> and KOH<sup>0</sup> complexes in the fluid at the run conditions.

In conclusion, this thesis presents the first systematic dataset for Rb, Sr, Ba, La, Yb, and Y partitioning between aqueous fluid and haplogranitic melt as function of fluid and melt composition, temperature, and pressure. All investigated trace elements show a preference for the melt over the studied PTx range, independent of the experimental and analytical technique even at high salinities. This finding differs from many other experimental studies, e.g., Webster et al. (1989), Bai and Koster van Groos (1999), Reed et al. (2000) who report a preference for the fluid particularly at higher salinities. The deviations of the results of this thesis from those of other experimental studies are probably mostly related to different analytical methods, particularly for the determination of the element content in the fluid. The sampling and analysis of the quenched fluid is the most difficult part because of large intrinsic uncertainties caused by, e.g., back reactions between fluid and melt, the tendency of fluid to unmix, or precipitation of solutes during cooling. Moreover, the fluid amount is small in these experiments. Therefore, a small contamination from tiny crystals or melt droplets due to incomplete separation before analysis can result in much too high element concentrations in the aqueous fluid particularly for trace elements. The determination of trace elements contents in the fluid via mass balance (Webster et al., 1989) is also associated with substantial errors, because this approach requires modeling of undetermined parameters, e.g., H<sub>2</sub>O solubility in the silicate melt and dissolution of melt components in the aqueous fluid. In addition, this method requires a very accurate determination of trace element contents in the initial glass as well as in the quenched melt because otherwise, small trace element contents in the fluid cannot be calculated without significant errors. Finally, the mass balance method does not include additional phases that might form in the fluid during the experiment, but such phases can incorporate large amounts of the studied trace elements and will lead to an overestimation of partition coefficients.

The presented fluid–melt partition coefficients of Rb and Y are in good agreement with data from natural cogenetic fluid and melt inclusions (e.g., Audétat and Pettko, 2003, Rickers et al., 2006, Zajacz et al., 2008, Audétat et al., 2008). For Sr, Ba, La, and Yb, data from natural samples are either not available or are associated with large errors due to concentrations in the fluid that are close to or below the detection limit. A probable explanation for this is that Sr and Ba strongly partition into granite forming minerals, and that the rare earth elements fractionate into accessory phases, e.g., monazite during progressive crystallization. Modeling of the behavior of Sr during the evolution of a granitic system shows that the fractionation of strontium between chloridic fluids and aluminous melts is weaker than the fractionation between feldspars and melts (Chapter 3). That is, crystallization of Sr-bearing minerals will result in a depletion of Sr in the residual melt. Barium and strontium are divalent large-ion lithophile elements, and thus, show a geochemically similar behavior also with regard to fluid–melt partitioning (cp. Chapters 3 and 4). In contrast to Sr, barium also substitutes for potassium in micas. Therefore, one can reasonably assume a similar or even stronger effect of progressive granite crystallization on barium concentrations in the residual melt. In addition, the weight fraction of exsolved aqueous fluids is generally small in granites (2 to 3 wt.%). Therefore, the concentration of divalent LILE in residual granitic melts is mainly controlled by the abundance of and LILE incorporation into crystallizing phases. The obtained fluid–melt partition coefficients of divalent LILE are strongly affected by the composition of the silicate melt. Aqueous fluids reacting with peralkaline silicate melts have little ability to alter divalent LILE concentra-

tion in the melt, independent of the salinity of the fluid. In comparison, chloridic fluids are able to more efficiently leach these elements from peraluminous silicate melts ( $ASI \geq 1$ ). This suggests a slightly higher enrichment of the large-ion lithophile elements in peralkaline melts, and thus, much higher concentrations of these elements can be expected in minerals crystallized from peralkaline melts. This is consistent with data from natural samples, which show higher concentrations of Ba and Sr feldspars in peralkaline granites compared to those from granitoids with peraluminous bulk compositions (e.g., Mahood and Hildreth, 1983, Stix and Gorton, 1990, Ewart and Griffin, 1994, Bea et al., 1994). In contrast, the Rubidium fractionation in granitic systems between fluids and melts and crystals and melts shows no dependence on melt composition (e.g., White et al., 2003, and data presented in Chapter 3). Therefore, the Rb/Sr or Rb/Ba ratios in the melt are also primarily controlled by crystal–melt partitioning, and can thus be used to obtain information on the stage of evolution and particularly on the degree of fractional crystallization in a granitic system.

Fluid–melt partitioning of La, Yb, and Y depends both on fluid and melt composition (Chapter 4). The rare earth elements are characterized by a similar geochemical behavior. Therefore, it can be inferred that fluid–melt partitioning of all REE will depend in a similar manner on these parameters. The results presented here show that the preference of rare earth elements for the melt is much more pronounced than that of the LILE, particularly for peralkaline compositions. In contrast to large ion lithophile elements, the REE do not fractionate into granite forming minerals, except for  $\text{Eu}^{2+}$  which substitutes for Ca in plagioclase under reducing conditions. Therefore, exsolution of an aqueous fluid and fractional crystallization of feldspars, quartz, and mica will result in an enrichment of the REE in the residual melt in the absence of accessory phases. This behavior will be much more pronounced in the case of a peralkaline melt than for peraluminous compositions. REE enrichment in silicate melts will result to the formation of REE bearing phases as observed in the in-situ experiments (Chapter 4). This conclusion is in agreement with geological observations on REE ore deposits which are commonly associated with peralkaline granites (e.g., Kovalenko et al., 1995, Williams-Jones et al., 2000, Tassinari et al., 2001). The stronger affinity of REE to peralkaline melts is also consistent with their structural role in melts, where they can be considered as network modifiers due to their large ionic radius and thus high coordination number. Therefore, rare earth elements will rather coordinate with non-bridging oxygens of depolymerized melts (i.e.,  $ASI \leq 1$ ) (e.g., Ponader and Brown, 1989, Anderson et al., 1998, Park et al., 2002, Marchi et al., 2005). Rare earth element ore deposits are mainly linked to the formation of e.g., parisite and bastnaesite. Our experiments also show, for hydrothermal REE mineralizations derived from alkali granites, complexing of the REE must take place with other ligands than  $\text{Cl}^-$  to explain the enrichment in the fluid phase. These anions are probably  $\text{CO}_3^{2-}$ ,  $\text{HCO}_3^-$ ,  $\text{SO}_4^{2-}$  and  $\text{F}^-$ , and fluids rich in these components are mainly of external origin (e.g., Bea, 1996, Gieré, 1996, Williams-Jones et al., 2000). All in all, the concentration of REE in residual granitic melts is also strongly controlled by the nature and abundance of crystalline phases.

In conclusion, fluid–melt partitioning of large ion lithophile and rare earth elements were studied as function of pressure, temperature, fluid salinity, and melt composition using different experimental and analytical methods. The presented results extend the current data for Rb and Sr, and provide new insight into the fluid–melt partition behavior of Ba, La, Yb, and Y, par-

ticularly the dependencies on PTx conditions. The ability to perform in-situ determinations of trace element concentrations in aqueous fluids equilibrated with silicate melts is an important improvement in the study of fluid–melt interactions. The presented results of this thesis enhance to knowledge on the role of fluids and their interaction with magma in the late stages of the evolution of magmatic complexes and also during the formation of magmatic-hydrothermal ore deposits.

## Chapter 6

# Outlook

The results of this thesis highlight the importance of an in-situ method to study fluid–melt systems. In the following paragraphs will discuss further improvements of the in-situ technique. Firstly, I present some possibilities and their limitations to quantify trace element contents in aqueous fluids and silicate melts at elevated PT conditions. And secondly, I will show first results of an ongoing spectroscopic study on the complexation of Sr in the aqueous fluid equilibrated with silicate melts at high PT conditions.

### 6.1 Further improvements of the in-situ method

In-situ fluid–melt partition coefficients obtained in this study are based on the analysis of trace element contents of the aqueous fluid at elevated PT conditions and of the quenched melt. As described before, back reactions occur between the coexisting aqueous fluid and the silicate melt upon cooling. Although the observed changes of trace element contents in the aqueous fluid are small, one need to determine the trace element concentrations at high pressures and temperatures in both phases to avoid quench effects. At present, the melt droplets cannot be analyzed in-situ with confidence due to coexcitation of the aqueous fluid around the droplets. Even if the incident beam is focused, a portion of these X-rays will be scattered in the diamond anvil, and a contribution from coexcited fluid to the XRF signal is therefore inevitable. Nevertheless, two improvements can be made to obtain completely in-situ fluid–melt partition coefficients.

1. At present, the bulk trace element concentration is not known in these experiments. That is due to the small amount of trace element doped glass used in in-situ experiments, and to small heterogeneities of the trace element concentrations of the initial glass. One can determine the bulk trace element concentration in the system by XRF measurements in a one phase silicate fluid. Therefore, the trace element doped glass should be completely dissolved in the aqueous fluid at a temperature that is roughly 50°C above the experimental temperature. This requires smaller glass amounts than used in these experiments. After the collection of XRF spectra of the one phase fluid, the temperature is shifted to the experimental temperature. Upon cooling, the one phase fluid unmix to aqueous fluid and silicate melt, and XRF spectra of the aqueous fluid can be taken. This

technique has two main sources of error. Firstly, one has to know the density of the one phase fluid, and secondly one needs to determine the fluid/melt ratio at P and T where spectra are collected. The latter information can be most probably achieved by mapping of the sample chamber. The density of the one phase silicate fluid can be calculated using the known initial fluid/melt mass ratio and changes of the sample volume due to creeping of the recess material upon heating. All in all, one would have to test, if this is an applicable method, and how large the errors are in comparison to the method used within this study.

2. The other possibility includes the analysis of coexisting fluid and melt at elevated pressures and temperatures, but requires comprehensive changes of the hydrothermal diamond-anvil cell. The cell has to be constructed that the diamonds are perpendicular to the incoming beam, and both diamonds need to have a recess. If so, one can use gravitational differences of fluid and melt because the melt will fall in the lower recess. The most critical point is that the melt has to fill the lower recess completely. This may become difficult because of the surface tension of the silicate melt and the wetting properties of diamond.

## 6.2 Strontium complexation in fluids equilibrated with silicate melts at high PT conditions

In Chapter 3 a distinct effect of melt and fluid composition on the Sr fluid–melt partition coefficient is discussed. This dependence on melt composition is either related to changes in the speciation in the aqueous fluid, or to changes in the incorporation of these elements in the melt, or to both parameters. Kohn et al. (1990) studied structural environments of Sr in dry and hydrous silicate glasses using extended X-ray absorption fine structure (EXAFS) spectroscopy. For strontium, no changes in the first-shell geometry in these glasses are observed. Thus, they infer that the melt composition does not play a direct role in controlling the melt compositional dependence of trace element partition coefficients. Based on the results of Kohn et al. (1990) we can not explain the effect of melt composition on  $D^{f/m}$  presented in Chapter 3. So far, statements on the complexation of (trace) elements in aqueous fluids equilibrated with silicate melts are based on correlations between trace element contents or fluid–melt partition coefficients and anion concentrations of the quenched fluid and the derivation of an appropriate exchange equilibria. Very often these equilibria are difficult to define because in many cases several possibilities for element species and element complexes may exist, particularly in the fluid. Furthermore, the activities of many components are unknown, which makes the definition of such exchange equilibria more difficult. Spectroscopic investigations may provide new insights to the nature of element complexes at high PT conditions. X-ray absorption near edge structure (XANES) analysis is sensitive to the local geometry and atomic position of the absorbing atom and its oxidation state. In comparison to EXAFS scans, XANES spectra are simpler to measure, the observed features are more intense and concentrated in smaller energy region, and there are less problems with diffraction peaks from the diamond anvil of a HDAC. Furthermore, EXAFS analysis could be afflicted by multiple electron excitations (MEE), e.g., in the case of Sr, the simultaneous excitation of 1s4s, 1s3d, and 1s3p electrons (e.g.,

D'Angelo et al., 1996).

X-ray absorption techniques have been widely used to study the local structure of trace elements in silicate glasses and melts (e.g., Ponader and Brown, 1989, Kohn et al., 1990, Farges et al., 2001a,b, Wilke et al., 2002, 2007) and aqueous solutions (e.g., D'Angelo et al., 1996, Seward et al., 1999, Mayanovic et al., 2007a,b, 2009a,b). At present, no attempt has been made to study the complexation of strontium or any other trace element in aqueous fluids in equilibrium with silicate melts as a function of fluid and melt composition.

In an ongoing study, the complexation of Sr in aqueous fluids coexisting with silicate melts is analyzed directly at high pressures and temperatures. This is realized using a HDAC and X-ray absorption near edge structure (XANES) analysis. The experiments were done at ID26 (ESRF, Grenoble, France). XANES spectra are collected using an emission spectrometer with Bragg crystals that spectrally analyzes the fluorescence from the sample and reflects it onto a photon detector.

Figure 6.1 show Sr XANES spectra of peralkaline and peraluminous glasses. The spectra show distinct differences in the pre-edge region and different positions of the first EXAFS maximum, which are 16163 eV for the peralkaline glass and 16155 for the peraluminous composition. The position of the white line differs slightly from 16119.2 eV for the peralkaline glass to 16119.7 eV for the peraluminous composition. The white line peak of the peralkaline glass is smaller and broader compared to that of the peraluminous glass. These variations in the spectra clearly prove that the incorporation of Sr in silicate melts strongly depends on the ASI of the melt. Therefore, the XANES data are different to the results of Kohn et al. (1990), who may not be able to resolve these structures because they collected EXAFS spectra, and studied also different glass compositions. In addition, comparison of the results reported by D'Angelo et al. (1996) with the data by Kohn et al. (1990) show that the EXAFS spectra presented by Kohn et al. (1990) were affected by multiple electron excitations.

Sample spectra were collected in one phase silicate-rich fluids at  $\geq 750^\circ\text{C}$  and various pressures. The starting material for the silicate-rich fluids consist of an aqueous solution,  $\text{H}_2\text{O}$  or 1 *m* (Na,K)Cl + 0.01 *m* HCl, and a peralkaline or peraluminous glass chip. The dimensions were chosen such that the glass amount was  $\sim 10$  wt.% of the desired bulk composition. This small amount is necessary because the melt should be completely dissolve in the aqueous fluid at run conditions due to a relatively large beam in this case. Three different fluid-melt systems were studied, peralkaline melt +  $\text{H}_2\text{O}$ , peralkaline melt + chloridic solution, and peraluminous melt + chloridic solution. The three Sr XANES spectra are presented in Fig. 6.2. The collected spectra show distinct differences in the pre-edge region and on the high energy side of the white line. The position of the white line peak also depends on the system composition, and is 16119.3 eV for the chloride-free peralkaline fluid, 16118.7 eV for the  $\text{Cl}^-$  bearing peralkaline solution, and 16119.4 eV for the  $\text{Cl}^-$  bearing peraluminous fluid. The shape of the white lines distinctly differ in spectra of peralkaline aqueous solutions with or without chlorine, and also in chloridic solutions containing dissolved peralkaline or peraluminous melt. The peak of the peralkaline chloridic fluid is broader and smaller compared to those of the other solutions. The position of the first EXAFS maximums are also variable, and are shifted to higher values in peralkaline solutions. All in all, the obtained XANES spectra of the three studied silicate solutions point to different local geometries around strontium as a function of melt and fluid

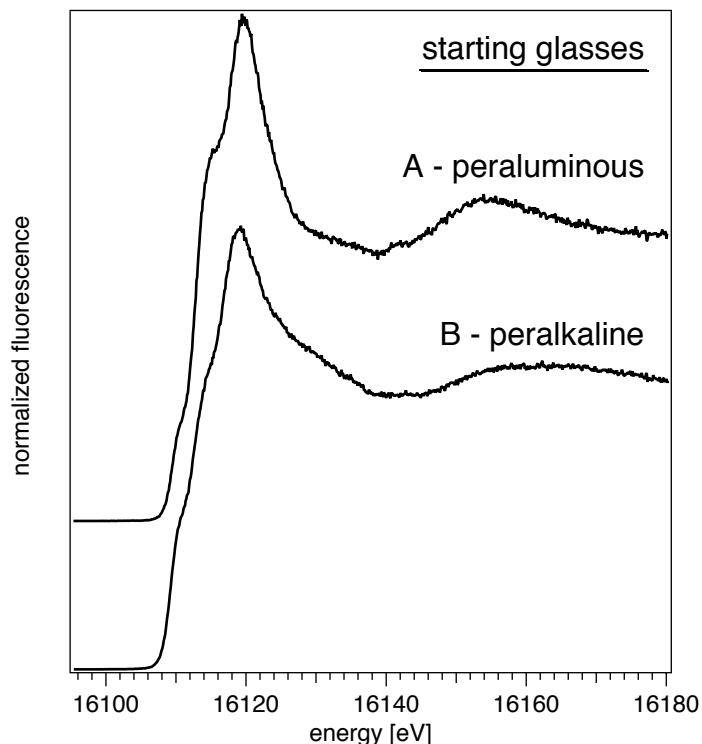


Figure 6.1: Strontium XANES spectra of peralkaline and peraluminous starting glasses.

composition. For chloridic silicate solutions, one can reasonably assume that more than one Sr complex will form dependent on melt composition because of distinct differences in XANES spectra of peralkaline and peraluminous chloridic solutions. The spectra of the peralkaline solution is very similar to that of the peralkaline glass, whereas the spectra of the peraluminous solution does not look like that of the peraluminous glass. The peraluminous solution also do not resemble the spectra of a  $\text{SrCl}_2$  standard solution measured at  $600^\circ\text{C}$ . This is in contradiction to interpretations of quench data using metaluminous or mildly peraluminous starting glasses (Bai and Koster van Groos, 1999, Webster et al., 1989) who suggested that Sr will form mainly chlorine complexes in the fluid at high pressures and temperatures.

The data analysis of these spectra is still in progress. Quantitative information from the sample spectra will be obtained in two steps. Firstly, measured XANES spectra of crystalline references and standard solutions are simulated. Secondly, the spectra from the samples are compared to these modeled reference spectra to gain information on the local geometry around Sr.



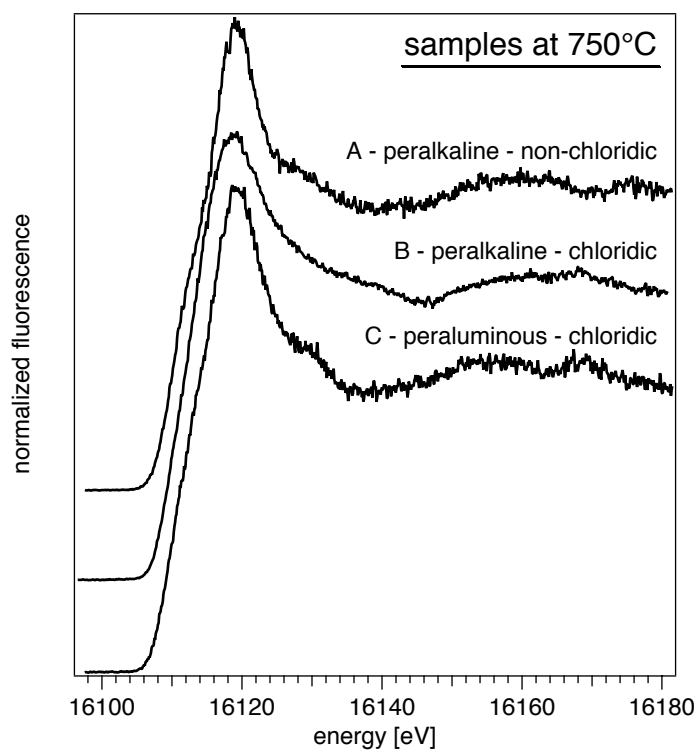


Figure 6.2: Strontium XANES spectra of peralkaline and peraluminous silicate fluids.

# References

- Adam, J., Green, T. H., Sie, S. H., and Ryan, C. G. (1997). Trace element partitioning between aqueous fluids, silicate melts and minerals. *Eur. J. Mineral.*, 9:569–584.
- Akella, J., Vaidya, S. N., and Kennedy, G. C. (1969). Melting of Sodium Chloride at Pressures to 65 kbar. *Physical Review*, 185(3):1135–1140.
- Albarede, F. (1975). Some trace element relationships among liquid and solid phases in the course of the fractional crystallization of magmas. *Geochimica et Cosmochimica Acta*, 40:667–673.
- Anderson, G. M. and Burnham, C. W. (1965). The solubility of quartz in supercritical water. *American Journal of Science*, 263:494–511.
- Anderson, R., Brennan, T., Mountjoy, G., Newport, R. J., and Saunders, G. A. (1998). An EXAFS study of rare-earth phosphate glasses in the vicinity of the metaphosphate composition. *Journal of Non-Crystalline Solids*, 232-234:286–292.
- Asimov, P. and Ghiorso, M. (1998). Algorithmic modifications extending MELTS to calculate subsolidus phase relations. *American Mineralogist*, 83:1127–1131.
- Atherton, M. P. (1993). Granite magmatism. *Journal of the Geological Society*, 150:1009–1023.
- Audétat, A. and Keppler, H. (2005). Solubility of rutile in subduction zone fluids, as determined by experiments in the hydrothermal diamond anvil cell. *Earth and Planetary Science Letters*, 232:393–402.
- Audétat, A. and Pettke, T. (2003). The magmatic-hydrothermal evolution of two barren granites: A melt and fluid inclusion study of the Rito del Medio and Canada Pinabete plutons in northern New Mexico (USA). *Geochimica et Cosmochimica Acta*, 67(1):97–121.
- Audétat, A., Pettke, T., Heinrich, C. A., and Bodnar, B. J. (2008). The Composition of Magmatic-Hydrothermal Fluids in Barren and Mineralized Intrusions. *Economic Geology*, 103(5):877–905.
- Ayers, J. C. and Eggler, D. H. (1995). Partitioning of elements between silicate melt and H<sub>2</sub>O-NaCl fluids at 1.5 and 2.0 GPa pressure: Implications for mantle metasomatism. *Geochimica et Cosmochimica Acta*, 59(20):4237–4246.

- Bai, T. B. and Koster van Groos, A. F. (1999). The distribution of Na, K, Rb, Sr, Al, Ge, Cu, W, Mo, La, and Ce between granitic melts and coexisting aqueous fluids. *Geochimica et Cosmochimica Acta*, 63(7/8):1117–1131.
- Bandura, A. and Lvov, S. (2006). The ionization constant of water over a wide range of temperatures and densities. *Journal of Physical and Chemical Reference Data*, 35:15–30.
- Bassett, W. A., Anderson, A. J., Mayanovic, R. A., and Chou, I.-M. (2000). Modified hydrothermal diamond anvil cells for XAFS analyses of elements with low energy absorption edges in aqueous solutions at sub- and supercritical conditions. *Zeitschrift für Kristallographie*, 215:711–717.
- Bassett, W. A., Shen, A. H., Bucknum, M., and Chou, I.-M. (1993). A new diamond anvil cell for hydrothermal studies to 2.5 GPa and from 190 to 1200°C. *Review of scientific instruments*, 64:2340–2345.
- Bau, M. and Dulski, P. (1995). Comparative study of yttrium and rare-earth element behaviours in fluorine-rich hydrothermal fluids. *Contributions to Mineralogy and Petrology*, 119:213–223.
- Bea, F. (1996). Residence of REE, Y, Th and U in Granites and Grustal Protoliths; Implications for the Chemistry of Crustal Melts. *Journal of Petrology*, 37(3):521–552.
- Bea, F., Pereira, M. D., and Stroh, A. (1994). Mineral/leucosome trace-element partitioning in a peraluminous migmatite (a laser ablation-ICP-MS study). *Chemical Geology*, 117:291–312.
- Bédard, J. H. (2006). Trace element partitioning in plagioclase feldspar. *Geochimica et Cosmochimica Acta*, 70:3717–3742.
- Behrens, H. and Jantos, N. (2001). The effect of anhydrous composition on water solubility in granitic melts. *American Mineralogist*, 86:14–20.
- Best, M. G. (2003). *Igneous and Metamorphic Petrology*. Blackwell.
- Blundy, J., Robinson, J., and Wood, B. (1998). Heavy REE are compatible in clinopyroxene on the spinel lherzolite solidus. *Earth and Planetary Science Letters*, 160:493–504.
- Blundy, J. D. and Wood, B. J. (1991). Crystal-chemical controls on the partitioning of Sr and Ba between plagioclase feldspar, silicate melts, and hydrothermal solutions. *Geochimica et Cosmochimica Acta*, 55:193–209.
- Bodnar, R. J. (2003). *Fluid Inclusions: Analysis and Interpretation*, volume 32, chapter Introduction to aqueous fluid systems., pages 81–99. Mineralogical Association of Canada.
- Bodnar, R. J. and Vityk, M. O. (1994). *Interpretation of microthermometric data for H<sub>2</sub>O-NaCl fluid inclusions. Fluid Inclusions in Minerals: Methods and Applications*, pages 117–130. Virginia Tech.
- Borchert, M., Wilke, M., Schmidt, C., and Rickers, K. (2009). Partitioning and equilibration of Rb and Sr between silicate melts and aqueous fluids. *Chemical Geology*, 259:39–47.

## REFERENCES

---

- Borchert, M., Wilke, M., Schmidt, C., and Rickers, K. (2010). Rb and Sr partitioning between haplogranitic melts and aqueous solutions. *Geochimica et Cosmochimica Acta*, 74:1057–1076.
- Brunetti, A., del Rio, M. S., Golosio, B., Simionovici, A., and Somogyi, A. (2004). A library for X-ray-matter interaction cross sections for X-ray fluorescence applications. *Spectrochimica Acta*, 59:1725–1731.
- Bureau, H. and Keppler, H. (1999). Complete miscibility between silicate melts and hydrous fluids in the upper mantle: experimental evidence and geochemical implications. *Earth and Planetary Science Letters*, 165:187–196.
- Bureau, H., Ménez, B., Khodja, H., Daudin, L., Gallien, J.-P., Massare, D., Shaw, C., and Métrich, N. (2003). The partitioning of barium and lead between silicate melts and aqueous fluids at high pressures and temperatures. *Nuclear Instruments and Methods in Physics Research*, 210:434–440.
- Bureau, H., Ménez, B., Malavergne, V., Somogyi, A., Simionovici, A., Massare, D., Khodja, H., Daudin, L., Gallien, J.-P., Shaw, C., and Bonnin-Mosbah, M. (2007). In situ mapping of high-pressure fluids using hydrothermal diamond anvil cells. *High Pressure Research*, 27(2):235–247.
- Burnham, C. W. (1967). *Hydrothermal fluids at the magmatic stage*. In: *Geochemistry of Hydrothermal Ore Deposits*, pages 34–67. John Wiley, New York.
- Burnham, C. W. (1979). Magmas and hydrothermal fluids. In Barnes, H. L., editor, *Geochemistry of hydrothermal ore deposits.*, pages 71–136.
- Burnham, C. W. and Jahns, R. H. (1962). A method for determining the solubility of water in silicate melts. *American Journal of Science*, 260:721–745.
- Candela, P. A. and Holland, H. D. (1984). The partitioning of copper and molybdenum between silicate melts and aqueous fluids. *Geochimica et Cosmochimica Acta*, 48:373–380.
- Candela, P. A. and Piccoli, P. M. (1995). *Model ore-metal partitioning from melts into vapor and vapor/brine mixtures*. In: *Magmas, Fluids, and Ore Deposits*, volume 23, pages 101–127. Mineralogical Association of Canada Short Course.
- Carroll, M. R. and Holloway, J. R. (1994). *Volatiles in magmas*. *Reviews in Mineralogy*, volume 30, page 517 p. Mineralogical Society of America.
- Carron, J.-P. and Lagache, M. (1980). Étude expérimentale du fractionnement des éléments Rb, Cs, Sr et Ba entre feldspaths alcalins, solutions hydrothermales et liquides silicatés dans le système Q.Ab.Or.H<sub>2</sub>O à 2 kbar entre 700 to 800°C. *Bull. Mineral.*, 103:571–578.
- Chappell, B. W. and White, A. J. R. (1974). Two contrasting granite types. *Pac Geol*, 8:173–174.

- Christiansen, E. H., Bikun, J. V., Sheridan, M. F., and Burt, D. M. (1984). Geochemical evolution of topaz rhyolites from the Thomas Range and Spor Mountain, Utah. *American Mineralogist*, 69:223–236.
- Cullers, R. L., Medaris, L. G., and Haskin, L. A. (1973). Experimental studies of the distribution of rare earths as trace elements among silicate minerals and liquids and water. *Geochimica et Cosmochimica Acta*, 37:1499–1512.
- Currie, K. L. (1968). On the solubility of albite in supercritical water in the range 400 to 600°C and 750 to 3500 bars. *American Journal of Science*, 266:321–341.
- D'Angelo, P., Nolting, H.-F., and Pavel, N. V. (1996). Evidence for multielectron resonances at the Sr K edge. *Physical Review A*, 53(2):798–805.
- Driesner, T. (2007). The system H<sub>2</sub>O-NaCl. Part II: Correlations for molar volume, enthalpy, and isobaric heat capacity from 0 to 1000°C, 1 to 5000 bar, and 0 to 1 X<sub>NaCl</sub>. *Geochimica et Cosmochimica Acta*, 71:4902–4919.
- Ewart, A. and Griffin, W. L. (1994). Application of Proton-Microprobe Data to Trace-Element Partitioning in Volcanic-Rocks. *Chemical Geology*, 117:251–284.
- Farges, F., Brown Jr, G. E., Petit, P.-E., and Munoz, M. (2001a). Transition elements in water-bearing silicate glasses/melts. Part I. A high-resolution and anharmonic analysis of Ni coordination environments in crystals, glasses, and melts. *Geochimica et Cosmochimica Acta*, 65(10):1665–1678.
- Farges, F., Munoz, M., Siewert, R., Malavergne, V., Brown Jr, G. E., Behrens, H., Nowak, M., and Petit, P.-E. (2001b). Transition elements in water-bearing silicate glasses/melts. Part II. Ni in water-bearing glasses. *Geochimica et Cosmochimica Acta*, 65(10):1679–1693.
- Flynn, R. T. and Burnham, C. W. (1978). An experimental determination of rare earth partition coefficients between a chloride containing vapor phase and silicate melts. *Geochimica et Cosmochimica Acta*, 42:685–701.
- Frank, M. R., Candela, P. A., and Piccoli, P. M. (2003). Alkali exchange equilibria between a silicate melt and coexisting magmatic volatile phase: An experimental study at 800°C and MPa. *Geochimica et Cosmochimica Acta*, 67(7):1415–1427.
- Ghiorso, M. and Sack, R. (1995). Chemical mass transfer in magmatic processes. IV. A revised and internally consistent thermodynamic model for the interpolation and extrapolation of liquid-solid equilibria in magmatic systems at elevated temperatures and pressures. *Contrib Mineralogy Petrology*, 119:197–212.
- Gieré, R. (1996). *Formation of rare earth minerals in hydrothermal systems. In: Rare earth minerals: Chemistry, origin and ore deposits*, chapter 5, pages 105–150. Chapman & Hall.
- Green, T. H. (1980). Island arc and continent-building magmatism - A review of petrogenic models based on experimental petrology and geochemistry. *Tectonophysics*, 63:367–385.

## REFERENCES

---

- Green, T. H. and Pearson, N. J. (1983). Effect of pressure on rare earth element partition coefficients in common magmas. *Nature*, 305:414–416.
- Haar, L., Gallagher, J., and Kell, G. (1984). *Steam tables*; chapter Thermodynamic and transport properties and computer programs for vapor and liquid states of water in SI units, page 320. Hemisphere Pub. Corp., Washington, D.C.
- Hall, D. L., Sterner, S. M., and Bodnar, R. J. (1988). Freezing Point depression of NaCl-KCl-H<sub>2</sub>O Solutions. *Economic Geology*, 83:197–202.
- Haller, M. and Knöchel, A. (1996). X-ray fluorescence analysis using synchrotron radiation- (SRXRF). *Journal of Trace Microprobe Technics*, 14:461–488.
- Hanley, J. J., Pettke, T., Mungall, J. E., and Spooner, E. T. C. (2005). The solubility of platinum and gold in NaCl brines at 1.5 kbar, 600 to 800°C: A laser ablation ICP-MS pilot study of synthetic fluid inclusions. *Geochimica et Cosmochimica Acta*, 69(10):2593–2611.
- Hanson, G. N. (1980). Rare earth elements in petrogenetic studies of igneous systems. *Annual Reviews Earth Planetary Sciences*, 8:371–406.
- Hedenquist, J. W. and Lowenstern, J. B. (1994). The role of magmas in the formation of hydrothermal ore deposits. *Nature*, 370:519–527.
- Helgeson, H. (1964). *Complexing and Hydrothermal Ore Deposition*. Pergamon, New York.
- Holland, H. D. (1972). Granites, Solutions, and Base Metal Deposits. *Economic Geology*, 67(3):281–301.
- Holtz, F., Behrens, H., Dingwell, D. B., and Johannes, W. (1995). H<sub>2</sub>O solubility in haplogranitic melts: Compositional, pressure, and temperature dependence. *American Mineralogist*, 80:94–108.
- Holtz, F., Behrens, H., Dingwell, D. B., and Taylor, R. P. (1992). Water solubility in aluminosilicate melts of haplogranite composition at 2 kbar. *Chemical Geology*, 96:289–302.
- Holtz, F., Roux, J., Behrens, H., and Pichavant, M. (2000). Water solubility in silica and quartzofeldspathic melts. *American Journal of Science*, 85:682–686.
- Huang, R. and Bilderback, D. H. (2006). Single-bounce monochromators for focusing synchrotron radiation: modeling, measurements and theoretical limits. *Journal of Synchrotron Radiation*, 13:74–84.
- Hui, H., Zhang, Y., Xu, Z., Del Gaudio, P., and Behrens, H. (2009). Pressure dependence of viscosity of rhyolitic melts. *Geochimica et Cosmochimica Acta*, 73:3680–3693.
- Icenhower, J. and London, D. (1995). An experimental study of element partitioning among biotite, muscovite, and coexisting peraluminous silicic melt at 200 MPa (H<sub>2</sub>O). *American Mineralogist*, 80:1229–1251.

- Icenhower, J. and London, D. (1996). Experimental partitioning of Rb, Cs, Sr, and Ba between alkali feldspar and peraluminous melt. *American Mineralogist*, 81:719–734.
- Jochum, K. P., Dingwell, D. B., Rocholl, A., Stoll, B., Hofmann, A. W., and many others (2000). The preparation and preliminary characterisation of eight geological MPI-DING reference glasses for in-situ microanalysis. *Geostandards Newsletter*, 24(1):87–133.
- Jochum, K. P., Stoll, B., Herwig, K., Willbold, M., Hofmann, A. W., and many others (2006). MPI-DING reference glasses for in situ microanalysis: New reference values for element concentrations and isotope ratios. *Geochemistry, Geophysics, Geosystems*, 7(2):1–44.
- Johannes, W. and Holtz, F. (1996). *Petrogenesis an Experimental Petrology of Granitic Rocks*. Springer, Berlin.
- Keppler, H. and Wyllie, P. J. (1990). Role of fluids in transport and fractionation of uranium and thorium in magmatic processes. *Nature*, 348:531–533.
- Keppler, H. and Wyllie, P. J. (1991). Partitioning of Cu, Sn, Mo, W, U, and Th between melt and aqueous fluid in the systems haplogranite-H<sub>2</sub>O-HCl and haplogranite-H<sub>2</sub>O-HF. *Contributions to Mineralogy and Petrology*, 109:139–150.
- Koepke, J. and Behrens, H. (2001). Trace element diffusion in andesitic melts: an application of synchrotron X-ray fluorescence analysis. *Geochimica et Cosmochimica Acta*, 65:1481–1489.
- Kohn, S. C., Charnock, J. M., Henderson, C. M. B., and Greaves, G. N. (1990). The structural environments of trace elements in dry and hydrous silicate glasses; a manganese and strontium K-edge X-ray absorption spectroscopic study. *Contributions to Mineralogy Petrology*, 105:359–368.
- Kovalenko, V. I., Tsaryeva, G. M., Goreglyad, A. V., Yarmolyuk, V. V., Troitsky, V. A., Hervig, R. L., and Farmer, G. L. (1995). The peralkaline granite-related Khaldzan-Buregтей rare metal (Zr, Nb, REE) deposit, western Mongolia. *Economic Geology*, 90:530–547.
- Leeman, W. and Phelps, D. (1981). Partitioning of rare earths and other trace elements between sanidine and coexisting volcanic glass. *Journal of Geophysical Research*, 86:10193–10199.
- London, D. (2005). *Geochemistry of alkali and alkaline earth elements in ore-forming granites, pegmatites, and rhyolites*. In: *Rare-element geochemistry of ore deposits*, volume 17, pages 17–43. Geological association of Canada Short Course Handbook.
- London, D., Hervig, R. L., and Morgan, G. B. (1988). Melt-vapor solubilities and elemental partitioning in peraluminous granite-pegmatite systems: experimental results with Macusani glass at MPa. *Contributions to Mineralogy and Petrology*, 99:360–373.
- Mahood, G. A. and Hildreth, E. W. (1983). Large partition coefficients for trace elements in high-silica rhyolites. *Geochimica et Cosmochimica Acta*, 47:11–30.

## REFERENCES

---

- Manning, C. E. (1994). The solubility of quartz in H<sub>2</sub>O in the lower crust and upper mantle. *Geochimica et Cosmochimica Acta*, 58:4831–4839.
- Manning, C. E. (2004). The chemistry of subduction-zone fluids. *Earth and Planetary Science Letters*, 223:1–16.
- Manning, C. E. (2007). Solubility of corundum + kyanite in H<sub>2</sub>O at 700°C and 10 kbar: evidence for Al-Si complexing at high pressure and temperature. *Geofluids*, 7:258–269.
- Manning, C. E., Wilke, M., Schmidt, C., and Cauzid, J. (2008). Rutile solubility in albite-H<sub>2</sub>O and Na<sub>2</sub>Si<sub>3</sub>O<sub>7</sub>-H<sub>2</sub>O at high temperatures and pressures by in-situ synchrotron radiation micro-XRF. *Earth and Planetary Science Letters*, 272:730–737.
- Marchi, J., Morais, D. S., Schneider, J., Bressiani, J. C., and Bressiani, A. H. A. (2005). Characterization of rare earth aluminosilicate glasses. *Journal of Non-Crystalline Solids*, 351:863–868.
- Mayanovic, R. A., Anderson, A. J., Bassett, W. A., and Chou, I.-M. (2007a). On the formation and structure of rare-earth element complexes in aqueous solutions under hydrothermal conditions with new data on gadolinium aqua and chloro complexes. *Chemical Geology*, 239:266–283.
- Mayanovic, R. A., Anderson, A. J., Bassett, W. A., and Chou, I.-M. (2007b). Synchrotron X-ray spectroscopy of Eu/HNO<sub>3</sub> aqueous solutions at high temperatures and pressures and Nb-bearing silicate melt phases coexisting with hydrothermal fluids using a modified hydrothermal diamond anvil cell and rail assembly. *Review of scientific instruments*, 78:1–9.
- Mayanovic, R. A., Anderson, A. J., Bassett, W. A., and Chou, I.-M. (2009a). Steric hindrance and the enhanced stability of light rare-earth elements in hydrothermal fluids. *American Mineralogist*, 94:1487–1490.
- Mayanovic, R. A., Anderson, A. J., Bassett, W. A., and Chou, I.-M. (2009b). The structure and stability of aqueous rare-earth elements in hydrothermal fluids: New results on neodymium(III) aqua and chloroaqua complexes in aqueous solutions to 500°C and 520 MPa. *Chemical Geology*, 259:30–38.
- Metrich, N. and Rutherford, M. J. (1992). Experimental study of chlorine behavior in hydrous silicic melts. *Geochimica et Cosmochimica Acta*, 56:607–616.
- Morgan VI, G. B. and London, D. (1996). Optimizing the electron microprobe analysis of hydrous alkali aluminosilicate glasses. *American Mineralogist*, 81:1176–1185.
- Morgan VI, G. B. and London, D. (2005). Effect of current density on the electron microprobe analysis of alkali aluminosilicate glasses. *American Mineralogist*, 90:1131–1138.
- Muñoz, M., Bureau, H., Malavergne, V., Ménez, B., Wilke, M., Schmidt, C., Simionovici, A., Somogyi, A., and Farges, F. (2005). In situ speciation of nickel in hydrous melts exposed to extreme conditions. *Physica Scripta*, 115:921–922.



- Murray, M. M. and Rogers, J. W. (1973). Distribution of rubidium and strontium in the potassium feldspar of two granite batholiths. *Geochemical Journal*, 6:117–130.
- Mysen, B. O. and Acton, M. (1999). Water in H<sub>2</sub>O-saturated magma-fluid systems: Solubility behavior in K<sub>2</sub>O-Al<sub>2</sub>O<sub>3</sub>-SiO<sub>2</sub>-H<sub>2</sub>O to 2.0 GPa and 1300°C. *Geochimica et Cosmochimica Acta*, 63:3799–3815.
- Mysen, B. O. and Armstrong, L. (2002). Solubility behavior of alkali aluminosilicate components in aqueous fluids and silicate melts at high pressure and temperature. *Geochimica et Cosmochimica Acta*, 66(12):2287–2297.
- Nash, W. P. and Crecraft, H. R. (1985). Partition coefficients for trace elements in silicic magmas. *Geochimica et Cosmochimica Acta*, 49:2309–2322.
- Newton, R. C. and Manning, C. E. (2000). Quartz solubility in H<sub>2</sub>O-NaCl and H<sub>2</sub>O-CO<sub>2</sub> solutions at deep crust-upper mantle pressures and temperatures: 2-15 kbar and 500-900°C. *Geochimica et Cosmochimica Acta*, 64(17):2993–3005.
- Pailat, O., Elphick, S. C., and Brown, W. L. (1992). The solubility of water in NaAlSi<sub>3</sub>O<sub>8</sub> melts: a re-examination of Ab-H<sub>2</sub>O phase relationships and critical behaviour at high pressures. *Contributions to Mineralogy Petrology*, 112:490–500.
- Park, B., Li, H., and Corrales, L. R. (2002). Molecular dynamics simulation of La<sub>2</sub>O<sub>3</sub>-Na<sub>2</sub>O-SiO<sub>2</sub> glasses. I. The structural role of La<sup>3+</sup> cations. *Journal of Non-Crystalline Solids*, 297:220–238.
- Pearce, J. G., Perkins, W. T., Westgate, J. A., Gorton, M. P., Jackson, S. E., Neal, C. R., and Chenery, S. P. (1997). A compilation of new and published major and trace element data for NIST SRM 610 and NIST SRM 612 glass reference materials. *Geostandards Newsletter*, 21(1):115–144.
- Philpotts, A. R. (1990). *Principles of igneous and metamorphic petrology*. Prentice Hall, London.
- Philpotts, A. R. and Ague, J. J. (2009). *Principles of igneous and metamorphic petrology*. Cambridge University Press, 2nd edition.
- Pichavant, M., Holtz, F., and McMillan, P. F. (1992). Phase relations and compositional dependence of H<sub>2</sub>O solubility in quartz-feldspar melts. *Chemical Geology*, 96:303–319.
- Ponader, C. W. and Brown, C. E. (1989). Rare earth elements in silicate glass/melt systems: II. Interactions of La, Gd, and Yb with halogens. *Geochimica et Cosmochimica Acta*, 53:2905–2914.
- Reed, M. J., Candela, P. A., and Piccoli, P. M. (2000). The distribution of rare earth elements between monzogranitic melt and the aqueous volatile phase in experimental investigations at 800°C and 200 MPa. *Contributions to Mineralogy and Petrology*, 140:251–262.

## REFERENCES

---

- Ren, M., Parker, D. F., and White, J. C. (2003). Partitioning of Sr, Ba, Rb, Y, and REE between plagioclase and peraluminous silicic magma. *American Mineralogist*, 88:1091–1103.
- Rickers, K., Thomas, R., and Heinrich, W. (2006). The behavior of trace elements during the chemical evolution of the H<sub>2</sub>O-, B-, and F-rich granite-pegmatite-hydrothermal system at Ehrenfriedersdorf, Germany: a SXRF study of melt and fluid inclusions. *Mineralium Deposita*, 41:229–245.
- Robb, L. (2005). *Introduction to ore-forming processes*. Blackwell Publishing, Oxford.
- Roedder, E. (1984). *Reviews in Mineralogy 12: Fluid Inclusions*. Mineralogical Society of America.
- Roedder, E. and Bodnar, R. J. (1997). *Fluid inclusion studies of hydrothermal or deposits*. In: *Geochemistry of Hydrothermal Ore Deposits*. John Wiley & Sons, New York.
- Sanchez-Valle, C., Martinez, I., Daniel, I., Philippot, P., Bohic, S., and Simionovici, A. (2003). Dissolution of strontianite at high P-T conditions: An in-situ synchrotron X-ray fluorescence study. *American Mineralogist*, 88:978–985.
- Schäfer, B., Frischknecht, R., Günther, D., and Dingwell, D. B. (1999). Determination of trace-element partitioning between fluid and melt using LA-ICP-MS analysis of synthetic fluid inclusions in glass. *European Journal of Mineralogy*, 11:415–426.
- Schmidt, C. and Rickers, K. (2003). In-situ determination of mineral solubilities in fluids using a hydrothermal diamond-anvil cell and SR-XRF: Solubility of AgCl in water. *American Mineralogist*, 88:288–292.
- Schmidt, C., Rickers, K., Bilderback, D. H., and Huang, R. (2007). In situ synchrotron-radiation XRF study of REE phosphate dissolution in aqueous fluids to 800°C. *Lithos*, 95:87–102.
- Seward, T. M., Henderson, C. M. B., Charnock, J. M., and Driesner, T. (1999). An EXAFS study of solvation and ion pairing in aqueous strontium solutions to 300°C. *Geochimica et Cosmochimica Acta*, 63(16):2409–2418.
- Shen, A. H., Bassett, W. A., and Chou, I.-M. (1993). The alpha-beta quartz transition at high temperatures and pressures in a diamond-anvil cell by laser interferometry. *American Mineralogist*, 78:694–698.
- Shmulovich, K., Graham, C., and Yardley, B. (2001). Quartz, albite and diopside solubilities in H<sub>2</sub>O-NaCl and H<sub>2</sub>O-CO<sub>2</sub> fluids at 0.5-0.9 GPa. *Contrib Mineralogy Petrology*, 141:95–108.
- Simon, A. C., Frank, M. R., Pettke, T., Candela, P. A., Piccoli, P. M., Heinrich, C. A., and Glascock, M. (2007). An evaluation of synthetic fluid inclusions for the purpose of trapping equilibrated, coexisting, immiscible fluid phases at magmatic conditions. *American Mineralogist*, 92:124–138.
- Small, H., Stevens, T. S., and Bauman, W. C. (1975). Novel ion exchange chromatographic method using conductimetric detection. *Analytical Chemistry*, 47:1801–1809.

- Solé, V. A., Papillon, E., Cotte, M., Walter, P., and Susini, J. (2007). A multiplatform code for the analysis of energy-dispersive X-Ray fluorescence spectra. *Spectrochimica Acta*, B 62:63–68.
- Stalder, R., Ulmer, P., Thompson, A. B., and Günther, D. (2000). Experimental approach to constrain second critical end points in fluid/silicate systems: Near-solidus fluids and melts in the system albite-H<sub>2</sub>O. *American Mineralogist*, 85:68–77.
- Stebbins, J. F. and Du, L.-S. (2002). Chloride ion sites in silicate and aluminosilicate glasses: A preliminary study by <sup>35</sup>Cl solid-state NMR. *American Mineralogist*, 87:359–363.
- Stix, J. and Gorton, M. P. (1990). Variations in trace element partition coefficients in sanidine in the Cerro Toledo Rhyolite, Jemez Mountains, New Mexico - Effects of composition, temperature, and volatiles. *Geochimica et Cosmochimica Acta*, 54:2697–2708.
- Streck, M. J. and Grunder, A. L. (1997). Compositional gradients and gaps in high-silica rhyolites of the Rattlesnake Tuff, Oregon. *Journal of Petrology*, 38(1):133–163.
- Tagirov, B. R., Zotov, A. V., and Akinfiev, N. N. (1997). Experimental study of dissociation of HCl from 350 to 500°C and from 500 to 2500 bars: Thermodynamic properties of HCl<sub>(aq)</sub><sup>o</sup>. *Geochimica et Cosmochimica Acta*, 61(20):4267–4280.
- Tassinari, M. M. L., Kahn, H., and Ratti, G. (2001). Process mineralogy studies of Corrego Do Garimpo REE ore, Catalao-I alkaline complex, Goias, Brasil. *Minerals Engineering*, 14(12):1609–1617.
- Tuttle, O. F. and Bowen, N. L. (1958). *Origin of granite in the light of experimental studies in the system NaAlSi<sub>3</sub>O<sub>8</sub>–KAlSi<sub>3</sub>O<sub>8</sub>–SiO<sub>2</sub>–H<sub>2</sub>O*. The Geological Society of America.
- Urabe, T. (1985). Aluminous granite as a source magma of hydrothermal ore deposits: an experimental study. *Economic Geology*, 80(1):148–157.
- Watson, E. B. (1979). Zircon saturation in felsic liquids: Experimental results and applications to trace element geochemistry. *Contributions to Mineralogy and Petrology*, 70:407–419.
- Webster, J. D. (1992a). Fluid-melt interactions involving Cl-rich granites: Experimental study from 2 to 8 kbar. *Geochimica et Cosmochimica Acta*, 56:659–678.
- Webster, J. D. (1992b). Water solubility and chlorine partitioning in Cl-rich granitic systems: Effects of melt composition at 2 kbar and 800°C. *Geochimica et Cosmochimica Acta*, 56:679–687.
- Webster, J. D. (1997a). Chloride solubility in felsic melts and the role of chloride in magmatic degassing. *Journal of Petrology*, 38:1793–1807.
- Webster, J. D. (1997b). Exsolution of magmatic volatile phases from Cl-enriched mineralizing granitic magmas and implications for ore metal transport. *Geochimica et Cosmochimica Acta*, 61:1017–1029.

## REFERENCES

---

- Webster, J. D. and De Vivo, B. (2002). Experimental and modeled solubilities of chlorine in aluminosilicate melts, consequences of magma evolution, and implications for exsolution of hydrous chloride melt at Mt. Somma-Vesuvius. *American Mineralogist*, 87:1046–1061.
- Webster, J. D., Holloway, J. R., and Hervig, R. L. (1989). Partitioning of Lithophile trace elements between H<sub>2</sub>O and H<sub>2</sub>O+CO<sub>2</sub> fluids and topaz rhyolite melt. *Economic Geology*, 84:116–134.
- White, J. C. (2003). Trace-element partitioning between alkali feldspar and peralkalic quartz trachyte to rhyolite magma. Part II: Empirical equations for calculating trace-element partition coefficients of large-ion lithophile, high field-strength, and rare-earth elements. *American Mineralogist*, 88:330–337.
- White, J. C., Holt, G. S., Parker, D. F., and Ren, M. (2003). Trace-element partitioning between alkali feldspar and peralkalic quartz trachyte to rhyolite magma. Part I: Systematics of trace-element partitioning. *American Mineralogist*, 88:316–329.
- Whitney, J. A. (1988). The origin of granite: The role and source of water in the evolution of granitic magmas. *The geological Society of America Bulletin*, 100:1886–1897.
- Wilke, M., Behrens, H., Burkhard, D. J. M., and Rossano, S. (2002). The oxidation state of iron in silicic melt at 500 MPa water pressure. *Chemical Geology*, 189:55–67.
- Wilke, M., Farges, F., Partzsch, G. M., Schmidt, C., and Behrens, H. (2007). Speciation of Fe in silicate glasses and melts by in-situ XANES spectroscopy. *American Mineralogist*, 92:44–56.
- Williams-Jones, A. E., Sampson, I. M., and Olivo, G. R. (2000). The genesis of hydrothermal fluorite-REE deposits in the Gallinas mountains, New Mexico. *Economic Geology*, 95:327–342.
- Winter, J. D. (2001). *An Introduction to Igneous and Metamorphic Petrology*. Prentice Hall, New Jersey.
- Wolf, A. V., Brown, M. G., and Prentiss, P. G. (1981). *Concentrative properties of aqueous solutions: conversion tables*. In: Weast, R.C. (Ed.), *CRC Handbook of Chemistry and Physics*, pages D198–D247. CRC Press.
- Xiong, Y. and Wood, S. (2002). Experimental determination of the hydrothermal solubility of ReS<sub>2</sub> and the Re-ReO<sub>2</sub> buffer assemblage and transport of rhenium under supercritical conditions. *Geochemical Transactions*, 3:1–10.
- Yamashita, S. (1999). Experimental study of the effect of temperature on water solubility in natural rhyolite melt to 100 MPa. *Journal of Petrology*, 40(10).
- Zajacz, Z., Halter, W. E., Pettke, T., and Guillong, M. (2008). Determination of fluid/melt partition coefficients by LA-ICPMS analysis of co-existing fluid and silicate melt inclusions: Controls on element partitioning. *Geochimica et Cosmochimica Acta*, 72:2169–2197.

## Appendix A

# Additional fluid–melt partitioning data - the system albite-quartz

Fluid–melt partition coefficients of Rb and Sr were also determined between the end member composition albite-quartz (AQ) and various NaCl-bearing solutions at 750°C and 200 MPa. These experiments were performed to test if the behavior of Rb and Sr vary significantly, if the system is reduced by one component (in this case K) which means a reduction in the degree of freedom as determined by the Gibb's phase rule  $F = 2 + C - \Phi$ , where C are number of components and  $\Phi$  refers to the number of present phases. Furthermore, these additional experiments are used to evaluate the effect of  $\text{Cl}^-$  concentration on Rb and Sr partitioning which was not studied in detail in the system albite-orthoclase-quartz. Therefore, we choose two starting compositions, AQ1 starting glass is more enriched in the albite component, while AQ2 is more  $\text{SiO}_2$  rich (cp. Tab. A.1). The starting AQ glasses were doped with ~2500 ppm Rb or Sr. A detailed description of the glass preparation can be found in Chapter 2.2.1. The solutions were produced from distilled de-ionized water and analytical grade powders of NaCl. The molality of the aqueous fluids varied from 1 to 4 *m* NaCl. Rapid or slow quenched experiments were conducted in externally heated cold-seal pressure vessels using  $\text{H}_2\text{O}$  as pressure medium, and for a duration of 120 hours. A detailed description of the preparation of starting materials and samples, and experimental setup can be found in chapters 3.2.1 and 3.2.2.

Table A.1: Composition of AQ starting glasses from EMP analyses and normative composition based on the components albite, quartz and corundum. TE - trace element as indicated by sample name.

	$\text{SiO}_2$ [wt.%]	$\text{Al}_2\text{O}_3$ [wt.%]	$\text{Na}_2\text{O}$ [wt.%]	ASI	TE [ppm]	normative composition
AQ1_Rb	76.98	15.36	7.66	1.22	2609±203	$\text{Ab}_{64.81}\text{QZ}_{32.42} + \text{C}_{2.76}$
AQ1_Sr	77.38	15.19	7.43	1.24	2517±256	$\text{Ab}_{62.86}\text{QZ}_{34.16} + \text{C}_{2.97}$
AQ2_Rb	82.04	12.03	5.93	1.23	3070±329	$\text{Ab}_{50.16}\text{QZ}_{47.53} + \text{C}_{2.28}$
AQ2_Sr	82.18	11.90	5.91	1.23	2899±329	$\text{Ab}_{49.98}\text{QZ}_{47.81} + \text{C}_{2.2}$

Table A.2: Analytical data and determined fluid–melt partition coefficients of Na, Rb, Sr, and Cl from experiments at 750°C and 200 MPa. For each run, the first line of the analyses refers to the quenched glass and second line to the quenched fluid.

experimental conditions	starting materials				analyses of run products				partition coefficients		
	method	SiO <sub>2</sub> [wt %]	Al <sub>2</sub> O <sub>3</sub> [wt %]	Na <sub>2</sub> O [wt %]	Rb [ppm]	Sr [ppm]	ASI	Na	Rb	Sr	
SK1_1	SQ	75.23	11.91	3.01	1653±246	nd	2.40	0.27±0.05	0.07±0.01	nd	
					118±4	nd					
SK1_2	SQ	77.74	12.85	6.47	2513±341	nd	1.21	0.36±0.01	0.13±0.02	nd	
					293±4	nd					
SK1_3	SQ	76.51	13.05	6.57	1869±263	nd	1.21	0.70±0.02	0.25±0.03	nd	
					476±12	nd					
SK1_4	SQ	78.19	12.37	6.69	1740±265	nd	1.12	0.77±0.09	0.29±0.05	nd	
					511±15	nd					
SK2_1	SQ	77.92	11.43	5.93	2517±265	nd	1.19	0.35±0.01	0.12±0.01	nd	
					305±6	nd					
SK2_2	SQ	76.77	10.92	6.39	2374±367	nd	1.04	0.44±0.01	0.17±0.03	nd	
					411±3	nd					
SK2_3	SQ	77.99	11.40	5.89	2099±309	nd	1.18	0.41±0.01	0.12±0.02	nd	
					282±3	nd					
SK2_4	SQ	78.28	11.66	6.10	2070±309	nd	1.16	0.94±0.03	0.26±0.04	nd	
					536±4	nd					
SL1_1	SQ	76.57	12.82	6.50	nd	652±306	1.20	0.16±0.01	nd	nc	
					nd	nd					
SL1_2	SQ	75.43	12.88	6.66	nd	689±360	1.18	0.50±0.02	nd	0.04±0.02	
					nd	nd					
SL1_3	SQ	76.11	13.33	7.18	nd	1045±494	1.13	0.64±0.05	nd	0.01±0.00	
					nd	nd					
SL1_4	SQ	75.35	12.37	6.61	nd	621±321	1.16	0.55±0.02	nd	0.03±0.01	
					nd	nd					
SL2_1	SQ	77.40	11.39	5.74	nd	2162±315	1.21	0.19±0.01	nd	0.03±0.00	
					nd	nd					
SL2_2	SQ	77.91	11.33	5.77	nd	2118±333	1.19	0.43±0.01	nd	0.10±0.02	
					nd	nd					
SL2_3	SQ	76.86	11.43	5.71	nd	1876±332	1.22	0.66±0.02	nd	0.18±0.03	
					nd	nd					
SL2_4	SQ	78.92	11.67	6.10	nd	1807±318	1.16	0.98±0.05	nd	0.32±0.06	
					nd	387±3					
RQK2_1	RQ	76.85	11.20	5.69	2087±158	nd	1.20	0.32±0.03	0.11±0.01	nd	
					223±22	nd					
RQK2_2	RQ	77.48	11.16	5.66	1891±186	nd	1.16	0.45±0.05	0.16±0.02	nd	
					386±31	nd					
RQK2_3	RQ	77.38	11.17	5.70	1663±182	nd	1.19	0.42±0.02	0.14±0.01	nd	
					236±5	nd					
RQK2_4	RQ	77.13	11.14	5.90	1660±193	nd	1.15	1.29±0.05	0.41±0.05	nd	
					688±20	nd					
RQL2_1	RQ	78.14	11.10	5.62	nd	2031±238	1.16	0.17±0.01	nd	0.02±0.002	
					nd	40±1					
RQL2_2	RQ	77.21	11.06	5.66	nd	1877±217	1.19	0.37±0.02	nd	0.13±0.02	
					nd	241±5					
RQL2_3	RQ	76.04	10.96	6.27	nd	1706±230	1.06	0.91±0.03	nd	0.36±0.05	
					nd	610±20					
RQL2_4	RQ	75.56	10.85	6.13	nd	1563±238	1.08	0.78±0.03	nd	0.32±0.05	
					nd	502±18					

The experimental conditions, the composition of glasses and fluids after quenching, and the determined fluid–melt partition coefficients of Rb, Sr, and Na are listed in Table A.2. The fluid–melt partition coefficients of Rb, Sr and Na are shown in Figs. A.1.1 to A.2.2.

In Fig. A.1.1 fluid–melt partition coefficients of Rb, Sr, and Na are compared for experiments with rapid and slow quench rates. The data show a relatively good agreement although Rb and Sr show a tendency to higher partition coefficients obtained from rapid quenched experiments. In contrast, no clear trend can be found in the case of Na.

The dependence of fluid–melt partition coefficients of Na, Rb, and Sr on the initial salinity of the fluid is illustrated in Fig. A.1.2. In all experiments, except one, partition coefficients are smaller than one, and therefore, show a preference for the melt even at high fluid salinity. For all elements, partition coefficients increase with increasing salinity of the fluid. This increase is much more pronounced in the case of Na than for Rb and Sr which show  $D^{f/m}$  smaller than 0.4 using 3 or 4 *m* NaCl solutions. Nevertheless, Na partition coefficients show strong scattering that is more pronounced at higher fluid salinities, and is independent of the melt composition.

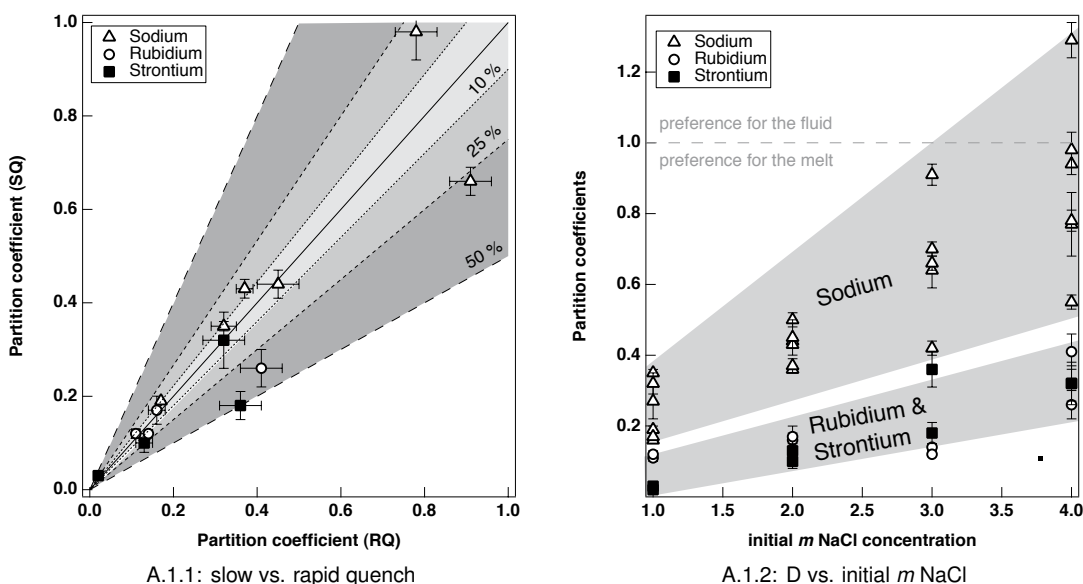


Figure A.1: Comparison of partition coefficients of Na, Rb, and Sr from slow and rapid quenched experiments (Fig. A.1.1) and dependence of  $D^{f/m}$  on the initial NaCl concentration in the fluid (Fig. A.1.2).

The correlation between  $D_{Na}^{f/m}$  and trace element partition coefficients as a function of melt composition are shown in Fig. A.2.1 for Rb and in Fig. A.2.2 for Sr. In addition, dependent of the composition of the melt, feldspar or quartz crystallized in some of the experiments. In the case of Rb, no effect of melt composition is observed. The  $D_{Rb}^{f/m}$  increase with increasing Na partition coefficient (Fig. A.2.1). The increase can be described by the following linear correlation  $D_{Rb}^{f/m} = 0.01 + 0.31 * D_{Na}^{f/m}$ . For strontium, a strong effect of melt composition is observed. In experiments with albite-rich melts (AQ1) Sr partition coefficients scatter between 0.01 and 0.04, whereas a linearly increase with  $D_{Na}^{f/m}$  is observed in runs using AQ2 melt composition

(Fig. A.2.2). The latter can be characterized by the linear equation  $D_{Sr}^{f/m} = -0.05 + 0.42 * D_{Na}^{f/m}$ . In the case of the albite-rich composition, the very low Sr partition coefficient can easily explained by the formation of Sr-bearing feldspars.

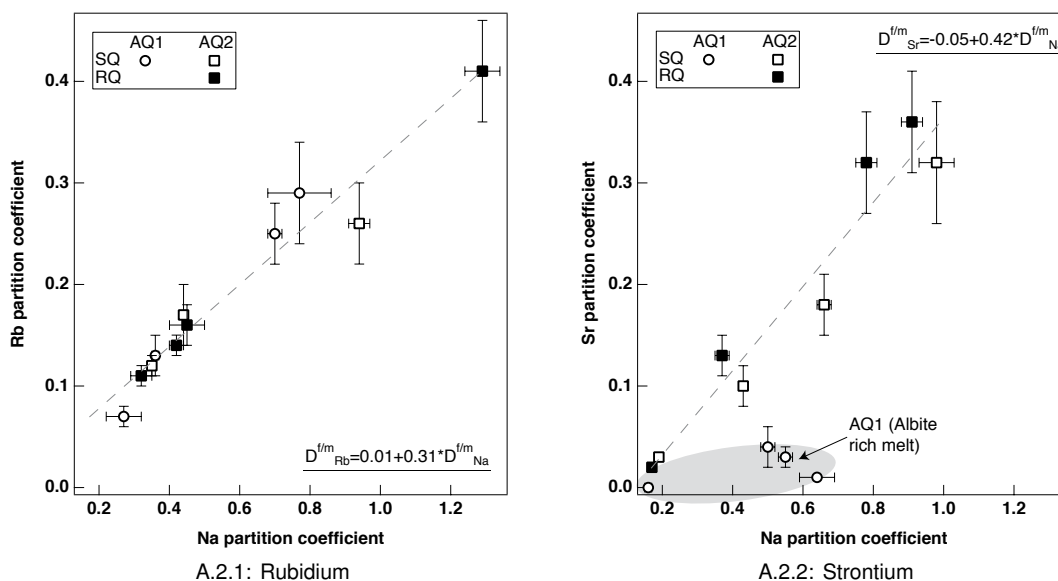


Figure A.2: The dependence of fluid–melt partition coefficients on the  $D_{Na}^{f/m}$  as a function of melt composition are shown in Fig. A.2.1 for Rb and Fig. A.2.2 for Sr.

These experiments clearly show that neither Rb nor Sr preferentially partition into the fluid even at high fluid salinities. Partition coefficients of Rb and Sr at similar fluid salinity are only slightly lower than the data from experiments in the system albite-orthoclase-quartz. Another observation in the AQ system is that Rb and Sr partition coefficients are almost similar, whereas in the AOQ system  $D_{Rb}^{f/m} > D_{Sr}^{f/m}$  at similar fluid salinity. The main difference between experiments in both systems besides the composition is a reduction of the number of trace elements in a experiment to one (AQ) whereas AOQ compositions were doped with four trace elements. Therefore, the results suggest that interactions between trace elements themselves may also contribute to fluid–melt partitioning. In general, this may be of minor importance.



## Appendix B

# Methods for fluid analyses in quenched experiments

Inductively-coupled plasma–optical emission spectrometry and Ion Chromatography are used to determine the element concentrations in fluids from quenched experiments. Due to the relatively high fluid amount that is needed for the analyses, measurements are carried out in H<sub>2</sub>O–diluted samples. The results are recalculated to the weight of the undiluted fluid. This is done by subtracting the weight of capsule material and quenched glass from the weight of the unopened capsule after the run.

### B.1 Inductively-coupled plasma - optical emission spectrometry

The measurements were performed with a simultaneous inductively–coupled plasma – optical emission spectrometry (ICP–OES, Varian Vista-MPX, Institut für Geowissenschaften, Universität Potsdam) coupled to a V-groove nebulizer and equipped with a charge coupled device (CCD). The ICP conditions are shown in Tab. B.1.

Table B.1: ICP–OES instrumental conditions

Plasma	Argon
RF generator power [kW]	1.2
Plasma gas flow rate [L min <sup>-1</sup> ]	15.0
Auxiliary gas flow rate [L min <sup>-1</sup> ]	1.5
Nebulizer flow rate [L min <sup>-1</sup> ]	0.75
View high [mm]	10
Replicates	3
Sample uptake [s]	30
Rinse time [s]	10
Pump rate [rpm]	15

The fluids are analyzed for Na, K, Si, Al, Rb, Sr, La, Yb and Y. The calibration for each element was performed using a blank and two standard solutions. Standard solution one (two) contains

10 (25) mg/l Na and K, 2.5 (10) mg/l Si and Al, 1.25 (2.5) mg/l Rb and Sr, and 0.5 (1) mg/l La, Y and Yb. Argon was used as internal standard. For each element an emission line was chosen, preferably the most intensive one and undisturbed by emission lines of other elements (Tab. B.2). The detection limit ( $dl$ , B.2) of each element was determined experimentally using replicate measurements of a standard solution that contains 0.1 mg/l of each element, and calculated using

$$dl_X = c_X \cdot 3 \cdot \sqrt{B} / I_{net}$$

where  $c_X$  is the concentration of element  $X$  in the standard solution,  $B$  is the mean value of the background signal, and  $I_{net}$  is the mean signal from the net intensity.

Each sample was measured three times, and the mean value is used for determination of element concentrations.

Table B.2: Emission lines (upper line, [nm]) and detection limits (lower line, [mg/l]) for ICP analyses.

Na	K	Si	Al	Rb
588.995	766.491	288.158	396.152	780.026
0.02	0.23	0.05	0.06	0.14
Sr	Ba	La	Y	Yb
407.771	455.403	408.671	360.074	328.937
0.0004	0.002	0.01	0.01	0.004

## B.2 Ion Chromatography

Ion chromatography (IC, DIONEX DX 100 or 120, Helmholtz-Zentrum Potsdam Deutsches GeoForschungsZentrum) is used to determine the anion concentrations, e.g., fluoride, chloride, nitrate, and sulfate in aqueous solutions. The anions are separated based on their differential affinity for a low capacity, strongly basic anion exchange resin (Small et al., 1975). Here, we determine the concentration of  $\text{SrCl}^-$  in fluids from experiments using chloridic starting solutions. The operating conditions are listed in Tab. B.3. The calibration is accomplished by five standard solutions containing 20 to 100 mg/l  $\text{SrCl}^-$ . The calibration curve is determined from the peak area acquired for each different calibration level using a linear interpolation. The correlation coefficient ( $R^2$ ) has a value of 0.995. The concentration of  $\text{SrCl}^-$  in the sample is determined using

$$x_{Cl} = (K_1 \cdot \text{area}_{Cl}) + K_0$$

where  $x_{Cl}$  is the concentration of  $\text{SrCl}^-$  in the sample,  $\text{area}_{Cl}$  is the area of  $\text{SrCl}^-$  in the sample, and  $K_1$  and  $K_0$  are the slope and the y-axis intercept of the chlorine calibration curve.

Table B.3: Operation conditions for determination of chloride by Ion Chromatography

Guard column	AG9HC
Analytical column	AS9HC
Suppresser	ASRS 300 Anion self-regenerating suppresser
Eluent	9 mM $\text{Na}_2\text{CO}_3$ sodium carbonate
Flow rate	1.0 ml/min (eluent)
Detector cell	DS4 Detection stabilizer
Sample loop	50 $\mu\text{l}$
Sampler	AS50 Automated sampler



# Appendix C

## Curriculum Vitae

### Manuela Borchert

Universität Potsdam  
Institut für Geowissenschaften  
Karl-Liebknecht-Str. 24; Haus 27  
14476 Potsdam-Golm  
Germany  
Date of Birth: April 13, 1979  
Citizenship: german

Phone: +49 (0)331 977 5787  
Fax: +49 (0)331 977 5700  
Email: manu@geo.uni-potsdam.de

### Education

**since 10/2006:** Ph.D. student, Universität Potsdam

*Supervisors:* Prof. R. Oberhänsli (Uni. Potsdam) and Dr. Christian Schmidt (GFZ Potsdam)

*Project leader:* Dr. Max Wilke (GFZ Potsdam)

*Project:* Interactions between aqueous fluids and silicate melts (DFG projects Wi2000/3-1, Wi2000/3-2)

**09/2006:** Diploma in mineralogy, Universität Potsdam

*Supervisors:* Dr. Max Wilke, Dr. Christian Schmidt

*diploma thesis:* "Spurenelementverteilung zwischen silikatischen Schmelzen und wässrigem Fluid – eine experimentelle Studie"

**10/1999 – 09/2006:** Studies of mineralogy, Universität Potsdam,

04/2000 - 03/2001: academic leave of absence (pregnancy)

**10/1998 – 09/1999:** Studies of mathematics, Universität Potsdam,

## Scholarships

DAAD Fachkursstipendium für Doktoranden (HERCULES Specialized Course on Synchrotron Radiation and Neutron Techniques in Environmental Sciences (ESRF, 18 to 24 May 2008))

## Fields of Interest

*Experimental Mineralogy, Petrology and Geochemistry*

(Trace) element partitioning between melts, fluids and minerals

HP/HT techniques

Synchrotron Radiation (SR) applications in earth sciences

## Academic Experience

### Universität Potsdam, Institut für Geowissenschaften

field mapping course, Spain, March 2008

research assistant (exercises & tutorials)

supervision of a diploma thesis

## Research

### Manuscripts in preparation

Borchert, M.; Wilke, M.; Schmidt, C.; Kvashnina, K.: Strontium complexation in silicate fluids at high PT: insights from XANES spectroscopy.

Borchert, M.; Wilke, M.; Schmidt, C.; Cauzid, J.; R. Tucoulou: Partitioning of Ba, La, Yb and Y between haplogranitic melts and aqueous solutions: an experimental study.

### Publications

Borchert, M.; Wilke, M.; Schmidt, C.; Rickers, K. (in press): Rb and Sr partitioning between haplogranitic melts and aqueous solutions, *Geochimica et Cosmochimica Acta* (doi:10.1016/j.gca.2009.10.033).

Borchert, M.; Wilke, M.; Schmidt, C.; Rickers, K. (2009): Partitioning and equilibration of Rb and Sr between silicate melts and aqueous fluids, *Chemical Geology* 259, 39-47 (doi:10.1016/j.chemgeo.2008.10.019)

Borchert, M.; Wilke, M.; Schmidt, C.; Rickers, K. (2008): Partitioning of Rb and Sr between haplogranitic melts and aqueous fluids, *Geochimica et Cosmochimica Acta*, 72, 12, Suppl. 1, A97.

Borchert, M.; Schmidt, C.; Wilke, M.; Rickers-Appel, K. (2007): In-situ study of Rb equilibration between silicate melts and aqueous fluids, *HASYLAB Annual Report*, 1593-1594.

Borchert, M.; Wilke, M.; Schmidt, C.; Rickers-Appel, K.; Koepke, J. (2007): Partitioning of Rb and Sr between haplogranitic melts and aqueous fluids: Information from in situ experiments using SR-XRF, *Geochimica et Cosmochimica Acta*, 71, 15, Suppl. 1, A109.

## Conference Presentations

Schmidt, C.; Wilke, M.; Borchert, M.; Rickers, K. (2009): Determination of fluid densities in hydrothermal diamond-anvil cell experiments using SR-XRF intensities, XX ECROFI meeting, Granada (Sep, 23-25) - Poster.

Borchert, M.; Wilke, M.; Schmidt, C.; Rickers, K.; Kvashnina, K. (2009): Partitioning of Rb and Sr between silicate melts and aqueous fluids: effect of fluid and melt composition, XX ECROFI meeting, Granada (Sep, 23-25) - Poster.

Ebert, M.; Borchert, M.; Wilke, M. (2009): Partitioning of Barium and Lead between aqueous fluids and haplogranitic melts at 750 C and 200 MPa, DMG conference, Halle (Sep, 14-16) - Poster – **Posterpreis DMG 2009** –.

Borchert, M.; Wilke, M.; Schmidt, C.; Kvashnina, K. (2009): Partitioning of Rb and Sr between silicate melts and aqueous fluids: insights from Sr complexation analysis by XANES, DMG conference, Halle (Sep, 14-16) - Poster.

Borchert, M.; Wilke, M.; Schmidt, C.; Rickers, K. (2009): Rubidium and Strontium partitioning between haplogranitic melts and aqueous solutions, DMG Sektionstreffen Petrologie-Petrophysik, Mainz (May, 15-16) - Talk.

Borchert, M.; Wilke, M.; Schmidt, C.; Rickers, K. (2008): Fluid-melt partitioning of Rb and Sr: Classical quench vs. in-situ experiments, DMG conference, Berlin (Sep, 14-17) - Talk.

Borchert, M.; Wilke, M.; Schmidt, C.; Rickers, K. (2008): Effect of melt composition on the partitioning of Rb and Sr between haplogranitic melts and aqueous solutions at 750 C and 200 to 500 MPa, EMPG XII Conference, Innsbruck (Sep, 08-11) - Talk.

Borchert, M.; Wilke, M.; Schmidt, C.; Rickers, K. (2008): Partitioning of Rb and Sr between silicate melts and aqueous fluids, Goldschmidt Conference, Vancouver (July, 14-18) - Poster.

Borchert, M.; Wilke, M.; Schmidt, C.; Rickers, K. (2008): Partitioning and equilibration of Rb and Sr between silicate melts and aqueous fluids, DMG Sektionstreffen Petrologie-Petrophysik, Tübingen (May, 30-31) - Talk.

Borchert, M.; Wilke, M.; Schmidt, C.; Rickers, K. (2008): Partitioning and equilibration of Rb and Sr between silicate melts and aqueous fluids, Hercules Specialized Courses (HSC8) on Synchrotron Radiation and Neutrons Techniques in Environmental Sciences at ESRF, Grenoble (May, 19-23) - Poster.

Borchert, M.; Wilke, M.; Schmidt, C.; Rickers-Appel, K.; Koepke, J. (2007): Partitioning of Rb and Sr between haplogranitic melts and aqueous fluids: Information from in situ experiments using SR-XRF, Goldschmidt Conference, Cologne (Aug. 19- 24) - Poster.

Borchert, M.; Wilke, M.; Schmidt, C.; Rickers, K. (2007): Bestimmung von Verteilungskoeffizienten zwischen haplogranitischen Schmelzen und wässrigen Fluiden - vorläufige Ergebnisse, DMG Sektionstreffen Petrologie-Petrophysik, Kiel (June, 09-10) - Talk.

Borchert M., Wilke M., Schmidt C. (2006) Experimental study on the trace element partitioning between haplogranitic melts and chloridic aqueous fluid. DMG Conference (Sep. 25-27) - Talk.



## **Erklärung der Selbstständigkeit**

Hiermit versichere ich, die vorliegende Arbeit selbstständig verfasst und keine anderen als die angegebenen Quellen und Hilfsmittel benutzt sowie die Zitate deutlich kenntlich gemacht zu haben.

Potsdam, 26. April 2010

---

Manuela Borchert